The evolution of transform boundaries in response to plate motion changes

Georgios-Pavlos Farangitakis

A thesis submitted to Durham University in fulfilment of the requirements for the degree of

Doctor of Philosophy

September, 2020

Abstract

Transform margins and transform faults are first order tectonic features that accommodate or have accommodated motion between tectonic plates in our planet. Changes in plate motion that occurred in the past as tectonic plates moved are imprinted and documented on the planet's divergent and convergent plate margins. In a similar manner, these motion changes are expected to be found along transform systems. Thus, investigating transform margins and identifying structures that detail such plate motion changes is of great scientific interest to delineate their evolution. Moreover, areas around transform margins and faults have a significant resource potential (such as the hydrocarbon fields offshore Ghana or the geothermal potential of the Gulf of California) and earthquake hazard risk (such as the San Andreas or North Anatolian faults).

In this thesis, a multi-disciplinary and multi-scale approach using numerical and physical analogue modelling is applied to investigate the evolution of transform plate boundaries and faults when these are affected by changes in plate motions. The combination of analogue and numerical modelling was selected as these two methods complement each other by having different strong points. Numerical modelling offers fast and multiple iterations of experiments while analogue modelling offers straightforward observable physics.

First, a numerical modelling approach covering the lithosphere-scale is presented that highlights the differences between the effect obliquely inherited structures versus changes in plate motion have on transform margins. The main finding is that changes in plate motion affect transform margin evolution significantly both in duration and also in structure. Then, two analogue modelling studies follow. The first one focuses on the crustal scale and investigates what changes a transform margin and a rift-transform intersection undergo when a change in plate motion occurs. The most significant findings of this set of experiments are that the transform systems re-orient to accommodate the changes in the plate motion through the creation of new strike-slip faults and that faults in such systems display a dual character (i.e. oblique-normal or oblique-reverse). The second set of analogue modelling experiments represents an investigation into basin-scale transtensional rotations along releasing bends on transform faults (pull-apart basins). The key finding of this set of experiments is that the resulting pull-apart morphology from these models (such as an asymmetrical triangular shape and faults oblique to the extension trend) can be used as an identifying tool for pull-apart basins that have experienced a change in plate motion during their evolution.

The modelling results are compared against natural examples, such as the Gulf of California, the Tanzania Coastal Basin, and the Gulf of Aden. The very high degree of similarity between the models and nature, apart from validating the models, also indicates that changes in plate motion add a further degree of complexity to the evolution of transform plate boundaries. This complexity can be seen in the dual character of faulting along Principal Displacement Zones, or in oblique fault orientation in pull-apart basins, and even in rifting asymmetry in rift-transform intersections. Thus, plate motion changes should always be considered when investigating transform boundaries, as potentially they are the rule, and not the exception.

Table of Contents

List of Figures

List of Tables

Statement of Copyright

I declare that this thesis, submitted for the degree of Doctor of Philosophy at Durham University, is my own work and not substantially the same as any which has been previously submitted at this or any other university. Where appropriate, I have clearly indicated the contributions of colleagues to fully acknowledge all collaborative work.

Georgios Pavlos Farangitakis

Durham University

September 2020

Acknowledgements

So, although the world is heading again down the drain of lockdowns, infections and preventable deaths from this pandemic, I dare say I am actually quite happy at the moment as four wonderful years of research have reached a conclusion with this thesis being finalised. But it would not have been finished without every person mentioned below having played their part. I am well aware that the tendency is to write relatively short acknowledgements but I think you do a PhD once in your life and saying thank you for that doesn't need to be in a short small list.

First and foremost, I would like to thank my main supervisor Professor Ken McCaffrey. I'll be forever grateful that you offered me this opportunity to do this PhD back in February 2016. When we met for the first time in September 2016 as I was starting, you told me you wanted me to become an independent researcher so I should not be asking you what to do every time as my thesis progressed. At the time this freaked me out a bit I have to admit, as I was not sure what that meant. But now I am actually thankful for you challenging me to go about designing everything these four years (from the experiments, to the papers, to the thesis itself) by myself and then checking that idea with you. I hope I have lived up to what you wanted me to be at the end of these years. Having discussed PhD supervision with countless people the past few years I've arrived to the conclusion that what makes a good supervisor for each person is a subjective matter. I can say with absolute certainty though that you are objectively the perfect supervisor for me.

Next, I'd like to thank my second supervisor from Durham, Professor Jeroen van Hunen. When in the beginning of 2017 we were realizing that there won't be any luck with the seismic data from the industry, you suggested I met with this group from Utrecht that does analogue modelling and try and go about that way. That resulted in 66% of this thesis. A year later you introduced me to Phil who worked with ASPECT and that resulted in the remaining 33% of this thesis. Introducing me to these people was invaluable for this work to be completed. I am also grateful for your patience and perseverance when you were trying to explain to me how certain bits in the code work. You made geodynamics fun for me, even though I was daunted by the prospect of numerical modelling in the beginning. Finally, I think I can say that I kind of owe you the fact that I am now living in the Netherlands when you sent me to Utrecht to work with Dimi and Ernst.

Finally, I'd like to thank Doctor Lara Kalnins, from the University of Edinburgh. This thesis, the papers comprising it and every bit of work I have presented to the academic world would not have been possible without your diligent editing skills. I occasionally catch myself wondering even when I am writing an informal email "would Lara cut this sentence in half to make sense?". You

showed enormous amounts of patience editing all of my pieces of work and literally making them as academically sound and as perfectly formatted as possible. If a piece of my work did not have you as its last person that edited it, I always felt very hesitant to present it. You make a fantastic supervisor and anyone that is lucky enough to have you in their team, either as a collaborator or as a supervisor, is bound for success. Also, I hope the commas in the acknowledgements are all in the right place!

This PhD study was undertaken as part of the Natural Environment Research Council (NERC – now UKRI) Centre for Doctoral Training (CDT) in Oil & Gas [grant number NEM00578X/1]. It is co-sponsored by Durham University whose support is gratefully acknowledged.

One acquaintance I made during these four years that I enjoyed the most was the former head of the TecLab in Universiteit Utrecht, Professor Dimitrios Sokoutis (also known as The General). As I said in your retirement, I owe you a huge "thank you" for showing me how fun hands-on experimental work can be and how science does not need to be taking place in a sterile environment. It was amazing making the cakes (for non-analogue modellers that's how we call the experiments) and doing state-of-the-art science while at the same time discussing lamb recipes and the Battle of Crete. From the same lab I would also like to thank Professor Ernst Willingshofer, now head of the TecLab, who also helped an immense amount during these two experimental stints. Thank you for accommodating my stay there, for providing me with all the materials necessary and I really hope we can get to put some of our modelling ideas into action in the years to come. Finally, from Utrecht I'd also like to thank Antoine, Vera, Yola & Marjolein for keeping me great company, helping with the experiments (especially Vera) and showing me around in the Netherlands the first time I was there.

I'd also like to thank Phil Heron, who worked with me on the 4th Chapter of this thesis. Phil, you're one of the greatest people I got to work with. I am really grateful for you finding the time for me always. You helped me so much setting up the experiments of Chapter 4, writing the paper and getting through what was a rough process of reviewing it. I'll never forget how you came by my desk and sat and ran me through each reviewer's points and how to address them. I think that's not a common thing to see in academia nowadays. Another thing I'll never forget is the look on the eyes of that former inmate who was describing how you taught them science in prison as part of your outreach programme. You are a truly inspiring person and it's a shame academia is not keeping people like you in its ranks. Thanks for everything.

I'd like to also thank two more people who collaborated in the work presented here. Professor Patricia Persaud from Louisiana State University who provided very valuable insights on the

evolution of the Gulf of California as she is a world renown expert in that particular area. It was really great working with you and I'd have liked to meet in person in AGU this year but the pandemic had other plans. Finally, I'd like to thank Professor Mark Allen for heling with one of the natural examples shown in Chapter 6 of this thesis. I enjoyed working on this manuscript with you. Also let me say that during our induction in the Department as first year students you had said to us "work smart hours not long hours". I took that advice to heart and I believe it helped complete this thesis without any unnecessary panic the past few months.

Here I'd like to say thank you to four people I have worked with (or been taught by) in Greece before my PhD. First, I would like to say a huge thank you to Professor Ioannis Papanikolaou. If it was not for you, I would not have gotten this PhD. Thank you for recommending me to Ken, and for convincing me to apply for it. Second, I'd like to thank Professors and friends Giannis Alexopoulos and Manolis Vassilakis. I've known you since you first taught me some 7 or so years ago and it's been a pleasure working with you and seeing you everytime I am in Greece (Gianni) or we meet over some wings and ribs in Vienna (Manoli). Your advice on my career and life has always been spot on and I am really lucky to have made your acquaintance.

Finally, I'd like to thank the person that inspired me to go into Structural Geology. I sometimes try to think which was the defining moment that got me fascinated by faults, plate movements and decoding the structural history of outcrops in 3D. I can think of three of those. The first one was when I was reading your book "Introduction to Geology" and our planet, its mountains and oceans started making sense. The other one was in the amphitheatre a few years later when I heard you describe to us in "Geology of Greece" how the tectonostratigraphic terranes of Greece got accreted and how every stratigraphic unit had a specific evolutional pattern. Then, all the terminology I kept hearing in sedimentology, igneous, sedimentary or metamorphic petrology that never really got to me, suddenly started making sense again. Finally, in my last year, in the elective course "Geology of Europe" the day you summed up Europe's evolution Infront of that huge map in room G14 I was left gasping at how again the placement of Italy, Sardinia, the Urals and Scandinavia finally made sense. I am referring to Professor Emeritus Dimitrios Papanikolaou who back in my undergrad years used to teach us the Structural related courses. I am really happy that I got to also work with you on a paper and also teach a practical course under your supervision. The inspiration you gave me really contributed to me wanting to contribute in advancing the knowledge in Structural Geology.

I'd also like to say a big thank you to my friends from the Department of Earth Sciences in Durham. Nico, CJ, Max, Ilaria, Giacomo, Kate, Ahmed, Alex, Jordan, Chris Ward, Tim, and Phoebe you all made these four years contain a significant amount of fun and I'm really grateful for that.

I would also like to thank the departmental Greeks (sometimes termed by some as “the Greek mafia”). Dimitris M., Dimitris C., and Nikos (with the addition of Christos later) you all made life in what we between us called Mordor (sorry to the locals but when you’ve grown up in Greece, the weather and the amount of sunlight in Durham accurately fits that description) a bit more bearable by bringing a touch of home there.

During my PhD I took up the -annoying to my non-runner social circles- habit of running Marathons. For that I have no other person to thank but for my colleague Jack Lee. Thank you for keeping me sane these four years and motivating me to go for lunchtime runs. It was really nice having someone to motivate me when I was in a four-month training circle and did not want to get up from my desk and run. Thank you also for the constant stream of chocolate and artisan coffee that you brought my way. You’re a really good friend and I’ll be really happy every time we meet in the future to go for runs.

What also kept me even saner than running was the three daily breaks with our “smoking group”. Ines (and Pierre-Yves although you don’t smoke) and Jack I really appreciate the therapeutic conversations we had every day at 10, 1 and 3 over a cigarette. I know that in you I’ve made friends for life that I can count on. Thanks for giving me reality checks when necessary and for giving me really good advice on how to streamline my writing and editing process.

I also want to thank Tom and Rachel Utley (of House Utleakis). You provided me with a house in the last three years of my PhD that I was able to call a home. It’s really nice having like-minded people to live with and not be lonely during a PhD and you did exactly that for me. It was amazing spending this time with you and I wish you every success in life. I will always remember Tom’s Sunday roasts and the hours of conversations on politics with Rach. On a happy side-note I really appreciate you not throwing up on my first attempt to make a pastitsio.

I’d also like to thank my very good friend Bartek. We met 6 years ago starting our Master’s together in Aberdeen and luck had it that we’d also be doing a CDT PhD at the same time. It’s really nice to have a friend that comes from a very similar walk of life and faces almost identical problems as we both did. You are an amazing scientist, that even though has little idea about analogue modelling was always keen to help me brainstorm and bounce ideas back and forth. You are a person that it’s an honour to call a friend in one’s life. I wish you and Agata (and your baby girl) all the best in life because you really deserve it.

In the last six months of the process of this PhD, I relocated to the Netherlands to avoid the uncontrollable spread of the pandemic that was imminent in the UK. Here I was welcomed by my girlfriend’s family who took me in as their own and helped me get through these challenging

times. Nans, Michiel and Gijs I am really grateful to you for having me here and I hope I caused as minimal a disruption to your everyday lives as possible. I also want to thank my pets Karel, Willem and Nora for keeping me company while I was writing this PhD. Nothing calmed me down more than cuddling up to Karel and having a short nap while he was purring loudly.

I would also like to thank my family friend Eleni. Your advice the last 9 years that I know you has always been spot on. Everything you've ever suggested I do or think about has always proven to take me down the right path and I'll be forever grateful for that. I hope that as I've promised you graduation takes place with a crowd this time and I can invite you over.

Then, I'd like to thank my really good friends the past 13 years Orestis and Manolis. With Orestis I collaborated together writing our BSc research thesis under the supervision of Manolis and that gave birth to a friendship that lasts until now. Your advice, your understanding and you always being there for me is something I'll forever cherish. Who am I kidding, it's actually the memes and the PASOK jokes that make my day that keep me going. It's been an honour gentlemen. And to not forget… Ραντεβού στα γουναράδικα Σύντροφοι.

Second to last, I would like to thank my family. Without your contribution, both mental and financial earlier on, I would not have been where I am now. I want to say a couple of things to each of you separately so I will start with my father, Georgios Farangitakis. Although sometimes I have heard you wondering if you did the right job as a father, I want you to know you brought me up to be a person with values and ethics. You taught me to see right from wrong in the world and to know where I am coming from. This includes being a fan of AEK Athens by the way. You motivated me to get the right stimuli in music and art earlier on in life and that has had a massive bearing on who I am now. The poem that is my selected quote to lead this thesis is something you used to read to me as a kid and you always told me to remember that it was the journey and not the goal that matters. And I thank you so much for that. Next, my mother, Professor Margarita Arianoutsou-Farangitaki. Not many kids have the privilege of growing up as the child of an esteemed academic. You cultivated scientific thinking in me from a very young age, either by taking me to the University to play with the microscopes and look at the backstage of the Natural History museum, or by buying me National Geographics and child science books. At the time where kids were getting Action Man and Mad Max toys, you'd get me Legos and nature observation guides. You taught me to look at everything around me with a critical, informed and evidence backed view and I'm forever grateful for that (although in the modern world that's sometimes a curse and not a blessing). You also offered me top quality advice during my PhD on how to handle my writing, my presentations and even my supervisors (sorry folks I did ask her a couple of times how to handle you) and I really thank you for this. Σας αγαπάω από τα βάθη της

καρδιάς μου και τους δύο και σας ευχαριστώ για όλες τις θυσίες που έχετε κάνει για εμένα. Ελπίζω πως αυτό εδώ το διδακτορικό να αποτελεί μία μορφή ανταμοιβής γι' αυτό.

Finally, I would like to thank my girlfriend Fi. You have been by my side the last three years and I am 100% positive that if it was not for you, this PhD would not have been completed. You are a source of inspiration with the way you have handled everything life has thrown at you and kept powering through it. You've literally helped me with my actual PhD by offering your graphics designer skills on my first paper. You've been there on my breakdowns every time I got frustrated with a correction, or an edit, or when something was not working in my experiments. You've kept me sane throughout the process and I know I have taken a toll on your sanity by doing that. In the last 6 months you went out of your way to host me in your room during the pandemic, got me a desk to work on, a second monitor, a mouse, food and a bed to sleep on and so many more things that I don't think I can ever say enough "thank yous" for. And you did all that while being on the frontline of the fight against the virus, working overtime every day in your lab. Nothing I can say or do will ever be enough to repay you for how much you have helped me, cared for me and loved me. You are everything a man can ask for in his life. I love you from the bottom of my heart, from the moment we met in Utrecht 3 years ago when I started this work presented here. And I am so really looking forward to starting our life here together in the Netherlands.

Quote

Σὰ βγεῖς στὸν πηγαιμὸ γιὰ τὴν Ἰθάκη,
νὰ εὔχεσαι νἆναι μακρὺς ὁ δρόμος,
γεμάτος περιπέτειες, γεμάτος γνώσεις.

Τοὺς Λαιστρυγόνας καὶ τοὺς Κύκλωπας,
τὸν θυμωμένο Ποσειδῶνα μὴ φοβᾶσαι,
τέτοια στὸν δρόμο σου ποτέ σου δὲν θὰ βρεῖς,
ἂν μέν᾽ ἡ σκέψις σου ὑψηλή, ἂν ἐκλεκτὴ
συγκίνησις τὸ πνεῦμα καὶ τὸ σῶμα σου ἀγγίζει.

Τοὺς Λαιστρυγόνας καὶ τοὺς Κύκλωπας,
τὸν ἄγριο Ποσειδώνα δὲν θὰ συναντήσεις,
ἂν δὲν τοὺς κουβανεῖς μὲς στὴν ψυχή σου,
ἂν ἡ ψυχή σου δὲν τοὺς στήνει ἐμπρός σου.

Νὰ εὔχεσαι νά ῾ναι μακρὺς ὁ δρόμος.
Πολλὰ τὰ καλοκαιρινὰ πρωϊὰ νὰ εἶναι
ποὺ μὲ τί εὐχαρίστηση, μὲ τί χαρὰ
θὰ μπαίνεις σὲ λιμένας πρωτοειδωμένους·

νὰ σταματήσεις σ᾽ ἐμπορεῖα Φοινικικά,
καὶ τὲς καλὲς πραγμάτειες ν᾽ ἀποκτήσεις,
σεντέφια καὶ κοράλλια, κεχριμπάρια κ᾽ ἔβενους,
καὶ ἡδονικὰ μυρωδικὰ κάθε λογῆς,
ὅσο μπορεῖς πιὸ ἄφθονα ἡδονικὰ μυρωδικά.

Σὲ πόλεις Αἰγυπτιακὲς πολλὲς νὰ πᾷς,
νὰ μάθεις καὶ νὰ μάθεις ἀπ᾽ τοὺς σπουδασμένους.
Πάντα στὸ νοῦ σου νἄχῃς τὴν Ἰθάκη.
Τὸ φθάσιμον ἐκεῖ εἶν᾽ ὁ προορισμός σου.

Ἀλλὰ μὴ βιάζῃς τὸ ταξείδι διόλου.
Καλλίτερα χρόνια πολλὰ νὰ διαρκέσει.
Καὶ γέρος πιὰ ν᾽ ἀράξῃς στὸ νησί,
πλούσιος μὲ ὅσα κέρδισες στὸν δρόμο,
μὴ προσδοκώντας πλούτη νὰ σὲ δώσῃ ἡ Ἰθάκη.

Ἡ Ἰθάκη σ᾽ ἔδωσε τ᾽ ὡραῖο ταξίδι.
Χωρὶς αὐτὴν δὲν θἄβγαινες στὸν δρόμο.
Ἄλλα δὲν ἔχει νὰ σὲ δώσει πιά.

Κι ἂν πτωχικὴ τὴν βρῇς, ἡ Ἰθάκη δὲν σὲ γέλασε.
Ἔτσι σοφὸς ποὺ ἔγινες, μὲ τόση πείρα,
ἤδη θὰ τὸ κατάλαβες ἡ Ἰθάκες τί σημαίνουν.

Κωνσταντῖνος Καβάφης - Ἰθάκη

1 Introduction

1.1 Project motivation

Ever since the first world's explorers such as Magellan and Ortelius in the 16th century observed that the Earth's continents display a puzzle-like fit, scholars have tried to identify the driving force behind changes in the planet's continental configuration. Wegener (1912) was the first to suggest that our planet's crustal architecture is driven by plate motion through a process identified as continental drift. Since then, geologists have tried to delineate the manner in which the boundaries of these plates develop and interact. Transform boundaries are one of the three primary plate boundary classes (with the other two being convergent and divergent), where relative plate motion is predominantly parallel to the boundary. Transform margins, transform faults and large-scale strike-slip faults are first-order structural features present on the boundaries of almost every tectonic plate across the globe. Transform faults were first discussed and described in the context of shear margins in the 1960-1970s (e.g. Wilson, 1965; Le Pichon & Hayes, 1971; Turcotte, 1974; Mascle, 1976; Scrutton, 1979). These faults are important in the continental domain as they are often responsible for large, devastating earthquakes. Examples of such earthquakes include the 1906 San Francisco earthquake (San Andreas Fault), the 1999 Izmit earthquake (North Anatolian Fault) and the 2002 Denali earthquake (Denali-Totschunda Fault). Thus, deformation along these types of faults is a major threat to the well-being of nearby societies. Finally, areas along continental and continent-ocean transform margins and faults are of high economic importance due to their potential for hydrocarbon and geothermal resources (Nemcok et al., 2016; Prol-Ledesma & Moran-Zenteno, 2019).

Studies in the past three decades have provided improved conceptual models for the evolution of these structures (e.g. Lorenzo, 1997; Reid & Jackson, 1997; Basile & Brun, 1999; Bird, 2001; Gerya, 2010; Gerya, 2012; Basile, 2015; Mercier de Lépinay et al., 2016). Nevertheless, transform faults across the world remain considerably understudied compared to their extensional and

compressional counterparts. In particular, key questions on their origin and formation still remain, such as: a) the spontaneous transform generation between two rifts or spreading centres (Stoddard & Stein, 1988; Gerya, 2010; Illsley-Kemp et al., 2018), b) the origin of continental highs on transform margin flanks, termed marginal ridges (Lorenzo, 1997; Basile, 2015; Mercier de Lépinay et al., 2016) and c) the presence of zones of transpression along fracture zones (Davison et al., 2016; Phethean et al., 2016). In this thesis, the general issue of how transform margins and releasing bends along large strike-slip systems respond to changes in relative plate motion is examined. Furthermore, the role of structural inheritance versus changes in plate motion on a transform margin is also investigated. After a brief overview that places this study within the wider context of transform margin studies, the specific questions addressed in this work are posed and an outline of how they are investigated is presented.

1.2 The context of this study

Transform margins represent plate boundaries that accommodate or have accommodated strike-slip motion through a transform fault between two plates (Mascle, 1976; Scrutton, 1979). The detailed structural issues that concern transform margins are discussed in greater detail in Chapter 2. As mentioned above, in addition to their scientific interest, transform margins are also areas of established hydrocarbon production and exploration (Nemcok et al., 2016). In West Africa, the Jubilee oil field, situated between the St Paul and Romanche Fracture Zones, is believed to contain over a billion barrels of recoverable oil (Whaley, 2010), with similar types of petroleum plays existing in its conjugate margin across the Atlantic in Brazil (Mello et al., 2013). In the Exmouth Plateau in W. Australia, significant producing fields exist adjacent to the associated fracture zone (Exon & Willcox, 1978; Stagg et al., 2004). Finally, in the Falkland/Malvinas continental shelf, MacAuley (2014) reports four reservoir discoveries linked closely to the giant, South Atlantic-spanning Agulhas-Falkland Fracture Zone (Marishane et al., 2014). As Nemcok et al., (2016) report, the highest risk factors for exploration in transform margins are the uncertainty of the post-spreading uplift patterns in space and time and poor knowledge of the structural

architecture and transform activity evolution through time. Furthermore, areas with associated transform tectonics often display significant geothermal potential, such as the Gulf of California, which is considered to have an immense potential for providing geothermal energy (Prol-Ledesma & Moran-Zenteno, 2019).

While the three endmembers of classical tectonic plate motion theory (Figure 1.1 - divergence, convergence and strike-slip) are widely accepted as the dominant forms of plate boundaries, a number of plate boundaries do not display endmember characteristics, but rather a mixture of these. These are plate boundaries that undergo changes in the relative plate motion vector or are influenced by inherited structures, and hence in their lifespan can move into different domains as represented on the triangle (Figure 1.1). A particularly good example of the effect plate motion changes have on the evolution of a transform margin through time is the Gulf of California, which is one of the key areas studied in this thesis. In the Gulf of California, a change in the plate motion vector that favoured strike-slip over the pre-existing extension (Bennet & Oskin, 2014) led to the creation of seven en-echelon transform-spreading ridge systems with different structural styles, ranging from pull-apart basins, to narrow rifts, to magmatic and amagmatic rifts (Lizarralde et al., 2007). More generally, Brune et al. (2018) report that oblique rifting should be considered the rule and not the exception when investigating divergent margins, highlighting that endmember models are often misapplied to many natural examples.

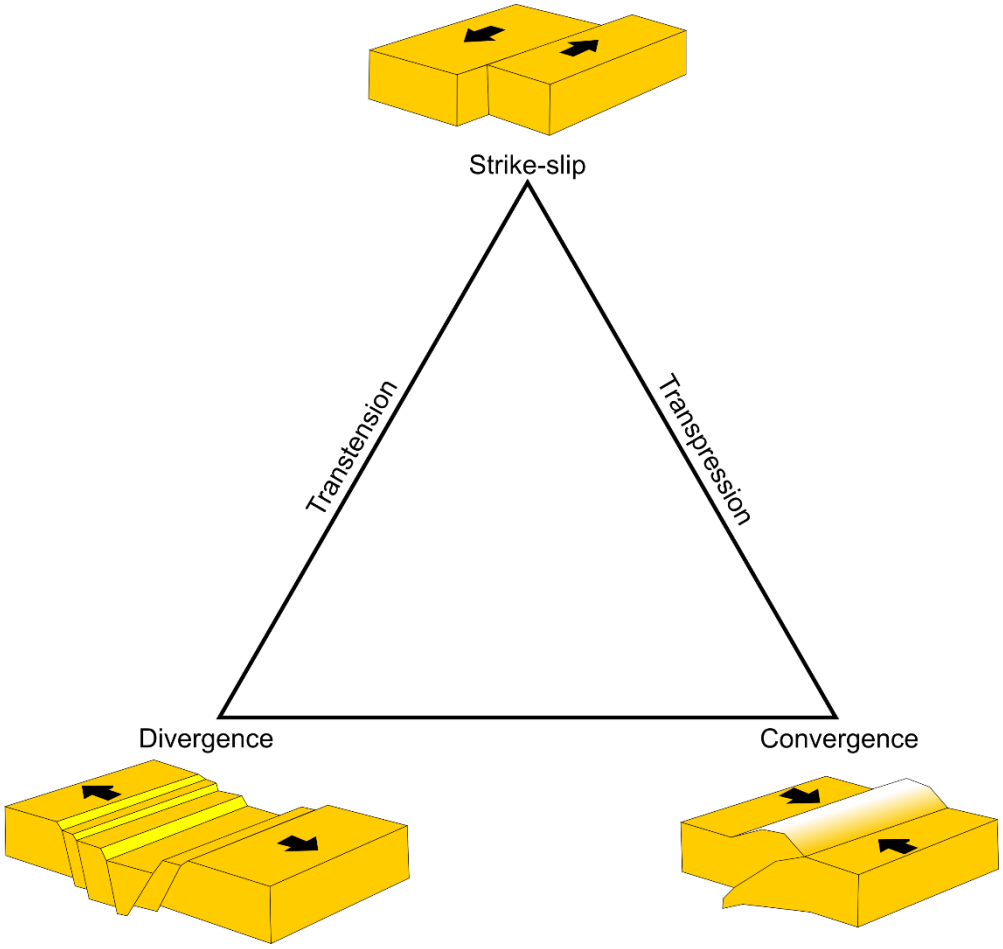

Figure 1.1 – Ternary diagram of plate boundary driving forces (Modified from Fossen, 2016)

Transtensional and transpressional deformation created by changes in plate motion along transform margins has been reported in a limited number of observational studies (e.g. Davison et al., 2016 in the Equatorial Atlantic; Umhoefer et al., 2018 in the Gulf of California). There have also been a small number of modelling studies of transtensional and transpressional deformation in strike-slip systems (e.g. Wu et al., 2009 on transtensional pull-apart basins). Nevertheless, modelling studies in these environments are significantly under-represented in comparison with the multitude of studies on extensional or compressional regimes. In particular, there is a lack of modelling, and multi-scale and temporal approaches, on the effect changes in kinematics have in transform margins, given their importance. Modelling is a unique and invaluable tool when investigating the evolution of an Earth structure, since most processes in the Earth are too slow and too deep to observe directly (Gerya, 2019). With the ability to model millions of years of

structural evolution in a matter of hours or days, observations can now be made throughout the lifespan of the modelled structure. Moreover, the process can be repeated in the case of a failed model or to test a concept, something that does not happen in nature. The modeller has the advantage of being able to vary different parameters to pinpoint the main driving factors behind the resulting architecture. Furthermore, it enables integration of observations across different scales depending on the structure under examination. However, in order for any type of modelling results to be considered meaningful, there is a need to combine the results with observations or measurements from the modelled prototype, ideally across different scales.

Multi-scale studies of structural features have become an indispensable tool in formulating and testing the theories of structural evolution. Stewart et al. (2009) demonstrated the need for cross-scale studies by investigating the kinematics of Proterozoic shear zones in Australia using small-scale fieldwork observations in addition to large-scale aeromagnetic and Bouguer gravity data. They highlighted the importance of the gravity data as a tool to delineate the subsurface structure and linking it to limited fieldwork observations in an area with almost no surface exposure. Another example of a multi-disciplinary – cross-scale study is that of Magee et al. (2018), which used advanced geophysical observations, remote sensing (InSAR, GPS and UAVs), numerical modelling, geochemical, and petrological data to delineate the evolution of magma plumbing systems. They concluded that only with the combined use of these methods were they able to pinpoint the exact location of current and ancient plumbing systems, locating potential volcanic eruptions and locating ore deposits. In this study, a multidisciplinary, multis-scale approach has been used to investigate the evolution of transform margins through time, through their lithospheric profiles and across different scales of observation, ranging from the tectonic plate-scale down to the basin-scale. Furthermore, it utilises and combines a variety of modelling (analogue and numerical) and imaging (seismic reflection interpretation) methodologies to address transform margin evolution during plate motion vector changes, within the broader subject of strike-slip tectonics, which is introduced in Chapter 2.

1.3 Thesis aims

The overall aim of this thesis is to increase our understanding of the structural evolution of transform faults. In particular the effects of oblique rifting and changes in relative plate motions are investigated across different scales of observations using modelling techniques and compared against real world data. The specific research questions this thesis addresses are:

1) How does a transform margin evolve through time when it is affected by a change in the relative plate motion vector between the two adjacent plates?
2) How do pre-existing structures affect the evolution of a transform margin, and can this control be distinguished from the effect of a change in the relative plate motion vector?
3) How does a change in the relative plate motion vector influence the development of structural features along large strike-slip systems, such as pull-apart basins, before they develop into transform faults?

1.4 Thesis outline

This main results chapters in this thesis are structured as a series of "journal-style" research papers. This thesis follows the outline presented below:

Chapter 1: 'Introduction'

This chapter provides an overview of the project structure, aims and rationale. It also presents a brief introduction on how this thesis contributes to the state of the art in strike-slip tectonics.

Chapter 2: 'Transform margins and strike-slip fault systems: formation, evolution and key concepts'

This chapter provides an overview of the literature on mechanisms that control the evolution of transform margins, strike-slip faults, and oblique systems. Their evolution in the context of plate tectonics is presented along with their main morphological characteristics. Finally, the main elements and key nomenclature that will be discussed in the latter chapters are defined.

Chapter 3: 'Methodological approach and study areas'

This chapter introduces the various methodologies used to study transform margins. It then provides an overview of the methodologies used in this thesis, their advantages and disadvantages, and why they were chosen to study transform margin response to plate motion vector changes and inheritance. It also presents a list of the data that have been used from around the world.

Chapter 4: 'The lithosphere-scale: The impact of oblique inheritance and changes in relative plate motion on the development of rift-transform systems.'

This chapter presents a set of numerical models investigating the evolutionary response of transform margins to obliquely inherited structures and plate motion vector changes. It represents the lithosphere observational scale. Our findings indicate that plate motion vector changes (or relative plate rotations) play a very important role in the evolution of transform margins and should always be considered when trying to decipher their evolution. The contents of this chapter have been published in their current form as:

Farangitakis, G.P., Heron, P.J., McCaffrey, K.J.W., van Hunen, J. & Kalnins, L.M. (2020). The impact of oblique inheritance and changes in relative plate motion on the development of rift-transform systems. *Earth and Planetary Science Letters, 541,* 116277 doi: https://doi.org/10.1016/j.epsl.2020.116277

As first author of this publication, I contributed to this work by designing and executing the numerical modelling experiments, analysing and interpreting the data and preparing the manuscript. The corresponding supplementary material of this work can be found in Appendix A.

Chapter 5: 'The crustal-scale: The evolution of transform margins and rift-transform intersections in response to changes in plate motion.'

This chapter presents the results of analogue modelling experimental work undertaken in Utrecht University between October 2017 and January 2018. It represents the crustal-scale observations. We propose that when relative plate rotations occur along transform margins and rift-transform intersections, the width of the resulting deformation zones is dependent on the coupling between the lower and upper continental crust. The results of this chapter have been published in their current form as:

> **Farangitakis, G. P.**, Sokoutis, D., McCaffrey, K. J. W., Willingshofer, E., Kalnins, L. M., Phethean, J. J. J., van Hunen, J. & van Steen, V. (2019). Analogue modelling of plate rotation effects in transform margins and rift-transform intersections. *Tectonics, 38*(3), 823-841. doi: https://doi.org/10.1029/2018TC005261

As first author of this publication, I contributed to this work by designing and executing the analogue modelling experiments, analysing and interpreting the results and preparing the manuscript. The corresponding supplementary material of this work can be found in Appendix B.

Chapter 6: 'The basin-scale: The evolution of shallow crustal structures in early rift-transform interaction'

This chapter presents the results of further analogue modelling experimental work (undertaken in October 2019) and integrates them with observations in geophysical datasets to study the development of shallow crustal structural elements in the N. Gulf of California and the Bohai Basin in N. China. This chapter represents the basin-scale observations.

The results of this chapter have been accepted for publication (and were under production and licence agreement at the time of this thesis submission) in their current form as:

> **Farangitakis, G. P.**, McCaffrey, K. J. W., Willingshofer, E., Allen, M.B., Kalnins, L. M., van Hunen, J., Persaud, P., & Sokoutis, D. The structural evolution of pull-apart basins in response to changes in plate motion. *Basin Research*

As first author of this publication, I contributed to this work by designing and executing the analogue modelling experiments, analysing and interpreting the results and preparing the manuscript. The corresponding supplementary material of this work can be found in Appendix C.

Chapter 7: 'Discussion, future work and conclusions

This chapter integrates the results from chapters 4-6 across different scales and methods. It also discusses the implications in the wider perspective of transform margins and strike-slip tectonics. Furthermore, future potential research subjects arising from this thesis are discussed. Finally, it summarises the overall conclusions drawn in these chapters and from this thesis as a whole.

2 Transform margins and strike-slip fault systems: formation, evolution and key concepts

2.1 A short historical overview of the understanding of transform margin evolution

Our initial understanding of strike-slip tectonics and subsequently transform fault and margin evolution took place in the early and mid-20th century, respectively. These advances were closely linked to the evolution of plate tectonic theory. Thus, in summarising the development of our current understanding of transform faults and margins, it is useful to first reflect on key advances in plate tectonic theory and its precursors.

Wegener (1912) was the first to propose that our planet's surface architecture is driven by continental drift. He argued that all the Earth's continents were once joined together in a single landmass and had since drifted apart. He proposed that the mechanisms causing the drift might be the centrifugal force of the Earth's rotation or the astronomical precession. Wegener's (1912) theory essentially set the groundwork for the later studies in plate tectonics, which in turn led to the development of transform margin studies. The first documentation of the term 'strike-slip faults' took place when Reid et al. (1913) defined them as faults where the net slip is practically in the direction of the fault strike. Then, Arthur Holmes (1931) suggested that tectonic plate junctions might be submarine features and that continental plates motion is driven by convection currents in the mantle. Carey (1958) presented the first timeline of plate motion including how South America and Africa could fit together in a simplified plate re-construction, essentially confirming Wegener's (1912) theory.

The team of Heezen et al. (1959) were the first to propose that continental drifting is accommodated by oceanic spreading using data acquired by Maurice Ewing's seafloor mapping cruise on the R/V *Atlantis* from Woods Hole Oceanographic Institution in 1947. They proposed this idea after having mapped the Mid-Atlantic ridge for the first time and having detected a

system of mid-oceanic ridges all around the Earth's seafloor. This idea revolutionised the way of thinking at the time, as it was now proven that new material was being generated in the Earth's surface along the mid-oceanic ridges (Heezen, 1960). The same research group would five years later identify the -until then- enigmatic linear features in the world's oceans, what we now define as fracture zones (Heezen et al., 1964a; Heezen et al., 1964b; Heezen et al., 1965). It is worth noting here that most of these studies actually utilised the work of Marie Tharp, who mapped the world's seafloor but was unfortunate to have been a woman in a time where science was dominated by men and thus was limited to being included as an "et al." in most of these research papers.

Dietz (1961) further built on the proposed oceanic spreading theory with an intuitive model that explained oceanic spreading ridge bathymetry. He proposed that the differentiation between continental and oceanic crust was due to the production of new material along oceanic spreading ridges. Hess (1962) described spreading ridges as the rising limbs of mantle convection cells where new crust is formed. He was the first to suggest a potential age for the Earth's current oceanic crust by identifying a trans-Pacific ridge linking the Marianas Trench to Chile aged 100 My. This study was of great importance as it would enable the identification of the lateral offsets of differently aged oceanic crust along what were later termed transform faults. The definition of the term "transform fault" was given by Wilson (1965). Wilson (1965) proposed a new class of faults that accommodated continental drift based on the changing nature of the crust on each tectonic plate along their strike (such as older oceanic crust *transforming* into younger oceanic crust), and the changing nature of features that existed in their terminations (such as a strike-slip fault *transforming* into a mid-ocean ridge). He defined these faults as "transform faults".

McKenzie (1967) published his ground-breaking findings on the viscosity of the mantle, where he applied for the first time thermodynamic theory in conjunction with tectonic plate motion, suggesting that tectonic plates move due to convection in the mantle. McKenzie and Parker (1967) used magnetic anomalies from the Mid-Atlantic Ridge observed from the Earth's magnetic field polarity reversals to test whether the same theory can be applied to spreading in the North

Pacific Ocean. They concluded that the theory can apply also to that mid-ocean ridge. Morgan (1968) suggested that the surface of the Earth can be approximated through the relative motion of a small number of rigid blocks. He proposed that each block is bounded by rises (where new surface is formed), trenches (where surface is being destroyed) and great faults where there is no stretching, folding or distortion of any kind. He was the first to propose that these blocks are rotating over the mantle on poles of rotation over a spherical surface. Le Pichon (1968) was the first to attempt a plate re-construction over the Cenozoic using information about spreading rates and sediment distributions, building upon Morgan's (1968) moving rigid block theory.

The term "transform margin" as a type of continental boundary was first proposed by Mascle (1976) and Scrutton (1979). Both these works advocated the addition of a third type of margin to the existing Atlantic (passive continental) or Pacific (active continental-subduction) type classification, since sheared/transform margins did not adhere to the existing margin classification types. These margins were distinct from their counterparts as they accommodated or had accommodated strike-slip motion through a transform fault between two plates (Mascle, 1976; Scrutton, 1979). Woodcock (1986) categorised strike-slip faults that appear on plate boundaries into four classes based on the structures that they link: a) ridge transforms (ocean-ocean, linking spreading ridges), b) boundary transforms (continent-ocean, continent-continent, rarely ocean-ocean, linking plate boundaries), c) trench-linked strike-slip faults (continent-continent, linking subduction trenches), and d) indent-linked strike-slip faults (continent-continent, associated with intra-plate compression). Finally, Sylvester (1988) distinguished two types of strike-slip faults depending on the depth of shear: transform faults that shear the lithosphere and transcurrent faults that cut through the crust. Sylvester (1988) also indicated that certain structures along shear zones are direct results of compression or extension concurrent with shearing (i.e. transpression and transtension). These concepts and their fundamental theory are further analysed in sub-section 2.2.3

Even though the key concepts were established fifty years ago, there is an ongoing debate on how transform faults, fracture zones and margins are formed and related. In particular, there is still

disagreement on a) whether the formation of transforms is spontaneous or pre-imposed and b) if the continental part of a transform boundary is linked to oceanic transform faults and fracture zones and if so, whether every transform fault is linked to a continental transform boundary. One of the first formation mechanisms proposed was from Turcotte (1974). He suggested that transform faults and fracture zones are thermal contraction cracks relieving the thermal stresses in the lithosphere. However, this mechanism, as Basile (2015) notes, was lacking a kinematic explanation and a link to the continental part of a transform margin. Wright (1976) argued that onshore northeast-southwest trending belts of major faulting in Nigeria represented the landward continuation of the Equatorial Atlantic Romanche and St Paul Fracture Zones. He noted that the intersection of these belts with the coastline coincides with the landward projection of the fracture zones. He suggested a kinematic explanation where these deformation belts represented lines of weakness in the continental crust and potentially controlled the initiation of the Romanche and St Paul Fracture Zones when Africa and South America separated.

A particularly good example of the debate on continental transfer faults being linked to oceanic transform faults and fracture zones can be found in the Bosworth et al. (1986) comment and reply to Lister et al. (1986). Lister et al. (1986) argued that although there is not a one-to-one correlation between every oceanic transform continuation and a respective continental transfer fault, there is a very distinct trend in some areas in the world that cannot be ignored. However, Bosworth et al. (1986) argued that the oblique transfer zones that are observed between continental rifts are unlikely to be precursors to transform faults. They used the East African Rift system as an example due to the oblique trend of the transform faults to the spreading direction. In the reply to the comment Lister and co-authors counter-argued that there was no available public data at the time to oppose their suggestion and that trends in areas around the world such as the Exmouth Plateau in W. Australia seemed to support their case. In the Exmouth Plateau, the gross structure of this continental marginal plateau appears to be at least partially controlled by continental transfer faults that can be traced ocean-wards into oceanic transform faults.

Lorenzo (1997) identified in a kinematic model two stages in a continent-ocean fracture zone's evolution. The first stage is characterised by continent–continent shearing dominating a narrow region in which the transform fault eventually ruptures. The second phase occurs when spreading commences and the younger oceanic block slides along the active transform, heating the older continental crust and possibly inducing thermal uplift. Taylor et al. (2009) argue that in the Woodlark Basin transform faults only occur after the onset of oceanic accretion to accommodate segmentation of spreading. They proposed that transform faults are not inherited from transverse rift structures and that any initial spreading offsets are very often non-transform. Gerya (2012) in a review paper on transform fault modelling highlighted the debate on whether these faults always result from pre-existing ridge offsets or can also form spontaneously at a single straight ridge during millions of years of accretion. In an earlier numerical modelling study (Gerya, 2010) concluded that the characteristic orthogonal ridge-transform fault pattern observed in the world's oceanic floor is a characteristic plate accretion pattern and does not link to rifting patterns in the continental part of the boundary. Bellahsen et al. (2013) in their study in the Gulf of Aden distinguished 3 types of fracture zones existing within the oceanic domain: a) Type 1 that form synchronously with rifting and are associated with the continental part of the transform margin, b) Type 2 that form during the spreading initiation and c) Type 3 that form within the oceanic crust domain, after spreading onset and are unrelated to the continental transform margin. Basile (2015) and Le Pourhiet et al. (2017) suggest that transform faults (and margins), can start their activity from a rift-connecting phase if the plate vector and rift obliquity are small enough to favour strike-slip motion. They refer to these faults as "intra-continental" transform faults. Finally, Illsley Kemp et al. (2018) identify in their models a "proto-transform fault" in East Africa representing a diffuse zone of oblique strike-slip motion. However, they argue that this is also an unlikely precursor to a transform fault but rather a precursor to what would develop into a transform margin.

From the aforementioned studies, it becomes evident that there is a considerable degree of disagreement (and potential differentiation of definitions) for transform margin and fault

formation, and the interplay between the oceanic and continental domains. Thus, in the following sub-sections the kinematic concepts, definitions and nomenclature used in this thesis will be defined and justified to avoid confusion in relation to transform margin evolution.

2.2 Transform margin structure and evolution

When considering transform structures in this work, they will be classified on the basis of the nature of the crust that is juxtaposed along their strike. Thus, when a transform fault is juxtaposing continental to continental crust - a transfer fault as defined by Sylvester (1988) - it will be referred to as a Continent-Continent Transform (CCT). This term is purely used for kinematic and distinction purposes and reflects a similar principle followed in Basile (2015) and Le Pourhiet et al. (2017) which refer to “intra-continental” transform faults. It is also worth noting that in this thesis, particularly at the early stages of their evolution, transform margins and transform faults are considered the same entity. Once oceanic spreading has further evolved, these two entities are differentiated and transform motion occurs along the active part of the transform margin’s strike accommodated by the transform fault, while the transform margin as an entity contains both passive and active parts. It is worth noting that there is also an ocean-ocean part to the transform fault as spreading further evolves. There is ample evidence to suggest that in the earlier points of their evolution transform margins and transform faults are the same structural entity (Lorenzo, 1997; Gerya, 2012; Bellahsen et al., 2013; Basile, 2015; Le Pourhiet et al., 2017). It would be logical to assume that in the early stages of evolution of a transform boundary when horizontal motion is accommodated between two rifts evolving into ridges, the localised shear zone connecting these rifts is a transform fault that will later evolve into a transform margin. It is, however, necessary to point out that there are a number of studies indicating this is not always the case, as not all initial shear zones correspond to a transform fault that accommodates plate motion after oceanic spreading has initiated (Taylor et al., 2009; Gerya, 2010; Bellahsen et al., 2013; Illsley-Kemp et al., 2018).

2.2.1 Key nomenclature and basic kinematic models of transform margins

One of the most simplified ways to describe the stages of evolution of transform margins and faults is as a plate boundary where horizontal boundary-parallel displacement takes place between two continental rift segments that evolve into spreading centres and accommodate plate motion. The basic steps in the elements of a transform boundary's evolution are as follows:

a) In the first stage of transform fault evolution, shear motion occurs along the strike of the zone connecting the two rift corners, leading to the initiation of strike-slip motion in a zone that will evolve to become the transform fault (and margin) (Figure 2.1a). The faults that accommodate motion at this stage can be referred to as Continent-Continent Transform Faults (CCTs) (or transfer faults).

b) Once the two plates separate, and after the onset of spreading, the transform boundary can be divided into three separate elements (corresponding to both conjugate margins) (Figure 2.1b):

    1) The Continent-Ocean Fracture Zone (COFZ), which represents the fossilised offset of a transform margin (Lorenzo, 1997). These zones represent very sharp transitions between the continental and oceanic domain, with an elevated profile along the continent followed by an almost vertical drop into the abyssal plain. This dramatic transition is thought to be the result of kinematic or thermal effects (or both) during transform fault evolution (Gadd & Scrutton, 1997; Lorenzo & Wessel, 1997; Huguen et al., 2001; Basile, 2015; Davison et al., 2016);

    2) The Continent-Ocean Transform Fault (COT), which represents the active part of the margin starting from the Ridge-Transform Intersection (RTI) and ending at the point where continental crust juxtaposes continental crust along the strike of the transform margin and;

    3) The remaining length of the CCT.

c) Finally, once the two continents are no longer juxtaposed, the plate boundary can now be distinguished into another 3 separate elements (Figure 2.1c):

1) The COFZ, which now runs the full length of the passive COT margin profile;
2) The Oceanic Fracture Zone (OFZ), representing the fossilised offset of the now inactive part of the oceanic transform fault (Lorenzo, 1997) that connects the two spreading ridges and;
3) The Oceanic Transform Fault (OT), which connects the two spreading ridges and accommodates motion between the plates (Wilson, 1965).

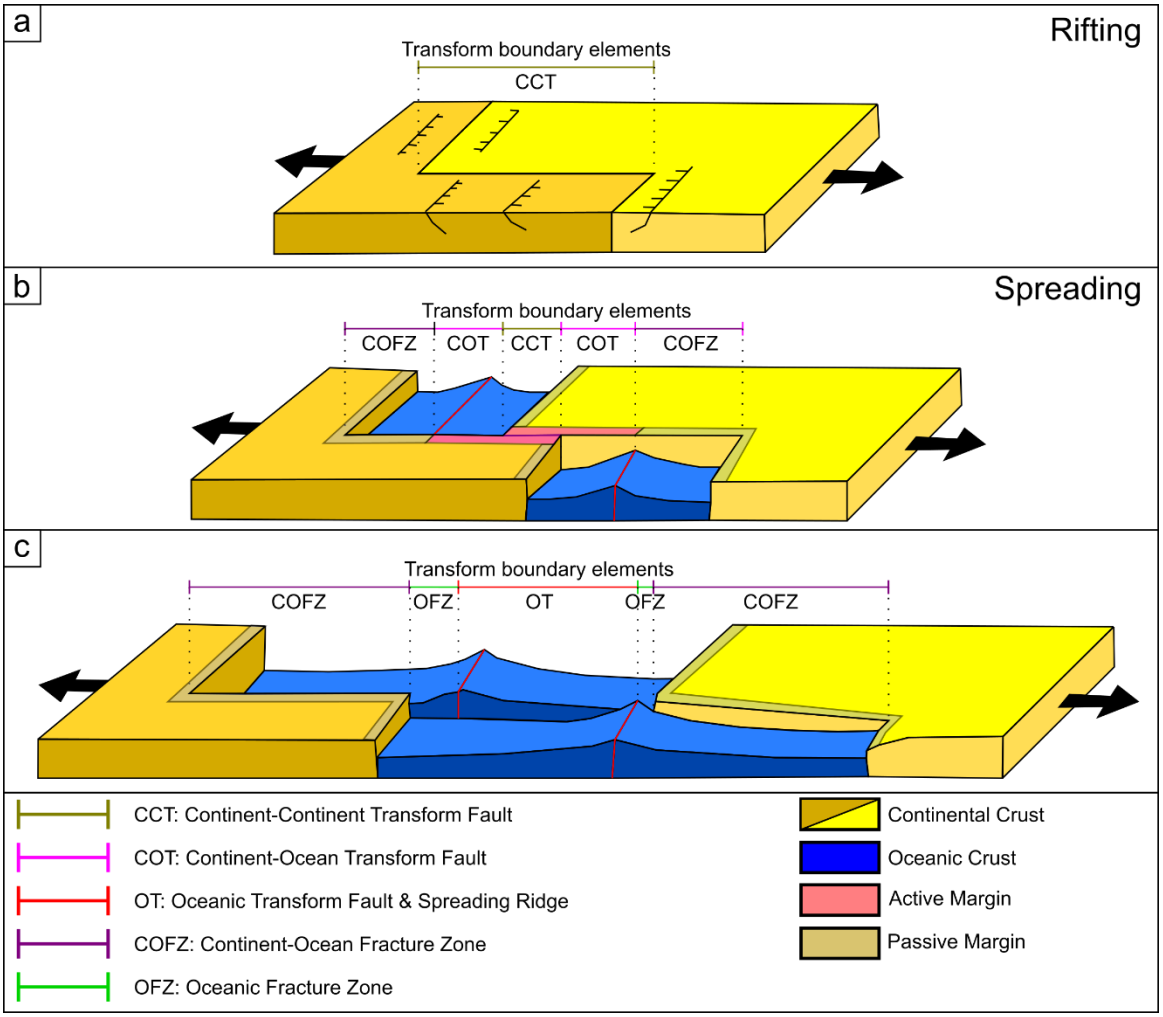

Figure 2.1 – Simplified evolution of a continental transform plate boundary margin between two moving plates (Modified from Lorenzo, 1997).

The Lorenzo (1997) model provides a useful schematic view of transforms but fails to account for all of the features that may be recognised in these systems. Thus, a number of features need to be further addressed regarding the evolution of structures along a transform boundary profile.

Figures 2.2 and 2.3 present a map view and a linear profile of a transform margin in greater detail to assist with the illustration of these issues:

a) A continental transform margin is created when offset rift segments are connected by a transverse shear zone of displacement. Continental transform margins can be defined as active or passive based on the relative position of the spreading ridge with respect to the margin corners (pink/active versus gray/passive shading in Figure 2.3). Kinematically, margin activity is determined by the intersection between the transform margin and the spreading ridge – the rift/ridge-transform intersection (RTI). Once the RTI has passed the inside corner of the continental margin the transform margin becomes passive.

b) The same principle applies for the whole length of the transform boundary (continental and oceanic). The position of the RTI defines the point where the plate boundary changes from active to passive. This is clearly demonstrated by tracing the trajectory of the black dot in Figure 2.2 and the yellow star in Figure 2.3.

c) The passing RTI (black dot in Figure 2.2 and yellow star in Figure 2.3), representing the intersection between the hotter spreading ridge and the colder continental crust, has a thermal effect on the continental transform margin. This is thought to have different effects according to various studies such as: a) the continental lithosphere heating from lateral conduction (Gadd & Scrutton, 1997), resulting in uplift of the transform margin outer edge; b) differential thermal subsidence in both the oceanic and continental parts along the transform margin profile after the RTI has passed (Lorenzo & Wessel, 1997); and c) magmatic underplating from lower crustal bodies underneath the continental part with little to no effect in the topography, which is mainly controlled by flexural uplift (Rupke et al., 2010)

d) Changes in the rate or obliquity of spreading or in the plate motion vectors can lead to segmentation of spreading ridges and generate new oceanic transform fault segments connecting them (Gerya, 2012). This is illustrated in Figure 2.2, where the original spreading ridge of Figure 2.2c becomes further segmented in Figure 2.2d, and then

acquires another set of spreading segments in Figure 2.2f. These new transform faults in turn leave behind their own “fossilised offset” in the form of Oceanic Fracture Zones (Lorenzo, 1997). This is an explanation for the numerous fracture zones in the world’s ocean floors that do not necessarily correspond to COFZs in the passive transform margins, as seen later in Figure 2.4. The existence of these non-rifting-related oceanic fracture zones is one of the main arguments in a debate on whether all continental transform margins and oceanic transform faults are formed in the same way (Bellahsen et al., 2013; Illsley-Kemp et al., 2018).

e) The same changes in the rate or obliquity of spreading can also influence the length of transform fault segments as seen in Figures 2.2e and 2.2f, where the original length of the central oceanic transform fault has been reduced due to the spreading ridge segmentation. Another factor that can be influenced is the comparative length of the transform boundary between two conjugate margins. The ridge segmentation occurring between Figures 2.2e and 2.2f has influenced the length of each conjugate transform boundary. The right-hand side passive margin in Figures 2.2f & 2.3f (up to the RTI) is now longer than the one in the left-hand side of the figures.

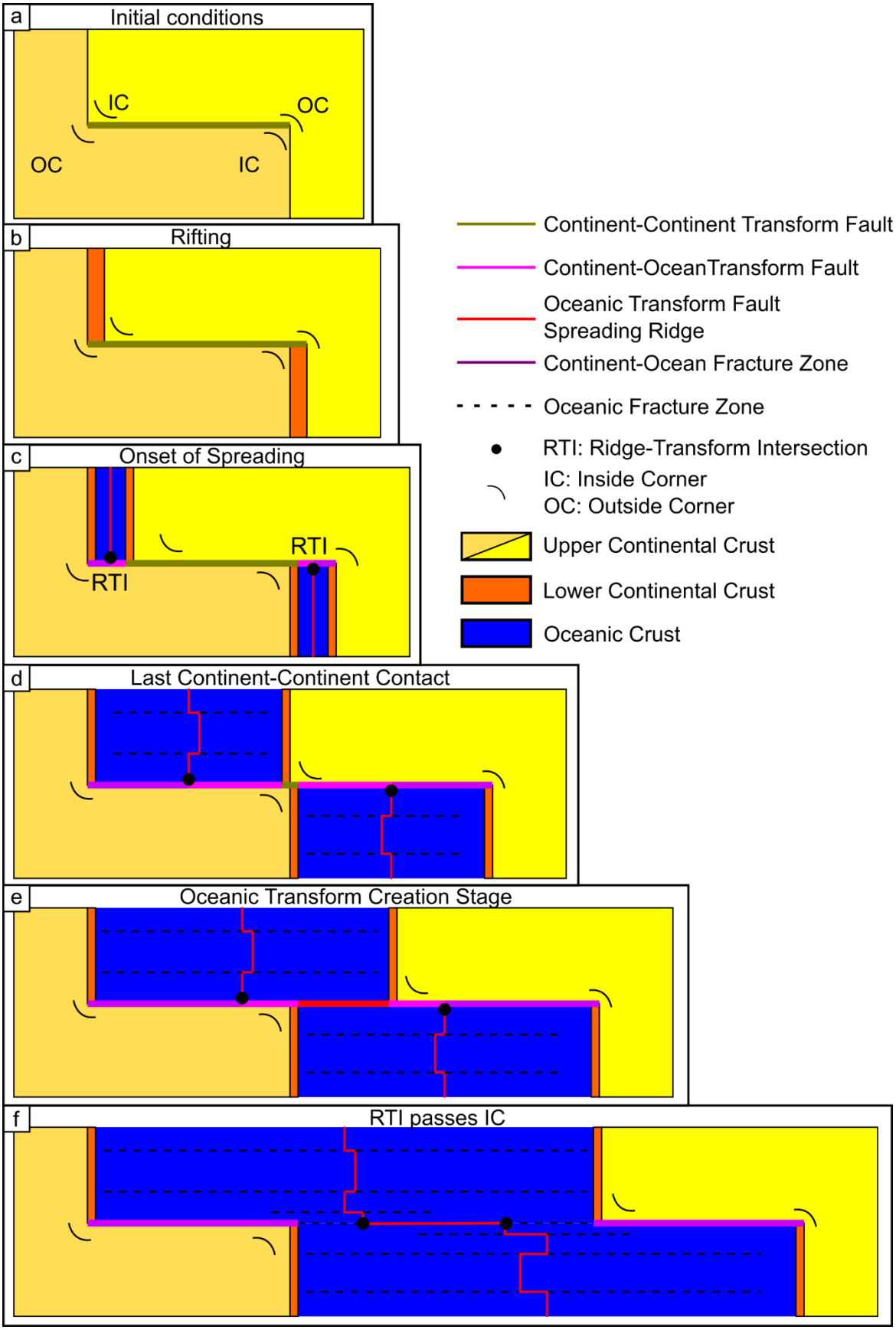

Figure 2.2 – Map view of the evolution of a transform boundary between two moving plates (Modified from Basile, 2015).

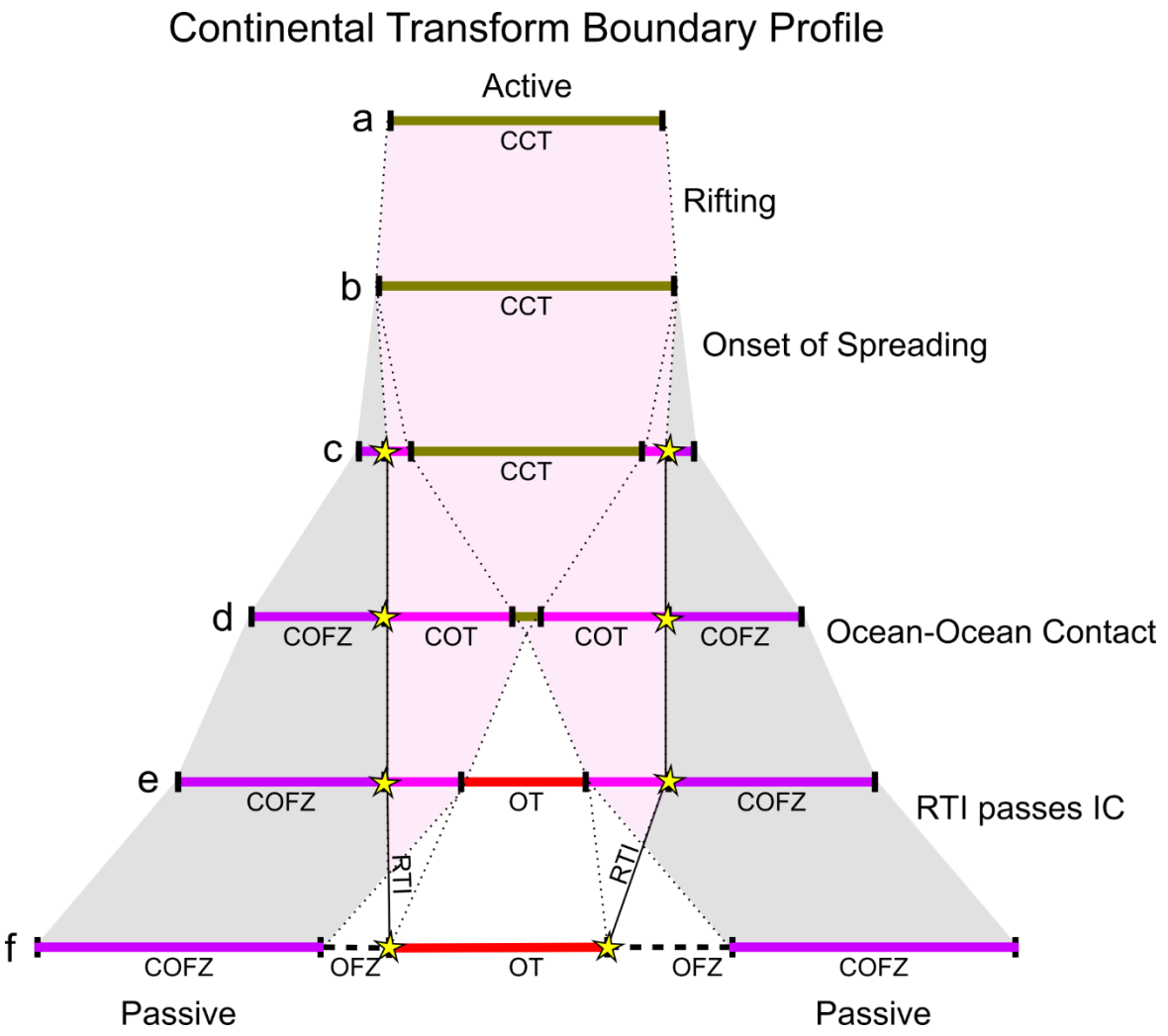

Figure 2.3 – Details on the profile of the transform boundary shown in Figure 2.2. Profiles a-f correspond to the panels a-f of Figure 2.2. Grey shading indicates a passive continental plate boundary, while pink shading indicates an active continental transform plate boundary. Yellow star represents the Ridge-Transform Intersection. CCT: Continent-Continent Transform Fault, COT: Continent-Ocean Transform Fault, COFZ: Continent-Ocean Fracture Zone, OT: Oceanic Transform Fault, OFZ: Oceanic Fracture Zone, MOR: Mid-Ocean Ridge, IC: Inside Corner.

2.2.2 Anatomy of a passive transform margin

As Mercier de Lépinay et al. (2016) note from their transform margin global catalogue and compilation of morphological profiles, transform margins display previously unexpected variability, both between margins and along-strike within a single margin.

A number of observations made along the profile of a transform margin provide further insight into the features observed:

a) The transition from continental to oceanic crust is generally sharp, and in general most margins have a sharp transition from the continental shelf to the abyssal plain (Figure 2.4a) (Mercier de Lépinay et al., 2016)
b) Fracture zones imaged in geophysical data, instead of following the sharp transition from the continental shelf to the abyssal plain, are generally wide zones of lithosphere deformation (although sharp, narrow cases also exist) (Davison et al., 2016; Sauter et al., 2018) (Black lines in Figure 2.4)
c) A third of the identified margins from Mercier de Lépinay et al. (2016) display in their across-strike profile a generally flat, wide surface, which sits at the edge of the continental shelf, termed the Marginal Plateau (Figure 2.4 b). These plateaus occur in some cases closer to the inside corner of the transform margin, but in general they are as long as their related transform margin. Mercier de Lépinay et al. (2016) suggest that these marginal plateaus should be considered as remnants of older rifted crust or divergent margins, cut by more recent transform faults. However, if they are as long as the transform margin and are remnants of older crust, it is more likely that the driving mechanisms behind their shape are the transient effect of the passing spreading ridge or a kinematic effect due to wider transpression. Mercier de Lépinay et al.'s (2016) suggestion would imply that the transform margin is parallel to an old divergent margin, which is not the case for the Equatorial Atlantic example, as there is no previous N-S directed extension on this margin.
d) In some transform margins, at the outer edge of the marginal plateau an even narrower uplifted part of crystalline basement can be found, named the Marginal ridge (Basile et al., 1993) (Figure 2.4c). Marginal ridges are thought to be associated with a phase of uplift along the transform border (Basile, 2015), but the origin and timing of this uplift is still being debated. A number of theories exist for the origin of the marginal ridge, such as

thermal uplift due to lateral heat conduction across the continent-ocean boundary (Gadd & Scrutton, 1997), differential thermal subsidence (Lorenzo & Wessel, 1997), or transpression (Davison et al., 2016; Farangitakis et al., 2019).

It is worth noting that not all transform margins display marginal plateaus; on the contrary, many continental margins are just tilted and deepen towards the ocean (Figure 2.4a). Similarly, marginal ridges do not occur along all transform margins. A marginal ridge occurs only on the transform margins that have marginal plateaus and even then, not over all of them (Mercier de Lépinay et al., 2016).

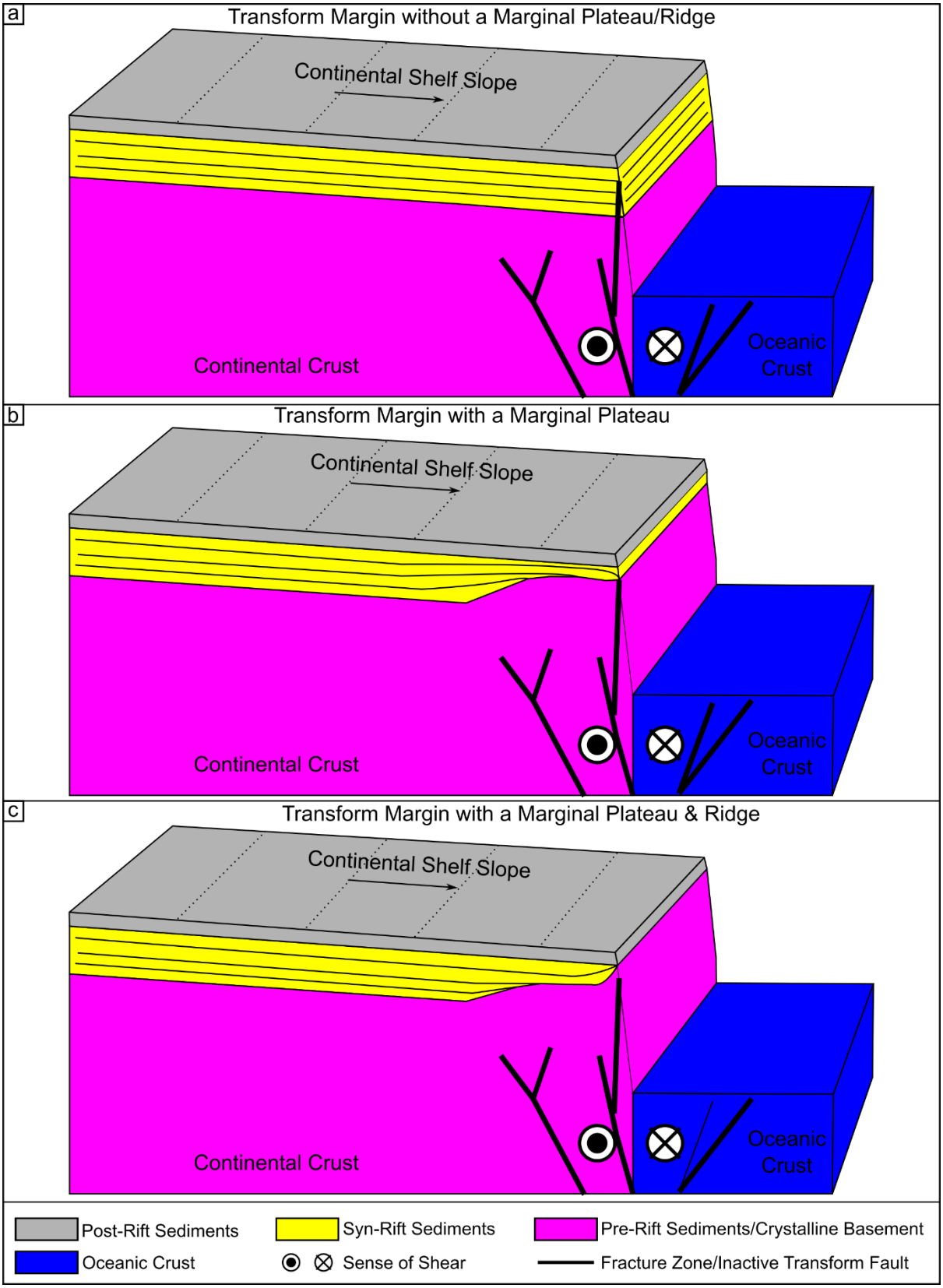

Figure 2.4 – Simplified anatomy of a transform margin (redrawn from Davison et al., 2016) a) without a marginal ridge or plateau, b) with a marginal plateau and c) with a marginal plateau & ridge.

2.2.3 Transform margins and their response to oblique rifting and changes in plate motion

A number of efforts have been made to catalogue transform margins across the world (Scrutton, 1982; Lorenzo, 1997; Bird, 2001). In this thesis I adopt the scheme developed by Mercier de Lépinay et al. (2016) in their continental transform margin review paper. To classify transform margins, Mercier de Lépinay et al. (2016) used a combination of a) the continent-ward continuation of oceanic fracture zones mapped by Matthews et al. (2011), b) a continent-ocean boundary map (Exxon World Mapping Project, 1985) or the edge of the oceanic crust mapped by Müller et al. (2008) and c) regional plate kinematic reconstructions for younger transform margins.

According to Mercier de Lépinay et al. (2016), there are 78 identifiable continental transform margins across the planet (cyan lines in Figure 2.5) representing about 16% of the cumulative length of all continental margins. They define transform margins as continent-ocean plate boundaries directly linked to active, or previously active, transform faults (fracture zones). It is worth noting that Mercier de Lépinay et al. (2016) argue that their definition of transform margins is directly linked to the angle between the continent-ocean boundary and the fracture zone/ transform fault trend. They argue that in an idealised situation this angle should be equal to zero to define a transform margin and that non-zero angle margins should be considered obliquely rifted. However, they use a 15^{o} tolerance between the oceanic fracture zone and the continent-ocean boundary, a value which would cover any “marginal” cases. From this classification, it is clear that a number of transform margins do not follow the perfect orthogonal trend usually described in the literature and are generally affected by obliquity in their evolution, resulting in angular relationships between the margin and its oceanward continuation in the transform fault. Furthermore, in the visualisation of the Mercier de Lépinay et al. (2016) classification (Figure 2.5) it also becomes clear that not every transform fault/fracture zone is correlated with a transform margin; however, every transform margin can be correlated to a transform fault/fracture zone.

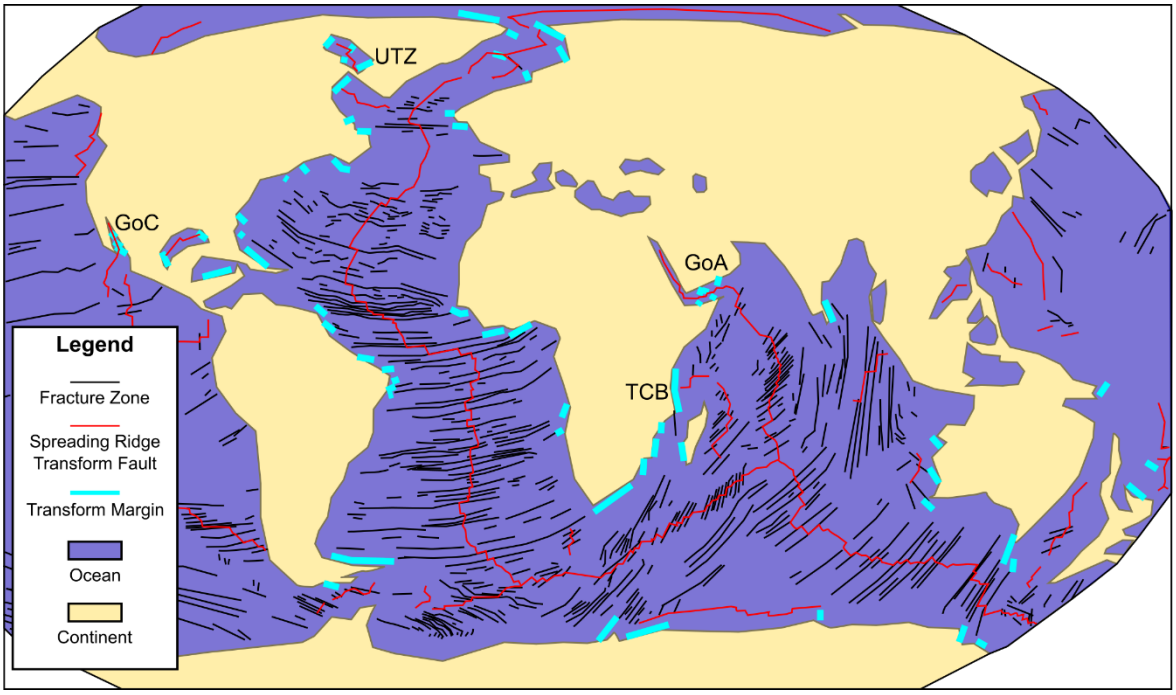

Figure 2.5 – Transform margins across the world (After Mercier de Lépinay et al., 2016). Fracture zone location from Müller et al. (2008) and Matthews et al. (2011). Continent-Ocean Boundary from Exxon World Mapping Project (1985). GoC: Gulf of California – Discussed in Chapters 4-5-6, UTZ: Ungava Transform Zone – Discussed in Chapter 4, GoA: Gulf of Aden – Discussed in Chapter 4, TCB: Tanzania Coastal Basin – Discussed in Chapter 5.

Brune et al. (2018), having analysed a database of kinematics containing all the rifts on the planet, suggested that oblique rifting might actually be the rule, rather than the exception, compared to orthogonal rifting. If so, the corresponding transform margins might also experience significant transtensional or transpressional deformation, which would influence their morphology and should be evident in many natural examples across the world. Recent studies have shown this to be the case, such as Ammann et al. (2018) that indicated the direct relationship between transform length and rifting obliquity. Thus, it becomes evident that transtension and transpression play a significant part in transform boundary evolution.

Harland (1971) was the first to document transtension and transpression as the combined effects of extension and compression during strike-slip motion in the shear zones of Spitzbergen. Having made his observations on these continental shear zones, he showed in a simple 2D plane plate

diagram how different structural regimes can occur due to different angles between the plate's motion and its boundaries (Figure 2.6). Transtension and transpression were later defined in the context of "wrench shear" as the concurrent action of "wrench" shear (strike-slip motion) and "pure" shear (compression or extension) along a zone of deformation (Wilcox, 1973; Dewey et al., 1998).

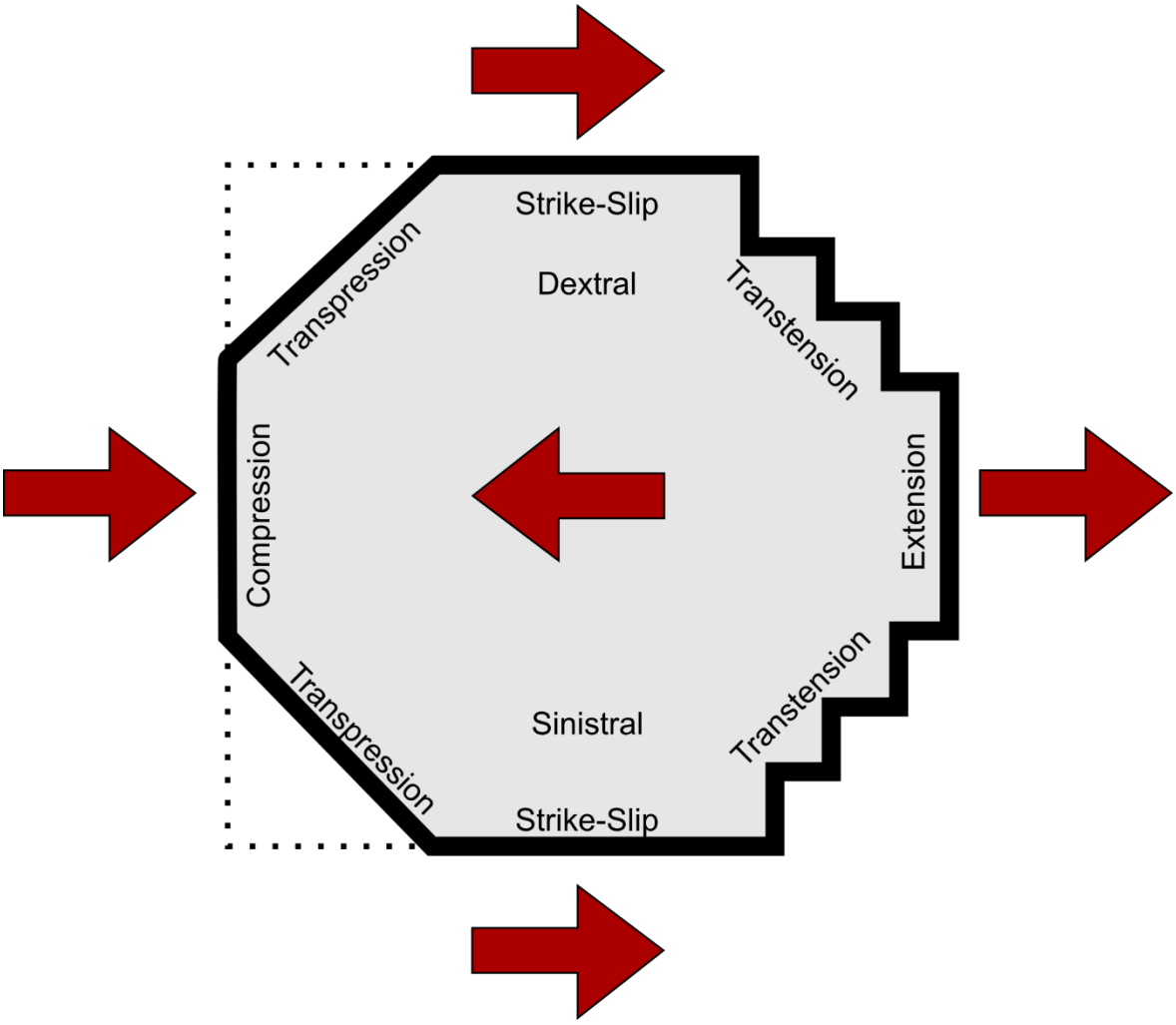

Figure 2.6 – Schematic diagram of two moving plates generating different structural regimes at their boundaries (modified from Harland, 1971).

It is worth noting that around the same time that these scientific advances on our understanding of transtension and transpression were occurring, releasing and restraining bends along shear zones were being described mainly in the Basin & Range and San Andreas Fault areas in California (Burchfiel & Stewart, 1966; Crowell et al., 1974; Mann et al., 1983). Releasing bends along strike-slip faults in the Basin & Range province form basins with distinct rhomboidal shapes that appear

as if someone had “pulled them apart” from their longitudinal edges and were thus termed “pull-apart basins” by Burchfiel and Stewart (1966). Such structures present in bends along strike-slip faults have also been termed, based on the relief they generate, negative (for releasing bends) or positive (for restraining bends) “flower structures”, as they were considered to look similar in cross-section to the petals of a flower (Harding, 1985).

Sanderson and Marchini (1984) extensively modelled transpression and transtension by designing various paths of deformation superposing small increments of stress. They used these models to interpret the development of structures, such as en-échelon folds, in transpression zones. Their models allowed them to predict the orientation of the principal stresses, and hence brittle structures, within transpressional zones. It is worth noting that Sanderson’s and Marchini’s (1984) model was also applicable to restraining bends along strike-slip faults. The main criticism of this model, which was addressed by Jones and Holdsworth (1998), was that it assumed that the non-coaxial component of deformation was described by a simple shear acting in the horizontal plane. Jones’s and Holdsworth’s (1998) model allowed for vertical and oblique zone boundary displacements and thus was able to model transtension and transpression in full 3D space. Sylvester’s (1988) seminal strike-slip work, apart from classifying strike-slip faults based on their lithospheric profile, raised another very significant point by stating that the structures that are present along shear zones are direct results of the amount of divergence or convergence that is concurrent to shearing (i.e. transtension and transpression).

Building upon the same notion, Holdsworth et al. (2002) and then De Paola et al. (2005) studied oblique partitioning in transpression and transtension, respectively. Holdsworth et al. (2002) found that a deformation zone in SE Scotland that had experienced sinistral shear and contraction displayed characteristics ranging from folds to strike-slip detachments and suggested that these features evolve contemporaneously (similar features can be identified in the transpressional example of Chapter 5). In a similar study, but for transtensional oblique partitioning in the Northumberland Basin, De Paola et al. (2005) concluded that in a transtensional domain oblique partitioning can result in compressional structures inside such basins, highlighting the implications

when interpreting such features as the result of basin inversion. Similar features can be identified in transtensional basins such as the Bohai Basin in Northern China shown in Chapter 6.

Nevertheless, the majority of studies on transtension and transpression concentrate on continental shear zones, with little focus on large-scale plate boundary transforms. One would expect that the same features observed in continental shear zones would occur in transform margins that undergo a change in the relative plate motion along the two crustal blocks. Thus: a) in a transform margin undergoing transtension, extensional features would exist, such as growth faults, with the branches of the transform fault zone behaving similarly to those of a negative flower structure (Figure 2.7a) and b) in a transform margin undergoing transpression, compressional features resembling the structure of positive flower structures would be expected (Figure 2.7b). In both cases, reactivation of initial strike-slip zones as oblique-normal or oblique-reverse is also another observable feature (Farangitakis et al., 2019).

The particular mechanisms behind the evolution of transtensional and transpressional transform margins in response to plate motion changes during their lifespan are discussed in further detail in the result chapters and in particular in the two crustal-scale analogue modelling chapters. In Chapter 5, the response of rift-transform intersections and transform boundaries to transtensional and transpressional rotations is modelled and compared against examples from transtensional and transpressional plate boundaries. Chapter 6 focuses on models investigating the evolution of releasing bends/pull-apart basins across large-scale transform faults and how these respond to a multi-phase evolution starting from pure strike-slip and transitioning to transtension due to rotation. The results are then compared with transtensional strike-slip systems across the world.

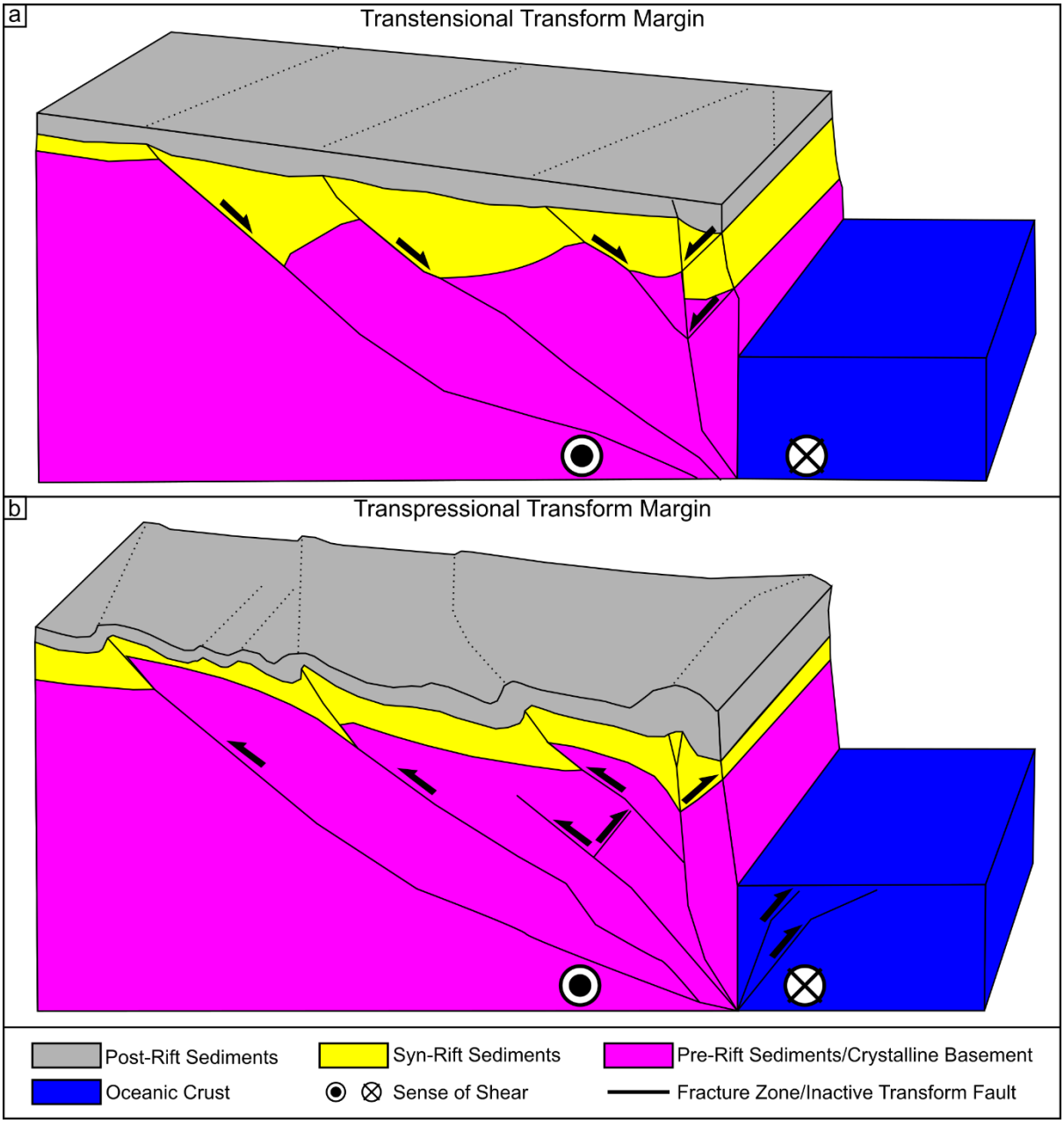

Figure 2.7 – Simplified anatomy of a transform margin having undergone: a) transtension or b) transpression (redrawn from Davison et al., 2016). Dashed lines over the post-rift sediment layers represent the approximate strike of the transtensional/transpressional structures on the surface. The effect of transtension/transpression is shown in the form of the result of partitioned strain for better visualisation of the corresponding structures.

3 Methodological approach and study areas

The methodological approach adopted in this study is to use experimental modelling to simulate the development of transform margins under changing plate motion domains. These results are compared with and validated against real world datasets. In this chapter, an overview of the foundations of each methodology used in the study are presented along with their application to transform margins. Within each result chapter, the specific methodology used is further described.

3.1 Assumptions and limitations

Before proceeding with the presentation of the methodologies and results in this thesis, three key points considering assumptions made and experimental limitations are addressed:

- As explained in detail in Chapter 2, there is evidence to suggest that during their early evolution, transform margins and transform faults are the same structural entity (Lorenzo, 1997; Gerya, 2012; Bellahsen et al., 2013; Basile, 2015; Le Pourhiet et al., 2017). Once oceanic spreading has further evolved the fault and margin are differentiated and transform motion is considered to occur along the active part of the transform margin's strike accommodated by the corresponding transform fault (and its ocean-ocean part), while the transform margin as an entity contains both passive and active parts. Thus:
    a. In the numerical modelling part of this study that investigates lithospheric-scale processes where continental break-up is present (Chapter 4), motion is accommodated along the active part of the transform margins by transform faults. At the same time, the inactive part of the transform margin is characterised as a continent-ocean fracture zone, making the transform margin and fault distinct entities.
    b. In the analogue modelling part of this study that investigates early crustal-scale features (Chapters 5 & 6), motion is accommodated in what

in nature would correspond to an early stage active continental transform plate boundary, since no oceanic spreading is present. This plate boundary in nature would be a zone that is tens of kilometres wide, especially due to the changes in plate motion that are modelled in this work. These structures in later chapters are termed Principal Displacement Zones, following the terminology that inspired the analogue modelling work in this thesis from Basile and Brun (1999).

- The driving force behind a transform fault's formation: There is increasing evidence of transform fault and large strike-slip deformation being a "bottom-up" driven process, meaning it is a process driven from the mantle lithosphere (Teyssier & Tikoff, 1998; Chatzaras et al., 2015; Heron et al., 2016). In particular, Chatzaras et al. (2015) present mounting evidence from upper mantle xenolith analysis in the San Andreas Fault system (a transform plate boundary) that there is a lithospheric feedback between the upper crust and lithospheric mantle, which act together as an integrated system. They propose that mantle flow controls displacement and loads the upper crust. In contrast, the upper crust controls the stress magnitude in the integrated system. Thus, within the framework of this thesis, the tectonic structure driven from beneath the continental lithosphere is the primary driver of processes observed in the models presented.
- Effects of transient heat flow and volcanism: Thermal effects, such as the passing of the spreading ridge along the transform margin (Gadd & Scrutton, 1997; Lorenzo & Wessel, 1997) and volcanism/magmatism (Tugend et al., 2018) are also factors that would influence a transform margin's evolution. These effects were not modelled due to the limitations of the techniques used in this work. Volcanism/magmatism is not modelled in any of the chapters presented in this thesis. Thermal effects are modelled in Chapter 4 of this thesis; however, in the analogue models presented in Chapters 5 & 6, these effects cannot be modelled. Thus, it is stressed again that in this study the main driver of processes is the tectonic driver from the lower continental lithosphere, so the purely

tectonic models presented capture the first-order factors affecting transform margin and fault evolution.

3.2 The value and reasoning behind following a cross-scale and multiple method approach to the evolution of transform margins

Modelling is a necessary tool for geodynamics since tectonic processes are too slow and (often) too deep in the Earth to be observed directly (Gerya, 2019). The combination of analogue and numerical modelling as investigative techniques for this thesis enables further understanding of transform margin evolution across different-scales of observation. Numerical modelling offers the unique advantage of (theoretically) infinite iterations of an experiment with varying parameters since no physical materials are used apart from the processing unit. Numerical modelling also provides the user with (again theoretically) infinitely replicable results if no changes are made into the parameter space. However, numerical models often face dimensional or resolution limitations due to limited available CPU power and discretization effects. Furthermore, numerical models only capture the specific physical processes that the coder or user prescribes (Reber et al., 2020). In analogue modelling, it is straightforward to combine model materials that deform in a continuous and discontinuous manner, leading to emergent physics. Moreover (as is the case in this thesis), the modeller is limited by the availability of materials and apparatuses in the laboratory, alongside budgetary and time limitations. These limitations often have an effect on the ability to carry out repeat runs of models to display the results' replicability (an issue not as prevalent in numerical modelling). However, this issue is addressed by providing open access to the exact apparatus configurations, materials and parameter space of each model, allowing for a repeat run of the model. If a model is set-up correctly, then the results of a repeat run are expected to be similar and the primary structures investigated are expected to develop in the same manner. As analogue modelling usually investigates first-order similarities, then the results of a repeat run are expected to be similar in a first-order of structures (i.e. for the results of Chapter 6, a repeat run would be finding a similar asymmetric triangular shape in a pull-apart

basin, oblique faulting and triangular principal displacement zones, but with potentially different numbers of secondary normal faults). In this thesis, all of the analogue modelling results are published in the public domain, with open access to them, allowing any other researcher to test their replicability. Furthermore, thermal effects or isostatic rebound effects often cannot be included. Thus, these two methods, rather than rendering one another obsolete, overlap by complementing each other's weak points. Finally, comparing the results of the experiments to natural examples, resulting in good correlations from both approaches, further enhances the validity of the final conclusions.

Having demonstrated the specific advantages and disadvantages behind each methodology and how these complement each other, it is worth explaining the reasoning behind following each particular modelling method to investigate the questions posed in this thesis. In this thesis, lithospheric scale modelling is carried out in the numerical domain while crustal/basin scale modelling is carried out in the physical analogue domain. This choice, apart from following the general trend in the scientific modelling community, was made also on a practicality point of view. Simple, generic lithospheric profile large-scale numerical models with basic fundamental parameter changes on each run (such as the ones in Chapter 4) are straightforward to construct and execute multiple times. However, crustal scale numerical models that study natural examples are considerably more time consuming to set up and run the risk of setting up the parameter space in a manner that is not investigative but rather set-up to replicate a natural process without allowing the model to display a certain degree of freedom. Thus, the choice was made for the numerical models in this thesis to model a generalised parameter space in a lithosphere scale in order to produce key fundamental first-order structuration with a view of comparing the results to first-order structures in natural examples. The reverse case applies for analogue modelling. Lithosphere scale analogue modelling is a considerably more time (and budget) consuming approach, that generally yields primary first order structural results (Reber et al., 2020). On the other hand, crustal scale analogue modelling is generally a straightforward, fast modelling

process, with high replicability and detail in the produced results, allowing for easier comparison to nature. This thesis's natural examples consisted mainly of 2D seismic reflection data (as seen in subsection 3.4) and thus comparison with the cross-sections of crustal scale analogue models was considerably more practical.

3.3 Modelling techniques

In this study, numerical modelling is used to simulate the lithosphere-scale evolution of a transform margin, while analogue modelling portrays the crustal and basin-scale evolution.

3.3.1 Numerical Modelling

The rapidly developing numerical methods of continuum mechanics are the logical consequence of both theoretical and technological progress in plate tectonics. A concise historical review of 2D/3D numerical geodynamic modelling can be found in Schubert et al. (2001) and Gerya (2019). The key methodological steps in the evolution of numerical geodynamic modelling are:

a) First 2D numerical models of subduction by Minear and Toksoz (1970), concurrent with the plate tectonic theory being established. These models were purely thermal, with a prescribed velocity field corresponding to the subducting slab inclined at 45◦.
b) First 2D mantle thermal convection models by Torrance and Turcotte (1971), investigating the implications of mantle convection with temperature dependent viscosity for plate motion. Thermomechanical models based on the stream function formulation for the mechanical part were explored.
c) First finite element numerical models of two-dimensional salt dome dynamics (Berner et al., 1972; Woidt, 1978).
d) First 2D mantle thermal-chemical convection models (Keondzhyan & Monin, 1977, 1980). They used a binary stratified medium to study the effects of compositional layering on mantle convection.

e) First numerical models of continental collision (Daignieres et al., 1978; Bird, 1978). These workers used mechanical models to explore the finite-element approach.

f) First 3D spherical mantle convection models (Baumgardner, 1985, Machetel et al., 1986).

g) First 3D Cartesian mantle convection models (Cserepes et al., 1988; Houseman, 1988).

Ever since, numerical geodynamic modelling has developed rapidly both in the number of techniques and in its applications, making it one of the most dynamic fields in the geosciences. This rapid development can be attributed to a number of contributing factors that occurred particularly in the last three decades:

a) Hardware and software development in personal computers: The continuously increasing better specifications in desktop computer hardware (and even laptop computers currently) allows the user to have access to modelling software in their personal computer, making modelling considerably more accessible and efficient (at least for simple low-resolution models). Furthermore, development of better visualisation software (along with hardware such as graphics cards) allows the modeller to image the results of their models in far greater detail, resulting in more accurate observations and a better understanding of the model result.

b) Open-source codes: Sharing of open-source modelling codes, meaning that a code that is available for anyone to download, use, modify, or contribute segments to it, allows for user-driven development and improvement of modelling software. This particular advancement has shifted access to modelling software from just the developers of the codes to researchers in institutions that could have otherwise not been able to purchase or build such software themselves.

c) Supercomputers: Although this development could be classified as an evolution of computer hardware, in reality it is a separate category in itself. The evolution of High-Performance Computing (HPCs) centres across academic institutions around the world has given modellers access to previously unavailable processing power. Using a

supercomputer, the modeller can submit multiple variations of a model to run simultaneously, saving considerable amounts of time.

3.3.1.1 Numerical Modelling in transform margins

The complex 3D nature of transform margins and the interplay between kinematic, dynamic and transient effects have always been a challenge for numerical models. To date, and following the classification from Gerya (2012), numerical models on transform margins and faults follow three different approaches:

a) Stress and displacement distribution: Fujita and Sleep (1978) used 2D anisotropic, finite element models to determine constraints on relative material properties and horizontal stress fields of mid-ocean ridges near transform faults. Phipps Morgan and Parmentier (1984) investigated stress distribution near an RTI to identify the mechanism of curved faulting towards the intersection using 2D finite element models with prescribed plate boundary stresses. They suggested that the curvature is a result of the interaction between ridge axis tensile stress and transform fault shear stress. Gudmundsson (1995) conducted a numerical boundary element study to explore the stresses acting inside oceanic transforms. They concluded that ridge-parallel and ridge-perpendicular (biaxial) tensile loading generates a stress field that makes transform fault slip easier and explains observed oblique geometries at ridge-transform intersections. Behn et al. (2002) investigated faulting pattern asymmetry and topography in the inside margin corners near the RTI. They proposed that the fault patterns observed are a result of aseismic creep or slow earthquakes.
b) Thermal structure and crustal growth: Phipps Morgan and Forsyth (1988) used a 3D numerical temperature solution in combination with a semi-analytical viscosity solution to study two spreading ridges offset by a transform fault and the resulting seafloor topography. Their study was inconclusive on whether the effects of melt production or melt migration dominate a ridge-transform intersection and are responsible for crustal

thinning along a transform fault. A more refined version of the previous model that included a variable viscosity of the mantle was presented by Shen and Forsyth (1992). They proposed that a variable viscosity model generated thicker crust and was less dependent on the strain rate than a constant viscosity model. They also concluded that melt production and mantle depletion decrease in the vicinity of a transform fault. Gregg et al. (2009) presented a combined 3D petrological–thermomechanical numerical study using finite element modelling software to examine mantle melting, fractional crystallization and melt extraction beneath fast slipping, segmented oceanic transform fault systems. They suggested that a visco-plastic rheology of the mantle and wide melt pooling are required to explain observed crustal thickness changes along a transform in the East Pacific Rise.

c) Formation and evolution: Stoddard and Stein (1988) presented a kinematic model of an orthogonal ridge-transform faults system subjected to asymmetric spreading on the principle that spreading ridge-transform geometries will remain stable only in case of ideally symmetric spreading, while asymmetric spreading will cause lengthening or shortening of transform segments. 3D finite element models of transform activity due to plate fragmentation were presented by Choi et al. (2008). They suggested that the driving force behind the orthogonal pattern of ridge-transform configurations is due to thermal stresses, which are also responsible for the creation of fracture zones. Gerya (2010) concluded that the distinct orthogonal ridge-transform fault pattern in oceanic crust should be considered as a characteristic plate accretion pattern. This orthogonal pattern does not correspond to rifting patterns that may have had completely different faults distribution and orientation. Allken et al. (2012) studied the connectivity of two rift segments by varying their offset and underlap/overlap, indicating that rift connectivity is heavily dependent on the distance between the interacting rifting tips. Le Pourhiet et al. (2017) investigated rift connectivity through strike-slip faulting depending on the thermomechanical properties of the lithosphere. They suggested that a strong continental

lower crust favours transform linkage between rifts at larger offsets. Furthermore, they proposed that reconstructions of plate motions at the edge of transform segments need to be done in two stages because obliquity in the system leads to stalled rifting. Finally, Illsley-Kemp et al. (2018) investigated the formation of a proto-transform fault between rifting segments. The same modelling code was used by Ammann et al. (2018), who investigated the relationship between oblique continental rifting and longer transform fault formation. They argued that longer transforms take longer to form and are a result of the combination of large rifting obliquity and slow extension rates.

Even though there are a significant number of numerical modelling studies on the formation, evolution and thermal structure of transform margins and transform faults, the interplay between rifting obliquity, inheritance and transform faulting is considerably understudied. Furthermore, even fewer studies address the aspect of the evolution of an active transform system coinciding with a change in relative plate motion. The notion behind most of the modelling studies mentioned above is that transforms go through their entire life-span with a rift-transform set-up that remains the same, with the extension direction and rate remaining constant throughout. This consistent model serves as a very useful end member (or basic) scenario for complexity to be added later. As discussed in Chapters 1 and 2, this is often not the case in nature. Thus, there is a gap of understanding on transform evolution when changes in relative plate motion (or oblique inheritance) occur. The numerical modelling work in this thesis addresses this gap.

3.3.1.2 Numerical modelling techniques presented in this thesis

The numerical modelling work presented in this thesis follows the third approach, that of studying the formation and evolution of a transform margin between two rift segments. Computations were carried out using the state-of-the-art open-source finite element numerical code ASPECT, version 2.1.0 (Kronbichler et al. 2012; Heister et al., 2017).

ASPECT was chosen because it has been proven to be a highly useful, state-of-the-art and recently developed modelling code for investigating lithosphere-scale rifting and transform activity and

their relation to inheritance (Heron et al. 2019; Naliboff et al., 2019; Corti et al., 2020; Glerum et al., 2020). Heron et al. (2019) used ASPECT in a similar modelling set-up as in the models in this thesis, with a weak seed straddling the top of the mantle, to investigate the effect of inherited structures on rifting segmentation between Canada and W. Greenland, an area which is also a natural example used for comparison with numerical models in this thesis. Naliboff et al. (2019) investigated localization of strain and fault development in continuously extending 3D rift geometries, taking advantage of ASPECT's adaptive mesh refinement features. Glerum et al. (2020) used ASPECT to investigate the interactions between two rift segments in the East African Rift system and to simulate the detachment and motion of the Victoria microplate. In the same area, Corti et al. (2020) used ASPECT to examine the abandonment of rift segments in the East African Rift. Both these studies have similar set-ups to the one used in this thesis, taking advantage of ASPECT's technical features such as a free-surface coupled with mesh refinement.

Unlike other codes, ASPECT has been created to be open-source and openly developed online and to be flexible across different-scales and dimensions (Kronbichler et al. 2012; Heister et al., 2017). ASPECT also provides its users with cookbooks and parameter files, which allow for the easy customisation of the key elements of the model (such as extension velocity, seed placement and shape or rheological parameters) without affecting the source code. As a result, ASPECT's object-oriented structure was deemed suitable for the project. The work conducted here needed to be in three dimensions to fully understand the tectonics of the area, as well as having the ability to analyse both large- and small-scale dynamics. By being built as a multi-purpose geodynamic tool, ASPECT has been able to provide a number of different solutions to the different tectonic problems the studies required. Existing numerical codes may tackle one or two aspects of the tectonics to a higher standard, but ASPECT allows for more complex geodynamic situations. For example, SOPALE can produce high resolution orogenesis (e.g. Heron & Pysklywec 2016), but not three-dimensional numerical simulations (e.g. Heron et al., 2019).

In this work, the model space of the experiments consisted of a box with dimensions of 800 by 800 km horizontally and 120 km vertically. Compositionally, the top 20 km is initially upper continental crust, with a 10 km lower continental crust beneath and 90 km of mantle lithosphere at the bottom. The models have prescribed constant (longitudinal) velocity boundary conditions on their x and bottom boundaries and prescribed tangential velocity boundary conditions on the y box boundary. The top boundary has a dynamically deformable free surface mesh, allowing for topography to be generated (Rose et al., 2017). The free surface (instead of a free slip or no-slip surface) is a more realistic approximation in a convecting Earth, since air and water should not prevent the flow of rock upwards or downwards. The free surface mesh is dynamically deformable, since in order to conserve mass the boundary of the domain has to be advected in the direction of fluid flow. On each of the models presented in this work, a weak seed is introduced 2 km beneath the base of the crust. The seed represents a zone of weakness, allowing deformation localise along it. In nature, this would be represented by an inheritance structure. The specific geometries and kinematics of each model are further discussed in Chapter 4.

The models in this study are governed by the equations of conservation of momentum, mass and energy in an incompressible medium with an infinite Prandtl number:

$$-\nabla \cdot (2\mu\dot{\varepsilon}) + \nabla P = \rho g \qquad \text{(Equation 3.1)}$$

where μ = viscosity, $\dot{\varepsilon}$ = deviatoric strain rate tensor, P = pressure, ρ = density and g = gravitational acceleration.

$$\nabla \cdot u = 0 \qquad \text{(Equation 3.2)}$$

$$\rho C_p \left(\frac{\partial T}{\partial t} + u \cdot \nabla T\right) - \nabla \cdot k \nabla T = \rho H \qquad \text{(Equation 3.3)}$$

where u = velocity vector, C_p = thermal heat capacity, T = Temperature, t = time, k = thermal conductivity, and H = internal heat production.

The compositional fields in the models adhere to the pure advection equation:

$$\frac{\partial C_i}{\partial t} + u \cdot \nabla C_i = 0 \quad \text{(Equation 3.4)}$$

where C_i = compositional field.

These equations are solved in a discretised domain of finite elements using an iterative Stokes solver (Kronbichler et al., 2012). The solution is then interpolated using Lagrangian polynomials as basis functions (Glerum et al., 2018). The models use a temperature-dependent density, but no pressure-dependence, since the model is incompressible (e.g., Heron et al., 2019).

The models have a nonlinear viscous flow (dislocation creep) with Drucker-Prager plasticity for the rheology, a set up used in many previous studies (e.g., Huismans and Beaumont, 2011; Naliboff and Buiter, 2015; Heron et al., 2019).

Dislocation creep is defined as:

$$\mu = 0.5A^{-\frac{1}{n}}\dot{\varepsilon}_e^{\frac{(1-n)}{n}}\exp\left(\frac{E+PV}{nRT}\right) \quad \text{(Equation 3.5)}$$

where A = viscosity prefactor, n = stress exponent (n>1), $\dot{\varepsilon}_e$ = square root of the deviatoric strain rate tensor second invariant, E = activation energy, V = activation volume and R = universal gas constant (Karato, 2008).

Viscosity is limited through a Drucker-Prager yield criterion where the yield stress in 3D is:

$$\sigma_y = (6Ccos\varphi + 2Psin\varphi)/(\sqrt{3}(3 + sin\varphi)) \quad \text{(Equation 3.6)}$$

where C = cohesion and φ = angle of internal friction. When φ equals 0, as in the imposed seed, the yield stress is fixed and equal to the Von Mises yield criterion. When the viscous stress ($2\mu\dot{\varepsilon}_e$) exceeds the yield stress σ_y, plastic yielding is applied by rescaling the effective viscosity (Willett, 1992; Kachanov, 2004) so that the stress is less than the yield value (e.g., Thieulot, 2011). To ensure numerical stability, viscosity is constrained between 10^{18} and 10^{26} Pa·s.

Strain weakening is applied for the internal friction angle and cohesion, which linearly reduce as a function of finite strain magnitude to 50% of their initial value at a strain of 50% (Bos, 2002; Heron et al., 2019).

The model compositional fields have individual values of thermal and rheological parameters. If more than one compositional field is present at the same time within a model cell, viscosities are averaged harmonically (Glerum et al., 2018). The rheology is similar to that of Naliboff and Buiter (2015), using wet quartzite flow laws for the upper crust (Rutter and Brodie 2004), wet anorthite for the lower crust (Rybacki et al., 2006), and dry olivine for the mantle (Hirth and Kohlstedt, 2003).

Finally, the models have a prescribed initial temperature field similar to a typical continental geotherm (Chapman 1986) with no lateral variations:

$$T(z) = T_o + \frac{q}{k}z - \frac{Hz^2}{2k} \quad \text{(Equation 3.7)}$$

where T_0 = surface temperature of each layer, H = heat production, q = heat flow through the surface of the specific layer, k = thermal conductivity and z = depth.

3.3.2 Analogue modelling

3.3.2.1 Historical background

Analogue models are smaller-scale (in both the temporal and spatial dimensions) representations of a particular component of the Earth's system (the natural prototype), using simplified geometries, rheologies and boundary conditions. The first physical analogue models were presented two centuries ago by Hall (1815), who used models that investigated the development of folding in layered sedimentary rocks. A number of studies followed investigating folding (Mead, 1920), thrusts and normal faults (Hubbert, 1951) and orogens (Griggs, 1939). However, two main advances changed the face of analogue modelling:

a) The development of the theory of plate tectonics in the 1960s led to a need for replicating the processes that shaped the planet's structural features. Therefore, there was an incentive to focus on modelling key plate tectonic processes such as subduction (Jacoby, 1973; Kincaid & Olson, 1987), rifting (Shemenda & Ghrocholskiy, 1994; Brun, 2002) or strike-slip deformation (Basile & Brun, 1999).

b) A greater change occurred in analogue modelling when it changed from being a qualitative descriptive tool to a quantitative technique due largely to the scaling theory established in the seminal works of Hubbert (1937, 1951) and Ramberg (1967, 1981). The cornerstone of scaling theory is that physical analogue models can be scaled to their natural prototypes based on the principle of maintaining similarity in the structural geometry, the kinematics and the rheology of the prototype. This meant that dimensions and properties in models were no longer arbitrarily selected in order to broadly replicate an observed structural process. Rather, dimensions and properties of analogue models had to be proportionally scaled to the dimensions and parameters of the natural prototype. Geometric similarity in a correctly scaled analogue model translates to a similar length ratio between the prototype and model in all three dimensions (thickness, width, length) (Hubbert, 1937). Kinematic similarity is achieved when the time required for the model and prototype to undergo similar changes in shape and position is directly proportional (Ramberg 1967). Finally, dynamic similarity requires a similar distribution of the driving mechanism behind the model (i.e. gravity or far-field forces) along with the resistive forces (friction, viscosity, cohesion) (Ramberg, 1981).

3.3.2.2 Driving forces

In terms of experimental modelling approaches in analogue modelling, Schellart and Strak (2016) define three different types:

a) The external approach, where the system is open and energy is added to the experimental system through the external application of a velocity, temperature gradient

or material influx (or combination of those). Deformation is hence driven by the externally imposed conditions. This approach is used to model micro- to upper crustal--scale processes such as rifting or orogenic belt formation, which are generally driven by far-field forces rather than internal forces. These types of experiments consist usually of granular materials (sand or glass microspheres) and are driven entirely by the imposed velocity boundary conditions. The pull-apart models from McClay & Dooley (1995) are a particularly good example of this type of approach, where two moving plates sit underneath a sand-pack and are pulled apart, driving the deformation.

b) The combined approach, again an open system, where energy is added to the system in a similar way as in the external approach. However, in this case deformation is partly driven by the externally imposed conditions and partly by buoyancy forces internal to the system. This approach is the most common analogue modelling approach and is used to model upper crustal- to mantle-scale processes such as rifting, subduction, salt diapirism or strike-slip faulting. These types of experiments consist usually of layers of different materials, depending on the prototype modelled. A layer of sand overlying a layer of silicon polymer is the most common set-up for modelling crustal processes (e.g. Philippon et al., 2015), while lithospheric-scale models usually consist of a silicon putty overlying a viscous fluid (e.g. Broerse et al., 2019)

c) The internal approach, where the system is closed, with any deformation driven by forces internal to the system. In this type of approach, the experimental conditions are imposed only initially by the modeller. The most common process that these models are used for is buoyancy-driven subduction, such as the early models of Jacoby (1973), who placed a rubber sheet (simulating the crust) on top of water (simulating the asthenosphere) to study how the crust sinks into the asthenosphere.

3.3.2.3 Materials

Another factor that differentiates between analogue modelling approaches is the selection of modelling materials to replicate the natural processes. This is a very crucial selection that the modeler faces when setting up an experiment, as it affects directly the dynamic similarity in scaling between the model and prototype. Thus, the selected material should always capture a good proportion of the properties observed in the prototype. While conventional materials such as sand, wax or clays have been used as analogues since the start of analogue modelling, rheological studies by material scientists (such as Klinkmuller et al., 2016 in quartz sand; Weijermars, 1986a in silicon polymers, Broerse et al., 2019 in viscous fluids) have significantly expanded the variety and applicability of available materials.

All rocks and modelling materials can be divided into three key end members according to how they deform: elastic, viscous and frictional-plastic. These end members can manifest separately or in combination with any other deformation type, leading to a variety of complex rheologies:

a) Under upper crustal conditions, rocks are generally considered to behave in a brittle manner, with brittle failure characterized by localized deformation associated with loss of strength. Thus, the brittle deformation in the upper crust can be constrained using the tensile strength and shear failure (Coulomb failure criterion). The materials used to replicate such processes must display similar properties and are usually represented by granular materials for the upper crust (with some exceptions such as gelatine, plexiglass or foam, Reber et al., 2020).
b) Deformation in the lower crust and mantle can be considered as viscous (Burg et al., 1994). All mineral phases in the lower crust and mantle share properties of volume conservation and are sensitive to strain rate (Turcotte and Schubert, 2002). In the early years of analogue modelling, the assumption was that the lower crust and mantle deform following a linear viscous flow law (Ramberg, 1967), leading to the use of numerous (Newtonian) linear viscous fluids such as honey, syrup or oils. These materials are

dynamically scalable to their prototypes, but only if they have similar flow-law curves and slopes (Weijermars & Schmelling, 1986). However, rocks that deform due to dislocation creep do not follow Newtonian behaviour. Due to dislocation creep (and other non-Newtonian creep mechanisms), strain localisation takes place. Such modelling materials include plasticine (Zulauf & Zulauf, 2004) or grain filled silicone (Broerse et al., 2019). Finally, yield stress fluids such as Carbopol, petrolatum and paraffin waxes display a significant elastic, in addition to viscous, rheology component. These types of materials have a wide range of use, ranging from fold formation (Cobbold, 1975) to mantle convection (Davaille et al., 2013)

Giving further examples, granular materials range from:

a) Quartz or K-Feldspar sand, or caster sugar, used to simulate the brittle upper crust (Schellart, 2000; Sokoutis et al., 2005)
b) Glass, aluminium microspheres, or mica flakes used to simulate weak detachment levels or brittle lithosphere (McClay, 1990; Schellart, 2000)
c) Silica or clay powder, used to increase the strength of a layer (McClay, 1990; Konstantinovskaia & Malavieille, 2005)
d) Sand and mica flakes used to simulate more distributed deformation (Gomes, 2013)
e) Walnut shells, used to increase layer height and avoid sidewall interactions (Cruz et al., 2008)

Materials with linear viscous, non-linear viscous, visco-plastic and complex ductile rheologies range from:

a) Silicone polymers with or without granular fillers that simulate the long-term deformation of the lower crust and lowermost lithospheric mantle (Weijermars, 1986a; Weijermars, 1986b; ten Grotenhuis et al., 2002)
b) Paraffin waxes that simulate the upper and lower crust (Shemenda, 1993)

c) Paraffin oil, petrolatum or mixes of the two acting as lubricants (Duarte et al., 2014)

d) Plasticine (mixed with granular fillers or oil) simulating dislocation creep in the lithosphere or a layering if a temperature gradient is present (Zulauf & Zulauf, 2004)

e) Syrups, honey or water that simulate diffusion creep in the sub-lithospheric mantle (Kincaid & Olson, 1987; Shemenda, 1993)

f) Gelatins and Carbopol hydrogels that simulate the visco-elastic brittle behavior of the crust and lithosphere or even the convective mantle (Davaille et al., 2013)

A simplified visualization of the breadth of selection versus the layer of the Earth that is to be modelled is given in Figure 3.1.

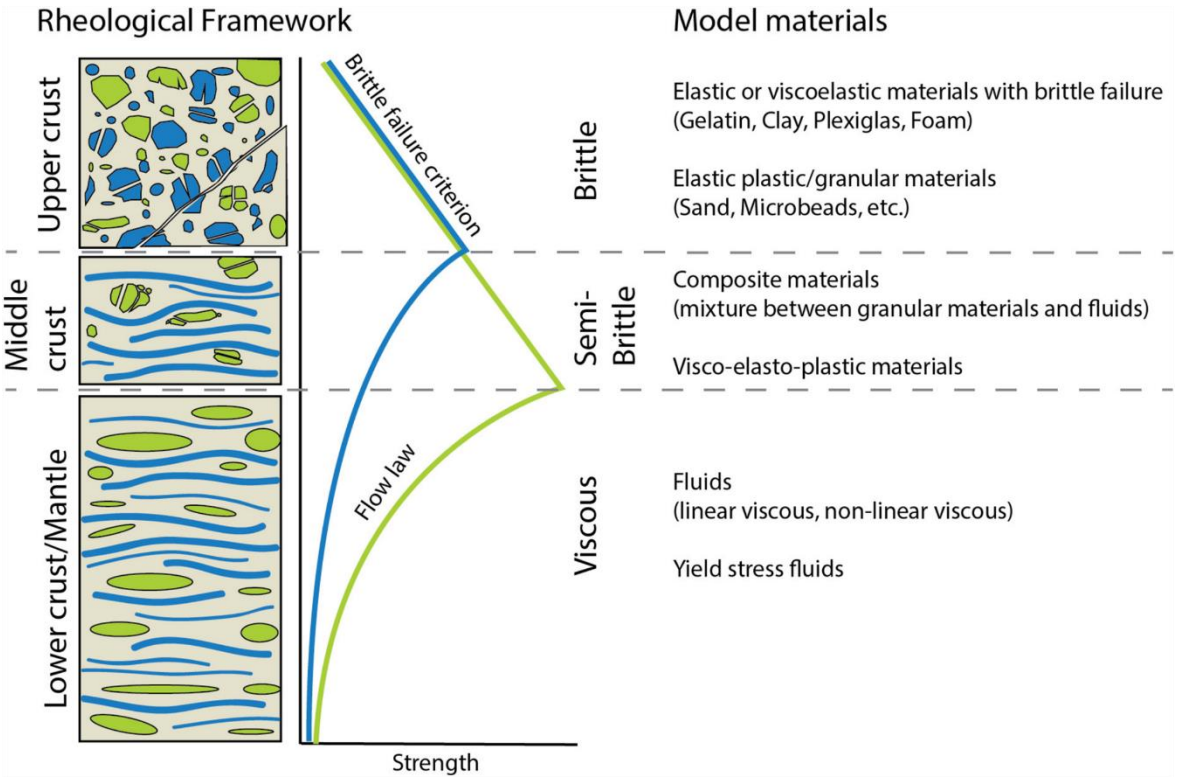

Figure 3.1 – (From Reber et al., 2020) Schematic diagram illustrating the rheological change with depth in a simplified bi-mineralic crust and its relation to potential model materials. Blue and green line represent the equivalent lithospheric strength profile.

3.3.2.4 Apparatus

The great variety of different available materials or driving forces used in analogue models applies also to modelling apparatuses. Before listing the different types of set-ups used to carry out analogue modelling, it is worth noting that the first and foremost constraint on the modelling apparatus that the modeller is going to use is the availability of materials and set-ups in the modelling lab that they operate at. Each modelling lab has usually their own array of different apparatuses constrained by budgetary restrictions, or research focus.

A first order classification of analogue modelling apparatuses can be done based on the depth of the profile of investigation into the simulated prototype lithosphere.

a) Lithosphere-scale model apparatuses: These are generally modelling apparatuses that consist of tanks that can be filled in with the viscous fluids mentioned in the above sub-sections. Such apparatuses can be used to investigate the full profile of the lithosphere driven by buoyancy forces (e.g. the case of slab break-off in Broerse et al., 2019). These tanks are usually made out of thick glass to allow visibility in the box. The walls of the tank can be either fixed (internal driving approach) or moving (combined external driving approach).
b) Crustal-scale model apparatuses: These types of apparatuses belong to the external and combined external force driving approach and greatly vary depending on the laboratory that uses them or the structure under investigation. Crustal-scale apparatuses can be further classified based on the gravity field in the experiment:
    i. Artificial gravity field/Centrifuge apparatuses: These apparatuses consist of a mechanism that rotates the model against a counterweight inside a box at great speeds, allowing for the scaling of gravity based on Ramberg's (1967) principles. This allows the modeller to use materials stronger than those used in conventional bench-top analogue modelling. An example of work using a centrifugal apparatus is that of Corti and Dooley (2015) investigating pull-apart

basin formation (Figure 3.2).

Figure 3.2 – Example of a centrifuge analogue modelling apparatus (From Corti & Dooley 2015)

ii. Natural gravity field/Bench-top (1-g) apparatuses: These apparatuses consist of set-ups that can be placed on a laboratory bench or table and have a natural gravity field. These types of apparatuses usually have either the form of pre-made boxes where the materials can be placed in or have the materials confined by detachable walls. A final distinction that can be made on bench-top apparatuses is on the driving force behind the localisation of deformation in the model:

    1. Apparatuses with pre-imposed velocity discontinuities (VDs): These types of modelling apparatuses pre-impose a basal boundary condition in the form of a velocity discontinuity. The velocity discontinuity can be imposed by introducing a discontinuity in the surface under the model materials. This discontinuity can be the contact between two moving basal plates or the contact between a single moving plate and the bench-top. Apparatuses using VDs in strike-slip environments are termed as Riedel boxes (Tchalenko, 1970). An example of such an apparatus is the Riedel box set-up by Basile and Brun (1999) to study strike-slip and pull-apart development in orthogonal

extension settings (Figure 3.3).

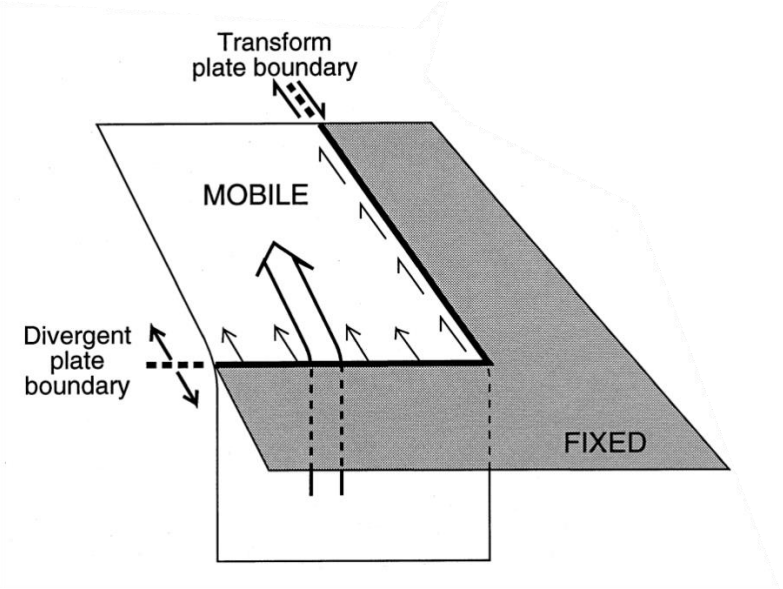

Figure 3.3 – Example of a modelling apparatus with a moving plate creating a velocity discontinuity (From Basile & Brun, 1999).

2. Apparatuses with movable walls or deformable bases with no VDs: These types of modelling set-ups do not have a VD in order to localise deformation, but instead initiate it solely through deforming the boundaries of the model. Usually within the model space a “seed” will be present, acting as a spot of different rheology. Such studies include the experiments of Autin et al. (2013), who used a deformable base model to study the effect of inheritance in oblique rifting, or the experiments of Zwaan and Schreurs (2017), who used a deformable wall and movable base model to study the interaction of rift segments under oblique extension (Figure 3.4).

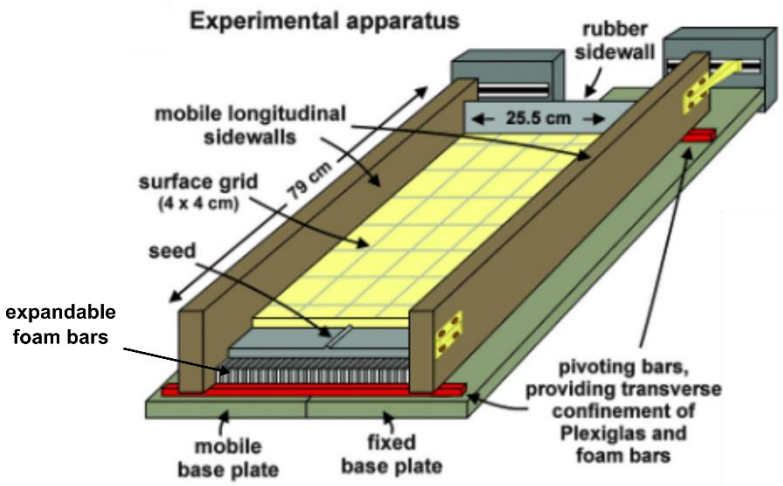

Figure 3.4 – Example of a modelling apparatus with a deformable side-wall and movable base-plate (from Zwaan & Schreurs, 2017). The mobile base plate and deformable side-wall move to create oblique extension. However, the model is not directly into contact with the base plates, but rather with a series of expandable foam bars that avoid the creation of a VD and instead distribute extension evenly beneath the model.

3.3.2.5 Analogue Modelling in transform margins

Analogue modelling of transform faults started from the seminal work of Oldenburg and Brune (1972; 1975), who performed a series of freezing wax experiments reproducing the orthogonal

ridge-transform pattern of oceanic plate separation. The first brittle/ductile analogue modelling experiments of transform margins were by Dauteuil and Brun (1993), who also presented the first analogue modelling experiment of oblique rifting or transform margins, investigating the Mohns and Reykjanes ridges in the N. Atlantic to identify segments of oblique transfer zones between the rift segments. Their rheology was comprised of a simple silicone putty/sand model. They extended two basal plates attached to moving sidewalls. Similarly, Basile and Brun (1999) used a Riedel experiment box (Tchalenko, 1970) with a similar brittle-ductile configuration to produce faulting patterns in continent-ocean transforms and pull-apart basins. Basile and Brun's (1999) work was the first to investigate the coupling vs de-coupling of the lower and upper crust in a ridge-transform or pull-apart basin setting. This work laid the groundwork for the experiments shown in this PhD thesis. The base configuration of Basile & Brun (1999) which is a moving plate being pulled in one direction cut in such a way that generates ridge-transform intersections is the one used (slightly modified) in the analogue models of Chapters 5 and 6.

Acocella et al. (1999) used a basal moving plate apparatus to show how orientation, geometry, and kinematics of transfer zones can depend upon pre-existing basement anisotropies, while Dauteuil et al. (2002) used a similar mechanism to test the influence of lithosphere strength on the development of deformation above a transform boundary. They concluded that major transform faults associated with fast-spreading ridges are formed by diffuse, complex arrays of strike-slip segments, while transform faults associated with slow-spreading ridges form deep, narrow linear valleys. The importance of these two pieces of work is that the study of Acocella et al. (1999) was one of the first to consider the implications of oblique inheritance on transform boundaries (a theme explored in Chapter 4 of this thesis), while Dauteuil et al. (2002) built upon the findings of Basile and Brun (1999) on "fast" versus "slow" transforms (a theme explored in Chapter 5 of this thesis).

Tentler and Acocella (2010) used an internal modelling approach with rising ductile material to simulate the transform-spreading ridge interactions in mid-ocean ridges. They concluded that the

type of interaction between ridges has a strong dependence on the initial configuration of the divergent plate boundary. These were the first lithosphere-scale analogue models that investigated ridge-ridge interaction and transform response. Autin et al. (2013) used a four-layer brittle/ductile/brittle/ductile extending base-plate model of the Gulf of Aden to investigate how inherited basins could partly control present-day geometry of an oblique rift and localization of fracture zones. Philippon et al. (2015) investigated the relationship between dip-slip and strike-slip displacements along orthogonal and oblique faults in relation to extension direction. Finally, Zwaan and Schreurs (2017) tested the effects of oblique extension and inherited structural offsets on continental rift interaction and linkage using a model with a deformable base constructed of foam bars. They noted that linkage between rift segments depends both on the obliquity of rifting and the overlap between the adjacent rifting tips. The last three workers (Autin et al., 2013; Philippon et al., 2015; Zwaan & Schreurs, 2017) provided significant contributions in our understanding of oblique inheritance and the response of strike-slip systems to oblique rifting.

Finally, it is worth mentioning that while temperature-dependent material analogue modelling is not very common, a research group from Moscow has demonstrated that the use of such materials is viable in transform fault modelling. These experiments include the work of Shemenda and Grokholskii (1994), Grokholskii and Dubinin (2006) and Dubinin et al. (2018), who used heat and a mix of paraffins in their models to replicate the strike-slip structures created in rifts. Similar work has been carried out by the Sibrant et al. (2018) group that used saline-sensitive materials to study oceanic transforms. These materials were used as a proxy for temperature effects with diffusion acting in a fundamentally similar way for both heat flow and chemical composition. Despite this extensive body of work summarised above, to date there is a significant under-representation in the literature of analogue modelling studies that have investigated the effects of changes in plate motion on transform margins and rift-transform intersections. However, as demonstrated in Chapter 2 these effects play a significant role on transform margin evolution.

3.3.2.6 Analogue modelling methods used in this thesis

This sub-section introduces the fundamental theory and concepts behind each of the analogue modelling experiments displayed in this thesis. It also presents a brief discussion on the reasoning behind the selection of this particular modelling construction. For a more detailed outline of the specific kinematic, scaling and processing properties of each model, the reader is referred to Chapters 5 and 6.

According to Reber et al. (2020), the key to successful experiments that simulate crustal processes is first understanding the conditions that control the process targeted for investigation. This helps the experimentalist design an experiment that has potential to be validated and can effectively investigate the deformational process of interest. Thus, three factors need to be considered:

a) The rheological framework of the process (e.g. does the experiment investigate continuous or brittle deformation?)

b) The scaling framework of the experiment (e.g. is the model dynamically scalable to natural example that it models?)

c) Practical limitations needed to be fulfilled by the material (e.g. the experimental apparatus, or the material compatibility)

As explained in Chapter 2, for the purposes of this study, transform fault generation is considered a "bottom-up" process driven from the lower lithosphere in the mantle to the top (Teyssier & Tikoff, 1998; Chatzaras et al., 2015). Since the analogue models in this work simulate the lower and upper continental crust, deformation to these layers is driven entirely by externally applied boundary conditions in the mantle (Schellart & Strak, 2016).

The analogue models presented in this thesis follow a modified experimental array based on that of Basile & Brun (1999), where a moving plate slides away from a static plastic sheet at the base of a brittle/ductile layer configuration (Figure 3.5). Deformation is entirely driven through the

applied basal boundary conditions, with pre-imposed velocity discontinuities (VDs), similar to those in Allemand and Brun (1991) and Tron and Brun (1991). The VD configuration is:

a) For the crustal-scale chapter (Chapter 5): that of two rift-strike-slip system intersections consisting of two parallel strike-slip discontinuities connected through a rift discontinuity. (Figure 3.5a).

b) For the basin-scale chapter (Chapter 6): that of an en-echelon rift and strike-slip system, consisting of two sets of alternating parallel and perpendicular to orthogonal plate motion discontinuities (Figure 3.5b).

Following an initial orthogonal extension phase, an anticlockwise rotation of 7^{o} in the principal stress direction is introduced to the moving plate's motion, consistent with observations from natural examples.

The brittle/ductile experiments were performed at varying extension rates scaled to the natural examples. Changes in topography were mapped using a 3D surface scanner. Finally, at regular intervals, alternating colour layers of feldspar sand were added in the topographic lows. These layers represent syn-and post-rift sedimentation and are particularly useful in correlating structures and identifying the locus of extension when the models are cut for cross-sections and re-constructed in 3D. At the end of the experimental run, the models are also covered with a thick protective layer of black sand for the wetting and cutting process.

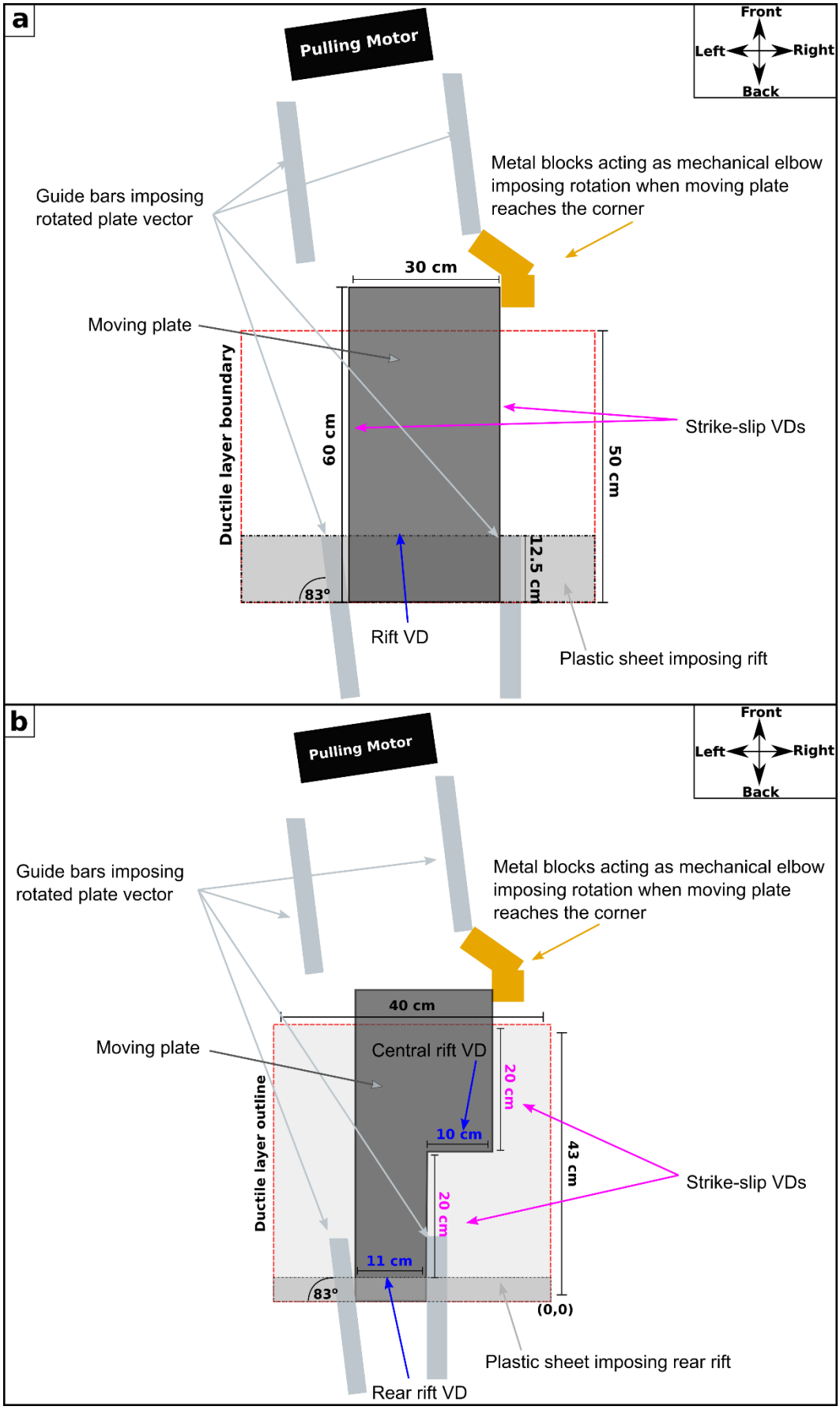
a
Pulling Motor
Front
Left
Right
Back
Guide bars imposing rotated plate vector
Metal blocks acting as mechanical elbow imposing rotation when moving plate reaches the corner
30 cm
Moving plate
Ductile layer boundary
60 cm
50 cm
Strike-slip VDs
12.5 cm
83°
Rift VD
Plastic sheet imposing rift
b
Pulling Motor
Front
Left
Right
Back
Guide bars imposing rotated plate vector
Metal blocks acting as mechanical elbow imposing rotation when moving plate reaches the corner
40 cm
Moving plate
Central rift VD
20 cm
10 cm
Ductile layer outline
43 cm
Strike-slip VDs
20 cm
11 cm
83°
(0,0)
Plastic sheet imposing rear rift
Rear rift VD

Figure 3.5 – Model arrays used in the analogue modelling chapters of this thesis: a) Chapter 5, b) Chapter 6. Initial configuration, dimensions and distinct elements of model arrays are labelled on each panel. Red box symbolizes the model boundary, dark grey box symbolizes the moving plate. Yellow boxes represent the mechanical elbow used for the rotation. Elongate grey box in the back symbolizes the fixed plastic sheet acting as a rift.

The model configuration (Figure 3.5) allows us to investigate the effects of: a) overlap and underlap caused by the rotation of the moving plate on parallel strike-slip boundaries (Figure 3.5a) and b) transtensional rotation on a pull-apart basin developing between two strike-slip VDs (Figure 3.5b). At the trailing edge of the moving plate in each experiment, a thin plastic sheet is fixed above the moving plate to act as a VD, imposing rifting (Figures 3.5 & 3.6). The plate is guided by a series of metal bars at its front and trailing ends. These ensure that a) movement initially remains almost orthogonal and b) rotation at the later stage is not greater than 7^{o} (Figures 3.5 &3.6 , grey boxes labelled guide bars).

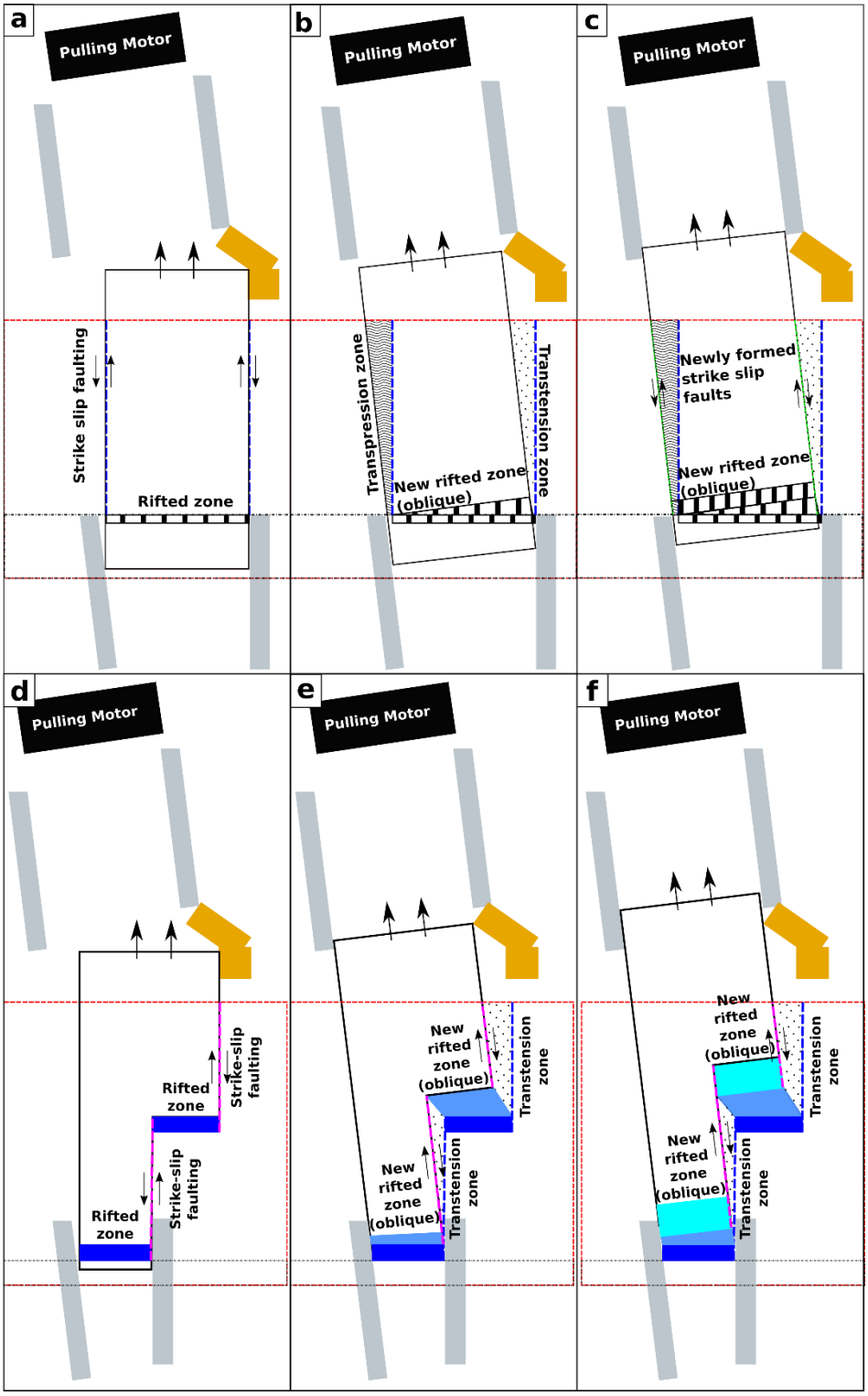

Figure 3.6 – Kinematics of the analogue models described in the analogue modelling chapters of this thesis: a-c) Chapter 5, d-f) Chapter 6. a,d) orthogonal motion stage, b,e) end of rotation stage, c,f) new oblique plate motion vector stage.

In each model, once motion through the step motor starts, the plate moves orthogonally, creating orthogonal rift-transform structures (Figure 3.6a,d). A construction of heavy metal blocks acting as a mechanical elbow (Figures 3.5 and 3.6, yellow boxes) then forces the plate to rotate until it leaves the top end of the elbow (simultaneously hitting the top left guide bar), having acquired a new vector of motion (Figure 3.6b,e). In this rotation stage, the previously formed structures undergo rotation and oblique rifting (Figure 3.6b,e). Finally, after rotation has ended, the plate is constrained by the top guide bars, moving with a new plate motion vector, oblique to the original (Figure 3.6c,f).

A set-up that was tested and abandoned prior to adopting the one discussed above consisted of only the front guide bars, which assign the new plate motion vector to the moving plate (Figure 3.7a). This configuration, however, resulted in the moving plate's pole of rotation being on the front end of the moving plate, along the strike-slip VD. However, this would not be the case in nature, as transform faults related to rifts are primarily controlled by the extension direction produced through rifting/spreading. Thus, the need to migrate the pole of rotation closer to rear end of the moving plate (and consequently the rift) required the addition of the rear guide-bars and mechanical elbow (Figures 3.5-3.7) in order to impose rotation. This kinematic mechanism was chosen because it allows for the pole of rotation to a) be located on the rift/spreading centre and thus is a more accurate representation of natural conditions and b) migrate with the moving plate when the rotation stage of the experiments is implemented (Figure 3.7a).

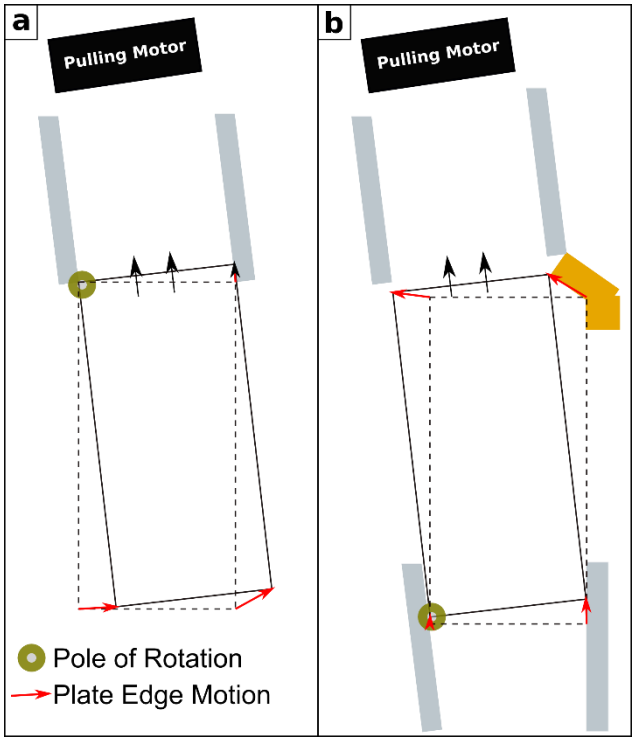

Figure 3.7 – The two different kinematic set-ups considered for the analogue modelling experiments. a) without rear guide bars or mechanical elbow, b) with rear guide bars and a mechanical elbow.

The brittle/ductile models in both the analogue modelling chapters represent a two-layer continental crust, while the brittle-only model represents a single layer of oceanic crust. Layers were as follows:

a) The brittle upper crust is represented by a 1.6 cm thick layer of dry feldspar sand (deformable according to the Mohr-Coulomb criterion) with a density of ρ = 1.3 g/cm^3 (Sokoutis et al., 2005; Willingshofer et al., 2005; Luth et al., 2010) and an internal friction coefficient of μ_{fric} of 0.6 (Willingshofer et al., 2018), sieved to a grain size d = 100-350 µm.

b) Ductile lower crust is modelled with a 0.8 cm thick layer of purely viscous transparent silicone putty SGM-36, from the PDMS group, a poly-dimethyl siloxane with a density of ρ = 0.970 g/cm^3, and viscosity at room temperature of μ_{vis} = 5*10^4 Pa s (Weijermars, 1986a; Weijermars, 1986b; Weijermars 1986c).

The governing equations for the layer strengths are derived from Brun (2002). In the brittle layers, the strength profile along the strike-slip faults is given by the equation:

$$\sigma 1 - \sigma 3_{(ss)} = \rho_b g z_b \quad \text{(Equation 3.8)}$$

where $\sigma 1\text{-}\sigma 3_{(ss)}$ is the brittle layer strength along the strike-slip faults, ρ_b is the brittle layer density g is gravitational acceleration and z_b is thickness of the sand layer (Brun, 2002).

For extension in the brittle layers, the governing equation is:

$$\sigma 1 - \sigma 3_{(r)} = \frac{2}{3}(\sigma 1 - \sigma 3)_{(ss)} \quad \text{(Equation 3.9)}$$

where $\sigma 1\text{-}\sigma 3_{(r)}$ is the extending brittle layer's strength (Brun, 2002).

For the ductile layer, the strength is:

$$\sigma 1 - \sigma 3_{(d)} = 2\left(\eta \frac{V}{z_d}\right) \quad \text{(Equation 3.10)}$$

where $\sigma 1\text{-}\sigma 3_{(d)}$ is ductile layer shear strength, η is ductile layer viscosity, V is extension velocity and z_d is ductile layer thickness (Brun, 2002).

The analogue models in this work are scaled to their natural prototypes based on the principle of maintaining similarity in the structural geometry, the kinematics and the rheology of the crust (Hubbert, 1937; Ramberg, 1982; Weijermars & Schmeling, 1986; Sokoutis et al. 2000; Sokoutis et al., 2005). Rheologic and dynamic similarity are retained by scaling the gravitational stress (Dombradi et al., 2010) (σ):

$$\sigma^{\propto} = \rho^{\propto} g^{\propto} z^{\propto} \quad \text{(Equation 3.11)}$$

Where ρ is density, g is gravitational acceleration, z is thickness and the $\propto$ symbols denote the model to nature ratio (Sokoutis et al., 2005). For the viscous deformation, the ratio between gravitational and viscous stresses is given by the Ramberg Number (R_m – Weijermars & Schmeling, 1986):

$$R_m = \frac{\rho_d g z_d}{\eta \dot{\varepsilon}} \quad \text{(Equation 3.12)}$$

Where ρ_d is the ductile layer density and $\dot{\varepsilon}$ is the strain rate.

Brittle deformation was scaled using the ratio between gravitational stress and cohesive strength, the Smoluchowski number (*Sm* – Ramberg, 1981):

$$S_m = \frac{\rho_b g z_b}{\tau_c + \mu_c \rho_b z_b} \quad \text{(Equation 3.13)}$$

Where τ_c is the cohesive strength and μ_c is the internal friction coefficient. For accurate scaling, the individual R_m and S_m values of models and natural prototypes should be as similar as possible (with the ideal value being a ratio of 1:1) (Dombradi et al., 2010). As previous work suggests, if the Reynolds number (*Re*) is relatively low in a model, then the inertial forces can be neglected compared to the viscous ones (Wickham, 2007; Del Ventisette et al., 2007; Dombradi et al., 2010). The Reynolds number is given by the equation:

$$Re = \frac{\rho V l}{\eta} \quad \text{(Equation 3.14)}$$

Where *V* is the extension velocity and *l* is the total extension length. Sufficiently low Reynolds numbers allow for the scaling of different forces to deviate from strict dynamic similarity, allowing the time and length ratios to be considered independent variables (Ramberg, 1981).

3.4 Real world data as comparisons for modelling results

Finally, in this thesis, the modelling results are compared to real world examples. In the following two sub-sections, these are listed for reference use and shown in Figure 2.5 of the previous chapter. Detailed geological backgrounds of these areas are given within each corresponding result chapter.

3.4.1 Gulf of California

In all of the three result chapters of this thesis, a comparison is made with the transtensional, obliquely partitioned Gulf of California area. The Gulf of California consists of en-echelon transform-spreading ridge systems, with a great variation in structural styles, ranging from pull-apart basins in the north to narrow, magmatic and amagmatic rifts in the south (Lizarralde et al., 2007). This configuration is thought to have occurred due to a change in plate motion around 6 Ma (Bennett & Oskin, 2014), leading to the transtensional opening of the Gulf from south to north (Umhoefer et al., 2018).

The specific dataset that is compared against the analogue modelling experiments presented in Chapters 5 and 6 is the high-resolution UL9905 seismic dataset (Stock et al., 2015) from the Northern Gulf of California. This dataset was collected by the Lamont-Doherty Earth Observatory's high-resolution multichannel seismic (MCS) system aboard Centro de Investigación Científica y Educación Superior de Ensenada's (CICESE) 28 m research vessel B/O *Francisco de Ulloa* between May-June 1999. It comprises of a 2D grid of 3500 km of reflection data shown in Figure 3.8.

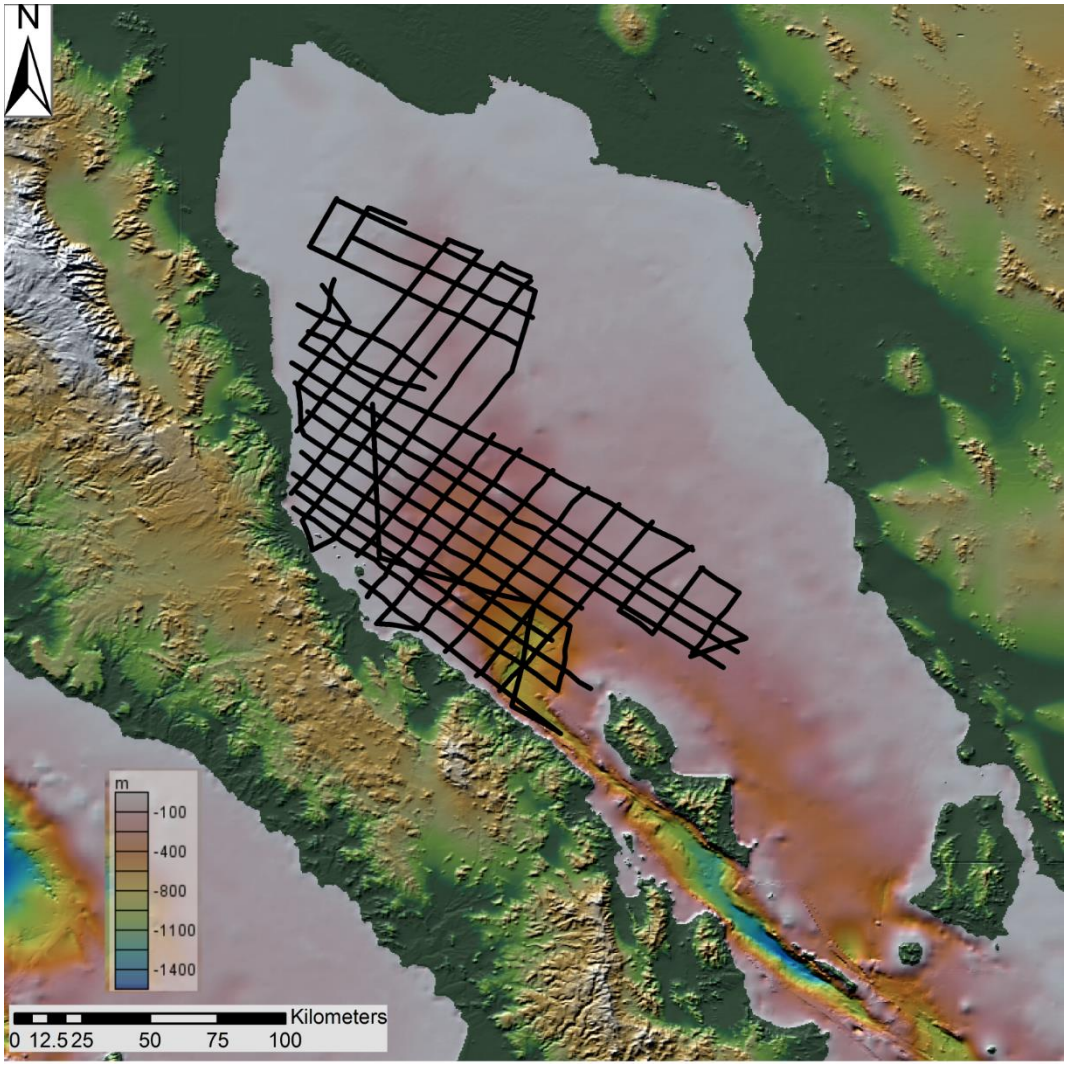

Figure 3.8 – Location of the UL9905 high resolution seismic reflection dataset (Stock et al., 2015). Bathymetry from GMRT Grid Version 3.3 (Ryan et al., 2009).

3.4.2 Other locations investigated in this work

Other locations shown in this thesis are (by chapter):

Chapter 4

The Ungava Transform Zone: The Ungava Transform Zone is a large, right-stepping transform zone in the Davis Strait between Greenland and Canada that accommodated horizontal motion between the (now extinct) oblique spreading ridges in Baffin Bay in the north and Labrador Sea in the south (Oakey & Chalmers, 2012). This area is studied as an example of a rift-transform intersection (and corresponding transform margin) undergoing transpression during its evolution.

The Gulf of Aden: The Gulf of Aden has undergone ~35 Ma of spreading and is characterised by oblique crustal inheritance in the form of Mesozoic basins, oblique rifting and a change in the plate motion vector observed 20 Ma ago (Bellahsen et al., 2013; Brune & Autin, 2013; Jeanniot & Buiter, 2018). This area is studied as an example of a rifted margin with fracture zones affected by plate rotations and transtension during its evolution, influencing margin asymmetry.

Chapter 5

The Tanzania Coastal Basin: This region is investigated because it underwent transpression due to a plate re-organisation ~150 Ma, resulting in the formation of the Davie Fracture Zone and leading to potential intra-oceanic crust thrusting (Phethean et al., 2016).

Chapter 6

The Bohai Basin: The Bohai Basin in Northern China is a 1000 km long by 600 km wide pull-apart structure, bound by lithosphere-scale strike-slip faults, which has undergone a transtensional phase in its evolution (Allen et al., 1998). This area is investigated as a further example for the evolution of releasing bends along transtensional lithosphere-scale strike-slip systems.

4 The lithosphere-scale: The impact of oblique inheritance and changes in relative plate motion on the development of rift-transform systems.1

4.1 Introduction

Transform margins and their accompanying transform faults are a relatively understudied feature of plate boundaries that accommodate predominantly boundary-parallel relative plate motion. Initially, they were investigated from a morphological perspective as features that accommodate oceanic spreading (e.g. Wilson, 1965; Le Pichon & Hayes, 1971) and, subsequently, by more complex thermo-mechanical models that investigated their evolution (e.g. Basile, 2015; Mercier de Lepinay et al., 2016). Continent-ocean transforms are found in settings where there has been: a) orthogonal extension between oceanic spreading segments (e.g. Gerya, 2013; Basile, 2015); b) oblique extension (e.g. Bellahsen et al., 2013; Brune & Autin, 2013); c) plate rotations (Morrow et al., 2019); or d) combinations of the above (Farangitakis et al., 2019). Transform margins start their life-cycle as transfer faults offsetting rift segments (Bosworth, 1986) or as proto-transform faults representing diffuse zones of oblique strike-slip motion initiating during the later stages of continental break-up (Illsley-Kemp et al., 2018). Basile (2015) and Le Pourhiet et al. (2017) refer to these early-stage continental lithosphere faults as “intra-continental transform faults”. In this study, we refer to these features as continent-continent transform faults (CCTs), based on the nature of crust being displaced on each side of the margin. Continent-ocean transform faults

1 This chapter has been published as: Farangitakis, G.P., Heron, P.J., McCaffrey, K.J.W., van Hunen, J., & Kalnins, L.M. (2020). The impact of oblique inheritance and changes in relative plate motion on the development of rift-transform systems. Earth and Planetary Science Letters, 541, 116277 https://doi.org/10.1016/j.epsl.2020.116277

(COTs) are the structures that link spreading ridges that have evolved from these connecting rifts (Figure 4.1a,b). Similarly, continent-ocean fracture zones (COFZs) and some ocean-ocean fracture zones (OOFZs) represent the fossilised remains of a transform fault (Figure 4.1a). The morphology and duration of activity of a continent-ocean transform margin is linked to tectonic parameters such as the orientation and position of pre-existing lithospheric structures, changes in plate motion vectors, and far-field forces (e.g. Basile, 2015; Le Pourhiet et al., 2017). Around the world, we observe transform faults that can be directly linked with a corresponding transform margin (Figure 4.1b). However, not all transform faults are directly associated with a transform margin, particularly along segmented spreading ridges (illustrated by the oceanic fracture zone OFZ in Figure 4.1b) (Bellahsen et al., 2013; Illsley-Kemp et al., 2018). Our work focuses on the first case: continental transform margins directly associated with transform faults.

Numerous modelling studies indicate that both oblique inheritance and changes in plate motion affect transform margin evolution. Bellahsen et al. (2013) suggest that pre-existing Mesozoic basins and transfer zones partially control the current Gulf of Aden oblique spreading. Basile (2015) shows that continent-ocean transform faults develop within continental lithosphere either by reactivating or cross-cutting pre-existing structural features. Farangitakis et al. (2019) demonstrate how changes in relative plate motion produce oblique rifts accompanied by transtension (Gulf of California) or transpression (Tanzania Coastal Basin) along transform margins. Ammann et al. (2018) argue that formation of long transform faults (such as those in the Central Atlantic) is favoured by high obliquity and slow extension rates during continental rifting. Peace et al. (2017) indicate that lithosphere inheritance could strongly control the evolution of an obliquely rifted margin in W. Greenland, while numerical modelling of the region inferred that ancient mantle scarring may also play a role (Heron et al., 2019).

By analysing a global rift database, Brune et al. (2018) suggested that oblique rifting might actually be the rule, rather than the exception. If so, the corresponding transform margins must

also experience significant transtensional or transpressional deformation (Figures 4.1c-f), which would influence their morphology and be evident in many natural examples across the world.

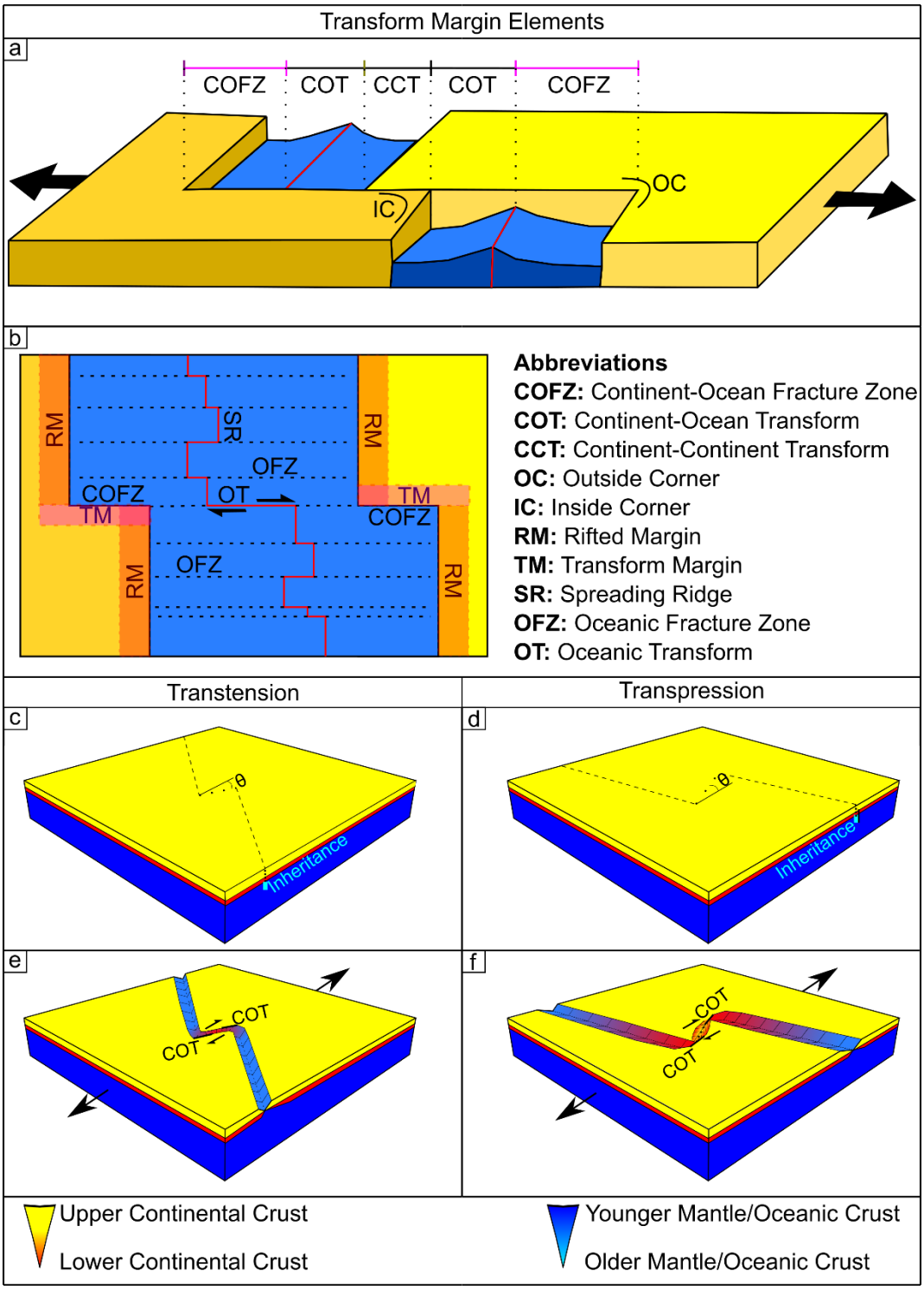

Figure 4.1 – a: Main elements of an active transform margin profile (redrawn from Lorenzo, 1997). b: Main elements of a passive transform margin (map view). c-f: Schematic representation of the response of an inherited structure to an oblique extensional deformation. c, d: two initial

conditions; e, f: transtensional and transpressional deformation on transform segment after extension/rifting. Cyan feature in the mantle in c and d represents the inherited feature projected onto the surface with a dashed black line. θ: angle of rotation between the extension direction and the transform segment.

In this study, we explore the overall effect of inherited obliquity and change in relative plate motion on continent-ocean transform margins through a series of numerical modelling experiments. The first set investigates how the obliquity of a pre-existing zone of weakness within the continental lithosphere affects continent-ocean transform margin evolution. The second set examines the role that a change in relative plate motion plays in margin evolution. We then link our observations to continent-ocean transform margins around the world. Our modelling focuses on the continental crust and therefore does not take into consideration oceanic crustal features; hence, our observations are focused on the evolution of the continental parts of the transform margins and stop when these become passive. Finally, we present a novel approach for linking transform margins' current morphology to their past evolution.

4.2 Methodology

The 3D nature of continent-ocean transform margins and the interplay between local and far-field kinematic, dynamic and transient effects pose a challenge for both numerical and analogue models. Thus far, modelling of transform margins and the parameters that affect their evolution has followed two approaches. The first examines the development of rift connectivity by placing isolated seeds in the lithosphere (either as zones of weakness or as modified Lithosphere-Asthenosphere Boundaries/LABs) and studying their interactions by varying their location (e.g. overlap, underlap), shape and orientation within an extensional model (e.g. Allken et al., 2012; Gerya, 2013; Zwaan & Schreurs, 2017; Le Pourhiet et al., 2017; Illsley-Kemp et al., 2018). The second modelling approach examines the deformation of already established shear zones or connected rift segments and how they respond to changes in extension direction or oblique rifting

(e.g. Brune et al., 2012; Brune & Autin, 2013) or to inherited structures situated at oblique angles to the established rifts (Autin et al., 2013).

Following the second approach, we use two different experimental scenarios to investigate the effects of obliquity of inherited structures and plate rotations on a rift-transform-rift configuration in 3D space. Computations were carried out using the open source finite element numerical code ASPECT, version 2.1.0 (Kronbichler et al. 2012; Heister et al., 2017) and follow the study of Heron et al. (2019). Our models are governed by a dislocation creep flow law and display Drucker-Prager plasticity as a rheology with strain weakening (e.g. Naliboff & Buiter, 2015, Table 4.1), using a "seed" configuration that represents an initial weak zone in the top of the mantle (Huismans & Beaumont, 2011).

Table 4.1 – Physical properties of the models (parameters obtained from a: Rutter and Brodie, 2004; b: Rybacki et al., 2006; c: Hirth & Kohlstedt, 2004; d: Heron et al., 2019; e: Naliboff & Buiter, 2015; f: Chapman, 1986)

Parameter	Unit	Upper Crust	Lower Crust	Mantle	Seed
Rheology		Wet Quartzite [a]	Wet Anorthite [b]	Dry Olivine [c]	Dry Olivine [c]
Thermal diffusivity [d]	m^2/s	$1.19x10^{-6}$	$1.15x10^{6}$	$1.33x10^{-6}$	$1.33x10^{-6}$
Density [e]	kg/m^3	$2.8x10^{3}$	$2.9x10^{3}$	$3.3x10^{3}$	$3.3x10^{3}$
Thermal expansivity [d]	1/K		$2.00x10^{-5}$		
Internal friction angles [d]	degrees	20	20	20	0
Cohesions [d]	Pa	$2.00x10^{7}$	$2.00x10^{7}$	$2.00x10^{7}$	10^{7}
Plasticity strain weakening interval [d]			0-0.5		
Temperature at top of layer [f]	K	273 (top)	681.6 (top)	823 (top)	
Heat production [f]	W/m^3	$1.50x10^{-6}$	0	0	0
Thermal conductivity [f]	W/(m*K)	2.5	2.5	3.3	3.3
Viscosity range [e]	Pa s		$1.00x10^{18}$ - $1.00x10^{26}$		

4.2.1 Experimental Setup

We use a box with dimensions of 800 by 800 km horizontally and 120 km vertically. Compositionally, the top 20 km is initially upper continental crust, with 10 km lower continental crust beneath and 90 km of mantle lithosphere at the bottom (Figure 4.2).

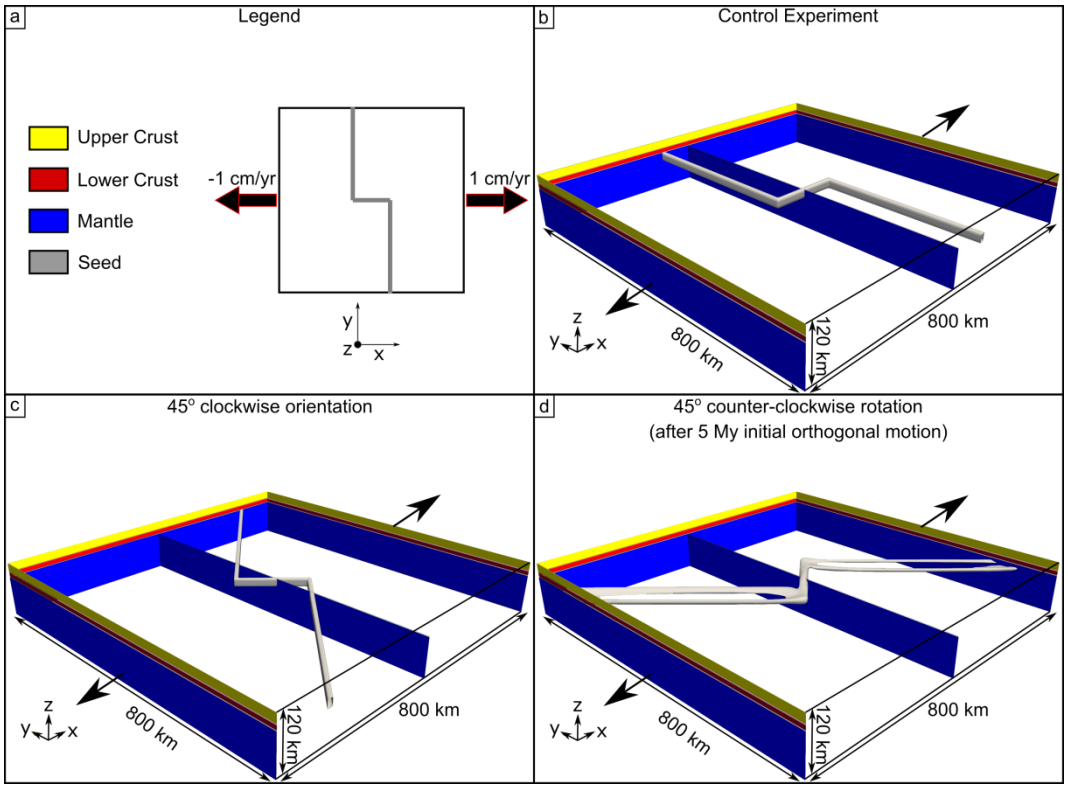

Figure 4.2 – Experimental set up. a: rheology and model set-up, b: control experiment configuration, c: obliquity experiment example set-up for transtension on transform boundary, d: set-up to simulate rotation of plate vectors, which creates transpression on the transform boundary following an initial orthogonal extension.

Resolution is uniform with 3.125 x 3.125 x 3.125 km per cell, totalling 262,144 active cells and 19 million degrees of freedom. Our models have prescribed boundary velocity conditions on their x = 0 km, x = 800 km and z = 120 km boundaries and tangential velocity boundary conditions on the y = 0 km and y = 800 km boundaries. The top boundary has a free surface, which allows for topography and is generated by an Arbitrary Lagrangian-Eulerian framework with 848691 degrees of freedom (Rose et al., 2017). The applied east-west extension is 1 cm/yr on each boundary (total of 2 cm/yr), and outflow on these edges is balanced by an inflow of 0.3 cm/yr at the base.

4.2.2 Seed configuration and obliquity

We introduce a simple left-stepping rift-transform-rift configuration, represented by a weak seed 2 km beneath the base of the crust straddling the horizontal midpoint (Figure 4.2). The seed is used as an inherited structure in the first set of experiments. In the second set, the seed is used to initiate orthogonal rifting that replicates the control experiment (Figure 4.2b) and is then rotated after 5 Myr. The rift seeds extend the full length of the box (even when rotated). We use a rift segment offset of 160 km, intermediate between the values used by Allken et al., (2012) and Le Pourhiet et al., (2017). We tested offsets between 120-200 km (Suppl Figures A1-A5) and find that transform faults are established at these offset lengths as well. We define positive angle change as clockwise obliquity between seed and extension direction, creating transtension (as in Figure 4.2c) on the transform fault, and negative angle change as counter-clockwise obliquity, creating transpression (as in Figure 4.2d). The models are then computed in the two different scenarios: one featuring inherited structures oblique to the extension direction and another that simulates rotation in relative plate motion.

4.2.2.1 Inheritance experiments

The models start from t_0=0 Ma with an inherited seed (e.g., Figure 4.2c). First, we conduct a control experiment with the rift-transform-rift configuration orthogonal (0^o) to the extension direction (Figures 4.2b and 4.3). We then perform 10 further experiments, with the seed at 10^o obliquity intervals from θ = -5^o to -45^o and 5^o to 45^o, representing increasingly oblique inherited structures (Figure 4.2c).

4.2.2.2 Effect of rotation experiments

In a second set of experiments, we use a three-step process to evaluate the effect of an imposed rotation of plate motion vectors on an existing continent-ocean transform. First, we calculate a 1200x1200x120 km orthogonal model with the same seed set-up as the control model shown in Figure 4.2b. The 5 Ma output of the larger 3D model is used as a “sampling box” of the temperature, composition (upper crust, lower crust, and mantle), seed and total strain rate after

5 Myr. We then rotate the box by the desired angle and sample a smaller 800x800x120 km domain around its 3D midpoint. The established spreading system now sits at an angle to the extension direction in this smaller domain. The rotation values range from θ = -45° to -5° and 5° to 45°, respectively (see Suppl. Material code repository). Finally, we use this new smaller domain as an initial composition and temperature field to run a suite of experiments on delayed rotation (Figure 4.2d).

4.2.3 Governing Equations

This study is governed by the equations of conservation of momentum, mass and energy in an incompressible medium with an infinite Prandtl number:

$$-\nabla \cdot (2\mu\dot{\varepsilon}) + \nabla P = \rho g \qquad \text{(Equation 4.1)}$$

where μ = viscosity, $\dot{\varepsilon}$ = strain rate tensor, P = pressure, ρ = density and g = gravitational acceleration.

$$\nabla \cdot u = 0 \qquad \text{(Equation 4.2)}$$

$$\rho C_p \left(\frac{\partial T}{\partial t} + u \cdot \nabla T\right) - \nabla \cdot k\nabla T = \rho H \qquad \text{(Equation 4.3)}$$

where u = velocity vector, C_p = thermal heat capacity, T = Temperature, t = time, k = thermal conductivity, and H = internal heat production.

Upper crust, lower crust, mantle and seed represent compositional fields that adhere to the pure advection equation:

$$\frac{\partial C_i}{\partial t} + u \cdot \nabla C_i = 0 \qquad \text{(Equation 4.4)}$$

where C_i = compositional field.

The above equations are solved with the finite element method in a discretised domain of finite elements using an iterative Stokes solver (Kronbichler et al., 2012). The solution is then

interpolated using Lagrangian polynomials as basis functions (Glerum et al., 2018). The models use a temperature-dependent density, but no pressure-dependence, since the model is incompressible (e.g., Heron et al., 2019).

The models have a nonlinear viscous flow (dislocation creep) with Drucker-Prager plasticity for the rheology, a setup used in many previous studies (e.g., Huismans & Beaumont, 2011; Naliboff and Buiter, 2015; Heron et al., 2019).

Dislocation creep is defined as:

$$\mu = 0.5A^{-\frac{1}{n}}\dot{\varepsilon}_e^{\frac{(1-n)}{n}} exp\left(\frac{E+PV}{nRT}\right) \quad \text{(Equation 4.5)}$$

where A = viscosity prefactor, n = stress exponent (n>1), $\dot{\varepsilon}_e$ = square root of the deviatoric strain rate tensor second invariant, E = activation energy, V = activation volume and R = universal gas constant (Karato, 2008).

Viscosity is limited through a Drucker-Prager yield criterion where the yield stress in 3D is:

$$\sigma_y = (6Ccos\varphi + 2Psin\varphi)/(\sqrt{3}(3 + sin\varphi)) \quad \text{(Equation 4.6)}$$

where C = cohesion and φ = angle of internal friction. When φ equals 0, as in the imposed seed, the yield stress is fixed and equal to the Von Mises yield criterion. When the viscous stress ($2\mu\ \dot{\varepsilon}_e$) exceeds the yield stress σ_y, we apply plastic yielding by rescaling the effective viscosity (Willett, 1992; Kachanov, 2004) so that the stress is less than the yield value (e.g., Thieulot, 2011). To ensure numerical stability, we constrain the viscosity in our models between 10^{18} and 10^{26} Pa·s (Table 4.1).

We apply strain weakening for the internal friction angle and cohesion. They reduce linearly as a function of finite strain magnitude to 50% of their initial value at a strain of 50% (Table 4.1; Bos & Spiers, 2002; Heron et al., 2019). Our sensitivity analysis for strain weakening parameters (Suppl. Figures A6-A11) indicates that no significant changes in the margin morphology occur, apart from

when the internal angle of friction of the seed is increased (Suppl. Figures A7 & A9). This change is expected since the rheological weakness that the seed represents is diminished, so the models resemble the result of a pure orthogonal rifting case.

The model compositional fields have individual values of thermal and rheological parameters (Table 4.1). If more than one compositional fields are present at the same time within a cell, viscosities are averaged harmonically (Glerum et al., 2018). We use a rheological setup similar to that of Naliboff & Buiter (2015), using wet quartzite flow laws for the upper crust (Rutter & Brodie 2004), wet anorthite for the lower crust (Rybacki et al., 2006), and dry olivine for the mantle (Hirth and Kohlstedt, 2004). The modelling set-up does not allow for the formation of brittle oceanic crust, but instead keeps the rheology of the mantle. Thus, we focus our observations on the continental crust aspects of the models.

4.2.4 Thermal model set-up

We prescribe an initial temperature field similar to a typical continental geotherm (Chapman 1986) with no lateral variations:

$$T(z) = T_o + \frac{q}{k}z - \frac{Hz^2}{2k} \quad \text{(Equation 4.7)}$$

where T_0 = surface temperature of each layer, H = heat production, q = heat flow through the surface of the specific layer, k = thermal conductivity and z = depth (see Table 4.1). Our sensitivity analysis for layer temperature parameters indicates no effect on the transform margin evolution timing. However, a colder top mantle surface increases the effect of the seed on the rifted margin asymmetry (see Suppl. Figures A12-A13).

4.3 Results

Our experimental results on the early development of transform margins are presented as maps of the surface evolution of the model. We also consider the kinematics observed in the surface velocity plots and evolving surface material. We first present the control orthogonal experiment

(Figure 4.3). We then present two sets of models (each with 5 experiments) for transtension (positive θ angles) (Figures 4.4 & 4.5), followed by two more sets for transpression (negative θ angles) (Figures 4.6 & 4.7). The first set in each case (Figures 4.4 & 4.6) represents oblique inheritance, while the second (Figures 4.5 & 4.7) represents a change in the relative plate motion vector after 5 Ma of orthogonal extension. In each figure, the seed configuration and direction of extension are shown in the first panel. Surface strain rate and surface velocity plots are presented in Suppl. Figures A15-A32 and further analysed in the discussion.

4.3.1 Development of structures (Orthogonal Extension)

In our control experiment, rifting initiates from the outer edges of the box, perpendicular to the extension direction (Figure 4.3b), and propagates towards the transform seed. Transform motion is expressed first as a continent-continent transform fault (CCT) followed by a continent-ocean transform fault (COT) (Figure 3c). In this case, the transform margin is active until 13 Ma (Figure 4.3d); by 15 Myr, the transform margin is expressed by two continent-ocean fracture zones (COFZs) separated by a spreading axis (Figure 4.3e).

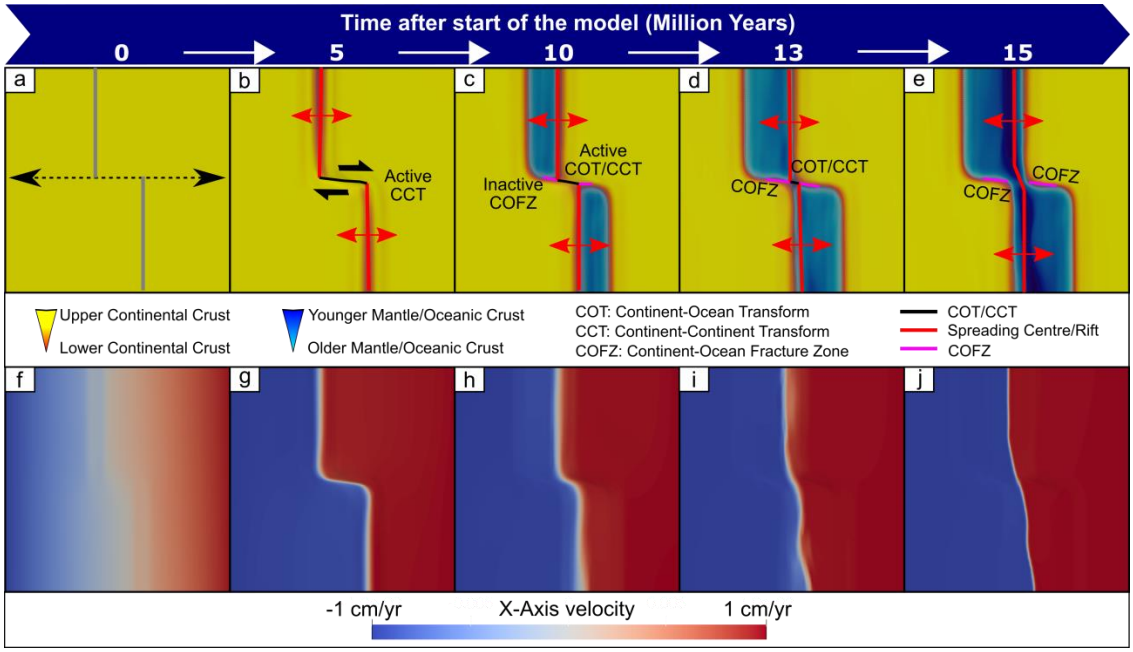

Figure 4.3 – Orthogonal extension control model. a-e: Individual panels show surface material evolution through time. Location of seeds (grey lines) and extension direction (dashed arrows)

shown in panel a. f-j: surface velocity in the x direction. For an uninterpreted version, strain rate patterns and cross-sections across the rifted margins, refer to Suppl. Figures A14-A16.

4.3.2 Transtensional deformation on the transform boundary (positive angle θ to extension direction)

4.3.2.1 Oblique inheritance experiments

Figure 4.4 shows the extension of a rift-transform-rift configuration oriented at a positive obliquity angle (with respect to the extension direction) between 5-45°. The transform structure undergoes transtensional deformation, which is illustrated by snapshots every 5 Ma from the initiation of extension. The duration of activity on the COTs and CCTs depends on the obliquity of the inherited structure, decreasing with increasing θ. For 5°, the transform margin is active until 12.5 Ma from the start of the model (Figure 4.4c); for 15°, until 11 Ma (Figure 4.4g); for 25°, until 9 Ma (Figure 4.4j); for 35°, until 7.5 Ma (Figure 4.4n); and for 45°, until 7 Ma (Figure 4.4r). After these times, the COTs become inactive COFZs (pink lines in Figure 4.4). In comparison to the 5°, 15° and 25° experiments (Figure 4.4a,e,i), the 35° and 45° experiments also produce a shorter transform segment connecting the two rifts (Figure 4.4n,r). Spreading localisation also depends on the angle of the inherited structure. At 5°, spreading localises in a quasi-uniform manner above the inherited rift structures. As obliquity increases, spreading increasingly localises near the transform seed first before spreading along the rift segments (darker mantle colourations on either side of the spreading ridges in Figure 4.4 at 10 Myr) (Suppl. Figure A17).

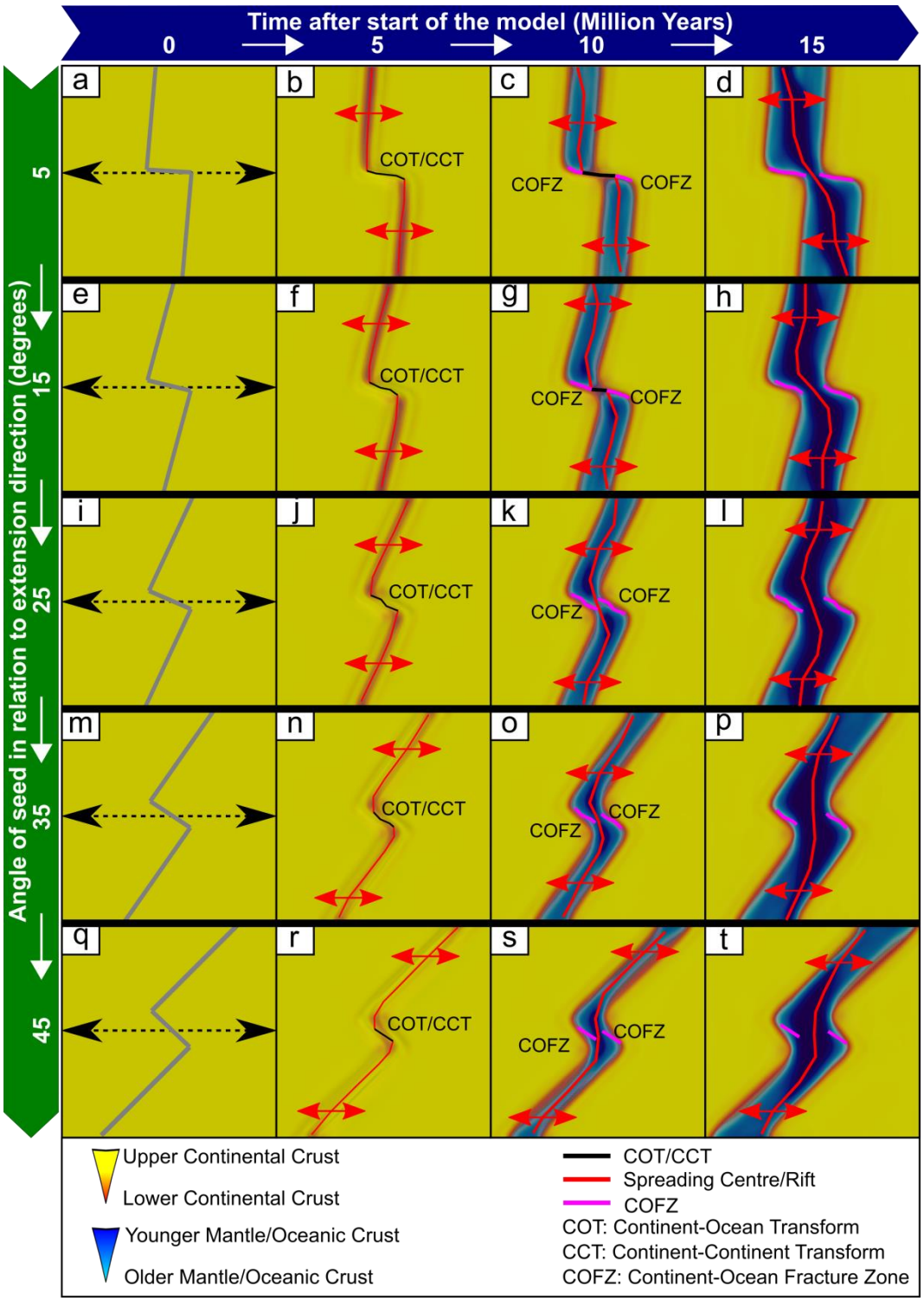

Figure 4.4 – Transtensional oblique inheritance models, with a seed oriented at a positive θ (with respect to the extension direction). Individual panels show surface material evolution through time. Location of seeds (grey lines) and extension direction (dashed arrows) shown in panels a,e,i,m,q. For an uninterpreted version, strain rate patterns, velocity plots and cross-sections across the rifted margins, refer to Suppl. Figures A17-A20.

4.3.2.2 Rotation experiments

We next present our experiments simulating a change in relative plate motion after rifting initiation (Figure 4.5). We perform orthogonal rifting for 5 Ma and then change the extension direction by 10^{o} increments from 5^{o} to 45^{o}. As marked in Figure 4.5, all model snapshots refer to the start of rotation after the initial rifting (e.g., Figure 4.5a is 0 Ma + 5Ma of initial rotation). In all models, spreading initiates at the outside corners of the rift-transform configuration, with a sigmoidal shape at the smaller angles (Figure 4.5c,g,k). As the angle increases, this sigmoidal shape progressively becomes rhomboidal (Figures 4.5o, s) (see also darker mantle colorations across both sides of the spreading ridge in Figure 4.5 after 15+5 Ma and Suppl. Figure A19).

COT and CCT activity time again are influenced by the angle of rotation. For 5^{o}, the transform margins are active until 11 Ma after the start of rotation (Figure 4.5c); for 15^{o}, until 9.5 Ma (Figures 4.5f,g); for 25^{o}, until 8.5 Ma (Figures 4.5j,k); for 35^{o}, until 7 Ma (Figures 4.5n,o); and for 45^{o}, until 6 Ma (Figures 4.5r,s). After these times, the passive transform margin is represented by COFZs (pink lines in Figure 4.5).

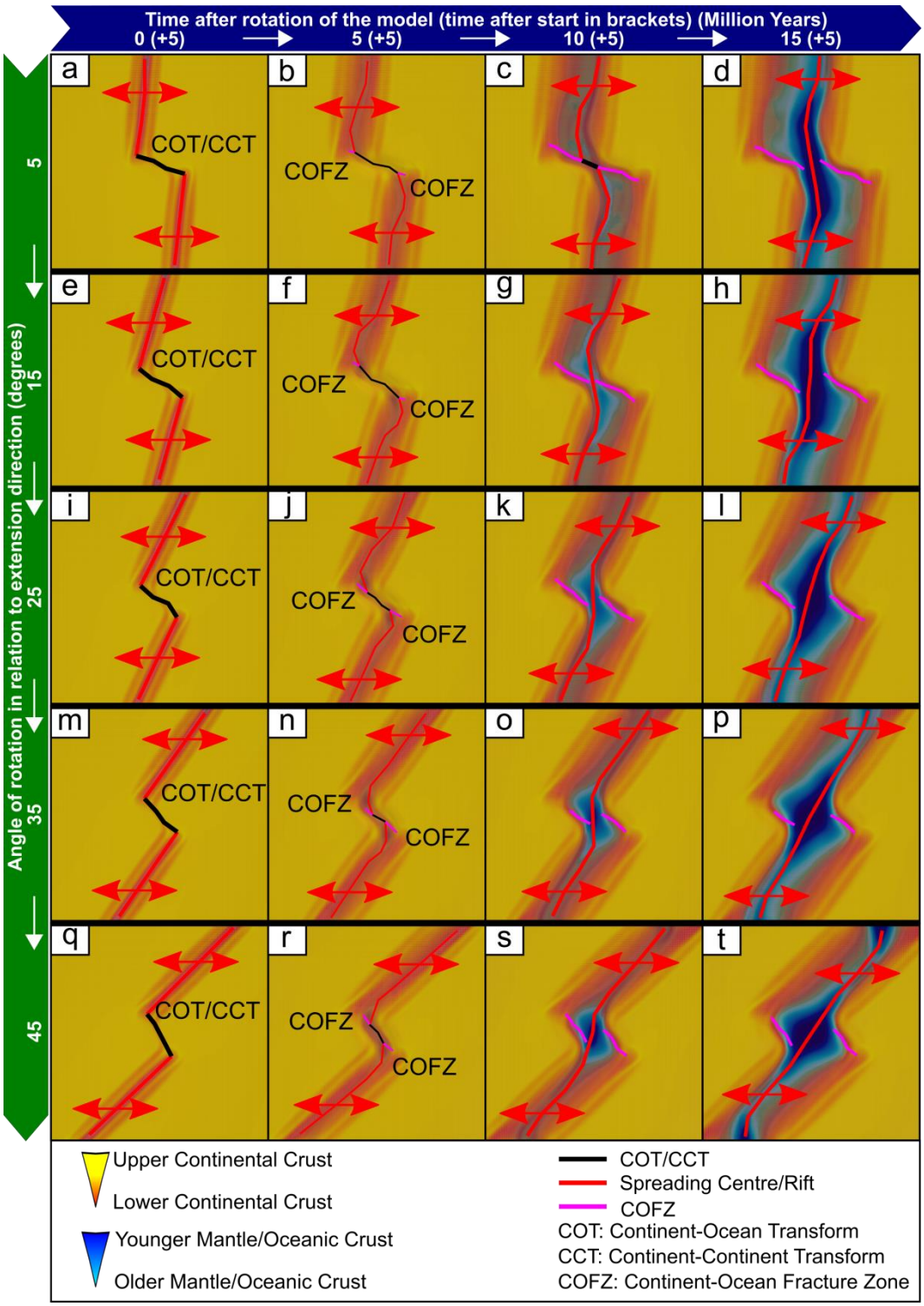

Figure 4.5 – Transtensional rotated models with a positive θ of rotation (with respect to the extension direction) after an initial 5 Ma of orthogonal extension. Individual panels show surface material evolution through time. For an uninterpreted version, strain rate patterns, velocity plots and cross-sections across the rifted margins, refer to Suppl. Figures A21-A24.

4.3.3 Transpressional deformation on the transform boundary (negative angle θ to extension direction)

4.3.3.1 Oblique inheritance experiments

In the transpressional oblique inheritance experiments, we investigate the case of oblique extension on a rift-transform-rift configuration oriented at a negative angle between -5° and -45° (Fig. 4.6). In all cases, rifting and subsequent spreading localise first at the outer boundaries of the box, perpendicular to the extension direction, and propagate towards the rift-transform corners. CCTs evolve into COTs, accommodating any horizontal motion, except for the -45° experiment (Figure 4.6u-y).

The length of time that the transform boundary remains active again depends on the obliquity of the inherited structure. For -5°, transform activity lasts until 15 Ma after the start of the model (Figure 4.6d); for -15°, until 17 Ma (Figure 4.6i); for -25°, until 22 Ma (Figure 4.6o); and for -35°, until 40 Ma (Figure 4.6t) before becoming inactive COFZs. The -45° experiment does not form a transform. Instead, the initial rifts propagate towards the centre and then away from each other (Figures 4.6v-w) as they evolve into two distinct spreading segments that do not interact (Figure 4.6y). The evolution of the -35° experiment displays a mixture of the tectonic characteristics shown in the -45° and -25° experiments. Rifting propagates inwards from the outer boundaries of the box. Although it initially seems that the rift segments are moving away from the transform zone, similar to the -45° experiment (Figure 4.6q), the spreading segments then connect through incipient transform motion (similar to -25 ° Figure 4.6l) and form an elongate transform zone (Figures 4.6r,t and strain rate patterns at 20 Ma in Suppl. Figure A26).

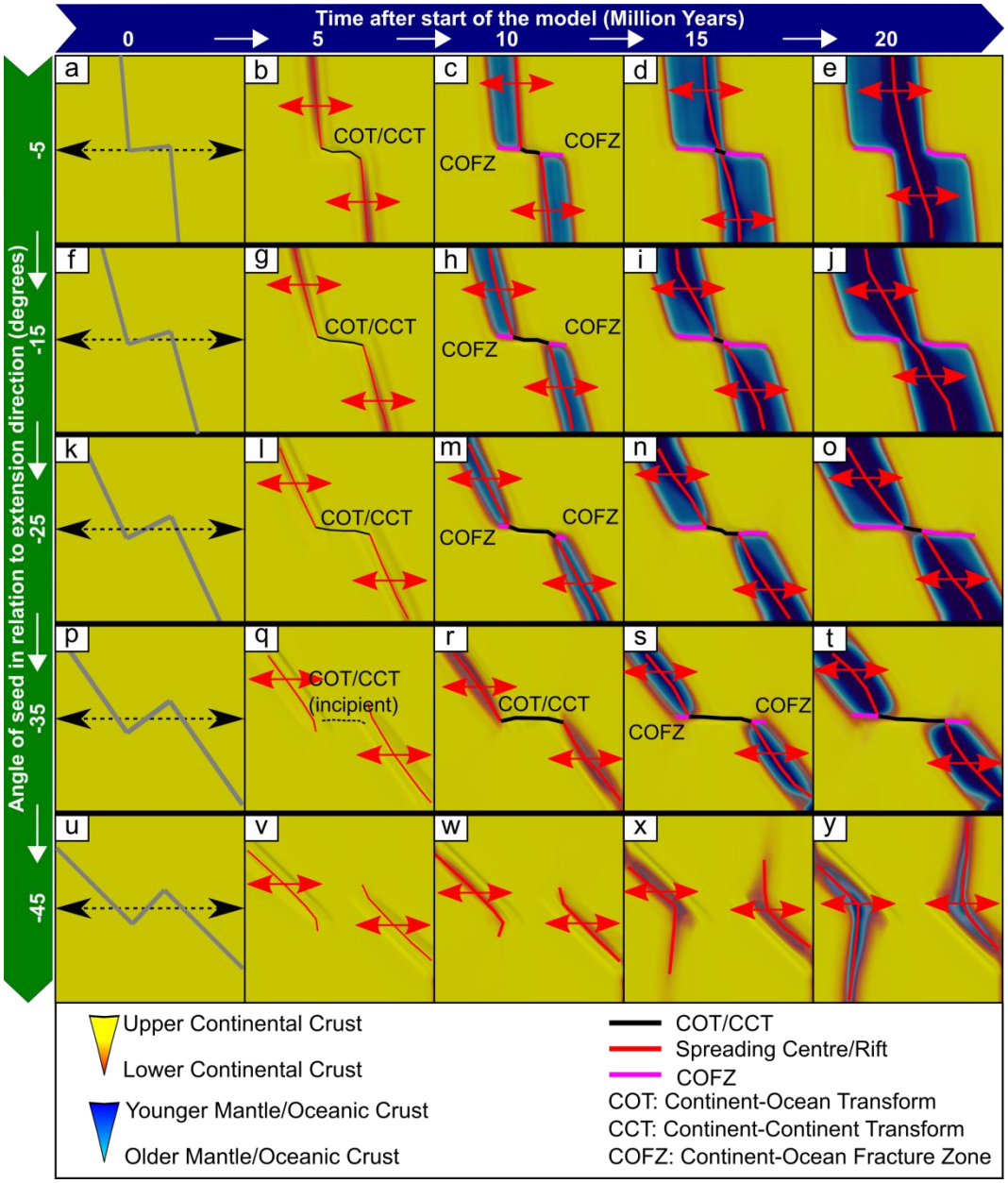

Figure 4.6 – Transpressional oblique inheritance models, with a seed oriented at a negative θ (with respect to the extension direction). Individual panels show surface material evolution through time. Location of seeds (grey lines) and extension direction (dashed arrows) shown in panels a,f,k,p,u. For an uninterpreted version, strain rate patterns, velocity plots and cross-sections across the rifted margins, refer to Suppl. Figures A25-28.

4.3.3.2 Rotation experiments

We next present the rotated experiments (for transpressional negative angles θ at 10° increments from -5° to -45°) simulating a change in relative plate motion after 5 Ma of orthogonal rifting (Figure 4.7). Similar to the oblique inheritance case, rifting and spreading localise from the outer boundaries of the box towards the rift-transform corners (note surface material on each side of

the rift/spreading ridges in Figure 4.7 after 10+5 Myr). The established transform zones accommodate any horizontal motion through CCTs and COTs. Transform activity duration increases with the angle of imposed rotation. For -5°, transform motion is active until 15 Ma after rotation (Figure 4.7c); for -15°, until 29 Ma (Figure 4.7j); for -25° until 35 Ma (Figure 4.7o); and for -35° and -45°, for at least 40 Myr, exceeding the model runtime (Figures 4.7t,y). An en-echelon pattern is observed at the surface around the transform zones for the lower rotation angle models (Figures 4.7c-d for -5°, 4.7i-j for -15°, and 4.7n-o for the -25° experiment). This pattern corresponds to diffuse zones where horizontal motion is accommodated. Within this zone, the transform boundary can be segmented into smaller, shorter lived transforms, such as in the -25° experiment (Figure 4.7o) or -15° experiment (Figure 4.7j). For a zoomed-in version of the -15° and -25° transpressional rotation experiments accompanied by velocity plots, see Suppl. Figures A33-A34.

By the end of the -5° experiment, spreading follows the rotation angle (Figure 4.7e). However, in the -15° model, spreading is focused on 3 segments, connected by oblique diffuse zones (Figure 4.7j). Finally, in higher angle models (-25 to -45°), spreading is focused on the inside corners of the rift-transform intersections while the transform faults are still active (Figures 4.7o,t,y).

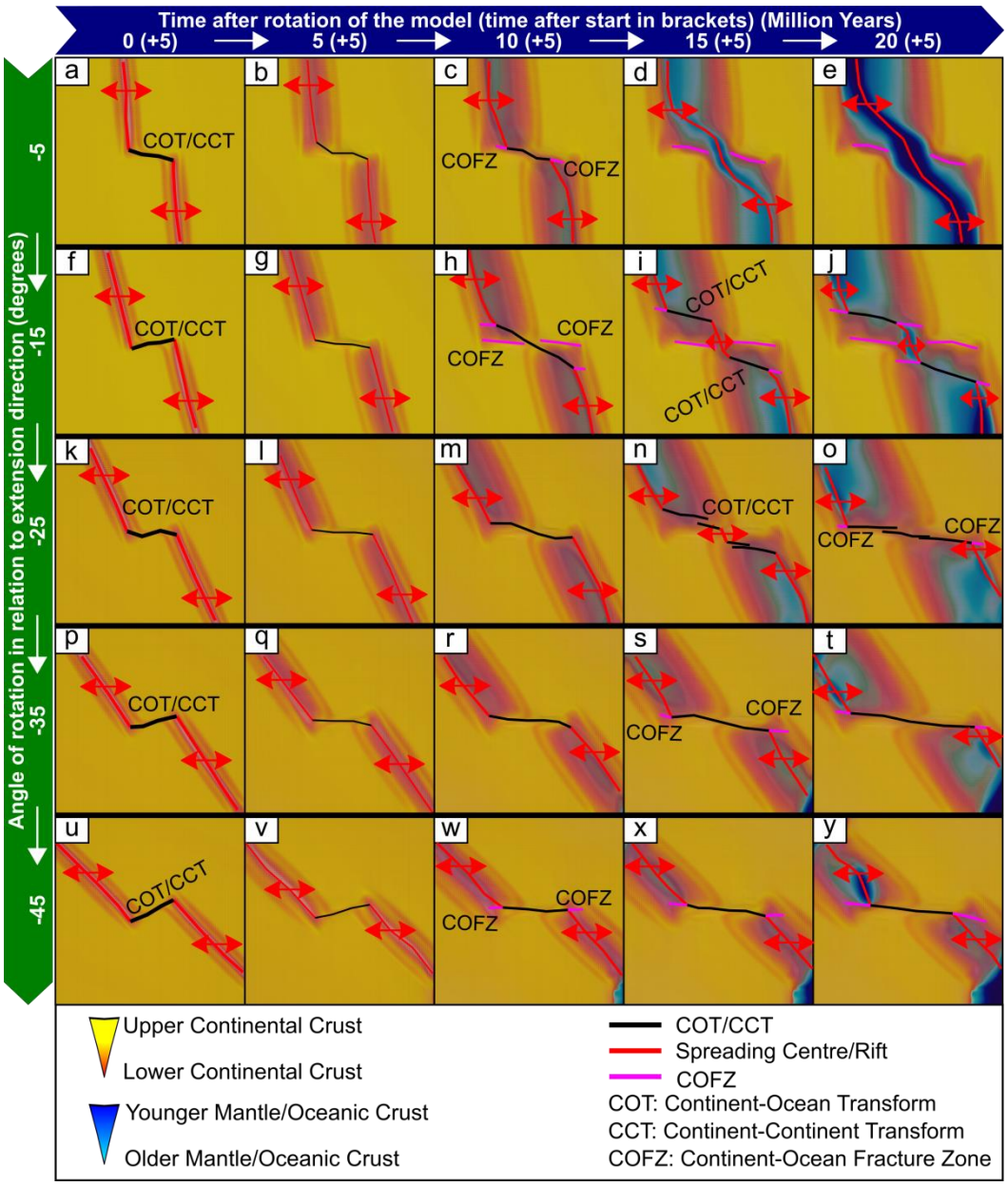

Figure 4.7 – Transpressional rotated models with a negative θ of rotation (with respect to the extension direction) after an initial 5 Ma of orthogonal extension. Individual panels show surface material evolution through time. For an uninterpreted version, strain rate patterns, velocity plots and cross-sections across the rifted margins, refer to Suppl. Figures A29-A32.

4.4 Discussion

Our two sets of numerical modelling experiments simulate the effect of a) oblique inheritance and b) a relative plate motion vector change in a rift-transform-rift setting. For both sets, we find that

for a left-stepping geometry, a positive angle of rotation (clockwise) from the extension direction results in transtension, accompanied by oblique rifting and spreading over the corners of the rift-transform-rift configuration (Figure 4.4 and 4.5). For negative (anti-clockwise) angles, where the transform experiences transpressional strain, increased obliquity increases the duration and length of the active transform segment in both the inheritance and relative plate rotation experiments (Figure 4.6 and 4.7). In the following sections we compare our results with natural examples.

4.4.1 Comparison with natural examples

4.4.1.1 Ungava Transform Zone, Davis Strait

We correlate our experiments with natural examples around the world (Figure 4.8), beginning with the Ungava Transform Zone in the Davis Strait between Canada and W. Greenland. The Ungava Transform Zone is a large right-stepping transform zone that accommodated horizontal motion between (now extinct) oblique spreading ridges in Baffin Bay in the north and Labrador Sea in the south (Oakey & Chalmers, 2012). Estimates for the obliquity of the rifts relative to spreading direction are poorly constrained, and range from 8-19^{o} for the Labrador Sea, and 25-40^{o} for Baffin Bay between 124-79 Ma (Jeanniot & Buiter, 2018). The area also underwent a 30^{o} clockwise change in its spreading direction around 35 Ma (Dore et al., 2016), resulting in widespread transpression and transtension.

The Ungava Transform Zone has thus experienced both oblique inheritance and later changes in plate motion, but the effects of the most recent phase of deformation, the relative rotation, are likely to be easiest to observe. Therefore, we compare the area with our 25^{o} transpressional rotation model (Figures 4.7k-o) (shown mirror-imaged for easier comparison, Figure 4.8a). Both our model and the Ungava Transform Zone evolve in a similar way. Opening of the first rifted basins occurred in an orthogonal extension zone, with a continental transform connecting the spreading centres (Oakey & Chalmers, 2012). Once the spreading direction changes and oblique

rifting is initiated, the juxtaposed continental crust is forced into transpression (velocity vector arrows in Suppl. Figures A33-34). This results in a zone of transpression onshore W. Greenland (Wilson et al 2006; Peace et al., 2017) and inversion structures offshore, analogous to the deformation we observe in our numerical model (grey circles marked TP in Figure 4.8b). Similarly, in our model, we observe a zone of high compressional stress on the inside corners of the rift-transform intersection (Suppl. Figure A35).

As spreading developed, a wide, transtensional region formed between the north and south Davis Straight spreading segments, the Ungava Transform Zone (Figure 4.8b, Reid & Jackson, 1997). Evidence of transtension includes oceanic material found along the transform (Wilson et al., 2006; Oakey & Chalmers, 2012; Peace et al., 2017). In our experiment, we also observed the formation of a diffuse transtensional zone (pink outline in Figure 4.8a, see also velocity vector arrows in Suppl. Figures A33-34). Because of the large range of estimates for obliquity and rotation in the Ungava Transform Zone, we also compare it with our 15° rotated model. This model includes a large segmented transform zone (Figure 4.7i,j), where transpression takes place in the corners of the rift-transform intersections and transtension occurs within the thinned crust, similar to the Ungava Transform Zone (Figure 4.7j).

4.4.1.2 Gulf of California

A natural example of transtension is the Gulf of California partitioned oblique margin, which undergone a 5-15° rotational change in relative plate motion (Bennett & Oskin, 2014). It formed a series of en-echelon pull-apart basins, which later developed into spreading centres (Umhoefer et al., 2018; Farangitakis et al., 2019) (Figure 4.8d). We match this to our 5° transtensional rotated model (Figure 4.5a-d), although the Gulf of California also displays similar features to the 15° experiment (Figure 4.5e-h). In our experiments, we model a single left-stepping rift-transform-rift system, so we do not replicate the complete architecture of the Gulf of California, but rather how each transtensional pull-apart would evolve. In both cases, the initial evolution begins with a transtensional zone forming near the outside corners of the rift-transform intersections (pink

areas in Figures 4.8c and 4.8d). Spreading in our models localises from the rift-transform intersections outwards, which is similar to the evolution of the N. Gulf of California, where spreading is more localised closer to the intersection of the Ballenas Transform Fault Zone and the Lower Delfin Basin spreading centre (Persaud et al., 2003).

4.4.1.3 Gulf of Aden

Finally, we correlate the rifted margin asymmetry in one of our rotation models with the evolution of the Gulf of Aden, where the transition from continent to ocean is wider in the outside corners of the Alula-Fartak and Socotra-Hadbeen Fracture Zones than in the inside ones (Figure 4.8g, orange zones marked COBZ; Bellahsen et al., 2013). Kinematically, the Gulf of Aden has undergone ~35 Ma of spreading (Bellahsen et al., 2013) and is characterised by 3 components: a) oblique crustal inheritance in the form of Mesozoic basins trending ~80-90^{o} clockwise to spreading (Autin et al., 2013); b) an oblique rift and spreading trend oriented 40^{o} clockwise to the direction of plate motion, segmented by left-stepping transform faults; and c) a ~26^{o} change in the plate motion vector reducing rifting obliquity from the previous oblique rifting trend of ~68^{o} observed 20 Ma ago (Bellahsen et al., 2013; Brune & Autin, 2013; Jeanniot & Buiter, 2018). The Gulf of Aden has also been influenced by the Afar hotspot (Leroy et al., 2012), and associated magmatism. However, our models do not take magmatic emplacement into account. Instead, we focus on understanding what features can be explained by just the kinematics and inheritance of the region.

We compare the transition across the spreading centre in the 5^{o} oblique inheritance model (Figure 4.8e and inset figure) to the continent-ocean boundary zone along two main fracture zones in the Gulf of Aden (Figure 4.8g, orange zones marked COBZ). This model fits two characteristics of the natural example: a) the obliquity of the inherited structures through the general orientation of the seed (green in Figure 4.8e) is in accordance with the Mesozoic fabric in the Gulf (green in Figure 4.8g); and b) the angular agreement of the spreading trend with respect to the relative plate motion (red lines in Figures 4.8e,f,g). The width of transition from continent

to oceanic crust is 115 km in the inside and 110 km (~5% shorter) in the outside corners of the rift-transform intersection, which does not agree with the Gulf's margin width.

However, if the 26^{o} transtensional plate motion vector change (Jeanniot & Buiter, 2018) is considered, then the Gulf of Aden can be compared to the 25^{o} positive rotation angle experiment (Figure 4.8f and inset figure). Here, the transition from oceanic to undisturbed continental crust is ~120 km in the inside and 260 km (116% longer) in the outside corners of the rift-transform intersection (inset in Figure 4.8f). Thus, considering the kinematics of the area (Bellahsen et al., 2013), we can infer that the change in plate motion in the Gulf of Aden is a key contributing factor in the resulting margin asymmetry.

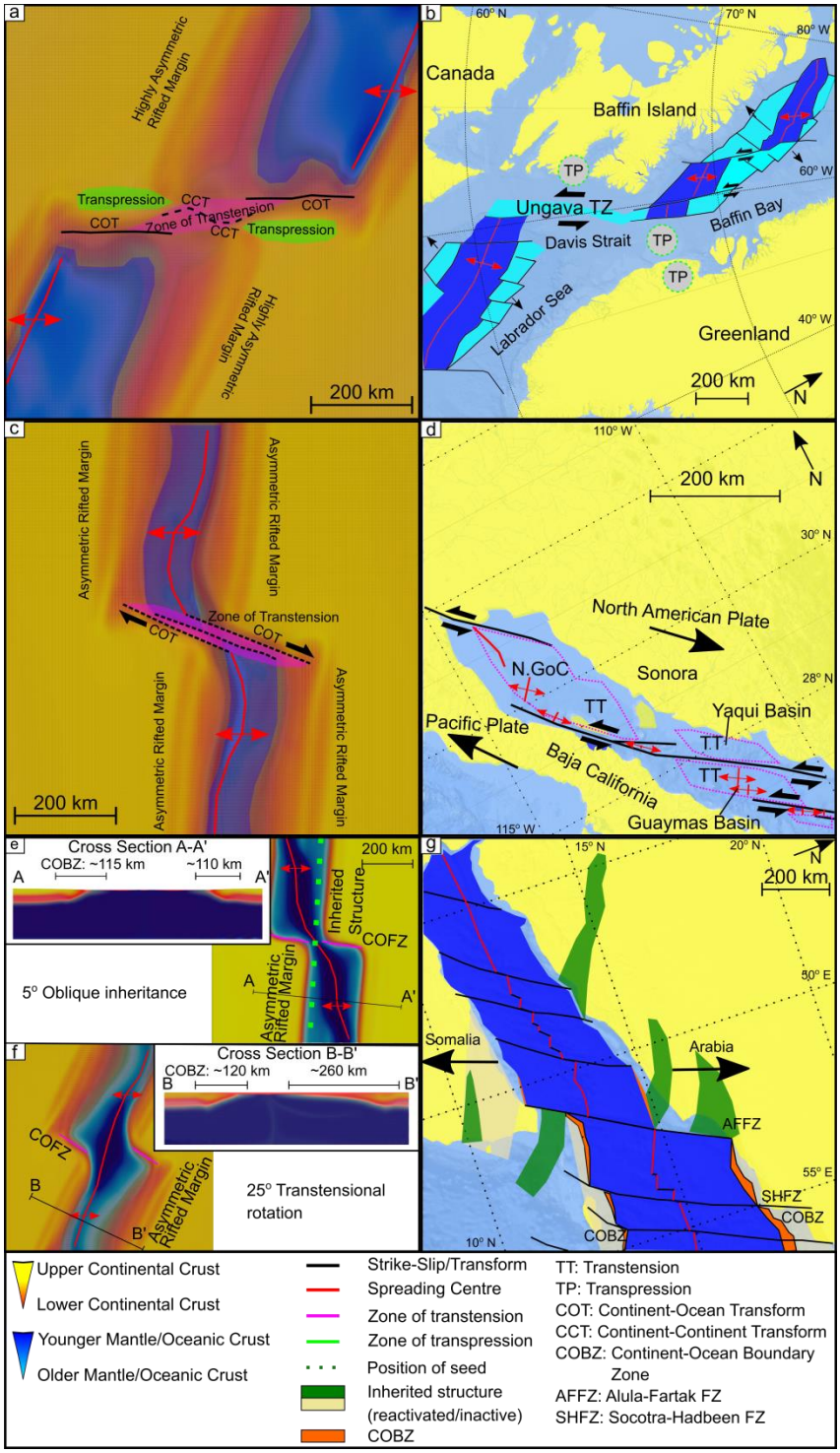

Figure 4.8 – Comparison with natural examples. a-b) Comparison of a -25° transpressional rotated model snapshot at 20 (+5) Ma with the Davis Strait. Note the zones of compression/transpression within the outer corners of the continent-ocean transforms shown in green; in the natural example, similar areas are indicated with grey circles marked TP (location of transpression from Peace et al., 2017). Also note the transtensional zone shown in pink between the two segments of the COT due to the nature of the rotation. c-d) Comparison of a 5° transtensional rotated model snapshot at 10 (+5) Ma with the Gulf of California. Note the zone of transtension in the model

shown in pink; in the natural example, similar areas are marked with dashed pink outlines. e-g) Comparison of a 5° transtensional oblique inheritance model snapshot at 15 Ma and a 25° transtensional rotated model snapshot at 20+5 Myrs with the Gulf of Aden (from Leroy et al., 2012; Bellahsen et al., 2013). Note the similarity in the general oblique rift trend with the rotated model, and the margin asymmetry shown in the inset cross-sections in the rotated model and in orange colour in the natural example (for a zoomed in version of the cross sections refer to Suppl. Figures A21 and A24).

4.4.2 Rift seed geometry and connectivity

We find that the rift seed spacing used in our study generates a transform margin independent of whether we include a transform seed or not. Our spacing of ~5H (where H is the thickness of the continental crust) produces transform linkage (Figure 4.3 and Suppl. Figure A1), and is consistent with most physical and numerical studies (e.g., a spacing of 4H in Allken et al. (2012) and > 4H in Le Pourhiet et al. (2017)). Such spacing allows the build-up of strain in the tips of the rift structures and the production of transform faults. Zwaan & Schreurs (2017) did not observe transform faults developing in a similar set-up, but used a much smaller spacing of 2H. Yet, in accordance with Zwaan & Schreurs (2017), we also found that an inherited structure located at a high negative (or transpressional) angle (such as the θ = -45° inherited structure in Figure 4.6y) does not produce any rift connectivity, but instead produces two non-interacting distinct rift segments.

4.4.3 Margin asymmetry

In terms of margin asymmetry, we find that hyperextension (coupling of upper and lower continental crust) occurs if the plate vector change induces transpression or transtension over the transform and results in stalling rifting, similar to Le Pourhiet et al. (2017). In our oblique inheritance experiments, this asymmetry appears mainly in the higher angle experiments (>25°). In Figures 4.4p,t, the rift flanks that correspond to the inside corners of the transform are wider

than their outside corner counterparts. The inverse happens in Figures 4.6o,t, where the outside corner flanks are hyperextended. Similarly, in our rotated models, hyperextension occurs on the outside corner rift flank in a positive θ rotation (e.g. Figures 4.5 after 15+5 Myr). On the other hand, when a negative θ rotation occurs, these wide zones of diffuse strain occur in the inside corner rift flanks (e.g. Figures 4.7 after 20+5 Myr, with cross sections of the margins shown in Suppl. Figures A20,24,28&32). Nonn et al. (2017) provide a potential explanation for this, suggesting rift migration might be responsible for hyperextension and margin asymmetry. Migration is observed in the positive θ oblique inheritance models, where spreading migrates clockwise, leaving behind a hyperextended margin (comparing 5 Ma and 10 Ma in Figure 4.5 and Suppl. Figure A22). Migration also occurs in the other models but in the region of exposed mantle. Similarly, Le Pourhiet et al. (2017) observe higher continental crust asymmetry across the rift flanks, which they attributed to an already-weakened lower crust in a rift-transform-rift setting. This compares to our rotational models, where the continental crust has already been weakened by the previous rotation and is then re-mobilised to accommodate asymmetry. When the crust is undisturbed, asymmetry is focused on the oceanic domain (e.g., Le Pourhiet et al., 2017), as is the case in our oblique inheritance models where the crust is not “disturbed” by a previous event of orthogonal extension.

As discussed in Section 4.4.1.3, another factor that shapes rifted margin asymmetry and evolution is magmatism. If our models included magmatism, we would expect the magmatism in magma-rich margins to be concentrated in zones of hyper-extension thinning (e.g. Mohriak & Leroy, 2013; Koopmann et al., 2016; Peace et al., 2016), altering their rheology and potentially amplifying the hyper-extension. The changes for magma-poor margins are naturally expected to be minimal. However, it is difficult to correlate the width of a rifted margin directly with volcanism (Tugend et al., 2018). A number of previous workers who have investigated margin asymmetry considering magmatic emplacement interpret their results as fundamentally controlled by simple shear rifting, with magmatism controlled by the amount and location of crustal thinning (e.g. Mohriak & Leroy,

2013 on the S. and N. Atlantic, Red Sea and Gulf of Aden; Koopmann et al., 2016 on the S. Atlantic; Peace et al., 2016 on the Labrador Sea). Thinning in a simple shear system is asymmetric; therefore the magmatism is asymmetric. Within this framework, the tectonic structure is the primary driver of asymmetry, so our purely tectonic models should capture the first-order factors affecting margin asymmetry and COBZ width.

4.4.4 Oblique inheritance versus rotation

We observe that in the case of a negative, transpressional angle change between the oblique inheritance or plate motion vector and the extension direction, the duration of transform margin activity increases substantially (Figure 4.9). This is probably due to the juxtaposition of a larger portion of continental crust across the transform imposed by the kinematic boundary conditions, which delays the surface linkage between the two spreading centres. This agrees with Ammann et al. (2018), who found that long transform fault formation is favoured by high obliquity. It is worth noting that, for this set of experiments, the transform margin always remains parallel to sub-parallel to the extension direction (Figures 4.6,4.7, and 4.8a).

In positive θ transtensional models, an increasing angle results in shorter duration of transform margin activity. Furthermore, spreading over the rift part of the seeds is delayed with increasing angle of rotation. However, the sigmoidal transtensional zone created above the transform seeds becomes wider in the centre with increasing positive rotation angle (Figure 4.4 after 15 Ma and Figure 4.5 after 15+5 Myr). This sigmoidal opening style of transtensional oblique inheritance and rotation experiments resembles that observed in Brune & Autin (2013) when they applied oblique extension to an inherited structure in the crust. This can be attributed to the response of the transform segment to the far-field extension. Rifting and subsequent spreading along that intersection is preferred due to the orientation of the pre-existing structures. As θ increases, the spreading component over the rift seeds becomes smaller, while over the transform seed it becomes larger.

Finally, comparing the oblique inheritance and relative plate rotation results, it becomes evident that introducing a rotation to the model delays the ocean-ocean breakthrough across the transform margin, meaning the margin is active for longer (Figure 4.9). In our models, this difference is about 5 Ma for positive angles, which is the duration of the orthogonal rifting stage. However, the difference is much greater for negative angles of rotation (Figure 4.9). In the transpressional models, stress and strain patterns need to rearrange and cross-cut the pre-existing tectonic fabric, making the transform zones active for longer. In a transtensional regime, this rearrangement would occur faster as the structures need to only re-orient themselves to the new extension direction. A more detailed view of this evolution can be seen in Farangitakis et al. (2019) analogue models, where a relative plate rotation leads to wide zones of transtension and transpression.

In Figure 4.9, we show our model results of transform margin activity and rotation angle alongside a compilation of various transform margin age ranges from Mercier de Lepinay et al. (2016) and obliquity/rotation ranges from Jeanniot & Buiter (2018) (with adjustments for the Gulf of California from Umhoefer et al., 2018 and Farangitakis et al., 2019; for the Tanzania Coastal Basin from Farangitakis et al., 2019; and for the De Geer-Spitzbergen transform from Dore et al., 2016). We observe that more transforms fall into a zone defined by the relative plate rotation experiments rather than a single phase rift dominated by inheritance. The exceptions are: the Voring Margin, which falls below the oblique inheritance trend line (very high transtensional angle resulting in a short-lived transform; Dore et al., 2016; Jeanniot & Buiter, 2018); and the TCB and De Geer Line, located above the relative rotation trend line. The TCB accommodated motion between supercontinents and is thus much larger scale than the others (Farangitakis et al., 2019), while the polyphase evolution of the De Geer Line is dominated by multiple changes in relative plate motion and far field-forces around the Arctic (according to Dore et al., 2016).

The natural examples in Figure 4.9 provide a qualitative comparison between oblique inheritance and changes in relative plate motion. Our models use a generalised continental lithosphere

rheology and do not vary its strength, thickness, mantle temperature or the depth or dip of the inheritance fabric. This generalised model set-up cannot provide as close a match for a specific natural example as area-specific studies (e.g. Brune & Autin, 2013 for the Gulf of Aden). However, despite this, most of the natural examples plot on the rotation trendline, potentially suggesting changes in relative plate motion influenced their evolution (Figure 4.9).

A particularly good example of this is given by the Gulf of Aden, which has experienced a combination of inheritance, oblique rifting and vector rotation (Bellahsen et al., 2013). We have plotted therefore two separate components of rifting for this example: the influence of rotation GoA(R) and the influence of inheritance GoA(I). However, we see that the observed duration of transform is consistent with the rotation trendline, not the inheritance one. As discussed above, our rotational model also produces margin asymmetry very similar to that observed in the Gulf. The 26^{o} spreading direction change thus appears crucial in the Gulf of Aden's evolution and margin structure. This complex example strengthens the emerging trend of Figure 9: that changes in plate motion play a key role in transform margin evolution and should be considered as equally, or potentially more, important than inheritance.

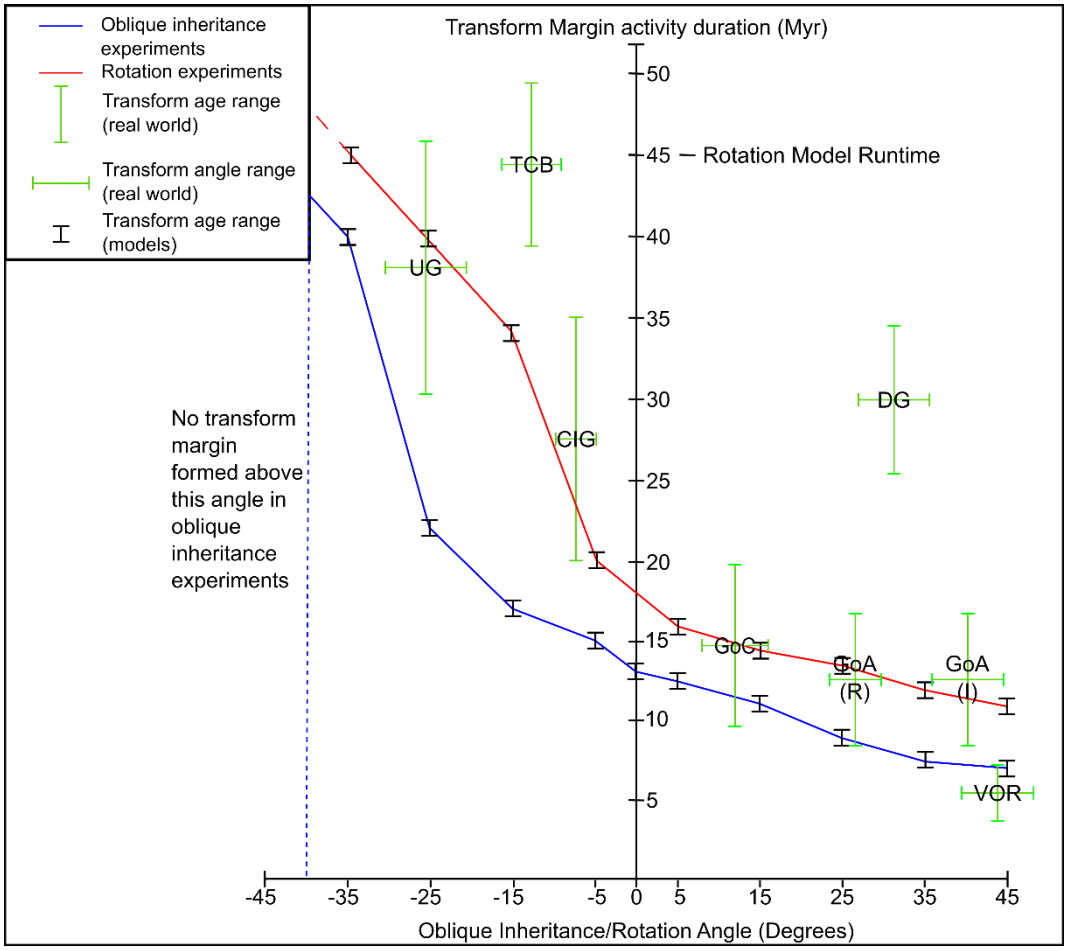

Figure 4.9 – Comparison between duration of transform margin activity between the oblique inheritance (blue) and rotation (red) experiments versus their angle. Selected transform margins across the world are also shown. Abbreviations: DG: De Geer Transform, TCB: Tanzania Coastal Basin, UG: Ungava Transform Zone, CIG: Cote d'Ivoire-Ghana Transform Marin, GoC: Gulf of California, GoA: Aden Gulf, VOR: Voring Margin.

4.5 Conclusions

We present a series of experiments replicating oblique structural inheritance and rotational changes in relative plate motion in a rift-transform rift setting. Our results show good agreement with natural examples in the Ungava Transform Zone, the Gulf of California and the Gulf of Aden (Figure 4.8).

High-angle relative plate rotations produce both transtension and transpression along a transform system. We show that the evolution of the Davis Strait can be simulated with a transpressional -25° degree relative plate rotation with respect to the extension direction, resulting in a diffuse

zone of transtension where the Ungava Fracture Zone is located and transpression on the inside corners of the COT (Figure 4.8a-b).

In a transtensional setting, the obliquity introduced by even a small rotation of existing orthogonal extension results in sigmoidal to rhomboidal opening along the transform margin. This is similar (for the smaller angles) to the evolution of the Gulf of California, where en-echelon pull-aparts developed from south to north and are now evolving into ridge-transform segments (Figure 4.8c-d).

Furthermore, we find that relative plate rotations can lead to rifted margin asymmetry. We compare the ocean-continent transition zone width of the Gulf of Aden to both oblique inheritance and rotation models. The width of the ocean-continent transition zone in the rotation models closely matches that of the Gulf of Aden, where the outside corners of the rift-transform intersection are significantly wider than the inside ones (Figure 4.8e-f).

We conclude that introducing a relative plate rotation in our models results in a longer transform margin activity lifespan and delayed spreading along the entire margin (Figure 4.9). This is due to the delay caused by the reorganisation of the diffuse strain patterns associated with transtension and transpression when a rotational change in plate motion occurs.

Therefore, the effects of relative plate rotations on rift-transform intersections should be considered alongside inheritance when understanding the evolution of a margin.

5 The crustal-scale: The evolution of transform margins and rift-transform intersections in response to changes in plate motion.[2]

5.1 Introduction

Transform margins and oblique rifts are first-order structural features present in almost every tectonic plate across the globe. Transform continental margins, in particular, represent 16% of the cumulative length of continental margins (Basile, 2015; Mercier de Lépinay et al., 2016) and accommodate or have accommodated oceanic spreading motion. These features were first discussed and described in the context of shear margins in the 1960-1970s (e.g. Wilson, 1965; Le Pichon & Hayes, 1971; Turcotte, 1974; Mascle, 1976; Scrutton, 1979). Studies in the past three decades have provided improved conceptual models for the evolution of these margins (e.g. Lorenzo, 1997; Reid & Jackson, 1997; Basile & Brun, 1999; Bird, 2001; Basile, 2015; Mercier de Lépinay et al., 2016). However, transform margins remain considerably less studied than their continental divergent and convergent counterparts. Studies of these margins across the world such as Vøring (Talwani & Eldholm, 1972), Gulf of Aden (Leroy et al., 2012; Autin et al., 2013),

---

2 This chapter has been published as: Farangitakis, G. -., Sokoutis, D., McCaffrey, K. J. W., Willingshofer, E., Kalnins, L. M., Phethean, J. J. J., . . . van Steen, V. (2019). Analogue modeling of plate rotation effects in transform margins and rift-transform intersections. Tectonics, 38(3), 823-841. doi:https://doi.org/10.1029/2018TC005261.

The methodology sub-chapter's presentation has been slightly modified from the published version to be consistent with the presentation of the methodology throughout the thesis. A more detailed table showing the scaling relationships has been added showing the ratios between nature and models that was not included in the paper.

India-Arabia plate boundary (Rodriguez et al., 2016), and West Greenland (Peace et al., 2017) suggest that they have a genetic relationship with pre-existing structures or anisotropy in the crust (or even the mantle). However, Basile (2015) argues that there are two types of transforms: a) transform faults that first form in continental lithosphere may reactivate or cross-cut pre-existing structural features (e.g., the Equatorial Atlantic) and b) transform faults that form after the initiation of oceanic accretion to connect propagating oceanic spreading axes (e.g., the Woodlark Basin, Gerya, 2012) that display little or no inheritance. Bellahsen et al. (2013) proposes a similar classification: Type 1 that form synchronously with the syn-rift structures, Type 2 that form during the continent-ocean transform and Type 3 that form within the oceanic domain, after the onset of oceanic spreading. Moreover, transform margins are areas of active hydrocarbon exploration with significant exploration risk factors such as uncertainty over the post-breakup uplift patterns in space and time, poor knowledge of structural architecture and associated topography, as well as diachronous timing of the transform fault activity (Nemcok et al., 2016).

In this study, we focus on examples where plate boundary re-organisations or changes in extension direction or rate have impacted a transform system. This is the case in the Gulf of California (GoC), where a change in extension direction between the Pacific and North American plates results in a large transtensional zone of oblique slip faults and sigmoidal horsetail splays, particularly in the north (e.g., Lizarralde et al., 2007; Seiler et al., 2009; Persaud et al., 2017). West of Madagascar, a plate re-arrangement led to the formation of the Davie Fracture Zone (DFZ) in the Tanzania Coastal Basin (TCB), overprinting the pre-existing spreading centre and fracture zones (Phethean et al., 2016). In Western Australia and the Jan Mayen Ridge near Greenland, changes in extension direction may have resulted in the formation of free-moving microcontinents (e.g., Heine et al., 2002; Stagg et al., 2004; Whittaker et al., 2016; Schiffer et al., 2018). Finally, Davison et al. (2016) suggest the existence of conjugate zones of compressional deformation along the Romanche Fracture Zone.

Dauteuil and Brun (1993) presented the first analogue modelling experiment of oblique rifting or transform margins, investigating the Mohns and Reykjanes ridges in the N. Atlantic to identify segments of oblique transfer zones between the rift segments. Thereafter, Basile and Brun (1999) used a Riedel box with a brittle-ductile configuration to produce transtensional faulting patterns in continent-ocean transforms and pull-apart basins. Acocella et al. (1999) showed how orientation, geometry and kinematics of transfer zones depend upon pre-existing basement anisotropies, while Dauteuil et al. (2002) tested the influence of lithosphere strength on the development of deformation above a transform boundary. They concluded that major transform faults associated with fast-spreading ridges are formed by diffuse, complex arrays of strike–slip segments, while transform faults associated with slow-spreading ridges form deep, narrow linear valleys. Autin et al. (2013) used a four-layer brittle/ductile/brittle/ductile model of the Gulf of Aden to investigate how inherited basins could partly control present-day geometry of an oblique rift and localisation of fracture zones. Philippon et al. (2015) investigated the relation between dip-slip and strike-slip displacement along orthogonal and oblique faults in relation to extension direction. Finally, Zwaan and Schreurs (2017) tested the effects of oblique extension and inherited structural offsets on continental rift interaction and linkage. Experiments with temperature-dependent materials include the work of Grokholskii (2005) and Dubinin et al. (2018), who used heat and a mix of paraffins in their models to replicate the structures created in rifts.

In this work, we report the results of a series of analogue experiments designed to investigate the role that small changes in relative plate motions play in the evolution of transform faults and of strike–slip plate boundaries more generally. We introduce a sequential three-step experiment where a) orthogonal motion, b) a rotation and then c) oblique motion are imposed on an initially orthogonal rift. This mimics the effect of a change in spreading direction due to a change in the relative Euler pole between the plates and leads to an oblique rift and accompanying transtensional and transpressional zones on the lateral margins. Observations are compared to seismic reflection images from two different margins: the transtensional Gulf of California

partitioned oblique margin and the transpressional Tanzania Coastal Basin offshore East Africa (Figure 5.1).

5.2 Geological Background

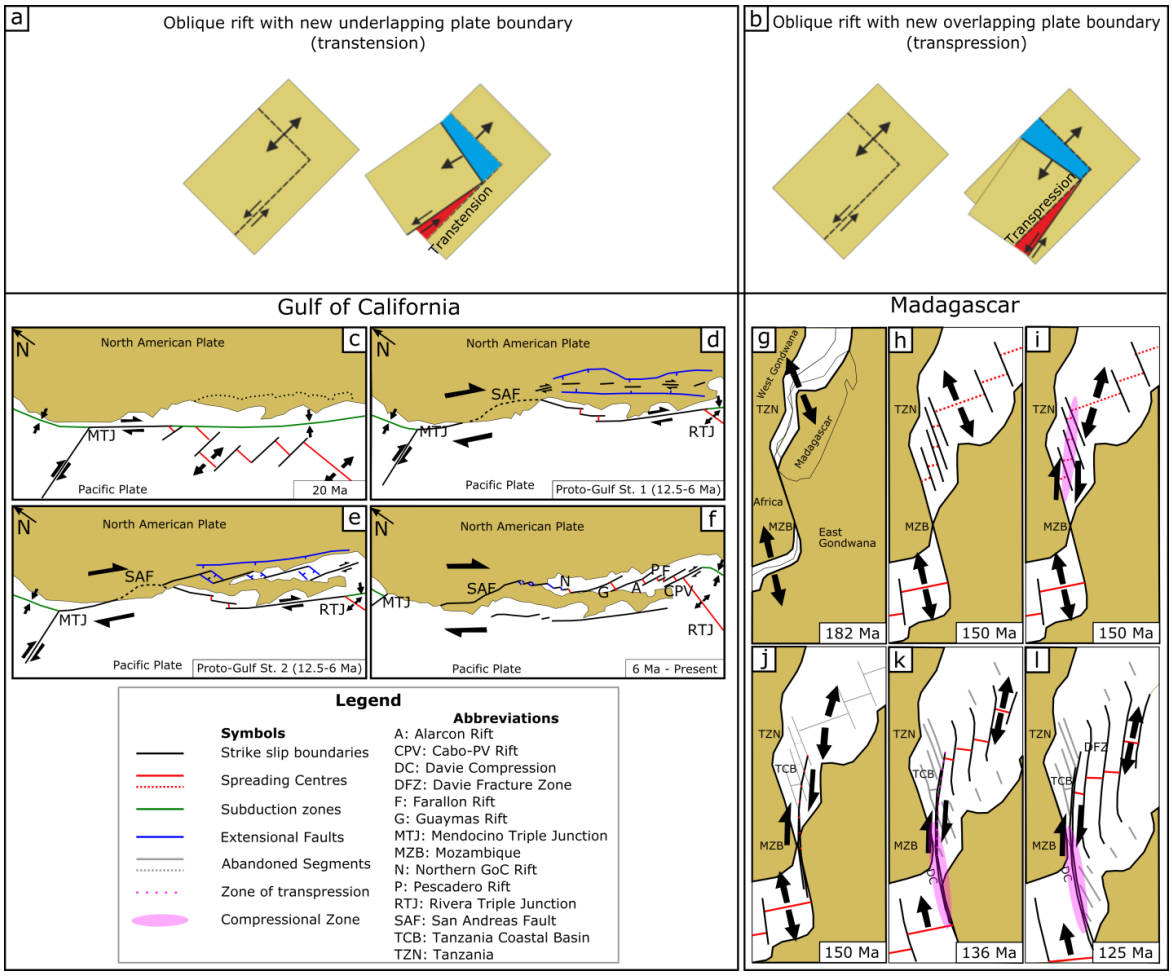

Figure 5.1 – Schematic interpretation of the evolution of a: a transtensional margin and b: a transpressional margin. c-f: evolution of the Gulf of California from 20 Ma to present (modified from Bennett et al., 2013). g-l: evolution of the Tanzania Coastal Basin between 182-125 Ma (Reeves et al., 2016; Phethean et al., 2016; Tuck-Martin et al., 2018).

The GoC is an early-stage transform margin, with seafloor spreading in the southern and central Gulf (Lizarralde et al., 2007), and rifting (with potential continental break-up) in the north (Martin-Barajas et al., 2013). Dextral transform motion between the Pacific and North American plates

began ~20 Ma ((Lonsdale, 1989; Axen, 1995; Atwater & Stock, 1998; Bennett et al., 2013) (Figure 5.1c), with extension in the Proto-Gulf of California beginning ~12 Ma (Persaud et al., 2003; Bennett et al., 2013) (Figure 5.1d). Bennett & Oskin (2014) suggest a 15^{o} clockwise rotation in the relative motion between the plates at ~8 Ma increased the rift obliquity and favoured the development of strike-slip faulting. Shearing localised in en-echelon strike-slip shear zones, which developed into nascent pull-apart basins by 6 Ma (Bennett et al., 2013), (Figure 5.1e) and then into a series of long dextral transform faults connected by smaller rift basins (Persaud et al., 2003; Lizarralde et al., 2007) (Figure 5.1f).

In the northern GoC, the nature and timing of continental rupture is still uncertain, with the presence of oceanic crust suggested in some basins (Martin-Barajas et al., 2013; Gonzalez-Escobar et al., 2014) and delayed rupture suggested for others (Lizarralde et al., 2007; Martin-Barajas et al., 2013). Deformation in the north is distributed across a pull-apart structure between the Cerro Prieto Fault (CPF) and the Ballenas Transfrom Fault Zone (BTFZ) (Persaud et al., 2017) (Figure 5.7a). This deformation migrated north from the Tiburon Basin ~3.5-2 Ma following a plate reorganisation (Seiler et al., 2009). The CPF and BTFZ strike 6-7^{o} more northerly (312^{o}) than the transforms in the south (305^{o}) (Lonsdale, 1989). Dorsey and Umhoefer (2012) and Van Wijk et al. (2017) argue that this increased obliquity contributes to the basin development and late or absent rupture, although initial fault geometries, thick sedimentation, and changing loci of extension may also be factors.

The N-S trending DFZ (Figure 5.1l) in the TCB is a fossil transform fault that guided the southward drift of East Gondwana (Antarctica, Australia, India, and Madagascar) away from West Gondwana (Africa and South America) during the Jurassic and Early Cretaceous (e.g., Coffin & Rabinowitz ,1987). Following continental breakup at approximately 170 Ma (Geiger et al., 2004), an initial phase of NNW-SSE plate separation resulted in the development of SSE trending oceanic fracture zones offshore Tanzania (e.g., Davis et al., 2016; Phethean et al., 2016; Sauter et al., 2016; Tuck-Martin et al., 2018) (Figure 5.1g-h). By about 150 Ma, the strong continental cores of East and

West Gondwana were no longer juxtaposed. Together with the alignment of spreading segments to the north, this created an approximately N-S band of weaker lithosphere. This alignment coincided with a change in plate motion, resulting in N-S separation of East and West Gondwana (e.g. Davis et al., 2016; Phethean et al., 2016; Sauter et al., 2016) (Figure 5.1i). This change in plate motion was incompatible with SSE trending fracture zones offshore Tanzania, resulting in transpressional deformation along these structures. Recent work shows evidence of intra-plate deformation of the oceanic crust within the TCB adjacent to the DFZ. Sauter et al. (2018) describe buckle folding and thrusting in "deformation corridors" interpreted as pre-existing oceanic fracture zone fabric. This transpressional event was most likely ended by the development of the DFZ, which then accommodated N-S spreading (Figure 5.1-l) (Reeves et al., 2016; Phethean et al., 2016).

These two cases of transtension (GoC) and transpression (TCB) provide ideal natural examples to test our analogue modelling experimental approach. In turn, our models can provide insight into the structural evolution of margins such as these and the complexity that may arise.

5.3 Methodology

5.3.1 General definition of the models

We use a modified experimental array based on Basile and Brun (1999), which comprises a moving plate sliding underneath a brittle/ductile layer configuration that creates pre-imposed velocity discontinuities (VDs). In this approach, deformation is driven entirely by externally applied boundary conditions (Schellart & Strak, 2016), with pre-imposed VDs, similar to those in Allemand and Brun (1991) and Tron and Brun (1991). We also use a similar brittle to ductile ratio (2:1, to simulate continental crust) and imposed extension velocity (5 to 10 cm/h). To simulate similar processes in oceanic crust, we also use a brittle-only configuration (Burov, 2011).

Following an initial orthogonal extension phase, we introduce a rotation of 7^{o}, consistent with the amount of rotation observed in natural examples: Lonsdale (1989) and Bennett et al. (2016)

report evidence of ~7-15^{o} of rotation in the GoC from ~6.5 Ma. In Madagascar, the reconstruction in Figure 5.1c-h shows ~10^{o} of rotation. Mauduit and Dauteuil (1996) also report a series of transform zones with obliquities ranging between 3^{o} and 8^{o}. Finally, Whittaker et al. (2016) report up to 10^{o} rotation in the Exmouth Plateau in W. Australia.

The brittle/ductile experiments were performed at 5 cm/h and 10 cm/h to explore the influence of velocity, and through it, brittle-ductile layer coupling, with increased velocity corresponding to stronger coupling. This difference in pulling velocity also creates different crustal rheologies in the models (Brun, 2002). The strain rate in the ductile layer increases with increased pulling velocity, leading to more uniform behaviour between the ductile and brittle layers. The layer is non-newtonian, so the increased strain rate corresponds to an increase in apparent viscosity, with the brittle and ductile layers being more similar in strength (Figure 5.3a, b). This translates to more distributed strain and the formation of more diffuse structures. In contrast, the brittle experiment corresponding to oceanic crust is independent of velocity (and thus strain rate) (Figure 5.3c). Topography changes in the models are mapped using a laser scanner at discrete intervals. Finally, we use a small funnel to manually add alternating colour layers of feldspar sand in the topographic lows (and thrust fronts). This is done every 2-3 minutes after checking that new structural features have been created. These layers act as act as syn-rift sedimentation (and in the case of thrusts as an extra protective layer) and facilitate observations of deformation when the models are cut to produce cross-sections. At the end of each experiment run, the model is also covered with a thick protective layer of black and white sand for the wetting and cutting process.

5.3.2 Kinematic set-up

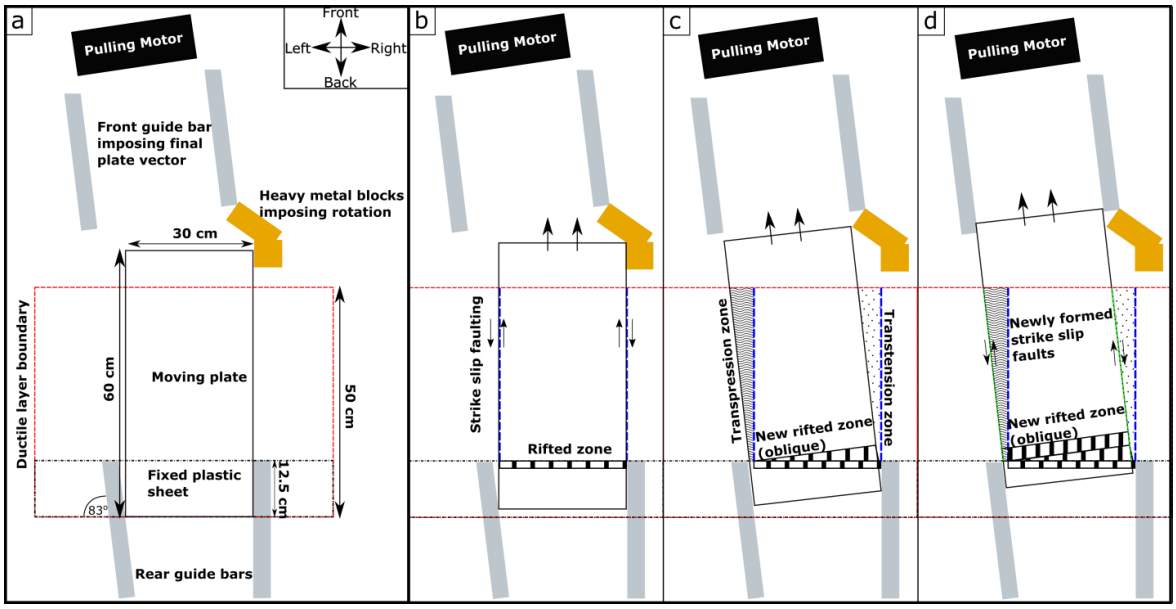

Figure 5.2 – Model array: a) initial configuration and dimensions, b) orthogonal motion stage, c) end of rotation stage, d) new oblique plate motion vector stage.

The model configuration (Figure 5.2) allows us to simultaneously investigate both overlap and underlap caused by the rotation of the moving plate on parallel strike-slip boundaries. The rotating plate is represented by a 60x30 cm plastic plate underneath the silicone putty/feldspar sand layers. At the trailing edge of the plastic plate, a second plastic sheet is fixed above the moving plate and acts as a VD imposing a rift (Figure 5.2). The moving plate is guided by a series of metal bars at the front and rear of the model. These a) guide the plate to move straight and then rotate and b) do not allow it to rotate more than 7°. Two heavy metal blocks act as a mechanical elbow (Figure 5.2, yellow boxes), forcing the plate to rotate until it hits the front left guide bar and acquires a new motion vector. Once the step motor is started, the plate moves orthogonally towards the mechanical elbow, creating two parallel strike-slip shear zones and a divergent (rift) zone above the VD imposed by the fixed plastic sheet (Figure 5.2b). During the rotation phase, zones of transtension and transpression are created on the right and left sides of the plate, respectively, and an oblique rift develops at the back (Figure 5.2c). After the rotation,

the plate is constrained by the top guide bars, creating new shear zones on each side (Figure 5.2d) that are oblique to the originals.

5.3.3 Model rheology and materials used

Our brittle/ductile models represent a two layer continental crust, while the brittle-only model represents a single layer of oceanic (Figure 5.3). Layers were as follows:

a) For brittle crust, we use dry feldspar sand (which deforms according to the Mohr-Coulomb criterion) with a density of ρ = 1.3 g/cm^3 (Luth et al., 2010), sieved to a grain size d = 100-350 μm and an internal friction coefficient of μ_{fric} of 0.6 (Sokoutis et al., 2005).

b) Ductile crust is represented by transparent silicone putty SGM-36 in the PDMS group, a poly-dimethyl siloxane with a density of ρ = 0.970 g/cm^3, no yield strength and viscosity at room temperature of μ_{vis} = 5*10^4 Pa.s (Tables 5.1 & 5.2 - Weijermars, 1986a; Weijermars, 1986b; Weijermars 1986c).

The governing equations for the strength in each layer are derived from Brun (2002). For the brittle layers, the strength profile along the strike slip fault is given by the equation:

$$\sigma 1 - \sigma 3_{(ss)} = \rho g z_b \qquad \text{(Equation 5.1)}$$

where $\sigma 1\text{-}\sigma 3_{(ss)}$ is brittle layer strength along the fault, g gravitational acceleration and z_b thickness of the sand layer.

For extension in the brittle layers, the governing equation is:

$$\sigma 1 - \sigma 3_{(r)} = \frac{2}{3}(\sigma 1 - \sigma 3)_{(ss)} \qquad \text{(Equation 5.2)}$$

where $\sigma 1\text{-}\sigma 3_{(r)}$ is the extending brittle layer strength.

For the ductile layer, the strength is:

$$\sigma 1 - \sigma 3_{(d)} = 2\left(\eta \frac{V}{z_d}\right) \qquad \text{(Equation 5.3)}$$

where $\sigma 1\text{-}\sigma 3_{(d)}$ is ductile layer shear strength, η is ductile layer viscosity, V is pulling velocity and z_d is ductile layer thickness.

These equations produce the rheological profiles shown in Figure 5.3. These strength profiles apply only to the very early stages of deformation in each experiment.

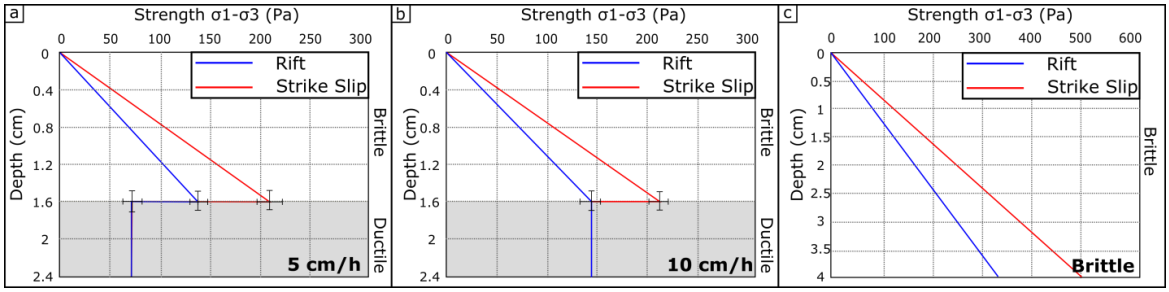

Figure 5.3 – Model strength profiles: a) 5 cm/h model run (weak brittle/ductile coupling), b) 10 cm/h model run (strong brittle/ductile coupling) c) brittle only run (oceanic crust). White background: brittle layers, grey background: ductile layers.

5.3.4 Scaling

Scaling of our analogue models to their natural prototypes was based on Ramberg's (1981) principles of maintaining similarity in the geometry of the structures, the kinematic evolution of the models, and the rheology of the crust in each model run (Hubbert, 1937,; Ramberg 1982,; Weijermars & Schmeling, 1986, ; Sokoutis et al. 2000,; Sokoutis et al., 2005). In the brittle/ductile models, the 2.4 cm thick model corresponds to a median value of 20 km assuming strike-slip motion occurred after at least 6 million years of pre-existing extension (Bennett et al., 2013; Persaud et al., 2015). This results in a model to nature ratio of 1.2×10^{-6} meaning 1 cm in the experiment equals around 8.33 km in nature. In the brittle-only configuration, the 4 cm of model thickness correspond to about 4-5 km of oceanic crust near the DFZ (Phethean et al., 2016), with a ratio of 8.9×10^{-6} .

Rheologic and dynamic similarity in our models is retained by scaling the gravitational stress (Dombradi et al., 2010) (σ):

$$\sigma^{\propto} = \rho^{\propto} g^{\propto} z^{\propto}$$ (Equation 5.4)

Where ρ is density, g is gravitational acceleration, z is thickness and the $\propto$ symbols denote the model to nature ratio (Sokoutis et al., 2005). For the viscous deformation, the ratio between gravitational and viscous stresses is given by the Ramberg Number (R_m – Weijermars & Schmeling, 1986):

$$R_m = \frac{\rho_d g z_d}{\eta \dot{\varepsilon}}$$ (Equation 5.5)

Where ρ_d is the ductile layer density and $\dot{\varepsilon}$ is the strain rate.

To scale brittle deformation, we used the ratio between gravitational stress and cohesive strength, the Smoluchowski number (S_m – Ramberg, 1981):

$$S_m = \frac{\rho_b g z_b}{\tau_c + \mu_c \rho_b z_b}$$ (Equation 5.6)

Where τ_c is the cohesive strength and μ_c is the internal friction coefficient. For accurate scaling, the model has to share similar R_m and S_m ratio values (Dombradi et al., 2010). In our brittle-ductile models these are 5.00 and 1.41 for the 5 cm/hr and 2.50 and 1.41 for the 10 cm/hr respectively (Table 5.1). This indicates that the 10 cm/hr experiment is more accurately corresponding to the natural example than the 5 cm/hr one.

Finally, as previous workers suggest (Wickham, 2007; Del Ventisette et al., 2007; Dombradi et al., 2010), if the Reynolds number (*Re*) is relatively low in a model, then the inertial forces can be neglected compared to the viscous ones. The Reynolds number is given by the equation:

$$Re = \frac{\rho V l}{\eta}$$ (Equation 5.7)

Where V is the extension velocity and l is the total extension length. The N. GoC has a relative plate velocity of 23 mm/a from 12-6 Ma and 50 mm/a onwards (Brune et al., 2016) and our models extend at 5 and 10 cm/hr (Table 5.1). Thus, we can estimate the extension width in both

cases, resulting in low Reynolds numbers for the two models and nature ($1.79x10^{-8}$, $5.38x10^{-8}$, and $2.91x10^{-23}$). This allows the scaling of different forces to deviate from strict dynamic similarity, allowing time and length ratios to be considered as independent variables (Ramberg, 1981).

Table 5.1 – Materials and parameters used in the brittle-ductile models for scaling to nature. For calculation of parameters refer to main text (Values obtained from a: Persaud et al., 2015; b: Sokoutis et al., 2005; c: Willingshofer et al., 2005; d: Luth et al., 2010; e: Burov, 2011; f: Willingshofer et al., 2018; g: Brace & Kohlstedt, 1980; h: Dombradi et al., 2010; i: Farangitakis et al., 2020; j: Weijermars, 1986a; k: Weijermars, 1986b; l:Weijermars, 1986c; m: Persaud et al., 2017; n: Brune et al., 2016).

Materials	**Parameters (SI units)**	**Model**		**Nature**	**Model/Nature Ratio**	
		5 cm/hr	**10 cm/hr**		**5 cm/hr**	**10 cm/hr**
Upper Crust (K-Feldspar sand)	Thickness (m)	$1.60x10^{-2}$		$1.33x10^{4}$ [a]	$1.2x10^{-6}$ *	
	Density (kg/m^3)	$1.30x10^{3}$ [b,c,d]		$2.70x10^{3}$ [e]	0.48	
	Internal friction coefficient	0.6 [f]		0.8 [g]	0.80	
	Cohesion (Pa)	15 [h]		$2x10^{6}$ [i]	$7.5x10^{-6}$	
	Strength (Pa)	$2.04x10^{2}$		$5.00x10^{8}$ [e]	$4.00x10^{-7}$	
Lower Crust (silicone polymer)	Thickness (m)	$0.8x10^{-2}$		$0.66x10^{4}$ [a]	$1.2x10^{-6}$ *	
	Density (kg/m^3)	$0.97x10^{3}$ [j,k,l]		$2.90x10^{3}$ [e]	0.33	
	Viscosity (Pa s)	$5x10^{4}$ [j,k,l]		10^{22} [m]	$5x10^{-18}$	
	Strength (Pa)	69	139	$4.4x10^{7}$ [a]	$1.60x10^{-6}$	$3.20\ x10^{-6}$
	General parameters (SI units)					

Extension velocity (m/s)	$1.39x10^{-5}$	$2.77 x10^{-5}$	$7.3x10^{-10}$ [n]	$1.9x10^{4}$	$3.80x10^{4}$
Strain rate	$1.73x10^{-3}$	$3.47x10^{-3}$	$1.09x10^{-13}$	$1.59x10^{10}$	$3.17x10^{10}$
Time (s)	$4.8x10^{3}$	$3.6 x10^{3}$	$1.89x10^{14}$ [n]	$2.1x10^{-11}$	$1.9 x10^{-11}$
Smoluchowski number	0.94	0.94	0.66	1.4	1.4
Ramberg number	0.88	0.44	0.17	5.00	2.50
Reynolds number	$1.79x10^{-8}$	$5.38x10^{-8}$	$2.91x10^{-23}$		

*Ratio calculated for the combined thickness of brittle and ductile crust

Table 5.2 – Materials and parameters used in the brittle only models for scaling to nature. For calculation of parameters refer to main text (Values obtained from a: Phethean et al., 2016; b: Sokoutis et al., 2005; c: Willingshofer et al., 2005; d: Luth et al., 2010; e: Burov, 2011; f: Willingshofer et al., 2018; g: Brace & Kohlstedt, 1980; h: Dombradi et al., 2010; i: Farangitakis et al., 2020).

Materials	**Parameters (SI units)**	**Model**	**Nature**	**Model/Nature Ratio**
Oceanic Crust (K-Feldspar sand)	Thickness (m)	0.04	$4.5 x10^{3}$ [a]	$8.9x10^{-6}$
	Density (kg/m^3)	$1.30x10^{3}$ [b,c,d]	$3.00x10^{3}$ [e]	0.43
	Internal friction coefficient	0.6 [f]	0.5 [g]	1.2
	Cohesion (Pa)	15 [h]	$2x10^{6}$ [i]	$7.5x10^{-6}$
	Strength (Pa)	510	$5x10^{8}$ [e]	$1.02x10^{-6}$
	General parameters (SI units)			
Smoluchowski number		0.94	0.26	3.6

5.3.5 Limitations

Our model does not have 100% orthogonal motion in the first centimetre of deformation. However, when scaled to the natural examples, the deviation (approximately 0.5°-1°) would still be classified as an orthogonal rift within experimental limits. For the brittle/ductile configuration, the experimental runs are stopped before the ductile layer is ruptured completely. In nature that would translate to the moment before continental rupture. Thus strictly speaking, the structures created are not transform faults but strike-slip faults or shear zones that would then be classified as transform faults after the onset of rupture. However, the transpressional and transtensional structures would remain imprinted on the margins, indicating past plate motion changes. Since our models represent only the crust, we are obliged to assume that the mantle underneath accommodates this motion. As in most brittle/ductile analogue models, there is no isostatic compensation, which contributes to the differences between the natural examples and our models (Schellart & Strak 2016). Finally, we do not account for the effects of erosion or heat transfer between the layers.

5.4 Results

We describe the fault kinematic evolution in the experiments, based on observations from top-view time-lapse images (Figures 5.4,5, and 6) and cross-sections from the end of each model run. We use the topography derived from the surface scanning in order to identify normal/reverse motion in faults and the pink marker lines in the top-view time-lapse images to identify strike-slip motion and temporal relationships between faults. Note that with respect to Figure 5.2, these models are presented in a 180° rotated manner for better presentation. When “forward motion” or the “front” of the model is inferred, we refer to the bottom of the panels in Figures 5.4-5.6 (and top of 5.2), while when the “rear/back” of the model is mentioned, we refer to the top of the panels in Figures 5.4-5.6 (and bottom of 5.2).

5.4.1 Experiment 1 (weak brittle-ductile coupling)

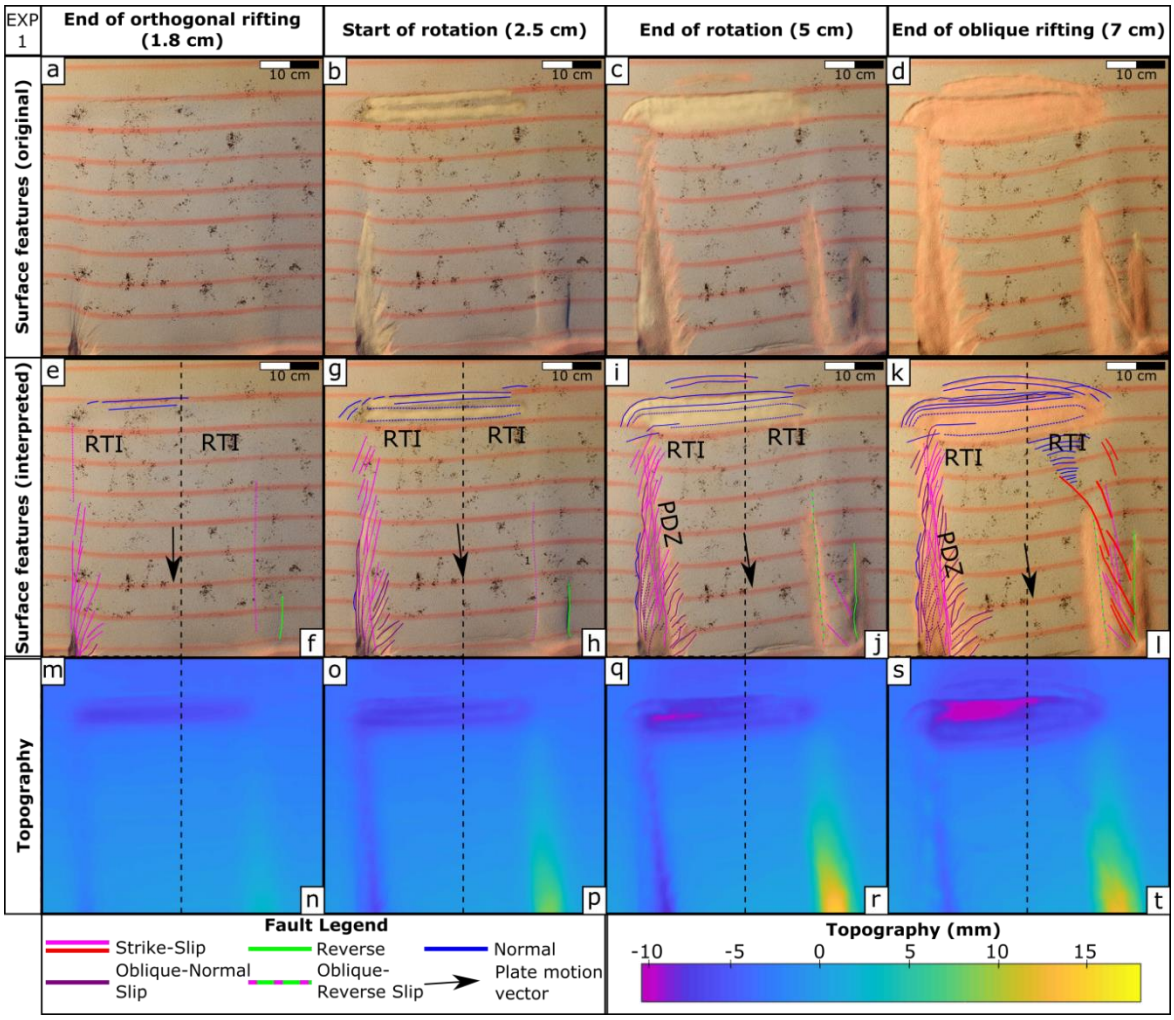

Figure 5.4 – Experiment 1 (5 cm/hr). a-d: Surface feature development. e-l: Surface feature development (interpreted). m-t: Topography development. Figure split into transtensional (panels e,g,i.k.m.o,q,s) and transpressional side (panels f,h,j,l,n,p,r,t). PDZ: Principal Displacement Zone, RTI: Rift-Transform Intersection. Note the evolution of normal faulting (blue faults) in the top of panels e-l. In the mid-section of each panel, note the evolution of transtensional (pink/purple faults) and transpressional (pink/green faults) deformation zones. The red faults in panel l correspond to the last strike-slip faults formed in the experiment. For higher resolution un-interpreted top views, see Figures B1-B4.

5.4.1.1 Orthogonal stage

Transtension side: After ~1.8 cm of orthogonal motion, a series of dextral Riedel (R) faults develops from the trailing edge of the plate, propagating towards the rift (Figure 5.4e). We interpret the higher angle (to the plate vector) shear structures near the front of the moving plate boundary (pink lines at the bottom left of Figure 5.4e), as potentially representing P shears (Tchalenko, 1970). The development of en-echelon strike-slip faults in this broad zone forms the initial transtensional shear margin. This zone is wider further away from the rift, with a maximum width of ~4 cm. Closer to the rift, there is no visible surface rupture, but localisation of this motion on incipient faults can be seen from the displacement of the pink marker lines.

Transpression side: At the other boundary, fault formation appears to be incipient throughout, with no surface expression apart from displacement of marker lines (Figure 5.4f, n). However, in the outer part of the plate boundary, a thrust front appears to form. This is due to the freedom of movement of the plate, which has already started rotating to produce the first transpressional features.

Rift: The rift zone in the back is focused on two main faults and has similar width throughout (Figure 5.4m, n).

5.4.1.2 Rotation Stage

Transtension side (start of rotation): After 2.5 cm of movement, the plate reaches the mechanical elbow, initiating rotation. The P shears described in the orthogonal stage now develop a normal-oblique slip character (Figure 5.4g). New strike-slip faults also form which cross-cut older structures to accommodate the rotating motion vector. The surface expression of horizontal motion propagates backwards in a diffuse zone ~5 cm wide as a series of strike-slip faults. On the fixed part of the experiment, the outermost faults in the transtension zone start to develop a normal-oblique slip character, as they no longer accommodate exclusively horizontal motion, and distinct fault scarps begin to form along them (Figure 5.4g). The topography change (Figure 5.4o)

indicates that the biggest depression lies at the front end of the moving plate, further from the pole of rotation, where plate separation is much larger.

Transpression side (start of rotation): Here, horizontal motion is accommodated by one main fault, which displays an oblique-reverse component (Figure 5.4h). Similar to the transtension side, the locus of deformation is focused near the front end of the moving plate, where plate overlap is significantly greater, resulting in a higher degree of compression (Figure 5.4p).

Transtension side (end of rotation): After approximately another 2.5 cm of movement (5 cm total), displacement takes place along a narrow zone of strike-slip faulting, the Principal Displacement Zone (PDZ) (Figure 5.4i). The PDZ now extends back to the rift-transform intersection (RTI) and is encased on both sides by oblique-normal faulting (Figure 5.4i). The topography shows further deepening occurring here (Figure 5.4q).

Transpression side (end of rotation): At the end of the 7^{o} plate rotation (Figure 5.2c), horizontal and vertical motion is still accommodated by the same two faults created at the start of the rotation phase (Figure 5.4j). Between those two faults, the total model thickness has increased by around 45% (Figure 5.4r).

Rift: The rift starts to develop an oblique character during the rotation, with the initiation of curved faults on its flanks (mainly on the transtensional side) (Figure 5.4g, i). By the end, it is already asymmetrical, ~ 4 cm wide at the transpressional RTI and ~6 cm at the transtensional RTI (Figure 5.4o-r). Further extension in the rift zone now propagates behind the initial rift zone (closer to the fixed plastic sheet) through a new graben (Figure 5.4i).

5.4.1.3 Final plate vector stage

Transtension side: The plate now has its final plate motion vector. After 2 cm of motion (7 cm in total), the PDZ is clearly more developed, with strike-slip faults extending all along the edge of the moving plate (Figure 5.4k). The majority of the P shears (with the exception of those adjacent to the RTI) are now oblique-normal, shown by the presence of fault scarps (Figure 5.4k, s).

Transpression side: The zone of transpression is now cross-cut by a series of strike-slip faults with clear surface expressions that accommodate horizontal motion between the two main thrust fronts (Figure 5.4l). Furthermore, at the inside corner of the RTI, a triangular-shaped series of normal faults has developed, bounded by a strike-slip fault. Reverse faulting appears to have stopped, and the motion is now purely horizontal with the original uplifted zone cross-cut by the newly formed strike-slip faults (Figure 5.4t).

Rifting: The new oblique rift is now very asymmetrical, with the part near the transtensional RTI >10 cm wide, while the part in the transpressional RTI is ~7 cm (Figure 5.4s, t). Topography (Figure 5.4s) shows the locus of deformation focused in a 1 cm deep depression near the transtensional RTI. New faults have formed at the back of the rift zone in the newly added sediments to accommodate the continuing extension. These faults appear to be oriented orthogonally to the new extension direction vector. The arcuate faults in the back now extend the whole length of the rift. (Figure 5.4k, l).

5.4.2 Experiment 2 (strong brittle-ductile coupling)

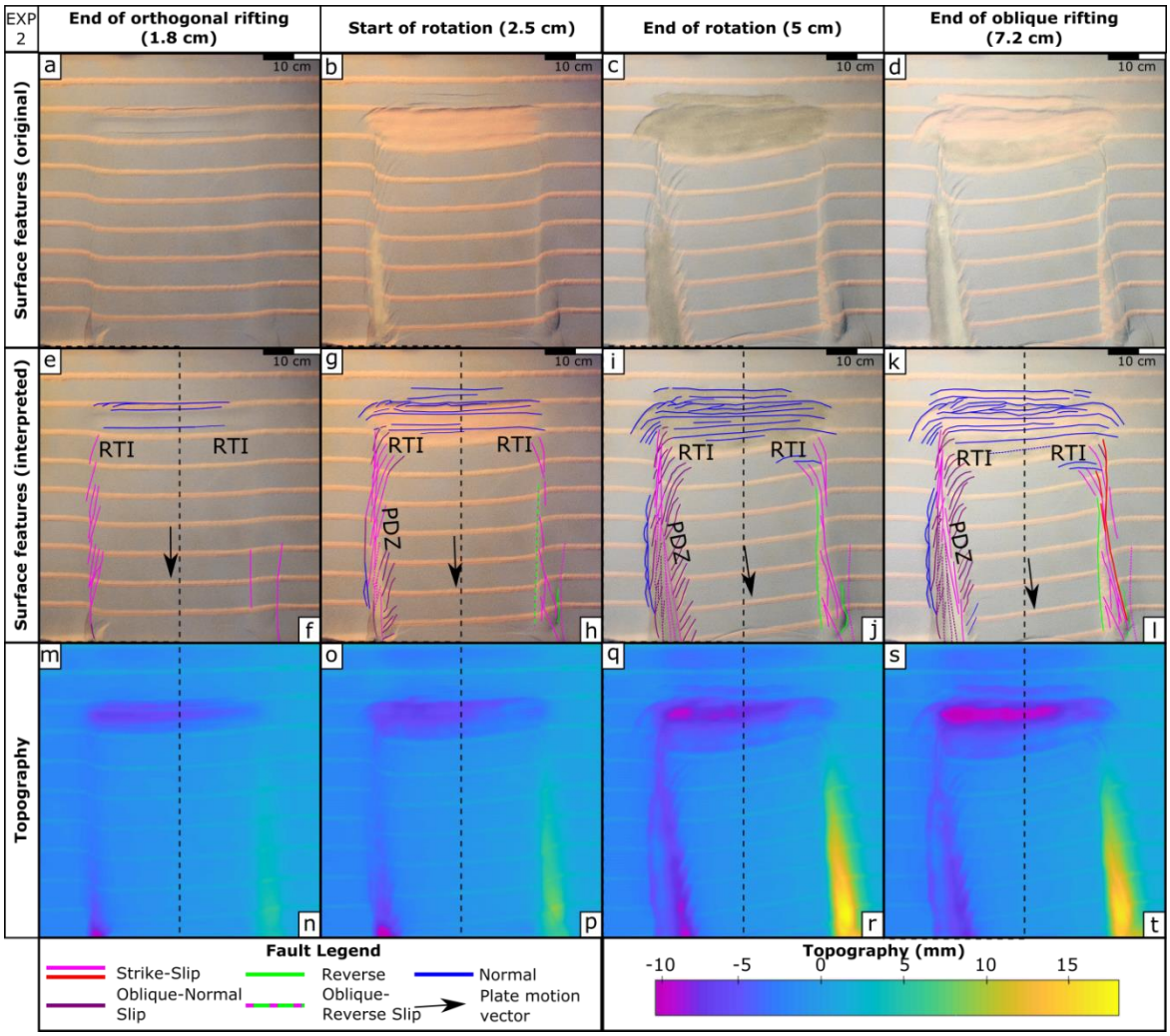

Figure 5.5 – Experiment 2 (10 cm/hr). a-d: Surface feature development. e-l: Surface feature development (interpreted). m-t: Topography development. Panels and abbreviations as in Figure 5.4. Note the evolution of normal faulting (blue faults) in the top of panels e-l. In the mid-section of each panel, note the evolution of transtensional (pink/purple faults) and transpressional (pink/green faults) deformation zones. The red faults in panel l correspond to the last strike-slip faults formed in the experiment. For higher resolution un-interpreted top views, see Figures B5-B8.

5.4.2.1 Orthogonal stage:

Transtension side: After ~1.8 cm of orthogonal motion, a series of dextral Riedel (R) faults develops from the edge of the moving plate, propagating towards the trailing edge of the plate

(Figure 5.5e). The first structure in the bottom of the panel is boundary-related, and thus is not interpreted as an R fault. The initial transtensional shear zone is ~4 cm wide throughout.

Transpression side: Any strike-slip faulting appears to be incipient and is only observable in the displacement of the pink marker lines (Figure 5.5f). However, the topography shows a slight rise of 3-5 mm, indicating the initiation of transpression in the area due to free plate movement (Figure 5.5n).

Rift: Rifting over the VD is considerably wider this time, and is focused in three main fault zones. The width of the rift is ~5 cm with curved faults developing at the edges (Figure 5.5e, f, m, and n).

5.4.2.2 Rotation Stage

Transtension side (start of rotation): After 2.5 cm of approximately orthogonal movement, the plate reaches the mechanical elbow, initiating rotation. A series of higher angle shear structures has developed, potentially representing P shears (Figure 5.5g). These are oblique-normal, as there are clearly visible fault scarps along them (Figure 5.5o). A few are more pronounced towards the RTI, displaying a horsetail splay character (Figure 5.5g). A PDZ develops at this stage, comprising a series of strike-slip faults aligned from the front to the trailing end of the moving plate, accommodating horizontal motion. Figure 5.5o shows that the deepest depression is located at the front end of the moving plate.

Transpression side (start of rotation): Here, horizontal motion is accommodated by an oblique-reverse fault and a series of cross-cutting strike-slip faults that are parallel to sub-parallel to the plate motion vector (Figure 5.5h). From the cross-cutting relationships between these strike-slip faults, it can be inferred that those parallel to the current plate vector are the youngest. Furthermore, a series of horsetail splays starts to develop adjacent to the RTI corner (Figure 5.5h).

Transtension side (end of rotation): After approximately another 2.5 cm of plate movement, the PDZ has followed the moving plate's vector change through the development of new motion-parallel en-echelon strike-slip faults, at a 7^{o} orientation to the original (Figure 5.5i). The PDZ is

now fully connected to the RTI at the trailing end of the moving plate. The P shears now extend throughout the right flank of the PDZ and display oblique-normal slip characteristics, with scarps visible in the topography and horizontal motion visible in the overhead views (Figure 5.5q, i). On the fixed side of the experiment, a series of normal faults develops to accommodate the extensional component of the transtensional shear (Figure 5.5i, q). The total width of the transtensional shear zone is ~8 cm throughout, but the PDZ is much narrower (~2.5 cm).

Transpression side (end of rotation): At the end of the rotation, the transpression zone has been uplifted more than 15 mm, increasing in thickness by about 60% (Figure 5.5r). More strike-slip faults have developed, with the newest formed parallel to the new plate motion vector, as inferred from their cross-cutting relationships (Figure 5.5j). Furthermore, near the RTI corner, the horsetail splays have developed further and are now accompanied by two normal faults. Finally, the initial oblique-reverse faults now only accommodate thrusting motion, as interpreted from the overhead views.

Rift: The rift acquires an oblique character during the rotation stage. A series of arcuate faults develops on its sides (mainly on the transtensional side) (Figure 5.5g, i). By the end of plate rotation, it is clearly asymmetrical, ~7 cm wide at the transpressional RTI and ~12.5 cm wide at the transtensional RTI (Figure 5.5q, r). Further extension in the rift zone propagates at the back of the initial rift zone (closer to the fixed plastic sheet) through a series of new grabens (Figure 5.5i, j).

5.4.2.3 Final plate vector stage

Transtension side: The plate now has acquired its final directional vector. After another 2.7 cm of motion (7.2 cm in total), the PDZ has developed further. The horsetail splays in the RTI are more pronounced and merge with the rift faults, giving the RTI a distinct corner shape (Figure 5.5k). Topographically, the part of the transtensional shear zone closer to the RTI does not appear to have experienced any significant extension apart from the topography disruptions directly above the faults (Figure 5.5s).

Transpression side: In the zone of transpressional shear, a series of new motion-parallel faults has developed, similar to those that developed at the end of the rotation stage (Figure 5.5l). The two long strike-slip faults between the thrust fronts appear to have accommodated all of the horizontal motion. Furthermore, an extensional triangle has developed in the RTI, bounded by a series of horsetail splays. These horsetail splays display an oblique-normal slip character, as is evident from the topographic depression along them (Figure 5.5t).

Rifting: The new oblique rift is now very asymmetrical, with the part near the transtensional RTI >13 cm wide, while the part in the transpressional RTI is ~7-8 cm (Figure 5.5s, t). Extension is focused in an elongated trough near the transtensional RTI (Figure 5.5s). Continuing extension is accommodated by newer faults forming at the back of the rift zone. These faults appear to be orthogonal to the original orthogonal plate vector, but curve at the ends (Figure 5.5k, l).

5.4.3 Experiment 3 (brittle only)

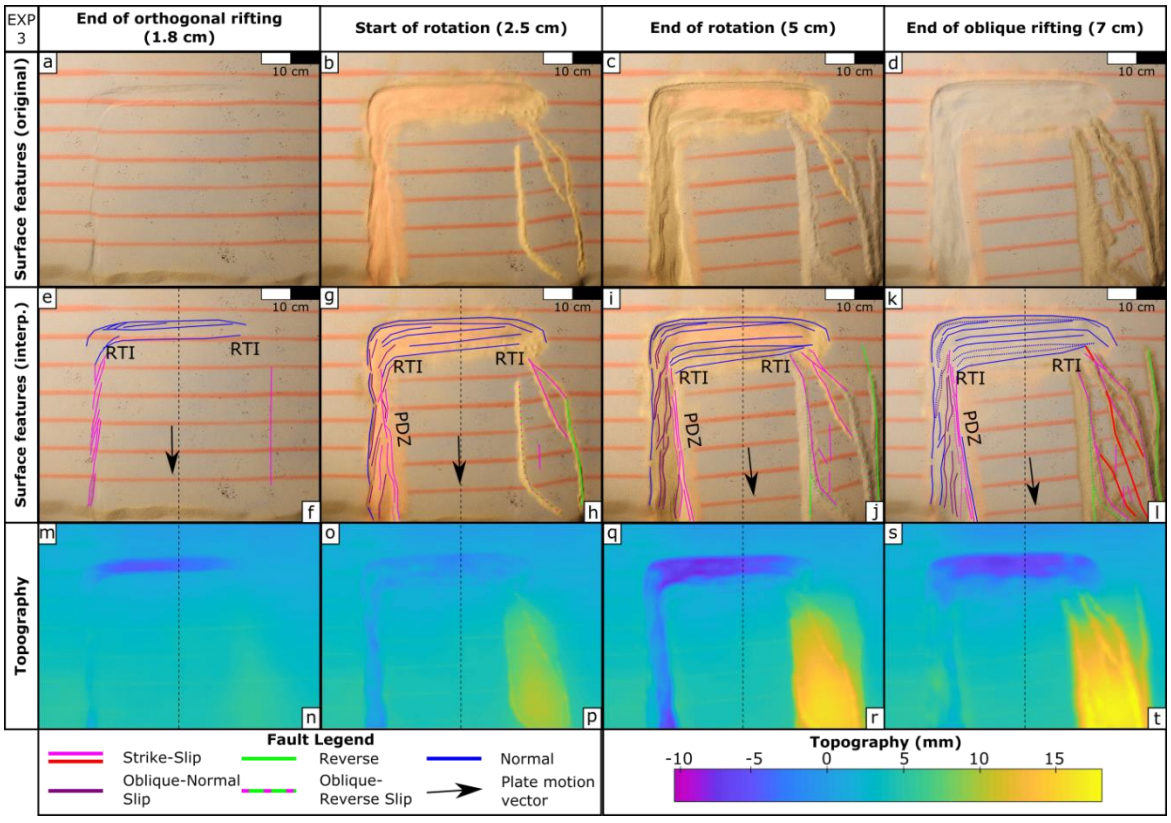

Figure 5.6 – Experiment 3 (Brittle Only). a-d: Surface feature development. e-l: Surface feature development (interpreted). m-t: Topography development. Panels and abbreviations as in Figure

5.4. Note the evolution of normal faulting (blue faults) in the top of panels e-l. In the mid-section of each panel, note the evolution of transtensional (pink/purple faults) and transpressional (pink/green faults) deformation zones. The red faults in panel l correspond to the last strike-slip faults formed in the experiment. For higher resolution un-interpreted top views, see Figures B9-B12.

5.4.3.1 Orthogonal stage

Transtension side: After ~1.8 cm of orthogonal motion, a series of dextral Riedel faults has developed from the edge of the moving plate to the RTI (Figure 5.6e). These Riedel faults define a series of en-echelon pull-aparts whose depressions can be seen in Figure 5.6i. The initial transtensional shear zone is a constant width of ~3 cm (Figure 5.6e).

Transpression side: Any faulting motion appears to be incipient and only observable in the displacement of the pink marker lines (Figure 5.6f). However, the topography shows a slight elevation increase of 1-2 mm in a broad triangular zone, indicating the very early stages of transpression due to free plate movement (Figure 5.6n).

Rift: Rifting initiates over the VD within a relatively narrow, symmetrical zone of extension. Two curved main faults are visible in the transpressional RTI side (Figure 5.6e, f).

5.4.3.2 Rotation stage

Transtension side (start of rotation): The moving plate intercepts the mechanical elbow after 2.5 cm of orthogonal movement. The en-echelon pull-apart basins now become more pronounced and start to merge, visible as undulations in topography (Figure 5.6o). The boundary of the pull-apart basins on the moving plate side is defined by a series of connecting strike-slip faults, representing the PDZ. The extensional component of this transtensional zone is accommodated by a series of oblique-normal and normal faults, representing the other boundary of the pull-apart basins (Figure 5.6g, o).

Transpression side (start of rotation): Two main thrust fronts develop over the overlapping plate boundary (Figure 5.6p). The fault situated above the moving plate displays an oblique-reverse slip character (Figure 5.6h). Between these two reverse faults, a series of strike-slip faults starts to develop, forming the initial RTI.

Transtension side (end of rotation): After approximately another 2.5 cm of plate movement, the PDZ has rotated a total of 7°, following the moving plate's vector change through the development of new motion-parallel strike-slip faults (Figure 5.6i). The PDZ is now fully connected to the RTI, forming a corner shape. The pull-apart basins have now almost completely merged, with similar depth across them (Figure 5.6q). The oblique-normal faults in the flanks of the fixed side of the experiment have also developed further (Figure 5.6i, q).

Transpression side (end of rotation): By the end of the rotation, new strike-slip faults have developed parallel to the new plate vector. The second of the two original thrust fronts (Figure 5.6h) has now also acquired an oblique component, as indicated by the displacement of the pink marker lines (Figure 5.6j). Topographically, the area has been thickened by ~25% between the two main thrust fronts (Figure 5.6r). Finally, another thrust front has formed at the right side of the transtensional shear zone (Figure 5.6j), potentially a boundary effect.

Rift: The rift acquires an oblique character in the rotation stage, with a series of arcuate faults developing on both sides (Figure 5.6g, h, i, and j). The obliquity leads to the rift being ~7 cm wide at the transpressional RTI and ~11 cm wide at the transtensional RTI (Figure 5.6i, j).

5.4.3.3 Final plate vector stage

Transtension side: The plate now has acquired its final directional vector, and we observe only horizontal motion. After 2 cm of further motion (7 cm in total), the PDZ is in the same location, following the motion of the moving plate (Figure 5.6k).

Transpression side (end): The new motion has now produced three long sub-parallel strike-slip faults that cross-cut the pre-existing ones. (Figure 5.6l). These faults extend from the front end of the moving plate to the RTI.

Rifting: The oblique rift is now more asymmetrical, >12 cm wide near the transtensional RTI and ~8 cm in the transpressional RTI (Figure 5.6k, l, s, and t).

5.5 Discussion

5.5.1 Comparison with natural examples

5.5.1.1 Gulf of California

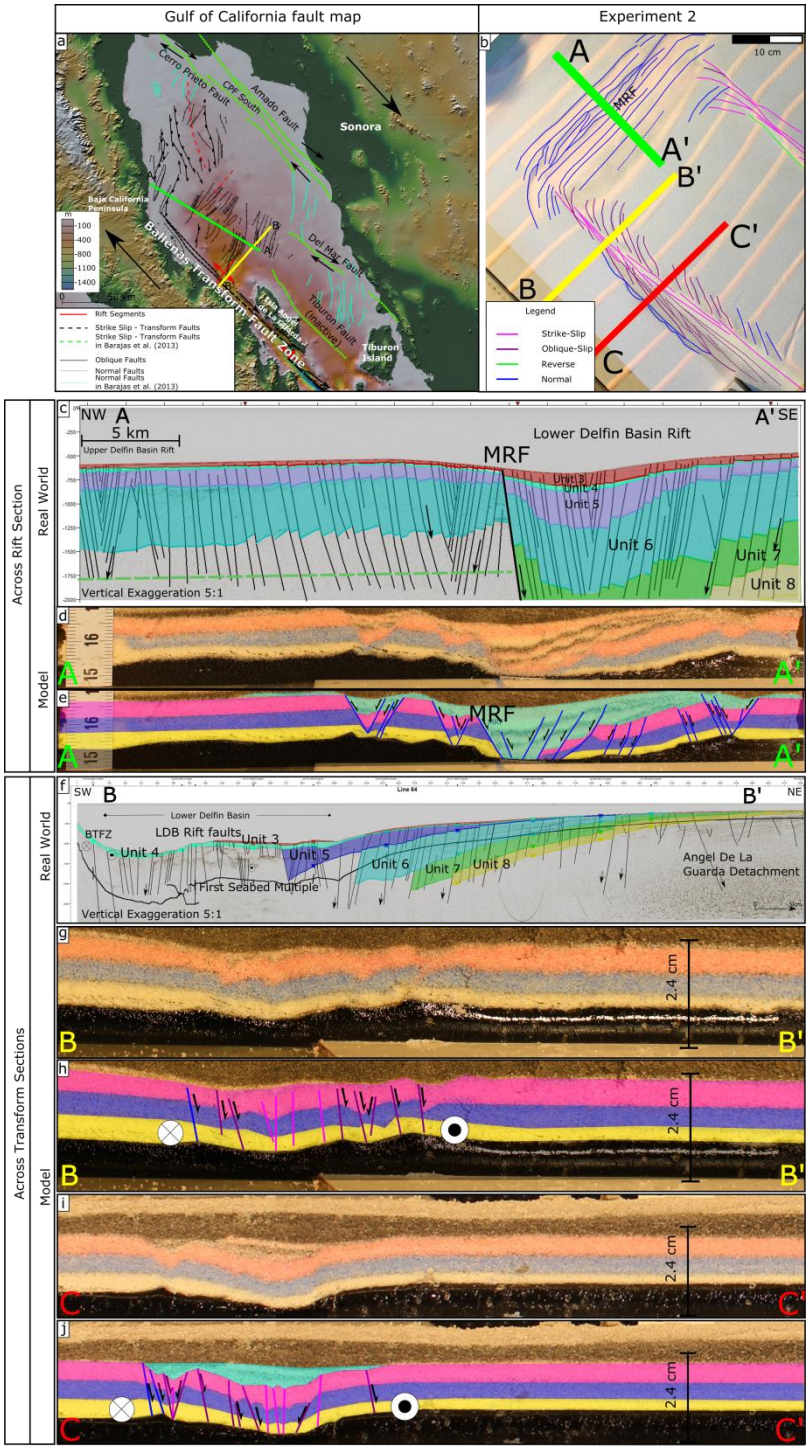

Figure 5.7 – Comparison between Experiment 2 and seismic cross-sections from the N. Gulf of California. a: Surface fault patterns in the N. GoC (modified after Persaud et al., 2003 and Martín-

Barajas et al., 2013). b: Surface fault patterns in Experiment 2. c, d, e: Comparison between a seismic cross-section across the Lower Delfin Basin (LDB) spreading centre and a section across the rift of Experiment 2. MRF: Main Rift Fault. f, g, h, i, j: Comparison between a seismic cross-section across the Ballenas Transform Fault Zone (BTFZ) and two sections across the transtensional RTI of Experiment 2. Original model layering from bottom to top: Black, Yellow, Blue, Pink. In figures e and j, the blue-shaded alternating white, black, and pale pink top layers represent the sediments added during the model run. The brown and white/cream layers above the models are the protective layer added before cutting. Seismic interpretations from the UL9905 high-resolution reflection seismic dataset (Stock et al., 2015). Bathymetry from GMRT Grid Version 3.3. For higher resolution uninterpreted model sections, see Figures B13-B15.

We use the high-resolution UL9905 seismic dataset (Stock et al., 2015) to compare profiles in the northern GoC with profiles through the transtensional side of Experiment 2 (Figure 5.7). The N. GoC is thought to have undergone a plate re-arrangement around 3 Ma, which corresponds to Unit 8 (yellow in Figure 5.7c, f) (Martin-Barajas et al., 2013). The seismic dataset images the first few km of crust, but it is reasonable to assume that the structures extend deeper and thus would scale to our models. The early stages of evolution of the transtensional side of Experiment 3 (Figure 5.6e, g, and i) are also compared with the evolution of the whole GoC area from 12.5 Ma onwards (Figure 5.1d, e, and f).

The fault patterns overall appear similar. In the northern GoC, there is a series of sigmoidal normal faults at the NW edge of the BTFZ (Figure 5.7a), similar to the series of horsetail splays formed at the end of Experiment 2, which appear to almost merge with the rift (Figure 5.7b). These sigmoidal faults accommodate the discrepancy between the plate motion vector and the direction of extension.

We next compare the change in fault motion and development due to the change in plate motion. In our model, faults that were strike-slip during the initial orthogonal phase (Figure 5.5g) became either oblique-normal or purely normal by the end of the rotation. Horizontal motion became

concentrated on faults aligned with the new plate vector (Figure 5.5i, k). This is analogous to examples of large transform faults in the northern GoC. These faults, such as the Tiburon fault, accommodated plate motion before the change in extension direction (Figure 5.7a). They were then abandoned because of this rotation and became either oblique-normal or purely extensional structures.

Figure 5.7f, g, h, i, j compares two sections across the dextral transform adjacent to the RTI in Experiment 2 with a seismic cross-section across the dextral Ballenas Transform Fault Zone. The strike-slip motion is accommodated by a main transtensional shear zone. Deformation is partitioned, with horizontal motion taken up by strike-slip and oblique-normal faults (Figure 5.7f, g, h, i, j). The latter also accommodate the extensional component of the tectonic regime, producing a topographic depression. This extension shifts northward with time, reflected in the northward migration of the locus of sedimentation. A similar pattern is observed in the syn-rift layers of our models (5.7g, h, i, j). In the northern GoC, a series of oblique-normal faults on the Baja California peninsula also accommodates that oblique motion (Bennett & Oskin, 2014).

We then compare a seismic profile across the Lower Delfin Basin rift (Figure 5.7c) with a profile across the rift in Experiment 2 (Figure 5.7d, e). In both, rifting is controlled by one major rift fault (MRF), accompanied by a series of antithetic faults on the opposite side (Figure 5.7c, d, e). A series of smaller grabens has also developed in the back of each rift. This is located directly NW of the MRF in Figure 5.7c for the northern GoC and to the left of the MRF in Figure 5.7d, e. The syn-sedimentary sequence is thickest over the main part of the rift. This is represented by the blue-shaded alternating white, black, and pale pink units above the pink layer in the model (Figure 5.7d, e) and the yellow layer Unit 8/Top Pliocene in the seismic cross-section (Figure 5.7c) (Martin-Barajas et al., 2013).

Finally, we compare the evolution of the whole GoC since 12.5 Ma with the surface evolution of the transtensional side of Experiment 3. We see a direct correlation in how the transtensional boundary evolves when a change in extension direction is imposed. In the beginning, Bennet et al.

(2013) argue that shearing was localised in en-echelon dextral strike-slip shear zones (Figure 5.1d and 6e). These shear zones evolved into pull-apart basins that formed the proto-Gulf (Figure 5.1e and 6g). Finally, when the extension direction changes, the margins of the GoC began to drift apart at varying rates (Figure 5.1f and 6i).

5.5.1.2 Tanzania Coastal Basin

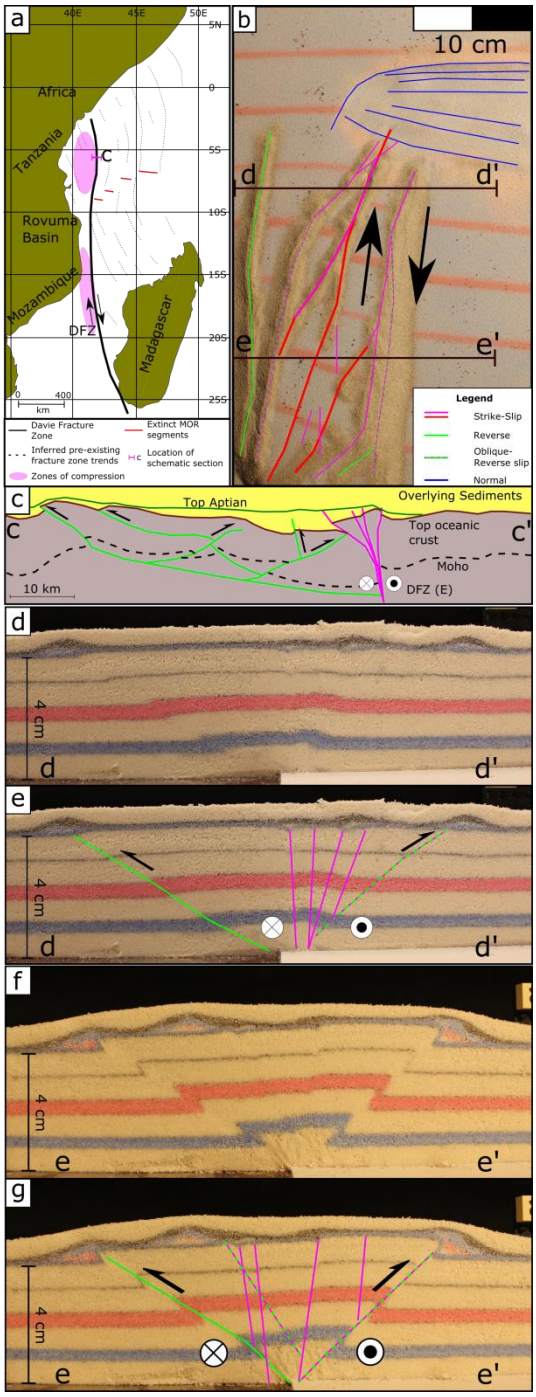

Figure 5.8 – Comparison between the TCB and Experiment 3. a, b: Surface fault patterns in the TCB and Experiment 3, respectively. c: Schematic cross-section across the DFZ. d, e, f, g: Cross-sections across the transpressional zone of Experiment 3. TCB configuration modified from Phethean et al., 2016. Seismic interpretation in c is re-interpreted from Sauter et al., (2018). In panel b, the red faults correspond to the last strike-slip faults formed. Syn-tectonic sedimentation

above the main structures is a protective layer. For higher resolution un-interpreted experiment sections, see Figures B16-B17.

The TCB underwent a plate re-organisation ~150 Ma, resulting in the formation of the DFZ. In both Experiment 3 (Figure 5.8b) and the TCB (Figure 5.1g-l and 8a), zones of compression develop adjacent to the main strike-slip structures as the motion changes, and the pattern of strike-slip faults evolves to accommodate the changed angle. In Experiment 3, some of the initial strike-slip faults are abandoned after the change in motion (Figure 5.6j, l, 8a, b – pink faults). Those that remain active reorient themselves by developing kinks, leading to a curved surface expression that is not completely aligned with the final plate motion (Figure 5.6l, 8a, b – red faults).The DFZ shows a similar pattern: the earliest transform faults have been abandoned, and the DFZ has a slightly kinked, 'open S' shape, reflecting this two-stage history (Figure 5.8a, Phethean et al., 2016).

The deep seismic cross-section from the DFZ (Figure 5.8c) shows clear evidence for intra-plate compressional deformation. The same coexistence of strike-slip and compression is apparent in the two profiles across the transpressional side of Experiment 3 (Figure 5.8d, e, f, g). During the plate rotation in Experiment 3, the compressional structures form to accommodate that component of motion (Figure 5.6h, j). These structures stop developing after rotation has ceased, when only the large strike-slip faults are active (Figure 5.6l). We can thus infer that intra-oceanic crustal thrusting may have occurred in the TCB to accommodate the plate motion change around 150 Ma, prior to the complete development of the DFZ. This is further supported by Sauter et al., (2018), who date the uppermost syn-deformational sediments (Figure 5.8c) as pre-Aptian (125 Ma). In the model cross-sections (Figure 5.8 d, e, f, g), thrusts develop on both sides of the strike slip zone, but this is not observed in the seismic example (Figure 5.8c). This is because the crust to the east of the DFZ is much younger and formed as the MOR passed this location, marking the end of deformation in this region. During the Jurassic, there probably was deformed crust on both

sides of the DFZ here, but the eastern side moved southwards with Madagascar and is now likely located in the Morondava Basin.

5.5.2 Further Discussion

Our results provide good first-order agreement with natural transform plate boundaries that have experienced a change in relative motion during their evolution, resulting in either transpression (TCB) or transtension (GoC). During the initial orthogonal phase, the structures that develop are similar to those observed by Basile and Brun (1999). Faster plate velocity results in strong brittle/ductile layer coupling and diffuse rifting (13 cm at its maximum width) (Figure 5.5s), while slower rifting velocity results in weak brittle/ductile coupling and narrower rifting (10 cm at its maximum width) (Figure 5.4s). Other parameters that can affect the model rheology and thus the rift width, such as the thickness of the brittle layer (Vendeville et al., 1987), are held constant, so the difference is due to the strain contrast between the layers being minimised when a higher velocity is imposed (Brun, 2002). The same appears to be the case even when rifting is oblique.

The opposite appears to be the case in the transtensional and transpressional shear zones. The transtensional shear zone in Experiment 1 reaches widths between 5-10 cm (Figure 5.4s), while in Experiment 2 it has a constant width of about 5-6 cm throughout (Figure 5.5s). Similarly, the transpressional zone of Experiment 2 (Figure 5.5t) is 50% narrower than the one in Experiment 1 (Figure 5.4t). This corresponds to natural transform examples where faster transforms have narrower deformation zones (see Table 5.1 – of Mauduit & Dauteuil, 1996, for spreading velocities and corresponding transform widths). However, all three experiments produce wide zones of oblique lateral deformation, recording several stages of fault evolution. This is consistent with the numerical modelling of Le Pourhiet et al. (2017), who argue that transforms experiencing obliquity do not develop as line segments, but form diffuse zones ~100 km wide recording several phases of deformation prior to oblique break-up.

The brittle-only experiment shows good correlation with the evolution of the Davie Fracture Zone. It supports the suggestion by Phethean et al. (2016) that ~150 Ma a change occurred in the plate motion that was accommodated by compression, with previous transforms cross-cut by a much larger structure that became the Davie Fracture Zone. In our experiment, the initial strike-slip faults become inactive once the final motion vector is established (Figure 5.6h, j, and l – pink strike-slip faults). Then, horizontal motion is taken up by new cross-cutting faults parallel to the final plate vector (Figure 5.6h, j, and l – red strike-slip faults).

Although the DFZ formed in oceanic crust, there is a strong similarity with the surface features developing on the transpressional part of Experiment 2 (Figure 5.5l). In particular, a large sigmoidal fault develops in Experiment 2, similar in shape to the DFZ (long red fault in Figure 5.5l). This could be explained by the strength profile of Experiment 2 (Figure 5.2b), where the maximum strength of the brittle layer and the ductile layer are almost identical, similar to oceanic lithosphere. Although the model is not scaled to represent oceanic lithosphere, this might potentially explain the morphological similarity.

Another natural example comparable to Experiment 2 is the Gulf of Aden. The Alula-Fartac Transform Fault is not characterised by a single narrow transform valley, but rather by two sub-parallel 180 x 10 km troughs that join two offset ridge segments (d'Acremont et al., 2010). The spreading direction has recently rotated counterclockwise, resulting in extension in the transform basins (d'Acremont et al, 2010). This results in the transform zones migrating in time and space, similar to Experiment 2.

In the transpressional sides of Experiments 1 and 2, we see a thickness increase in the models of approximately 45% and 60%, respectively (Figures 4t and 5t). Based on our experimental scaling, the crustal thickness range for these experiments is a median value between 15-25 km. Such a thickness increase would then imply real-world elevation changes of ~7-11 km for Experiment 1 and 9-15 km for Experiment 2. However, because our scaling is based on the density contrast

between the brittle and ductile layers, we need to apply a topographic correction factor C_{Topo} (Schellart & Strak 2016):

$$C_{Topo} = \frac{\rho_{LC}^{m}(\rho_{LC}^{p} - \rho_{UC}^{p})}{\rho_{LC}^{p}(\rho_{LC}^{m} - \rho_{UC}^{m})} \quad \text{(Equation 5.8)}$$

where ρ_{LC}^{m} is the model's lower crust density (0.970 g/cm^3), ρ_{LC}^{p} is the natural example's lower crustal density (2.9 g/cm^3), ρ_{UC}^{m} is the model's upper crustal density (1.3 g/cm^3) and ρ_{UC}^{p} is the natural example's upper crustal density (2.7 g/cm^3).

Applying equation (5.8) to our experiments, C_{Topo} is ~0.209, which would reduce the thickness changes to physically reasonable values of 1.4-2.3 km for Experiment 1 and 1.9-3.1 km for Experiment 2. In addition, the analogue models do not include isostatic compensation, which would further reduce the amount of crustal thickening expressed as topographic relief, perhaps by up to a factor of 2 (Schellart & Strak, 2016). Erosion would also reduce the topography.

Nonetheless, our experiments show that overlapping, transpressional transform margins are accompanied by topographic highs parallel to the plate motion. Features such as marginal ridges or plateaus (Mercier de Lépinay et al., 2016) are observed at transform margins that have experienced overlapping plate motions such as the Exmouth Plateau (Whittaker et al., 2016), the Romanche Fracture Zone (Davison et al., 2016), and, in our example, the Davie Ridge. As Euler poles typically migrate over a few Ma, other examples of these transpressive or transtensional feature might be preserved where oceanic fracture zones change curvature, indicating a past change in spreading direction (e.g. Iaffaldano et al, 2012; Schettino 2015).

5.6 Conclusions

A series of experiments designed to simulate the effects of a change in plate motion on transform margins and rift-transform intersections produces structural patterns and topographic effects that show good agreement with natural examples. They provide an understanding of the fault geometries and kinematics and the temporal and spatial relationship of structural features that

develop in transtensional and transpressional margins. These are caused by underlap or overlap on the transform margin when the plate motion vector changes.

In transtensional margins, such as the Gulf of California or the Gulf of Aden, we find oblique-normal faults that have developed from original strike-slip faults. These oblique-normal faults accommodate the extensional component of the plate rotation. As the plate vector changes, the PDZ's direction also rotates to accommodate the new horizontal motion.

In transpressional margins, such as the Tanzania Coastal Basin, we report thrust fronts developing to accommodate plate overlap. These thrust fronts are also often oblique and are accompanied by strike-slip faults. As motion in the new direction continues, newer strike-slip faults develop and cut through the pre-existing fabric. This is observed both in our lab experiments and in the natural example of the Davie Fracture Zone.

6 The basin-scale: The structural evolution of pull-apart basins in response to changes in plate motion[3]

6.1 Introduction

Pull-apart basins are structural depressions attributed to the presence of extensional features along strike-slip fault systems, found at releasing bends or steps (Rahe et al., 1998). They were first described in the Death Valley strike-slip fault system by Burchfiel and Stewart (1966), where they observed an oblique "pulling-apart" of the two sides of the valley due to an oblique slip segment in the Death Valley Fault Zone. In their global catalogue of releasing and restraining bends on strike-slip systems, Mann (2007) documented around 150 such examples of releasing bends with observable pull-apart structures.

Conceptual models of pull-apart basins traditionally show a rhomboidal depression between two main parallel strike-slip faults (Figure 6.1a), commonly referred to as principal displacement zones (PDZs) (Wu et al., 2009). This depression is bounded by oblique extensional faults termed basin sidewall faults (BSFs), linking the PDZs (Corti et al., 2020) (Figure 6.1a).

However, the evolution and current geometry of some well-known pull-apart basins around the world cannot be fully explained by pure strike-slip motion between two PDZs (Wu et al., 2009). There is a number of pull-apart basins around the world that display distinct transtensional characteristics. For example, Umhoefer et al. (2018) note that a plate motion variation at around 8 Ma (Atwater & Stock, 1998) potentially led to successive pull-apart basin opening and flooding from south to north in the Gulf of California. Allen et al. (1997) observe that the evolution of the Bohai Basin in China can be attributed to transtension (and a later transpressional event). Armijo

[3] This chapter has been accepted for publication in November 2020 and is under production at the submission of this PhD Thesis as: Farangitakis, G.,P., McCaffrey, K. J. W., Willingshofer, E., Allen, M. B., Kalnins, L. M., van Hunen, J., Persaud, P., Sokoutis, D. (2020?). The structural evolution of pull-apart basins in response to changes in plate motion. Basin Research

et al. (2002) describe submarine morphology in the Sea of Marmara that reveals a segmented fault system, including pull-apart features indicating a transtensional regime. Similarly, the Andaman Sea has been viewed traditionally as a large simple pull-apart basin but recent studies indicate that the initial orthogonal E-W or ESE-WNW extension is followed by a change in the direction of extension to SSE-WNW (e.g. Srisuriyon & Morley, 2014; Morley & Alvey, 2015; Morley, 2017; Morley & Searle, 2017). Finally, Decker (1996) and Lee and Wagreich (2017) indicate that the Vienna Basin displays similar transtensional characteristics with large negative flower structures formed over the main PDZs.

A transtensional component is sufficient to create two to three times more accommodation space for sediments compared to an orthogonal pull-apart basin (ten Brink et al., 1996). Transtensional pull-apart basins also form wider PDZs (Farangitakis et al., 2019), comprising transtensional zones ranging from elongate negative flower structures to complex zones with mini-basin characteristics themselves (Figure 6.1b). A transtensional pull-apart basin thus has a distinct form and evolutionary history compared with classic, purely strike-slip pull-apart basins. However, cases between these end-members can exist, where an individual basin may experience phases of both pure strike-slip and transtensional motion.

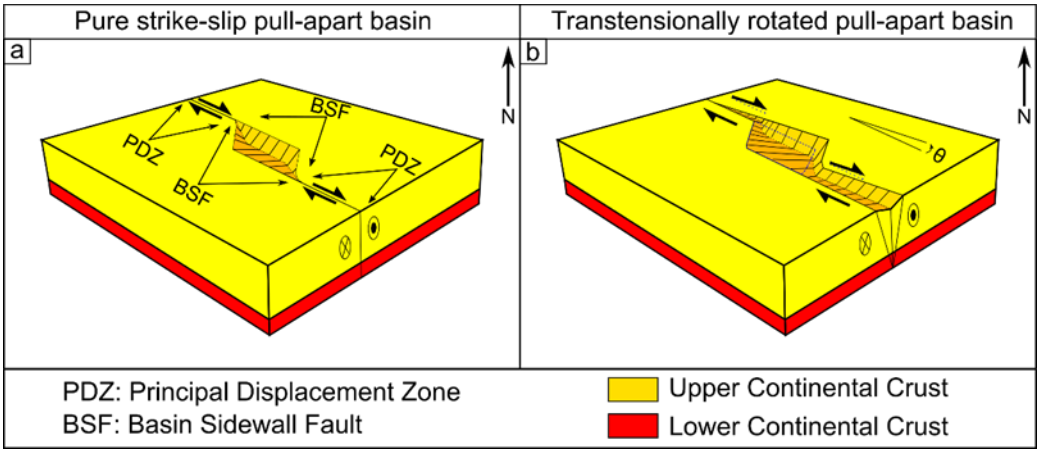

Figure 6.1 – Generalised conceptual models of a) a pure strike-slip pull-apart basin and b) a pull-apart basin experiencing transtension (with the northern block motion rotated by $\vartheta=7^{o}$ relative to the southern block).

Understanding pull-apart basin development through analogue modelling has proven to be a very useful approach. Analogue modelling utilises materials that deform in a continuous and discontinuous manner, leading to clear expressions of the structure over time (Reber et al., 2020), which makes this method ideal for studying the evolution of a pull-apart basin. The first analogue models of pull-apart basins were carried out by McClay and Dooley (1995), who used two diverging basal plates to produce the fault geometries and surface evolution of a pull-apart basin. Similar modelling approaches have since been used by Sims et al. (1999), who studied the role of ductile decollements in pull-apart basin shape, and Smit et al. (2008), who investigated the evolution of salt diapirs in the Dead Sea pull-apart system. Whitjack and Jamison (1986) explored fault patterns in oblique settings using clay models to simulate areas such as the Gulf of California and the Gulf of Aden. Basile and Brun (1999) investigated a number of parameters in pull-apart basins such as length to width ratio, brittle to ductile layer ratio, and extension velocity. Corti and Dooley (2015) and Corti et al. (2020) used centrifuge modelling apparatuses to test how the morphology of the developing pull-aparts depended on the interaction between the PDZs (underlapping, overlapping or neutral). Finally, Wu et al. (2009) used a similar array to that of McClay and Dooley (1995), imaging the development of transtensional pull-apart basins in 4D by varying the angle of the PDZ. Building on these previous studies, an in-depth investigation of the effect of changes in relative plate motion direction on pull-apart basin evolution is needed in order to understand the basin's structural response to changing boundary conditions. In this study, we use a combination of analogue modelling and seismic reflection data to further understand the evolution of pull-apart basins when transtension is imposed due to a change in extension direction during basin evolution. We then compare our model results to observations of pull-apart structures in the N. Gulf of California, where a known 10-15^{o} change in relative plate motion occurred at 8-6 Ma (Bennett & Oskin, 2014). Finally, we explore whether changes in extension direction during pull-apart basin evolution can explain first order features of the Bohai Basin in China. Our results show that it is important to consider changes in extension direction over time when investigating pull-apart basin evolution.

6.2 Geological Background

6.2.1 The Northern Gulf of California

The Gulf of California (GoC) is a relatively young transtensional margin, with active seafloor spreading centres in the southern and central Gulf (Lizarralde et al., 2007) and rifting (with potential continental break-up) in the north (Martin-Barajas et al., 2013). All the extensional components of the GoC (spreading centres and rifts) are connected through dextral transform faults (Figure 6.2d). The first occurrence of dextral transform motion between the Pacific and North American plates is believed to have happened ca. 20 Ma (Lonsdale, 1989; Axen, 1995; Atwater & Stock, 1998; Bennett et al., 2013) (Figure 6.2a), followed by the first phase of extension in the Proto-Gulf of California starting ca. 12 Ma (Stock & Hodges, 1989; Atwater & Stock, 1998) (Figure 6.2b). Bennett & Oskin (2014) suggest that a ~ 10-15^{o} clockwise rotation in the relative motion between the plates between 12.5-6.5 Ma increased the rift obliquity and favoured the development of strike-slip faulting. Shearing localised in en-echelon strike-slip shear zones, that began to create pull-apart basins by 6 Ma (Bennett et al., 2013; Figure 6.2c). These nascent pull-apart basins flooded from south to north successively due to higher transtensional deformation rates further from the Euler pole (Umhoefer et al., 2018). At the end of their evolution, and after a further plate re-organisation at ca. 3 Ma (Seiler et al., 2009), a series of long dextral transform faults was formed, connected by smaller rift basins (Persaud et al., 2003; Lizarralde et al., 2007) (Figure 6.2d). In the northern GoC, the nature and timing of continental break-up is still unclear, with the presence of oceanic crust suggested in some basins (Martin-Barajas et al., 2013; Gonzalez-Escobar et al., 2014) and delayed rupture suggested for others (Lizarralde et al., 2007; Martin-Barajas et al., 2013).

Deformation in the northern GoC is distributed across a broad, relatively shallow depression representing a pull-apart structure between the Cerro Prieto Fault (CPF) and the Ballenas Transform Fault Zone (BTFZ) (Persaud et al., 2017) (Figure 6.2e). Within this pull-apart structure, a dense network of mainly oblique-normal, small-offset faults forms a broad zone of brittle

deformation, with smaller sub-parallel basins along splays at the NW end of the Ballenas Transform Fault Zone (Persaud et al., 2003) (Figure 6.2e). Hence, the basal ductile shear zone underneath the brittle crust is expected to be as wide as the surface deformation (Persaud et al., 2003). Deformation within the pull-apart structure has experienced a westward jump from the Tiburon Basin ca. 3.5-2 Ma following a plate reorganisation (Lonsdale, 1989; Seiler et al., 2009). The Ballenas Transform Fault Zone and Cerro Prieto Fault have a 10° difference in strike, with earthquake and field data suggesting that between 7-15 mm/a of dextral slip is transferred from the northern end of the Ballenas Transform Fault Zone to the onshore faults in Baja California (e.g. Goff et al., 1987; Humphreys & Weldon, 1991; Bennett et al., 1996). Moreover, the Cerro Prieto Fault and Ballenas Transform Fault Zone strike 6-7^{o} clockwise (312^{o}) of the transforms in the south (305^{o}) (Lonsdale, 1989). Dorsey and Umhoefer (2012) and Van Wijk et al. (2017) argue that this increased obliquity, in combination with the geometry of the strike-slip faulting stepover, contributes to the northern Gulf's basin development and late or absent rupture. Other factors that contribute to the northern Gulf's development could include initial fault geometries, thick sedimentation, and changing loci of extension.

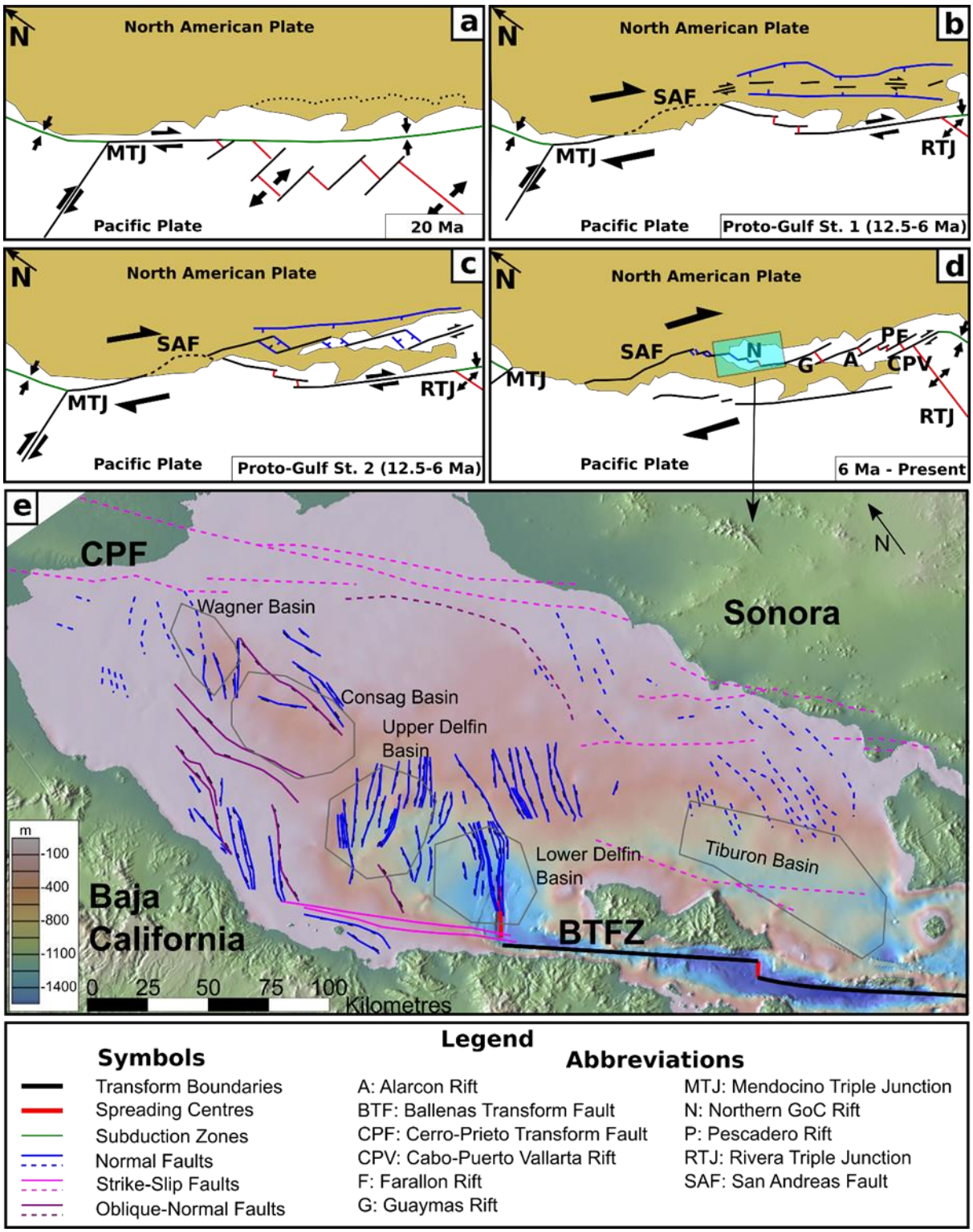

Figure 6.2 – a-d: Stages of evolution of the Gulf of California from 20 Ma to present (modified from Bennett et al., 2013), a: Initial occurrence of dextral transform motion, b: early extension in the proto-gulf, followed by c: transtension in the proto-gulf, d: current configuration. e: close-up map

of the northern Gulf of California (faults in continuous lines from this work and Persaud et al. 2003, faults in dashed lines from Martin-Barajas et al., 2013, basins outlined in grey).

6.2.2 The Bohai Basin, Northern China

The Bohai Basin in Northern China is a 1000 km long by 600 km wide extensional structure, formed mainly in the early Cenozoic (Hu et al., 2001; Liangjie et al., 2008), which has undergone a transtensional phase in its evolution (Allen et al., 1998). It has a NE-SW trend, bounded by lithospheric scale strike-slip faults, namely the dextral Tan-Lu strike-slip fault zone in the east (Klimetz, 1983; Allen et al., 1997) and the Lanliao and Shulu-Handan strike-slip fault zones in the west (Qi & Yang, 2010) (Figure 6.3c). It superficially resembles a giant pull-apart structure, controlled by dextral slip, with the Bozhong Depression (Figure 6.3a) being the main Cenozoic depocentre. Transtension in the basin occurred in the Early Cenozoic when the Pacific-Asia convergence vector rotated from NW-SE to E-W (Engebretson et al., 1985).

Results from different approaches such as seismic reflection (Qi & Yang, 2010; Feng & Ye, 2018), stress field modelling (Guo et al., 2009;), thermal subsidence (Hu et al., 2001) and hydrocarbon well data (Liangjie et al., 2008) suggest that the Bohai Basin has had a multi-phase evolution. The basement fabric of the Bohai Basin is of pre-Cenozoic age, and consists of Precambrian to Mesozoic metamorphic and sedimentary rocks that are cross-cut by the main boundary faults of the basin (Qi & Yang, 2010). In the Paleocene to Early Eocene, dextral transtension was localised in four regions in the basin, which acted as the main depocentres at the time (Allen et al., 1997) (Figure 6.3a). By the Middle Eocene, extension had propagated southwards from the current location of the Liaodongwan Depression, creating extensional overlap over the main depocentre of the central basin, the Bozhong Depression (BZHD Figure 6.3b). Extension along east-west normal faults in this region led to the thickest known sediments in the basin (Allen et al., 1997, Qi & Yang, 2010).

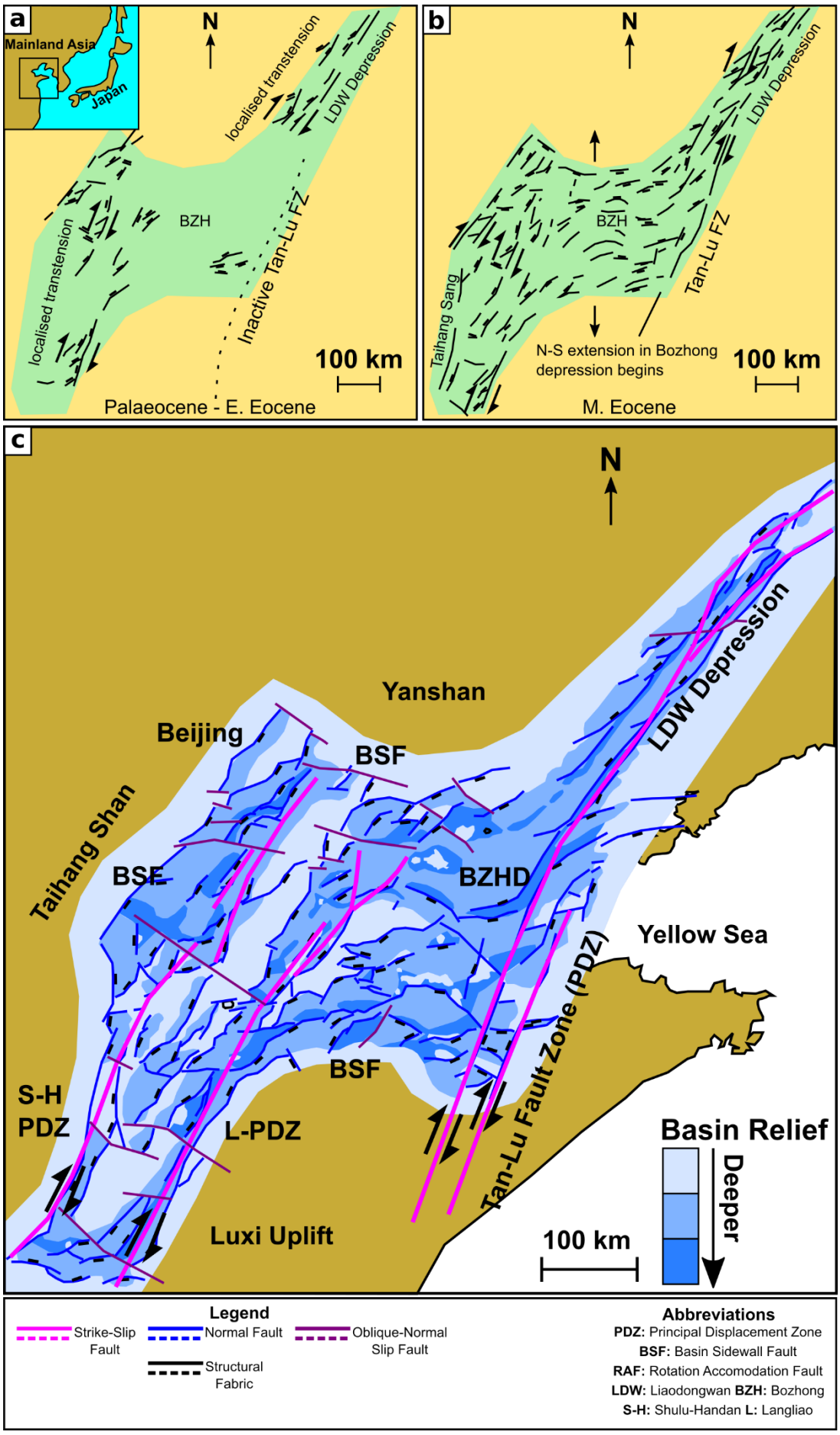
a
Mainland Asia
Japan
N
localised transtension
LDW Depression
BZH
Inactive Tan-Lu FZ
localised transtension
100 km
Palaeocene - E. Eocene
b
N
LDW Depression
BZH
Tan-Lu FZ
Taihang Sang
N-S extension in Bozhong depression begins
100 km
M. Eocene
c
N
Yanshan
Beijing
BSF
LDW Depression
Taihang Shan
BSF
BZHD
Yellow Sea
Tan-Lu Fault Zone (PDZ)
BSF
S-H PDZ
L-PDZ
Basin Relief
Deeper
Luxi Uplift
100 km
Legend
Strike-Slip Fault
Normal Fault
Oblique-Normal Slip Fault
Structural Fabric
Abbreviations
PDZ: Principal Displacement Zone
BSF: Basin Sidewall Fault
RAF: Rotation Accomodation Fault
LDW: Liaodongwan BZH: Bozhong
S-H: Shulu-Handan L: Langliao

Figure 6.3 – a-b: Evolution of the structural fabric of the Bohai Basin (modified from Allen et al., 1997). Location of the basin shown in pale green. Inset: regional location of panels a-c. c: Map of the structure and relative depth to Mesozoic basement and structural map of the Bohai Basin (modified from Allen et al., 1997 and Qi & Yang, 2010). Note that panels a-b refer only to the structural fabric of the area. BZHD: Bozhong Depression. The colours in the legend refer only to panel c.

6.3 Methodology

6.3.1 Analogue Models

6.3.1.1 General parameters of the models

We use a modified experimental apparatus based on Farangitakis et al. (2019) (originally inspired by Basile & Brun, 1999), where a moving plate slides away from a static plastic sheet at the base of a brittle/ductile layer configuration (Figure 6.4a). Hence, deformation is entirely driven through the applied basal boundary conditions, with pre-imposed velocity discontinuities (VDs), similar to those in Allemand and Brun (1991) and Tron and Brun (1991). The velocity discontinuity configuration is that of an en-echelon rift and strike-slip system, consisting of two sets of alternating discontinuities parallel and perpendicular to orthogonal plate motion (Figure 6.4a). The master strike-slip faults or PDZs are "neutral" (Corti and Dooley, 2015; Corti et al., 2020), meaning they do not overlap or underlap each other during orthogonal motion.

Following an initial orthogonal extension phase, we introduce a counterclockwise rotation of 7o in the extension direction, consistent with half the amount of rotation observed in the northern Gulf of California (10-15^{o} - Bennett and Oskin, 2014). We use 7^{o} of rotation mainly due to physical limits of the apparatus.

The brittle/ductile experiments were performed with the basal plate moving with a velocity of 7.5 cm/h, a velocity scaled to the natural example (see model scaling section). We capture the evolution of the model's surface features using a high-resolution digital camera taking snapshots

every 60 seconds (with a resolution higher than 1 cm). This allows for a time-based analysis of the developing surface features after the model run. We also map the changing topography using a 3D surface scanner (with accuracy >1mm) that scanned the model surface every 3 minutes. This technique enables us to a) quantify topographical changes in the model and b) identify structural features that have developed and might not be visible in the top-view images. Finally, at regular intervals (of approximately 2.5 minutes) we use a small funnel to manually add three alternating colour layers of feldspar sand in the topographic lows. These layers represent syn-and post-rift sedimentation and are particularly useful in correlating structures and identifying the locus of extension when the models are sectioned and reconstructed in 3D. At the end of the experimental run, the model is also covered with a thick protective layer of black sand prior to wetting and cutting.

6.3.1.2 Kinematic set-up of the analogue models

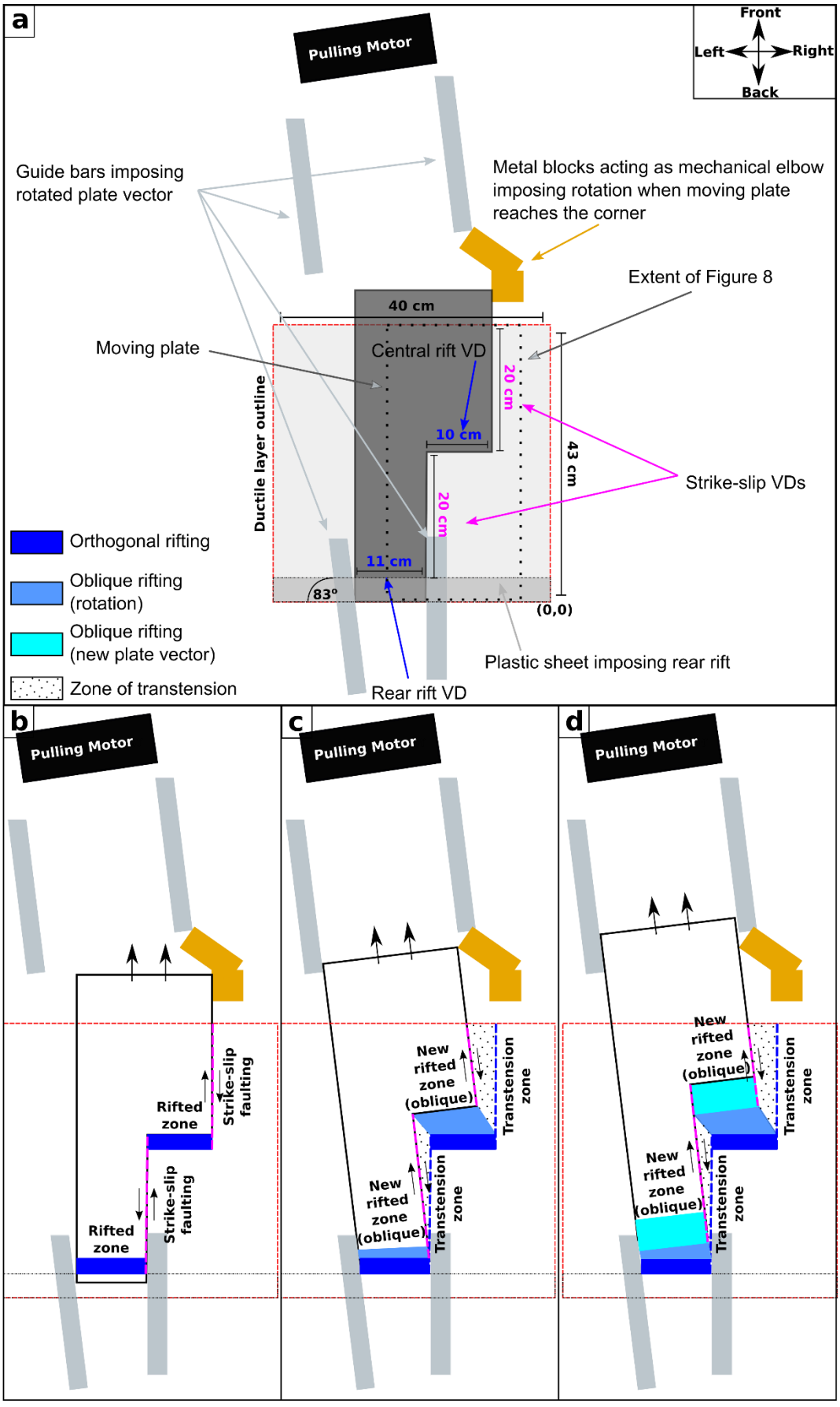

Figure 6.4 – Model apparatus: a) parts, dimensions, and initial configuration of the model apparatus b) orthogonal motion stage, c) end of rotation stage, d) new oblique plate motion vector stage. Red box marks the model boundary, dark gray box marks the moving plate. Yellow boxes represent the mechanical elbow that imposes the rotation. Elongate darker shaded gray area in the back of panel a marks the fixed plastic sheet acting as the second rift.

The model configuration (Figure 6.4) allows us to investigate the effects of transtensional rotation on a pull-apart basin developing between two strike-slip velocity discontinuities (Basile & Brun, 1999). The rotating plate is represented by a 46 x 21 cm plastic plate underneath the silicone putty/feldspar sand layers. The shape of the moving plate (as seen in Figure 6.4a) imposes two right-lateral strike-slip faults connected by a rift segment. At the trailing edge of the plate, a thin plastic sheet is fixed above the moving plate to act as a second velocity discontinuity, imposing another rift (Figure 6.4a). The plate is guided by a series of metal bars at its front and trailing ends. These ensure that a) movement initially remains almost orthogonal and b) rotation at the later stage is not greater than 7o (Figure 6.4a, gray boxes labelled guide bars). Once motion starts, the plate moves almost orthogonally, creating a pull-apart structure between the ends of the two strike-slip faults and a further rift at the back end (Figure 6.4b). A construction of heavy metal blocks, welded firmly on the table top, acts as a mechanical elbow (Figure 6.4a, yellow boxes). When the plate reaches the two boxes, which are placed at an angle, it is forced to rotate until it leaves the top end of the elbow, simultaneously hitting the top left guide bar. The top left guide bar stops any further rotation and ensures the plate has a consistent new vector of motion. (Figure 6.4c). In this rotation stage, the previously formed structures undergo rotation-dominated transtension and oblique rifting (Figure 6.4c). Finally, after rotation has ended, the plate slides between the top guide bars, moving with the new plate motion vector, oblique to the original boundary (Figure 6.4d). The model is extended for a total of 7 cm.

6.3.1.3 Model rheology, materials and scaling

Continental crust in our models is represented as follows (Figure 6.5 and Table 6.1):

a) For the brittle upper crust, we use a 1.6 cm thick layer of dry feldspar sand (deformable according to the Mohr-Coulomb criterion) with a density of ρ = 1.3 g/cm^3 (Sokoutis et al., 2005; Willingshofer et al .,2005; Luth et al., 2010), an internal friction coefficient of μ_{fric} of 0.6 (Willingshofer et al., 2018), and sieved to a grain size d = 100-350 µm. The sand is sieved evenly over the model during the modelling set-up stage.

b) Ductile lower crust is modelled with 0.8 cm thick layer of transparent silicone putty SGM-36, a poly-dimethyl siloxane with a density of ρ = 0.970 g/cm^3, no yield strength and viscosity at room temperature of μ_{vis} = 5*10^4 Pa s (Weijermars, 1986a; Weijermars, 1986b; Weijermars 1986c).

The selection of the model layer materials is based on feldspar (or quartz) sand being the most common material used to represent the upper brittle crust while PDMS silicones are a very good analogue for ductile layers (Reber et al., 2020).

Table 6.1 – Materials and parameters used in the models for scaling to nature. For calculation of parameters refer to main text (Values obtained from a: Persaud et al., 2015; b: Sokoutis et al., 2005; c: Willingshofer et al., 2005; d: Luth et al., 2010; e: Burov, 2011; f: Willingshofer et al., 2018; g: Brace & Kohlstedt, 1980; h: Dombradi et al., 2010; i: Farangitakis et al., 2020; j: Weijermars, 1986a; k: Weijermars, 1986b; l:Weijermars, 1986c; m: Persaud et al., 2017; n: Brune et al., 2016).

Materials	**Parameters (SI units)**	**Model**	**Nature**	**Model/Nature Ratio**
Brittle Upper Crust (K-Feldspar sand)	Thickness (m)	$1.60x10^{-2}$	$2.51x10^{4}$ [a]	$6.4x10^{-7}$ *
	Density (kg/m^3)	$1.30x10^{3}$ [b,c,d]	$2.70x10^{3}$ [e]	0.48
	Internal friction coefficient	0.60 [f]	0.80 [g]	0.80
	Cohesion (Pa)	15 [h]	$2.00x10^{6}$ [i]	$7.50x10^{-6}$
	Strength (Pa)	$2.04x10^{2}$	$5.00x10^{8}$ [e]	$4.00x10^{-7}$
Ductile Lower Crust (silicone polymer)	Thickness (m)	$0.8x10^{-2}$	$1.25x10^{4}$ [a]	$6.4x10^{-7}$ *
	Density (kg/m^3)	$0.97x10^{3}$ [j,k,l]	$2.90x10^{3}$ [e]	0.33

	Viscosity (Pa s)	$5x10^{4}$ [j,k,l]	10^{22} [m]	$5x10^{-18}$
	Strength (Pa)	104	$4.40x10^{7}$ [a]	$2.4x10^{-6}$
General parameters (SI units)				
Extension velocity (m/s)		$2.08x10^{-5}$	$7.3x10^{-10}$ [n]	$2.9x10^{4}$
Strain rate		$2.6x10^{-3}$	$5.9x10^{-14}$	$4.5x10^{10}$
Time (s)		$4.02x10^{3}$	$1.89x10^{14}$ [n]	$2.12x10^{-11}$
Length of pull-apart basin (m)		0.31	$2.00x10^{5}$	$1.60x10^{-6}$
Width of pull-apart basin (m)		0.15	10.00^{5}	$1.50x10^{-6}$
L/W ratio of pull-apart basin		2.1	2.00	1.05
Smoluchowski number		0.94	1.2	0.79
Ramberg number		0.59	0.61	0.95
Reynolds number		$3.38x10^{-8}$	$2.92x10^{-23}$	N/A

*Ratio calculated for the combined thickness of brittle and ductile crust

The governing equations for the layer strength are derived from Brun (2002). In the brittle layers, the strength profile along the strike-slip faults is given by the equation:

$$\sigma 1 - \sigma 3_{(ss)} = \rho_b g z_b \qquad \text{(Equation 6.1)}$$

where $\sigma 1\text{-}\sigma 3_{(ss)}$ is the brittle layer strength along the strike-slip faults, ρ_b is the brittle layer density, g is gravitational acceleration and z_b is thickness of the sand layer (Brun, 2002).

For extension in the brittle layers, the governing equation is:

$$\sigma 1 - \sigma 3_{(r)} = \frac{2}{3}(\sigma 1 - \sigma 3)_{(ss)} \qquad \text{(Equation 6.2)}$$

where $\sigma 1\text{-}\sigma 3_{(r)}$ is the extending brittle layer's strength (Brun, 2002).

For the ductile layer, the strength is:

$$\sigma 1 - \sigma 3_{(d)} = 2\left(\eta \frac{V}{z_d}\right) \quad \text{(Equation 6.3)}$$

where $\sigma 1\text{-}\sigma 3_{(d)}$ is ductile layer strength, η is ductile layer viscosity, V is the velocity of the moving plate and z_d is ductile layer thickness (Brun, 2002).

These equations produce a rheological profile as shown in Figure 6.5. This strength profile is applicable only to the very early stages of deformation in our model, in particular, before significant changes in thickness occur.

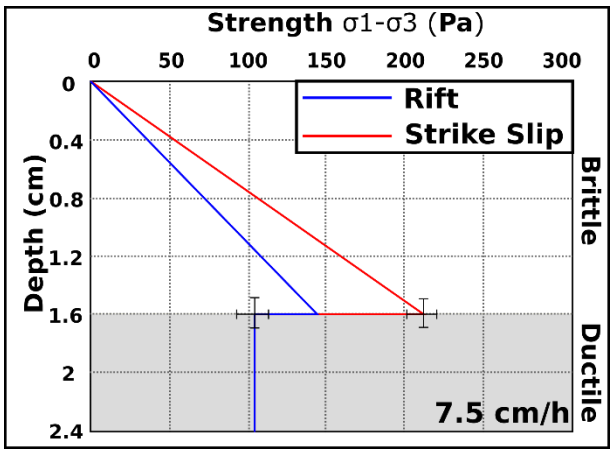

Figure 6.5 – Model strength profile. White background: brittle layer, grey background: ductile layer.

We scale our analogue models to their natural prototype based on the principle of maintaining similarity in the structural geometry, the kinematics and the rheology of the crust (Hubbert, 1937; Ramberg, 1982; Weijermars & Schmeling, 1986; Sokoutis et al., 2000; Sokoutis et al., 2005). For the initial crustal thickness, we used an average value of 37.6 km (Persaud et al., 2007; Persaud et al., 2015). In our model this translates to a model to nature ratio of 6.4×10^{-7}.

We achieve rheologic and dynamic similarity in our models by scaling the gravitational stress, σ (Dombradi et al., 2010):

$$\sigma^{\propto} = \rho^{\propto} g^{\propto} z^{\propto} \quad \text{(Equation 6.4)}$$

Where ρ is density, g is gravitational acceleration, z is thickness and the "$\propto$" symbols denote the model to nature ratio (Sokoutis et al., 2005). For the viscous deformation, the ratio between gravitational and viscous stresses is given by the Ramberg Number (R_m – Weijermars & Schmeling, 1986):

$$R_m = \frac{\rho_d g z_d}{\eta \dot{\varepsilon}} \quad \text{(Equation 6.5)}$$

Where ρ_d is the ductile layer density and $\dot{\varepsilon}$ is the strain rate.

To scale brittle deformation, we used the ratio between gravitational stress and cohesive strength, the Smoluchowski number (Sm – Ramberg, 1981):

$$S_m = \frac{\rho_b g z_b}{\tau_c + \mu_c \rho_b z_b} \quad \text{(Equation 6.6)}$$

Where τ_c is the cohesive strength and μ_c is the internal friction coefficient. For accurate scaling, the individual R_m and S_m values of models and natural prototypes should be as similar as possible (with the ideal value being a ratio of 1:1) (Dombradi et al., 2010). In our model, these ratios are 0.95 and 0.79, respectively (Table 6.1). As previous work suggests, if the Reynolds number (Re) is relatively low, then inertial forces can be neglected compared to viscous ones (Wickham, 2007; Del Ventisette et al., 2007; Dombradi et al., 2010). The Reynolds number is given by the equation:

$$Re = \frac{\rho V l}{\eta} \quad \text{(Equation 6.7)}$$

Where V is the velocity of the moving plate and l is the total extension length. The N. GoC has a relative plate velocity of 23 mm/a from 12-6 Ma and 50 mm/a onwards (Brune et al., 2016), and our model extends at 7.5 cm/hr (Table 6.1). Thus, we can estimate the extension length in both cases, resulting in low Reynolds numbers for model and nature (3.38×10^{-8} and 2.92×10^{-23} respectively). This allows the scaling of different forces to deviate from strict dynamic similarity, so the time and length ratios can be considered independent variables (Ramberg, 1981).

6.3.1.4 Digitising the analogue models

After the model run, the model is wetted with a mixture of water and soap and left overnight for the liquid to permeate through the brittle layer. We then proceed to cut the model in 12 equidistant cross-sections (every 4 cm). These are cut at an angle of 70^{o} to the orthogonal pulling direction, to capture as many of the emergent oblique structures as possible in each cross-section. Before the start of the experiment, graticules are drawn on the modelling surface to act as control points for georeferencing the top-view images taken during the model run and for locating the cross-sections. All of the top-view images are stacked in ArcGIS and georeferenced using these graticule points. A Cartesian coordinate system is assigned with point 0,0 being the bottom right corner of the model (as marked in Figure 6.4a). We then extract the exact coordinates of each cross-section in the form of a polyline feature. Photographs of the cross-sections are processed in Adobe LightroomTM, including lens and distortion corrections. Subsequently, the cross-sections are redrawn as vector graphics and inserted into the seismic interpretation software Schlumberger PetrelTM, where they are projected into 3D space (Figure 6.6a). We then interpret the interface between each different coloured sand layer as a horizon. Using the interpreted horizons, we produce a solid block model from the cross-sections, populating the space between each cross-section by interpolating linearly between the horizon points (Figure 6.6b).

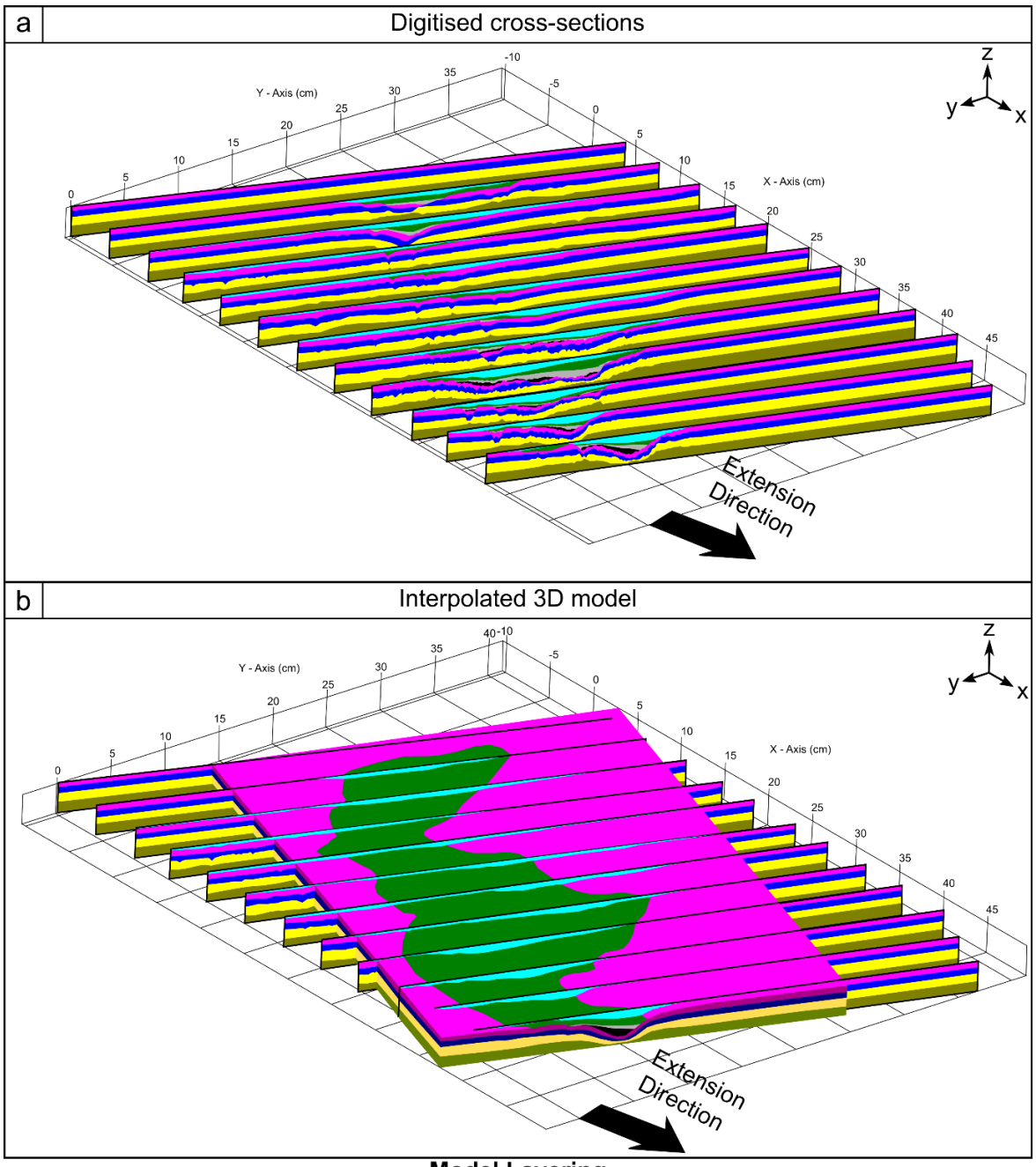

Model Layering

Original Layer Colour	Digitised Layer Colour	Description	Role of Layer
Black	Cyan	Quartz sand	Protective cover (added)
Green	Green	Feldspar sand	Post-rotational sediments (added)
White Black	Gray Black	Feldspar sand	Syn-rotational sediments (added)
Pink Blue Yellow	Pink Blue Yellow	Feldspar sand	Brittle upper crust (original)
Transparent	Brown	Silicone putty	Ductile lower crust (original)

Figure 6.6 – Digitised analogue model: a) Digitised model cross-sections, b) solid block 3D model. Note the changes in colour between the experiment and the digitized model for interpretation

purposes. To better show the geometry of the pull-apart, the lateral extent of the protective layer (cyan colour) is not shown. For an enlarged version of panels a and b, refer to Appendix Figures C1 and C2.

6.3.1.5 Analogue modelling limitations

Firstly, in this work we carry out a single specific experiment designed to replicate the evolution of the Gulf of California. However, it can be applied to other examples around the world with similar structure (as seen in Reber et al., 2020), and we extend our study with a comparison to the Bohai Basin. For a parametric study on the effects of transtension and transpression on strike-slip boundaries with a similar apparatus, we refer readers to Farangitakis et al. (2019). Relative motion between the basal plates varies during the first cm of deformation and deviates from purely orthogonal by approximately 0.5^{o} due to experimental conditions. Nonetheless, this early deformation remains within the range whereby natural examples would still be classified as orthogonal. Secondly, since our models represent only the continental crust, we operate under the assumption that the mantle underneath accommodates a similar plate motion. Finally, our physical analogue model does not include erosion, isostatic compensation or heat transfer between the layers.

6.3.2 Seismic Reflection Data

We use the UL9905 high resolution reflection 2D seismic dataset acquired by LDEO, Caltech, and CICESE (Stock et al., 2005), which is publicly available for download at the URL: http://get.iedadata.org/doi/303736. The data were acquired with a 48 channel, 600 m streamer, at a sampling interval of 1 ms (shot spacing of 12.5 for Lines 2-52 and 25 m for Lines 53-80) and were recorded for 2-3 s. (Stock et al. 2005). The spatial coverage of the data is presented in Figure 7. The seismic interpretation is based on Persaud et al. (2003) and Martin-Barajas et al. (2013) combined with new observations in 3D. For the 3D interpretation, faults were correlated based on their throw across adjacent seismic profiles. The main visible seismic horizons are picked and correlated to their mappable extent by tying observations between seismic cross-sections. Since

there are no publicly available well data, the age correlation between the picked seismic horizons is based on the well-tie constrained interpretations of Martin-Barajas et al. (2013). Finally, the sense of slip on faults is inferred for certain faults (such as the basin sidewall faults) from interpretations from pre-existing literature and after comparison with the analogue models (e.g. for faults that evolve from purely normal to oblique-normal). For the Bohai Basin, we reinterpret seismic data from Qi and Yang (2010) who used original 2D and 3D seismic data provided by the Bohai Oil Company of CNOOC and the Dagang Oil Company.

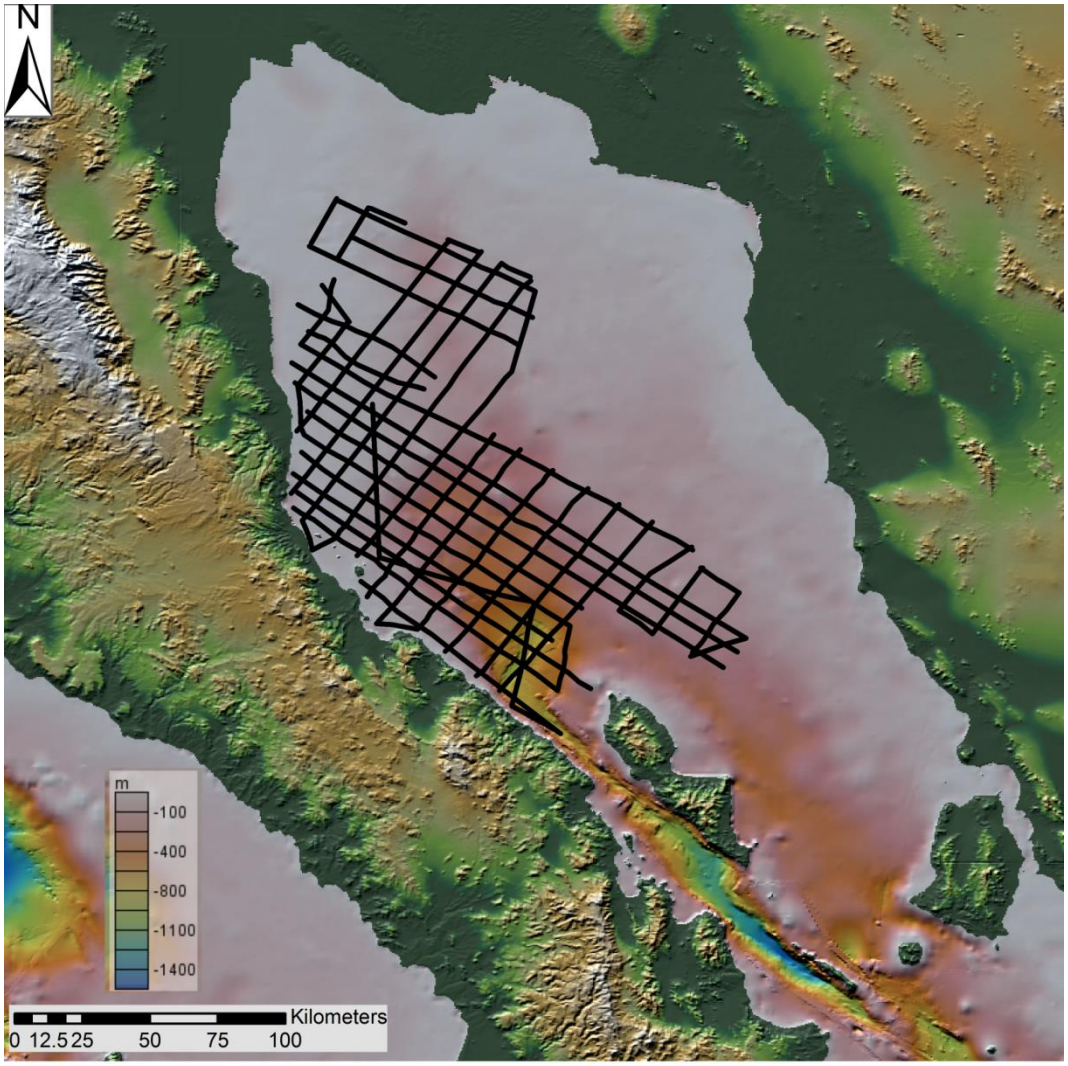

Figure 6.7 – Location of the UL9905 high-resolution reflection seismic dataset (black lines) (Stock et al., 2005). Bathymetry and topography from GMRT Grid Version 3.3 (Ryan et al., 2009).

6.4 Results

We describe the surface fault evolution, timing and kinematics of the model based on our observations of the model top-view photographs and cross-sections. We use the surface scanner-derived topography to identify normal faults and the pink marker lines to identify strike-slip motion (Figure 6.8). If a fault scarp displays both a change in topography and a horizontal displacement of marker lines, it is termed an oblique-normal structure. Note that with respect to Figure 6.4, the model is presented in a 180^{o} rotated manner for better presentation. When "forward motion" or the "front" of the model is inferred, we refer to the bottom of the panels in Figure 6.8 (and top of 6.4), while when the "rear/back" of the model is mentioned, we refer to the top of the panels in Figure 6.8 (and bottom of 6.4).

6.4.1 Orthogonal Stage

After about 0.7 cm of orthogonal motion of the moving plate, the first surface indications of strike-slip deformation on the PDZ appear as dextral displacement of the pink marker lines in a ~10 cm long region of the front end of the moving plate (Figure 6.8e, PDZ-F). The basinal depression begins to form in the middle of the moving plate as a subtle orthogonal depression feature in the surface scanner topography depiction (Figure 6.8i, center)

6.4.2 Rotation Stage

Start of rotation: After about 1.5 cm of movement, the basal plate reaches the mechanical elbow that imposes rotation. At that stage, the PDZ is about 5 cm wide, and is composed of multiple strike-slip segments, while the fixed side of the model displays components of normal displacement. Over the front edge of the moving plate, oblique-normal faults begin to appear at an angle between 15-30^{o} to the plate vector, resembling P shears (Tchalenko, 1970) (Figure 6.8f, PDZ-F). The basinal depression is more pronounced with higher topographic relief (approximately 4-5 mm – Figure 6.8j, center). The first basin sidewall faults start to develop (Figure 6.8f, middle), defining the basinal depression zone, which is 5 cm wide. The second PDZ can be seen through the slight displacement of the pink marker lines (Figure 6.8f, PDZ-B).

End of rotation: After another 2.5 cm of movement (4 cm in total), the PDZ has developed into a triangular-shaped transtensional zone almost 10 cm wide, with the main strike-slip motion migrating with the moving plate boundary. On the fixed side of the experiment, normal faults develop to accommodate the extensional component of transtensional shear (Figure 6.8g, PDZ-F). A series of oblique-normal faults developed along the whole length of the front PDZ in the part of the moving plate. The pull-apart depression is now well developed with elongate basin sidewall faults, which are oriented to accommodate transtensional rotation (Figure 6.8g, centre and Figure 6.8k). The main depression reaches a minimum elevation of about a 1cm below the original horizontal level to the top of the added sediments) and is about 12 cm wide (Figure 6.8k). From the displacement of the pink marker lines along the rear basin sidewall fault, we can infer an oblique-normal faulting character (Figure 6.8g, BSF-B). At the rear end of the plate, the second rift starts to develop as a narrow graben, approximately 2.5 cm wide (Figure 6.8g, top and Figure 6.8k, top – area labelled RR in Figure 6.8l).

6.4.3 Final plate vector stage

At this stage, the moving plate has acquired its final motion vector (Figure 6.8h). After a further 3 cm of motion, the front PDZ is well developed, with pure strike-slip motion occurring over a narrow zone visible in the surface evolution (Figure 6.8h, PDZ-F) and in the topography (Figure 6.8l, bottom). The PDZ at the rear end of the plate is now visible on the surface with two longer and a few shorter strike-slip fault segments (Figure 6.8h, PDZ-B). The basin sidewall faults on the trailing side of the plate are further developed (Figure 6.8h, BSF-B), while on the frontal edge, a new major oblique-normal fault has developed in response to the new motion vector, cross-cutting the previous basin sidewall faults (Figure 6.8h, BSF-F). The angle of this new oblique-normal fault is approximately 50^{o} to the previous normal faults and almost perpendicular to the new motion vector (80^{o}). The second oblique rift at the back end of the plate (Figure 6.8l, RR) is now fully developed with curved oblique-normal faults on its flank. Finally, two strike-slip faults

form oblique to the plate motion and appear to accommodate the rotation of the rear PDZ system (RAF in Figure 6.8h). We term these faults rotation accommodation faults (RAFs).

It is worth noting that while the model extends for 7 cm in the orthogonal sense, factoring in the extension velocity of 7.5 cm/hr and the model runtime (65 minutes), the total extension should amount to 8.4 cm. However, 16% of the total extension is accommodated through the rotational motion through oblique-normal faulting. Scaling to the natural example would result in approximately 115 km of orthogonal extension and 138 km of total extension.

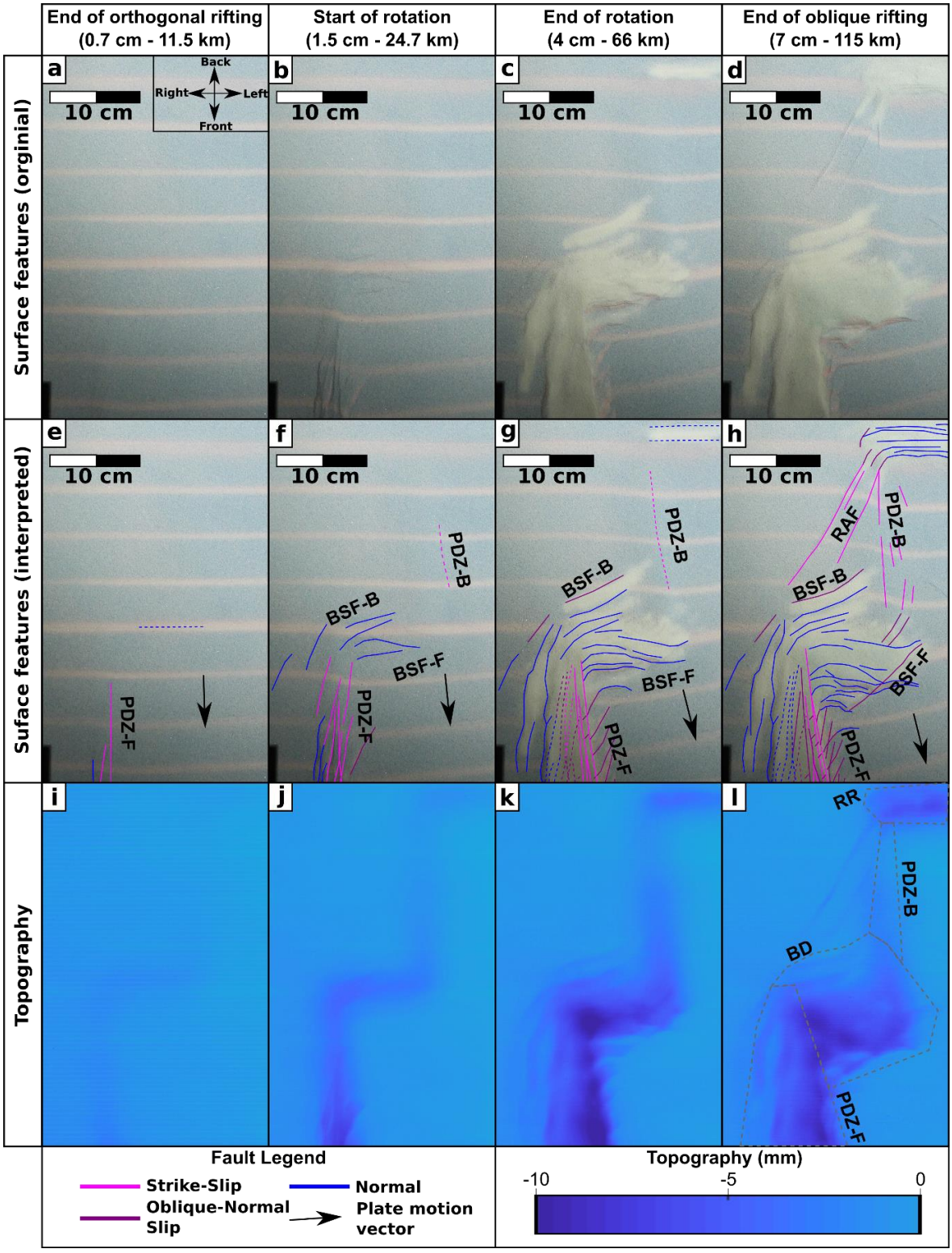

Figure 6.8 – Analogue modelling experiment results. (a–d) Surface feature development. (e–h) Surface feature development (interpreted), showing the development of normal, oblique and strike-slip faulting. (i-l) Topography evolution. PDZ-F/B: Principal Displacement Zone (Front/Back), BSF-F/B: Basin Sidewall Fault (Front/Back), RAF: Rotation Accommodation Fault, BD: Basinal

Depression, RR: Rear Rift. The terms Front/Back are defined in panel a. The PDZs and MBA are outlined in panel l of this Figure. For larger versions of the panels, refer to Appendix Figures C3-C14.

6.5 Discussion

6.5.1 Comparison with the N. Gulf of California pull-apart

We compare faulting and sedimentation patterns from the high resolution UL9905 seismic dataset (Stock et al., 2005) in the N. GoC to those in our model. The N. GoC is thought to have undergone a change in the relative plate motion vector 8 Ma (Atwater and Stock, 1998) and a plate boundary jump around 3 Ma (Lonsdale, 1989), giving it its current morphology. This plate boundary jump resulted in the abandonment of the basins in the eastern N. GoC. In our model, we can replicate the rotation that led to the formation of the pull-apart basin, but not the plate boundary jump. Therefore, we focus our observations on the effects the rotation has had on the broader N. GoC structure and, by comparison with our model, infer that the rotation set the initial structural framework for the current GoC. For the seismic interpretation of stratigraphic horizons, we interpreted the most prominent reflectors that were cross-correlatable across the 2D seismic line network and determined their relative age using work that infers ages of seismic stratigraphy in the region (Martin-Barajas et al., 2013)

6.5.1.1 Fault evolution

We observe similar first-order evolution patterns between our experiment and the Northern Gulf of California both in map and 3D view (Figure 6.9).

Examining the structures in map view, we observe that in both our experiment and in the N. GoC, the basins are bounded by oblique-normal slip faults (labelled as BSFs in Figure 6.9). In the north of the Gulf, these are the faults branching at a 60-90^{o} angle from the northern end of the Ballenas Transform Fault Zone (Figure 6.9a,c), which we interpret as horsetail splays of the transform zone. We consider these fault splays and the faults that define the Consag Basin (Persaud et al., 2003;

Gonzalez-Escobar et al., 2010) in the north (labelled BSF in Figures 6.9a,c) to be the most likely basin sidewall faults. In the analogue model, an oblique-normal slip fault bounding the rear of the pull-apart depression has developed at the trailing end of the plate (Figures 6.9b,d BSF-B). This fault begins approximately above the rift-transform intersection point of the starting model (RTI in Figure 6.9d).

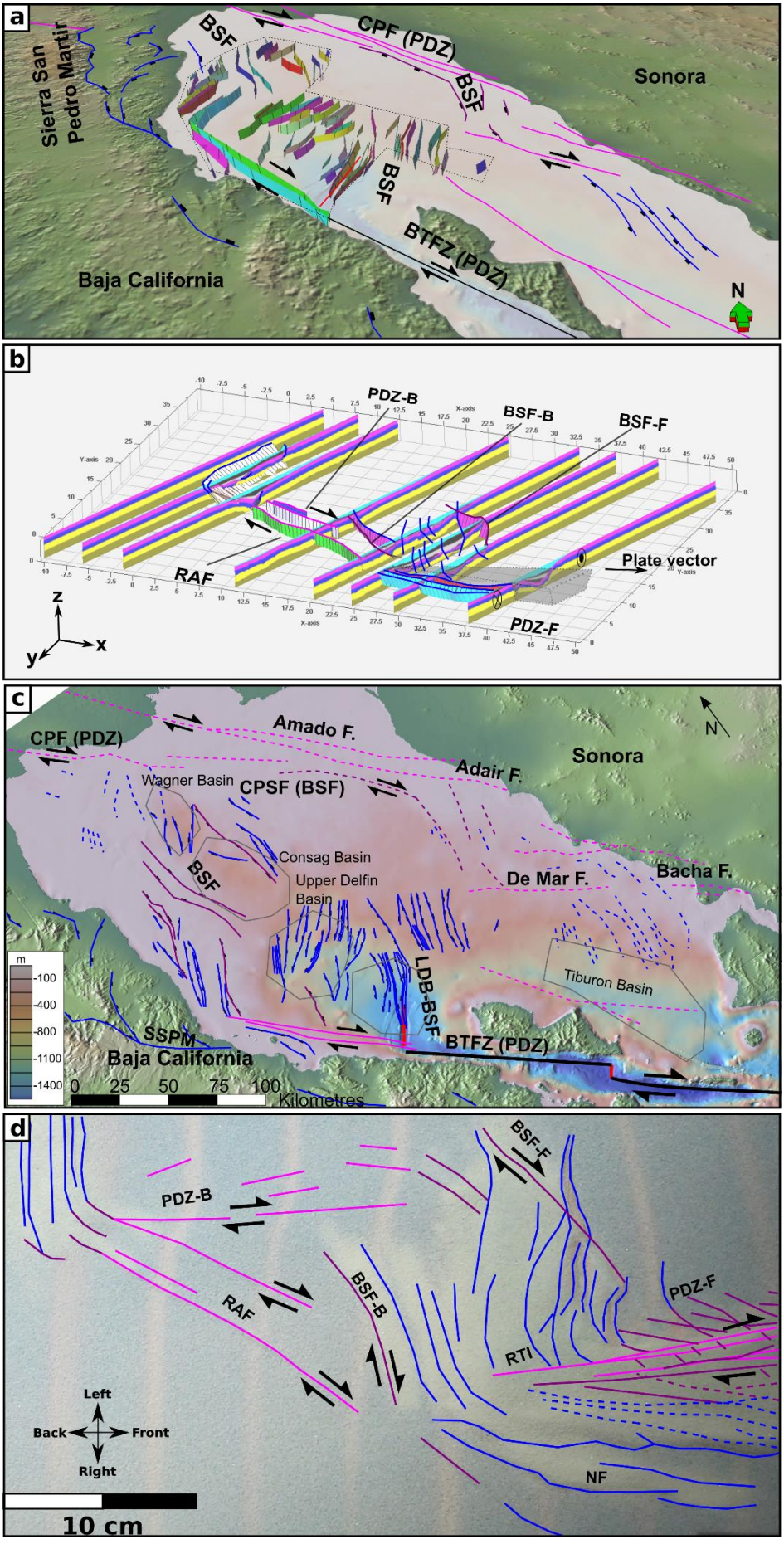

Legend

- Strike-Slip Fault
- Normal Fault
- Oblique-Normal Slip Fault
- Transform boundary
- Spreading Centre
- Transtensional PDZ

Abbreviations

CPF
Cerro Prieto Transform Fault

CPSF
Cerro Prieto Sur Fault

BTFZ
Ballenas Transform Fault Zone

SSPM
Sierra San Pedro Martir Fault

LDB-BSF
Lower Delfin Basin Basin Sidewall Fault

PDZ
Principal Displacement Zone

BSF
Basin Sidewall Fault

RAF
Rotation Accomodation Fault

Figure 6.9 – Comparison between our model and faulting patterns in the N. Gulf of California. a: 3D depiction of main faults interpreted in this work from the UL9905 seismic dataset (Stock et al., 2005). Linear features correspond to main structural elements added from Bennet et al. (2013) and Martín-Barajas et al. (2013). Vertical exaggeration of the 3D projection of the fault planes is 3:1. b: 3D depiction of the main faults in our digitized analogue model. Linear features correspond to faults which cannot be correlated across multiple cross-sections, but their presence is inferred from the model surface evolution. c: Surface fault patterns in the N. GoC (faults in continuous lines from this work and Persaud et al. 2003, faults in dashed lines from Martin-Barajas et al., 2013, basins outlined in grey). d: Surface fault patterns in our model. Topography and bathymetry from GMRT Grid Version 3.3 (Ryan et al., 2009). In panels a & b, the fault plane colours are randomly generated by the interpretation software. For larger versions of the panels, refer to Appendix Figures C15-C16

In the southern part of the N. GoC pull-apart structure, it appears that the role of the basin sidewall faults is played by two main faults: a) where continental break-up is active, the basin sidewall fault is primarily defined by a long normal fault, trending parallel to the Lower Delfin Basin rift, (LDB-BSF in Figure 6.9c); and b) in the east of the basin by the Cerro Prieto Sur (CPSF in Figure 6.9c), Amado and Adair Faults, which display both strike-slip and normal character (e.g. Martin-Barajas et al., 2013; Gonzalez Escobar et al., 2014). Similarly, in our model, a long oblique-normal slip fault defines the uppermost boundary of the pull-apart (along with two smaller structures towards the rear of the moving plate).

We also find a high degree of similarity between the transtensional PDZs in our model and the N. GoC. We exclude the southeastern part of the Ballenas Transform Fault Zone that mainly corresponds to a transform fault (south of the intersection with the Lower Delfin Basin), as we cannot replicate the creation of transform faults in our model. However, the part of the Ballenas Transform Fault Zone within the pull-apart structure displays very similar characteristics to the transtensional PDZs in our models. The main characteristic is the existence of normal faults that

have accommodated rotation in their lifespan, such as the onshore Sierra San Pedro Martir normal faults in Baja California (SSPM in Figures 6.9b,d) (Bennett et al., 2013). Similarly, in the front PDZ in our model (PDZ-F), a series of normal faults (labelled NF in Figure 6.9d) develops on the fixed part of the plate to accommodate the component of rotation.

Equally, in the rear parts of our model, we observe that transtensional deformation is bounded by a principal displacement zone containing a number of shorter and longer strike-slip faults (PDZ-B in Figure 6.9d), accompanied by faults that accommodate rotation. This agrees with observations in the northwestern part of the Cerro Prieto Fault in the Salton trough (northwest of Figures 6.9a,c), which is accompanied by other, smaller faults with a horizontal component (Gonzalez-Escobar et al., 2020).

The rotation accommodation faults (RAFs in Figures 6.9b,d) in our model would most likely correspond to the faults that bound the Consag Basin (purple faults labelled BSFs in Figure 6.9c), since there is evidence of lateral offset in the area and their orientation also matches that of the model (Gonzalez-Escobar et al., 2010). Furthermore, part of the dextral rotation can also be accounted for by the onshore strike-slip and oblique normal faults in Sierra San Pedro Martir (SSPM on Figures 6.9a,c) on the Baja California Peninsula (e.g. Goff et al., 1987; Humphreys & Weldon, 1991; Bennett et al., 1996) and Sonora Areas (Darin et al., 2016).

6.5.1.2 Basin morphology and sedimentation patterns

We compare the depth to the acoustic basement in the N. GoC (Figure 6.10a – modified from Gonzalez-Escobar et al., 2014) to the depth to the top of our 3D model's pre-rift stratigraphy (Figure 6.10b). Both of these surfaces represent strata present before extension and rotation and thus provide good reference horizons to track the evolution of deformation. In both cases, we observe a skewed triangular depression, with the widest part between the frontal PDZ and the top BSF. This in the N. GoC would correspond to a depression delineated between the Ballenas

Transform Fault Zone and the Cerro Prieto Sur Fault (Figure 6.10a) and in our model between the frontal PDZ and basin sidewall fault (PDZ-F and BSF-F (Figure 6.10b). This depression narrows and shallows towards the rear rift situated at the end of the rear PDZ. The rear rift in N. GoC would be represented by the Salton Trough in the NW of the pull-apart structure (outside of the map of Figure 6.10a). This narrower part occurs between the rear PDZ (CPF in the N. GoC and PDZ-B in our model in Figure 6.8a,b) and the rotation accommodation fault and rear basin sidewall faults (BSF in the N. GoC and BSF/RAF in our model in Figure 6.8a,b). In the case of the N. GoC, this corresponds to the Cerro Prieto Fault and the faults bounding the Consag and Wagner Basins (CPF/BSF in Figure 6.10a) and, in our model, to between the rear PDZ and basin sidewall/rotation accommodation faults (PDZ-B and BSF/RAF in Figure 6.10b). The deepest part of the depression lies close to the RTI in both cases (dark blue colour in Figure 6.10a,b). It is worth noting that the active PDZ during the rotation in the N. GoC was situated along the Tiburon Fault and Tiburon Basin (labelled TB in Figure 6.10a). Following a plate-jump at 3 Ma, the principal displacement zone migrated to its current location (Seiler et al., 2009). However even if we disregard the area containing the Upper and Lower Delfin Basins (UDB/LDB in Figure 6.10a) on the assumption that they did not participate in extension until after the plate jump, there is still a great degree of similarity with the model.

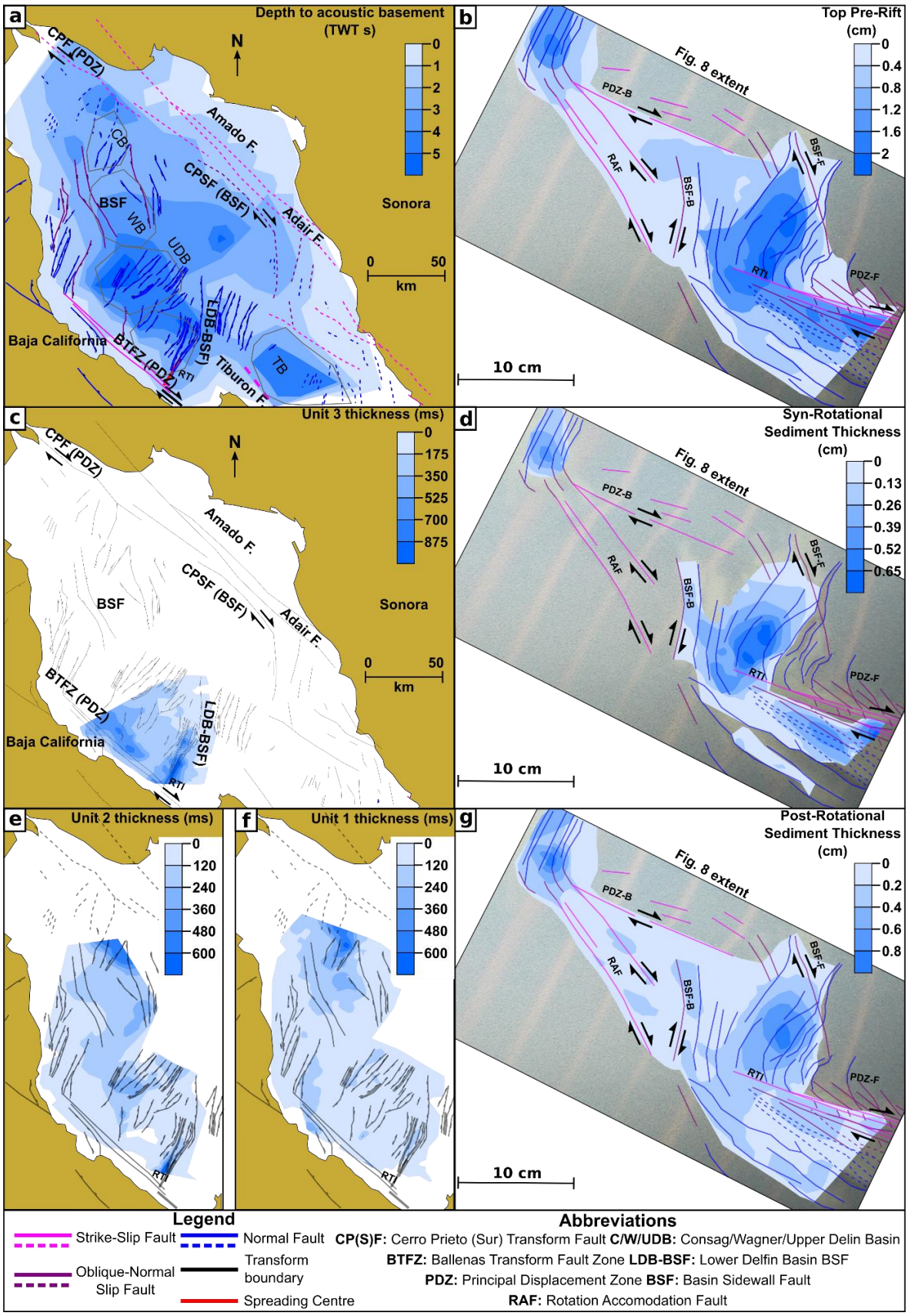
a
Depth to acoustic basement (TWT s)
N
0
1
2
3
4
5
CPF (PDZ)
Amado F.
CB
CPSF (BSF)
Adair F.
BSF
WB
UDB
Sonora
0
50
km
LDB-BSF
Baja California
BTFZ (PDZ)
RTI
Tiburon F.
TB
b
Top Pre-Rift (cm)
0
0.4
0.8
1.2
1.6
2
Fig. 8 extent
PDZ-B
RAF
BSF-B
BSF-F
RTI
PDZ-F
10 cm
c
Unit 3 thickness (ms)
0
175
350
525
700
875
N
CPF (PDZ)
Amado F.
CPSF (BSF)
Adair F.
BSF
Sonora
0
50
km
BTFZ (PDZ)
LDB-BSF
Baja California
RTI
d
Syn-Rotational Sediment Thickness (cm)
0
0.13
0.26
0.39
0.52
0.65
Fig. 8 extent
PDZ-B
RAF
BSF-B
BSF-F
RTI
PDZ-F
10 cm
e
Unit 2 thickness (ms)
0
120
240
360
480
600
RTI
f
Unit 1 thickness (ms)
0
120
240
360
480
600
RTI
g
Post-Rotational Sediment Thickness (cm)
0
0.2
0.4
0.6
0.8
Fig. 8 extent
PDZ-B
RAF
BSF-B
BSF-F
RTI
PDZ-F
10 cm
Legend
Strike-Slip Fault
Normal Fault
Oblique-Normal Slip Fault
Transform boundary
Spreading Centre
Abbreviations
CP(S)F: Cerro Prieto (Sur) Transform Fault C/W/UDB: Consag/Wagner/Upper Delin Basin
BTFZ: Ballenas Transform Fault Zone LDB-BSF: Lower Delfin Basin BSF
PDZ: Principal Displacement Zone BSF: Basin Sidewall Fault
RAF: Rotation Accomodation Fault

Figure 6.10 – Comparison between our model and the morphology and sedimentation patterns in the N. Gulf of California. a: Map of depth to N. Gulf of California basement (in seconds TWT, redrawn from Gonzalez-Escobar et al., 2014). Basin outlines are shown in gray. b: Map of depth to the top of the pre-rift model stratigraphy (in cm). c: N. GoC Unit 3 thickness (in ms TWT). d: Model syn-rotational sedimentary layer thickness (in cm). e,f: Units 2,1 thickness (in ms TWT). g: Model post-rotational sedimentary layer thickness (in cm). Faults and annotations are grayed out in panels c, e and f for clearer image view. Added sediment thickness is compared qualitatively, not quantitatively, as it is manually added to monitor depocentre focus and general sedimentation patterns.

In Figure 6.10c, we show the distribution of one of the older units in the basin, the Late Miocene-Early Pliocene-aged Unit 3 (ages derived from Martin-Barajas et al., 2013), deposited near the end of the plate rotation documented in Bennet and Oskin (2014) between 12.5-6.5 Ma and the plate re-organisation occurring at 3 Ma (Lonsdale, 1989; Seiler et al., 2009). We observe that this unit has two main depocentres: one along the BTFZ-PDZ (Figure 6.10c) and one over the Lower Delfin Basin-basin sidewall fault rift. In both cases, sediment thickness is quite significant, in places >700 milliseconds of sediment (potentially more than 500 m). Comparing the distribution of Unit 3 to the first two syn-rift sediment units in our model (Black and Gray in Figure 6.6), we observe that deposition is focused in two loci: a) above the RTI and the two large faults next to the frontal basin sidewall fault (Figure 6.10d) which represent the basin sidewall fault during rotation and b) within the transtensional frontal PDZ. As observed in the topography map in Figure 6.8k, there is no significant depression over the area where the rotation accommodation faults are located, so sedimentation terminates at the rear basin sidewall fault boundary. The main depocentre is thus located closer to the main basinal depression's centre, following the trajectory of the RTI as rotation occurs.

It is important to note, however, that our observations on Unit 3 are limited by its mappable extent in the seismic dataset, due to resolution loss and the presence of volcanics that make

cross-correlation of the seismic horizon across the intersecting seismic cross-sections difficult. However, we would expect the unmapped parts of Unit 3 to also behave in a similar way as the sediments in our model, since it is concurrent with the rotation in the N. GoC. Furthermore, given that the current basin configuration of the N. GoC resulted from the plate jump 3 Ma ago (Lonsdale, 1989; Seiler et al., 2009), this jump should not affect the thickness (or even presence) of these sediments in the younger basins in the Northern Gulf. The same sedimentation pattern applies to our model, where at the back there is an absence of sedimentation. Even when a plate jump is considered, Mar Hernandez et al. (2012) showed that the focus of sedimentation followed a similar pattern when the RTI migrated from the Tiburon to the Lower Delfin Basin.

Finally, we compare the sedimentation patterns across the N. GoC and our model. In the youngest two sediment layers in the N. GoC (units 2 and 1 in Figure 6.10e,f), as observed in this and previous work (Persaud et al., 2003, Martin-Barajas et al., 2013), the main depocentres follow the current sub-basin morphology. We regard these units as post-rotational, as they represent the youngest sequences in the basin, dated as Pleistocene (Martin-Barajas et al., 2013), and hence later than any plate re-organisation within the N. Gulf (Lonsdale, 1989). Unit 2 thickens between the BSF in the Wagner and Consag basins, but reaches its greatest thickness in the area adjacent to the active spreading centre in the Lower Delfin Basin basin sidewall fault, where the RTI is located (Figure 6.10e). Unit 1 (the top-most in the region) appears to be thickest in the Wagner and Consag basin area (Figure 6.10f). It is worth noting that in both cases no significant thickening occurs along the transform boundary of the Ballenas Transform Fault Zone (Figure 6.10e,f). We compare these two units to our model's top-most depositional layer (Green unit in Figure 6.6), which was added after rotation had finished. In our model, the highest sedimentation rate again is focused near the RTI (Figure 6.10g), with minor patches of thicker sediment over the rotation accommodation fault, rear PDZ and basin sidewall fault (Figure 6.10g, also seen in the topographic map in Figure 6.8l). These are areas with continuous accommodation space, as they progressively deepen once the final plate vector is established. In nature, in the later stages of the Gulf's

evolution younger basins represented more depositional space, so sediment was draped over a larger area of the basin.

Examining the differences between our model and the N. GoC, we note that our model does not replicate the plate jump at ca. 3 Ma (Lonsdale, 1989) that migrated the plate boundary in the N. GoC from the Tiburon Fault to the BTFZ. Therefore, our model does not replicate the formation of the Gulf's younger basins. Thus, sediment distribution and depocentre migration do not follow a direct one-to-one correlation. However, there is strong evidence that the rotation established the general structural framework of the N. GoC, affecting the major structures in the area (such as the PDZ and basin sidewall faults in the east of the Gulf). If we could replicate the plate jump in our model by migrating the plate boundary towards the fixed side of the model (as seen in Figure 6.9d) then we would expect that the structure on the moving side of the model (as seen in Figure 6.9d) and any further topographic depression (representing newer basins) would occur in the fixed side as is the case in the N. GoC. Varying the rate or amount of rotation that is applied in the model or using an apparatus that would replicate the change in motion along both plates would potentially allow for an even more accurate representation of features visible in the N. GoC and a further exploration of this parameter space. Furthermore, our model does not account for the presence of magmatism such as sills and volcanic knolls in the area (Persaud et al., 2003), nor does it explore the possibility of incipient oceanic crust in the Lower Delfin Basin or Ballenas Transform Fault Zone (Persaud et al., 2003). However, the similarity between the evolution of fault and basin architecture in our model and the Gulf of California is such that we can infer that the change in relative plate motion occurring around 8 Ma (Atwater & Stock, 1998) set the initial framework for the structure of the current Northern Gulf of California.

6.5.2 Comparison with the Bohai Basin in northern China

In addition to the N. GoC, our model can be compared to other transtensional basins, such as the development of the Bohai Basin in northern China.

Our model is not designed or scaled specifically to replicate the full evolution of the Bohai Basin. The basement to the Bohai Basin is thought to have a pre-existing fabric inherited from Mesozoic sinistral transpression and earlier deformation (Allen et al., 1997), while our model starts with no preexisting structural fabric (bar the velocity discontinuity created by the moving plates). Furthermore, the Bohai Basin is a basin about 1000 km long and 600 km wide, while our model would scale to a pull-apart approximately 200 km long and 100 km wide. However, both the Bohai Basin and our model are transtensional basins that build on pull-apart geometries with similar length to width ratios. These first-order similarities enable us to extend the applicability of our model to this basin by (invoking similarity scaling as seen in Reber et al., 2020).

We first compare our model's top pre-rift map to the Cenozoic sediment thickness in the Bohai Basin. In both, a main depocentre exists near the PDZ-BSF intersection. In the Bohai Basin, this is the Bozhong Depression (BZHD in Figure 6.11a), where sedimentation has been focused since the Eocene. In our model, the main depocentre is located at the end of the triangular transtensional PDZ (darker blue parts of the main pull-apart depression in Figure 6.11b).

In the Bohai Basin, Allen et al. (1997) observed a number of faults in an oblique orientation with respect to the main NE-SW structural fabric, indicating dextral transtension (Figure 6.11a). Qi & Yang (2010) also describe the existence of transfer zones following this oblique pattern as evidence for the same transtensional movement (Figure 6.11a, purple faults). We find that, in our model, faults created in the later stages of rotation and after rotation is finished follow the same pattern (Figure 6.11b, faults labelled as BSF-B and BSF-F).

The northeastern end of the Bohai Bazin PDZ, the Liaodongwan Depression, is a 500 km long, 100 km wide transtensional PDZ with well-developed elongate basins up to 10 km deep (Figure 6.11a,

labelled LDW Depression, and 6.11c). Similarly, in our model, some of the largest depositional thicknesses (bar the main pull-apart depression) can be observed at the advancing front of the frontal PDZ (darkest blue colour in PDZ-F in Figure 6.11b). These elongate transtensional basins are segmented by normal and oblique-normal faults, as can be seen both in map (Figure 6.11a, b) and cross-section view (Figure 6.11c, d, e). This is consistent with the observations indicating that, in transtensional PDZs, lateral slip is accommodated in broad deformation zones where the main strike-slip fault zone co-exists with oblique-normal faults at lower than 30^{o} angles that take up part of the motion (Farangitakis et al., 2019). This is particularly clear in the cross-section view of the main PDZ of the Bohai Basin (pink and purple faults in Figure 6.11c). These characteristic sets of oblique-normal slip faults usually form prior to the change in rotation aspure strike-slip faults and then later evolve to a more normal (or even exclusively normal) slip character as the PDZ develops its extensional character and migrates in space (Farangitakis et al. 2019). It is worth noting that in the Liaodongwan Depression PDZ (Qi & Yang, 2010) localised compression has been observed along the strike-slip faults (Figure 6.11c). This deformation is distinct in timing and extent from the regional late Cenozoic basin inversion in the greater Bohai Basin area (Allen et al., 1997). In our model, a small degree of compression is also observed along the strike-slip segments of the PDZ (observed in small thickness increases on the footwalls of oblique-normal faults in layers next to the PDZ, Figure 6.11e, next to the left hand side strike-slip zone) even when transtension occurs, which is consistent with the anticlines next to the active strike-slip faults observed in the Bohai Basin (Figure 6.11c, From Qi & Yang, 2010, above the main strike-slip zone).

These observations show first-order similarity between the architecture of our model and the Bohai Basin, including the sedimentation patterns, transtensional PDZs and fault patterns. This indicates that, in addition to a later basin inversion (Qi & Yang, 2010), a rotation of extension direction has taken place during the evolution of the Bohai Basin. This transtensional event could be attributed to the NW-SE to E-W change of the convergence vector between the Pacific and

Asia plates between the late Mesozoic and Early Tertiary (Engebretson et al., 1985; Liang et al., 2016).

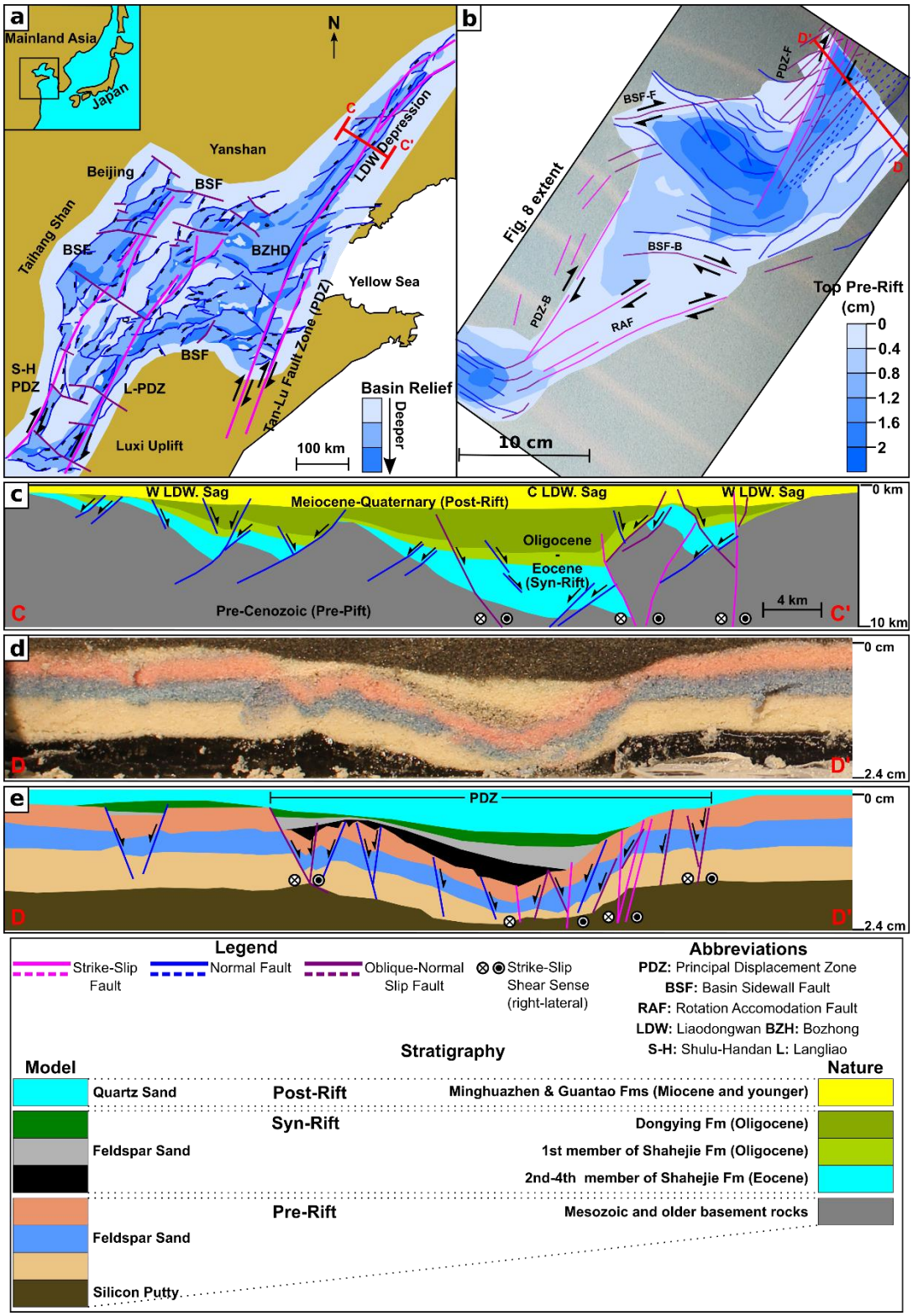

Figure 6.11 – Comparison between our model and the structure of the Bohai Basin in China. a: Map of the structure and depth to Mesozoic basement in the Bohai Basin (modified from Allen et

al., 1997 and Qi & Yang, 2010). b: Map of depth to the top of the pre-rift model stratigraphy (in cm). c: Seismic cross-section across the Liaodongwan depression in the Bohai Basin NE PDZ (location shown in panel a, re-interpreted from Allen et al., 1998 and Qi & Yang, 2010). d,e: Uninterpreted and interpreted cross-section across our model's front PDZ (location shown in panel b).

6.5.3 Further Discussion

As Wu et al. (2009) note, the main difference between pure strike-slip (such as the Dead Sea basin) and transtensional pull-apart basins (such as the Gulf of Elat) is the co-existence of extension inside the PDZ and the presence of more than one depocentre in the transtensional case. Our model starts as a pure strike-slip pull-apart, proceeds into rotation and then, with a new plate motion vector, develops as a transtensional system. Basins with this multiphase development show distinct structural characteristics compared with pull-apart basins that were consistently either pure strike-slip or transtensional from the onset. The main distinguishing features from the two end-members are the migrating depocentres due to rotation (Figures 6.8 & 6.10), the Rotation Accommodation Faults (Figure 6.8) and the oblique-slip character of the BSFs that occur during the rotation (Figure 6.8). These features can be used as diagnostic tools for the identification of other natural examples where pull-apart basins have experienced multi-phase evolution. A possible further example could be the Cinarcik Basin in the Sea of Marmara, where the rotating Anatolia microplate vector has led to curvature of the North Anatolian Fault, creating transtensional pull-apart basins (Sugan et al., 2014).

6.6 Conclusions

We present a physical analogue model designed to simulate the effect of transtensional deformation imposed on pull-apart basins due to a change in plate motion vectors. Our model produces structural and depositional patterns that are in very good agreement with natural examples and enhance our understanding of fault geometry and development in pull-apart basins with a multiphase transtensional evolution across the world.

Our model was designed to study the setting of the northern Gulf of California and successfully reproduces the principal features of its transtensional evolution. Both the N. Gulf of California and our model develop an asymmetrical triangular pull-apart basin, bounded by strike-slip faults on either side. Both also show similar patterns of sedimentation, with pre-rotational sediments focused within the pull-apart basin's main structural elements, whilst the post-rotation sediments have a broader spatial extent, and are thickest over the younger extensional features.

Additionally, we find substantial first-order similarity between our model and the Bohai Basin in northern China, despite our model not being designed to replicate that basin's opening history or scale. In both model and nature, we observe faults oblique to the main basin trend and depocentres along the transtensional PDZ controlled by series of oblique-normal faults. These similarities support the interpretation of the Bohai Basin as a multiphase transtensional pull-apart basin, and suggest that a rotation in extension direction could have taken place during the late Mesozoic or early Tertiary, resulting in its current transtensional architecture.

Our observations indicate that the combination of features such as asymmetrical triangular pull-apart basins, migrating depocentres, wide principal displacement zones with oblique faulting and normal faults with an oblique component can be a strong indication that a pull-apart basin has undergone a transtensional rotation change due to a change in the plate motion vector along the strike-slip zones that define it.

7 Discussion, future work and conclusions

The discussion and conclusions of this thesis are presented in a similar way as the result chapters. First, a summarized discussion of the comparison between natural examples and the models presented in this work is presented. Then, a discussion on the methodology follows, firstly by re-iterating some of the limitations of this study and then highlighting the value of following a cross-scale multi-disciplinary approach in transform boundary evolution by demonstrating how each methodology compliments each other. Finally, a discussion on the wider implications of transform margin and fault evolution during plate motion changes is presented. This discussion is followed by a series of potential future studies that could be done building upon the work presented in this thesis and some concluding remarks.

7.1 Discussion

7.1.1 Model correlation with natural examples

Throughout the result chapters of this thesis, comparisons are made with five natural examples across the world. The range of comparisons enhances the value of the observations in this work, as most modelling studies display comparisons to one or two natural examples (e.g. Le Pourhiet et al., 2017). The Gulf of California region is discussed in all of the findings of this work and thus is listed first, followed by the rest of the natural prototypes listed in the order that they are presented in the result chapters.

7.1.1.1 Northern Gulf of California

The Gulf of California partitioned oblique margin consists of seven en-echelon transform-spreading ridge systems, each one with a different structural style (Lizarralde et al., 2007). The Northern Gulf of California's initial structural framework is thought to have occurred due to a rotation in the plate motion vector around 12.5-6.5 Ma (Atwater & Stock, 1998; Bennett & Oskin, 2014), leading to the transtensional opening of the Gulf from south to north (Umhoefer et al.,

2018). Later at 3 Ma, a plate jump resulted in the current active basin formation in the Gulf (Lonsdale, 1989).

Due to modelling limitations, the plate jump at 3 Ma in the area cannot be modelled. This is because it would require the model to be paused and a new plate boundary to be introduced, which is not possible with the modelling apparatus used. However, the experiments show that in both the rift-transform intersection (Chapter 5) and the pull-apart basin (Chapter 6) scenarios, a rotation in the extension direction occurring 12.5-6.5 Ma is enough to set the initial structural framework for the area to develop in a similar way to the experiments, creating the basin-bounding faults and various depocentres in the N. GoC. In both scenarios, the modelled faulting patterns correlate well with the actual faulting patterns in the Northern Gulf of California. In particular:

a) The induced plate rotation in the model generates transtensional Principal Displacement Zones (PDZs) characterised by strike-slip faults that progressively acquire an oblique to normal character (Figures 5.5i,k and 6.7f,h,i). Similar patterns are observed bounding the Gulf's pull-apart structure: the Ballenas Transform Fault Zone and the Cerro Prieto Fault (Figure 6.8) (Persaud et al., 2003; Gonzalez-Escobar et al., 2020). This similarity is also demonstrated in seismic cross-sections from the area (Figure 5.7).
b) Oblique-normal characters are noted between the horsetail splays and basin sidewall faults in the analogue models (Figure 5.7a and Figure 6.8). Equivalent faults in the N. GoC are the Wagner and Consag oblique slip boundary faults in the northwest (Persaud et al., 2003; Gonzalez-Escobar et al., 2010) and the Cerro Prieto Sur, Amado and Adair Faults in the southeast, which display both strike-slip and normal characters (e.g. Martin-Barajas et al., 2013; Gonzalez Escobar et al., 2014).
c) In the pull-apart basin experiment (Ch 6), rotation is also accommodated by faults that lie outside the main basin depression (Figure 6.8), such as the onshore faults in the N. GoC

both in the Baja California Peninsula (e.g. Goff et al., 1987; Humphreys & Weldon, 1991; Bennett et al., 1996) and Sonora Areas (Darin et al., 2016).

From both the numerical modelling and analogue modelling experiments, it appears that in a transtensional setting, the localisation of rifting/spreading occurs near to the RTI (Figure 4.8d,e, Figure 5.5s and Figure 6.10b). The N. GoC has evolved in a similar way: pre 3 Ma ,extension was localised at the intersection between the (now inactive due to the plate jump) Tiburon Basin rift and Tiburon transform fault (Figure 6.10a), while currently the highest rates of extension can be found in the intersection between the Lower Delfin Basin spreading centre and the Ballenas Transform Fault (Figure 6.10a) (Persaud et al., 2003; Martin-Barajas et al., 2013).

In all three of the models of the Gulf of California there is a high degree of correlation. The control on the structural framework of the Gulf of California appears to be the change from extension to transtension, leading to successive pull-apart opening from south to north (Umhoefer et al., 2018). Similarly, the general models presented in Chapter 4 indicate that even a small change in plate motion significantly affects the evolution of a rift-transform intersection by introducing transtension in the style of opening of the transform margin (Figure 4.8c,b). Investigating the same transtensional case of rotation at a smaller scale in the Northern Gulf of California (Ch 6), the same high degree of similarity in structural styles and sedimentation patterns between model and nature is observed. Although there is no direct one-to-one correlation since the plate jump cannot be replicated in analogue models, the findings from the models suggest that the main driving force behind the particular rift-transform intersection and pull-apart basins is the change in plate motion that shaped the greater Gulf area and provided the structural framework for the Northern Gulf's current morphology.

7.1.1.2 Ungava Transform Zone, Davis Strait

The Ungava Transform Zone is a large, right-stepping transform zone that accommodated horizontal motion between (now extinct) oblique spreading ridges in Baffin Bay in the north and Labrador Sea in the south (Oakey & Chalmers, 2012). The wider area has also undergone a 30°

clockwise change in its spreading direction due to changes in plate motion between Greenland and Canada around 35 Ma (Dore et al., 2016), resulting in widespread transpression and transtension.

This area is compared to one of the transpressional lithosphere-scale numerical models of Chapter 4 with a similar angle of rotation (Figures 4.7k-o, Figure 4.8a). In the area, once the plate motion vector changed, the juxtaposed continental crust was forced into transpression, resulting in a zone of transpression onshore W. Greenland evidenced in field mapping (Wilson et al., 2006; Peace et al., 2017) and inversion structures offshore visible in seismic data (Peace et al., 2017). The model structure is analogous to the deformation observed in nature (Figure 4.8b). Further oceanic spreading led to the formation of a wide, transtensional region between the north and south Davis Straight spreading segments called the Ungava Transform Zone (Figure 4.8b, Reid & Jackson, 1997). The same wide transtensional zone occurs in the corresponding numerical model (Figure 4.8a). The similarity between the models presented in Chapter 4 and the evolution of the natural example highlights the importance of considering the change in spreading direction as a key factor influencing the current configuration of the area.

7.1.1.3 Gulf of Aden

The Gulf of Aden is a particularly useful example to highlight the importance of considering changes in plate motion in the evolution of transform systems. This is because it is a natural example that contains both inherited structures and has undergone a rotation in its evolution, thus allowing for direct comparison. Specifically, the Gulf of Aden has undergone ~35 Ma of spreading and is characterised by oblique crustal inheritance in the form of Mesozoic basins, an oblique rift and a change in the plate motion vector of about 26^{o} observed 20 Ma ago (Bellahsen et al., 2013; Brune & Autin, 2013; Jeanniot & Buiter, 2018).

In the Gulf of Aden, the continent-ocean transition is wider along the outside corners of two main fracture zones (Figure 4.8g), the Alula-Fartak and Socotra-Hadbeen Fracture Zones (Bellahsen et al., 2013). This area is compared against an oblique inheritance numerical model and a

transtensional rotation model, and the continent-ocean transition in the rotated model is almost twice as wide as in the inheritance model (Figure 4.8f insets). Therefore, the plate motion vector change appears to be the key controlling factor of rift asymmetry in the area.

7.1.1.4 Tanzania Coastal Basin

The Tanzania Coastal Basin underwent a plate reorganization ~150 Ma resulting in the formation of the Davie Fracture Zone, a 3000 km long fossilised oceanic transform fault that formed along a zone of aligned spreading centres (Phethean et al., 2016). In both the analogue modelling experiments shown in Chapter 5 (Figure 5.8b) and in nature (Figures 5.1g–5.1l and 5.8a), zones of compression develop adjacent to the Principal Displacement Zone as the plate vector changes, and the pattern of strike-slip faults evolves to accommodate this change. The active strike-slip faults at the end of the experiment have a curved surface expression that is not completely aligned with the plate vector (Figures 5.6l, 5.8a, and 5.8b—red faults). The Davie Fracture Zone shows a similar slightly kinked, 'open S' shape, reflecting this two-stage evolutionary pattern (Figure 5.8a; Phethean et al., 2016).

Equally, in deep seismic cross-sections along the Davie Fracture Zone (Figure 5.8c) there is clear evidence for intraplate compressional deformation within the oceanic crust, similar to the transpressional side of Experiment 3 (Figures 5.8d-g). It can thus be inferred that intra-oceanic crustal thrusting may have occurred in the Tanzania Coastal Basin to accommodate the plate motion change around 150 Ma, prior to the complete development of the Davie Fracture Zone. The importance of this natural example is that it highlights that plate motion can have similar effects in the oceanic domain as in the continental, although with different evolutional characteristics due to the more brittle nature of the oceanic crust (which is why it is modelled with a purely brittle configuration).

7.1.1.5 Bohai Basin

Finally, the last comparison made in Chapter 6 is between the basin-scale pull-apart analogue models and the Bohai Basin in northern China. The Bohai Basin is a NE-SW trending basin that

resembles the shape of a giant pull-apart structure, controlled by dextral transtension developing mainly in the Cenozoic (Allen et al., 1998).

Similar to the analogue models presented in Chapter 6, deposition in the Bohai Basin is focused near the intersection between the Principal Displacement Zone and the basin sidewall fault. In the case of the Bohai Basin, this is represented by an area called the Bozhong Depression (Figure 6.11a), where sedimentation was focused from the Eocene onwards. Similarly, in the model, the top pre-rift surface map displays the deepest depocenter at the end of the triangular transtensional Principal Displacement Zone where it intersects the Basin Sidewall Fault (Figure 6.11b). Further to that, the oblique-normal fault patterns that developed in the Bohai Basin and are considered evidence of dextral transtension (Qi & Yang, 2010) are also present in the model (Figure 6.11a,b). Finally, there is a very high degree of similarity between the northeastern transtensional Principal Displacement Zone of the Bohai Basin, and that of the model in Chapter 6. This is particularly highlighted when cross-sections are compared across the two transtensional zones. Both these areas display high depositional thickness at their widest points, and very similar fault patterns. Specifically, the segmented oblique and normal faults are consistent with the observations in transtensional Principal Displacement Zones from Farangitakis et al. (2019) (Ch 5). These findings highlight the importance of considering a transtensional change in plate motion at some stage of a pull-apart basin's history when similar structures are present.

7.1.2 Methodology discussion

While each separate results chapter lists the methodology, limitations present in each experimental approach, it is worth listing them again to highlighting that even when such limitations are present, there is still a high degree of similarity between the models presented in this work and their natural analogues. Furthermore, overcoming these limitations can be a potential objective of future research. These limitations are (as presented in chapter order within this thesis):

- Numerical modelling: The numerical code used in this work does not produce oceanic crust. Thus, the observations in this work focus mainly on the continental part of the transform boundary and do not take into consideration oceanic crustal features. Furthermore, in the numerical models presented in this work, there is no presence of magmatism to account for rifted margin asymmetry. However, as explained in more detail in Chapter 4, in simple shear systems any influence of magmatism on margin asymmetry would follow the tectonic structure as the primary driver of asymmetry.
- Analogue modelling: In the analogue models of this work, there are no isostatic effects below the limit of the ductile layer (since that is limited by the table-top where the experiment is set up) or thermal effects due to the materials used. Furthermore, as mentioned in the N. Gulf of California particular example, the plate jump at 3 Ma (Lonsdale, 1989) cannot be replicated. This is due to the nature of the analogue modelling apparatus not allowing changes in the velocity discontinuities after the experiment is set up.

Despite these limitations, the results presented in this thesis show a very high degree of similarity between models and natural prototypes, indicating that the first-order observations made from the models capture both the correct first-order factors driving the models and the changes that these produce.

The limitations listed above further indicate the need for an integrated approach when studying structures that undergo changes during their lifespan. The two modelling methodologies (analogue and numerical) complement each other's respective weaknesses. Numerical modelling provides the opportunity for direct scaling to the natural properties, including thermal effects and theoretically infinite iterations of experiments only limited by processing power. Analogue modelling offers the advantage of straightforward observable physics with materials that are real and scalable to nature. Numerical modelling offers the user the ability to "pause" a natural process and impose new boundary conditions (such as the change from orthogonal extension to

oblique extension in Chapter 4), while in analogue modelling this process has to be introduced before the experiment starts and must be compatible with the mechanical apparatus. Numerical modelling allows the user to investigate processes at any scale with little technical complexity (from the micro- to the tectonic plate-scale), while analogue modelling is limited by the scaling relations and properties of available materials. Having shown how these methodologies complement each other, it is also worth noting that both the analogue and numerical modelling experiments in this work demonstrate how changes in relative plate motion along a transform margin add complexity to its structure from lithosphere down to basin-scale. Having two different experimental methods arrive at the same conclusion across different scales gives confidence that changes in relative plate motion along transform margins are significant in transform evolution.

7.1.3 The structural development of transform margins and its connection to plate motion vector changes

A central finding of this study is that plate motion vector changes play a very important part in controlling a transform margin's evolution. Furthermore, as demonstrated in Chapter 4, the first-order control of plate motion changes in a transform margin's evolution is potentially greater than the effects of pre-existing structures or even magmatism. This would imply that the driving forces behind the formation of transform faults and margins would be forces in the lower lithosphere. This notion is in line with the "bottom-up" approach in large strike-slip fault evolution (Teyssier & Tikoff, 1998; Chatzaras et al., 2015), where large-scale strike-slip faults (and transform faults) are thought to first originate from the lower layers of the lithosphere. The models presented in this work follow the same principle, with the driving forces being "bottom-up". The zones of weakness/seeds in the numerical modelling work of Chapter 4 sit underneath the continental crust, and so do the velocity discontinuities in the analogue models of Chapters 5 and 6; hence, processes root from the lower lithosphere layers and travel upwards to the surface in transform faults. When considering the major driving force for plate tectonics to be slab pull by

subduction (i.e. tectonic plate slabs sinking into the mantle), then transform faults must form on lateral edges of plates or along velocity discontinuities (similar to the models in this work).

It is worth noting here once again, that while at certain points in a transform margin's evolution the transform fault and the transform margin constitute the same structural entity in space (Lorenzo, 1997; Gerya, 2012; Bellahsen et al., 2013; Basile, 2015; Le Pourhiet et al., 2017), this is not always the case, as indicated in a number of studies that suggest the initial shear zones do not necessarily correspond to the transform faults accommodating plate motion (Taylor et al., 2009; Gerya, 2012; Bellahsen et al., 2013; Illsley-Kemp et al., 2018). Thus, there are oceanic transform faults and fracture zones that do not correspond to a continental transform margin (Gerya, 2010), but rather form to accommodate the segmentation of spreading ridges. However, even in the case of oceanic transform faults and fracture zones, it appears that changes in plate motion may be imprinted on the transform faults and fracture zones. Ammann et al. (2018) note that rifting obliquity significantly increases the length of active transform faults, using the two longest oceanic transform faults of the Equatorial Atlantic as a natural example. A similar case is also observed in the Murray and Clarion Oceanic Fracture Zones in the Pacific Plate, where changes in plate motion vector have put the transform faults into transpression, leading to multiple fracture zone segments coalescing into one main segment (Morrow et al., 2019).

This study shows that the geometry of transform margins is also heavily influenced both by directional and velocity changes in the plate motion. In Chapter 4, it is shown that higher transpressional angles during oblique spreading or changes in plate motion result in longer transform margin segments, which are also active for a longer period of time (Figures 4.6, 4.7, and 4.9). This is consistent with the observations in Ammann et al. (2018), who demonstrate that elongate transform formation is favoured by higher degrees of spreading obliquity. In the analogue models of Chapter 5, it is shown that in transtensional and transpresssional PDZs, the transform boundary width is influenced by the extension velocity. The transtensional PDZ in Experiment 1 (5 cm/hr) reaches widths between 5-10 cm (45-90 km in nature) (Figure 5.4s), while

in Experiment 2 (10 cm/hr) it has a constant width of about 5-6 cm (45-55 km in nature) throughout (Figure 5.5s). Similarly, the transpressional zone of Experiment 2 (Figure 5.5t) is 50% narrower than the one in Experiment 1 (Figure 5.4t). This corresponds to natural transform examples where "faster" (spreading rates are relatively high) transforms have narrower deformation zones (Mauduit & Dauteuil, 1996). Finally, when transpressional changes in plate motion occur, the corresponding margins appear to be accompanied by topographic highs parallel to the plate motion. Features such as marginal ridges or plateaus (Mercier de Lépinay et al., 2016) are observed at transform margins that have experienced changes in plate motion leading to transpression such as the Exmouth Plateau (Whittaker et al., 2016), the Romanche Fracture Zone (Davison et al., 2016). The correlation between transform boundaries that have undergone transpression and the presence of marginal highs could indicate these features might be evidence of transpression. Other mechanisms proposed for the formation of these ridges consist of thermal uplift due to lateral heat conduction across the continent-ocean boundary (Gadd & Scrutton, 1997) or differential thermal subsidence (Lorenzo & Wessel, 1997). This work shows that transpression is sufficient to create this type of feature (without ruling out that some might be primarily created by or contain evidence for the operation of one of the other mechanisms proposed).

A key finding reported in this thesis is that changes in relative plate motion acting on a transform plate boundary shape its evolution to a far more significant degree than previously considered. Acknowledging that other factors can control a transform margin's evolution and structure – such as oblique inheritance or magmatism – the experimental results and their comparisons to natural examples indicate that changes in plate motion are one of the most important (if not the most important) driving factor behind a transform margin's structure. Recent studies indicate that oblique rifting is potentially the rule, and not the exception, across the globe (Brune et al., 2017). It would then be logical to suggest that the same oblique principle would apply to corresponding transform faults (and thus margins) in older rift-transform and ridge-transform intersections. This

obliquity can either be introduced by de-facto oblique rifting or by a change in plate motion after orthogonal rifting.

Nevertheless, when investigating the evolution of a transform margin its lifespan may be represented in a similar manner to the strain triangle shown in Chapter 1 (after Fossen, 2016). Perfectly orthogonal transform margins do exist (although most commonly in the purely oceanic domain such as the Woodlark Basin). However, since the Earth's tectonic plates move around a globe, all motions are around poles of rotations. Transform faults form on the circumference of the small circles around the poles of rotations; thus when a pole shifts, it leads to plate boundaries commonly under- or overlapping. In addition to that, transform plate boundaries are elongate, relatively weak, linear features and are more prone to heavily reflect a change in plate motion in their evolution. Rifts, spreading centres and zones of plate convergence are usually zones of several tens (if not hundreds) of kilometers wide and long and hence any changes of plate motion are imprinted more uniformally (such as in oblique rifts or oblique convergence zones). Moreover, since the planet's surface is a free surface, in zones of plate convergence or divergence, plate motion changes are imprinted with gravity influenced structures. This is not the case in transform boundaries, where it is considerably harder (if not impossible) to shift a plate boundary laterally. Plate motion changes in transform plate boundaries are reflected through considerably more favourable gravity-driven structuration such as the transtensional or transpressional deformation produced in the models of this thesis. Thus, when the transform margin under investigation resembles more closely the types in the bottom of the Figure 7.1 triangular diagram, a change in plate motion during its evolution should be considered.

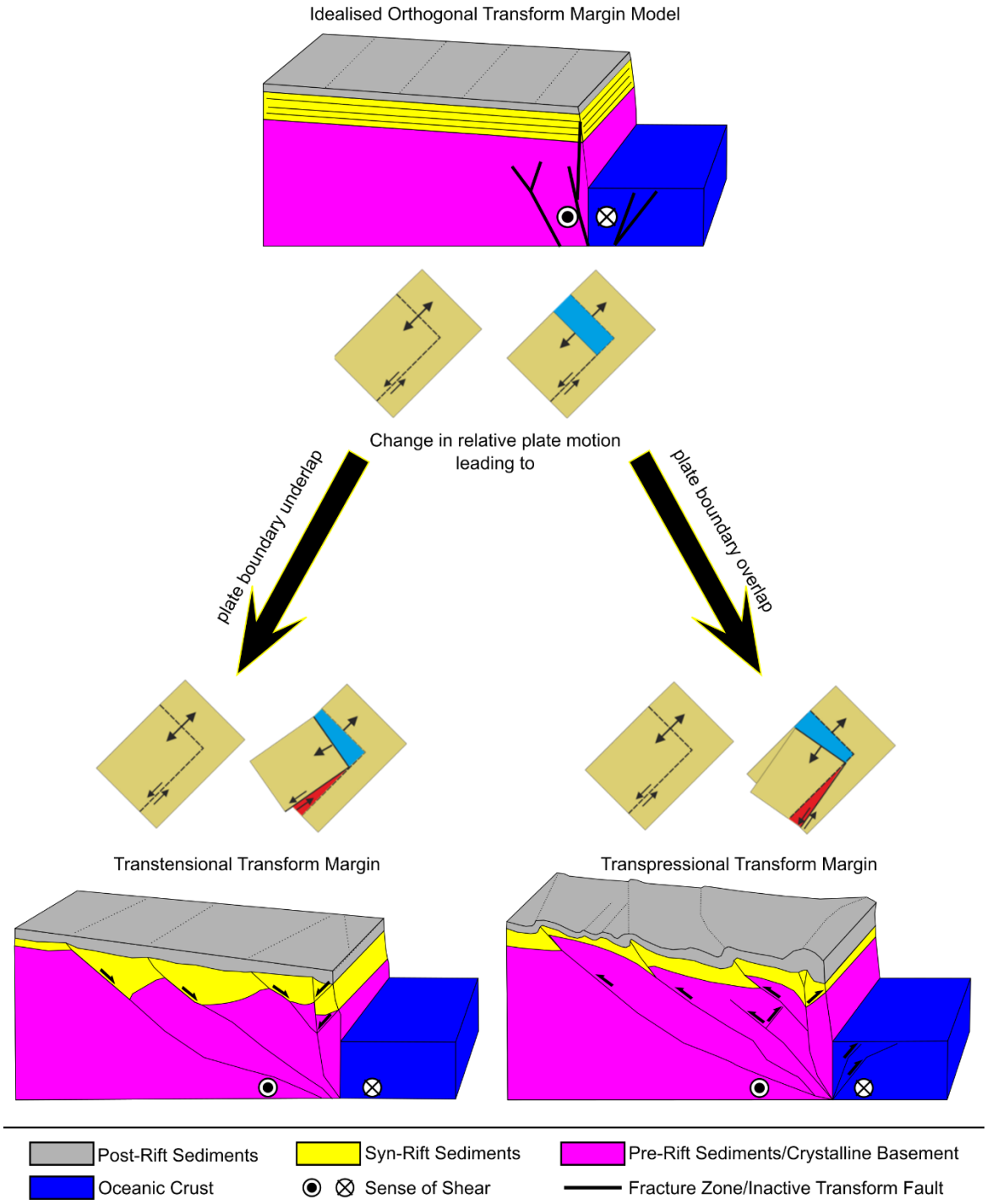

Figure 7.1 – 3D schematic of the evolution of an orthogonal transform plate boundary when it undergoes a change in the relative plate motion. Smaller panels in the middle indicate relative plate motion.

7.2 Future work

Although this work has provided significant insights into the evolution of transform margins and rift-transform intersections in response to changes in plate motion, there still remain substantial

unexplored aspects both within the matters addressed in this thesis and along new research directions that have arisen as a result of this thesis. A number of them stem from the limitations mentioned in the methodology sub-section of this chapter, while some arise from the (constant) need for better quality data on natural examples. For this reason, a list of possible research topics that could be investigated to address these knowledge gaps follows below.

7.2.1 Timing, amount and duration of rotation due to changes in plate motion

Having established already through this work that changes in plate motion leading to transtension and transpression in transform margins have a first-order control in their evolution, it would be a logical step to investigate and quantify the temporal and spatial aspect of these plate motion changes. It is suggested that the next step arising from this work could be the variation of "when", "how much" and "over how long" these rotations occur. In particular, in analogue modelling, this can be done by changing the configuration of the mechanical elbow imposing the rotation (Figure 3.5):

a) If the modeler is investigating the timing of the imposed rotation, then the metal boxes imposing the rotation can be moved along the original strike of the transform, placing the rotation earlier or later in the margin's lifespan. This could provide insights in why some transform margin profiles have such a high degree of variability even along their own strike (Mercier de Lépinay et al., 2016). As an example, imposing transpression at a later stage, would imply that the margin profile closer to the initial RTI would potentially remain unaffected, since the plate boundary would have moved away from it. The effects of compression would then be visible in the more distal parts of the margin.

b) If the modeler is investigating the amount of imposed rotation, the angle between the metal boxes and guide bars can be changed to allow for the angle of rotation to increase or decrease. An increased or decreased angle would have a direct impact on the spatial distribution of transtension and transpression along a margin. Comparing models with

different rotation angles can allow for the quantification of depositional space (i.e. in a pull-apart basin), or uplift in the case of transpression.

c) If the modeler is investigating the duration of the imposed rotation, then the angle between the metal boxes can change (as seen in the zoomed in Figures 7.2b and 7.2c), allowing for the duration of the rotation to be decreased or increased accordingly. A change in the rotation would modify the effect of the extensional or compressional component of motion and the corresponding features (oblique/normal faults or oblique/reverse faults).

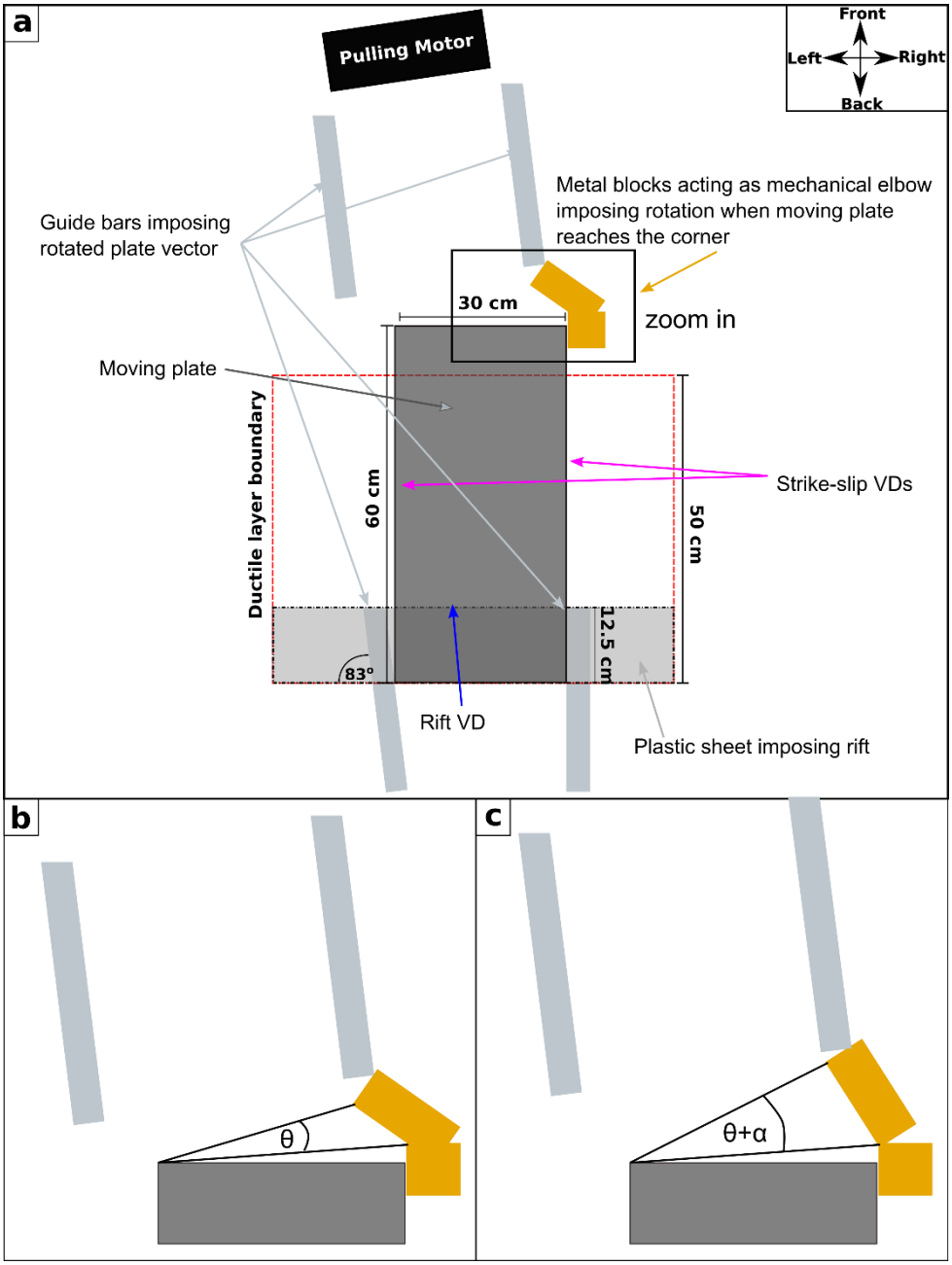

Figure 7.2 – a) Experimental set-up used in Chapter 5. b-c) change in the angle between the metal boxes comprising the mechanical elbow that results in extended rotation duration.

The motivation behind such a study lies in the significant resource potential of transform margins. As ten Brink et al. (1996) indicate, even a small change in the transtensional component in a pull-apart basin's evolution can increase the available deposition space two or three times. Both the pull-apart basins investigated in this thesis have a high resource potential, with the N. Gulf of California being a key geothermal area of interest (Prol-Ledesma & Moran-Zenteno, 2019) and the

Bohai Basin being the most oil-rich basin onshore China (Qi & Yang, 2010). Quantification of these variabilities in such areas can lead to the development of standardized methods to approach transform margins when investigating for economic resources. Furthermore, in regions of active seismicity, identifying such structures can provide a very useful tool to identify the location and size of potentially blind strike-slip faults or dip-slip faults with a strike-slip component. In particular the second category of faults could appear as less of a risk than what they actually are since their actual hazard capability would not be visible. Finally, the same investigation into parameter space can be carried out in a numerical modelling study.

7.2.2 Restraining bends on transform margins under transpression

Chapter 6 investigates the effects of plate motion vector changes on releasing bends along an early stage transform. An aspect for further investigation (that during this study was limited by time and budgetary restrictions) is to study the effects of plate motion vector changes on the compressional counterpart, which is a restraining bend. The modelling set-up for this experiment would be the same as in Chapter 6 but mirrored, leading to the rift-PDZ-rift-PDZ system going into transpression. It would be expected that the resulting geometries would have similar configurations to the transpressional systems shown in Chapter 5, with thrusts cross-cutting previous ones once rotation begins. Mann (2007) notes that the vast majority of the 49 restraining bends identified in his strike-slip catalogue occur in continental boundary strike-slip fault systems. Such areas are usually close to human activity, such as the San Andreas Fault or the North Anatolian Fault, and pose significant seismic hazards with devastating earthquakes. Thus, being able to map the evolution of such systems and potentially predict the stage at which they are at present and how they could evolve, could provide insights on potential seismic hazards.

7.2.3 Introduction of magmatism and oceanic accretion

A particular aspect of numerical modelling that is worth investigating further is the addition of magmatism effects and oceanic accretion in the models. In this study, this was limited by available research time, the high-performance computer's processing capacity, and the capacity of the

code used in Chapter 4. Adding oceanic accretion to the models would enable investigation of the oceanic crustal part of the transform faults and margins even further and would provide an opportunity to examine segmentation of spreading and spontaneous transform fault generation in oblique spreading ridges. Having a system that develops oceanic crust would imply that the entire lifespan of a transform margin could be studied to better understand how changes in plate motion affect its evolution. Further to that, the addition of magmatism would make for a more accurate depiction of the early stages of rifting with magmatic emplacement. This would in turn indicate what effect magmatism has on the rheology of the margins, how (a)symmetrically it is distributed and if and how it controls their asymmetry.

7.2.4 4D and lithosphere-scale analogue modelling of transform boundaries

A fourth dimension can be added in analogue models (time) by accessing the development of structures in real time intervals. This can be achieved through the use of CT scanning of the experimental set-up similar to that in Zwaan and Schreurs (2017). This can allow for a full 4D evolution to be mapped for any of the experiments displayed in this work, allowing comparison with geophysical and geodetic data from the surface and the subsurface of natural examples. Such a set of experiments can be quite useful to investigate the exact timeline of structure formation when changes in plate motion occur (e.g. what structures form and when, which are abandoned and when) and can also be combined with the study on duration of rotation shown in subsection 7.3.1. The societal importance of such work is that it can have significant implications for both the resource potential of transform boundaries and also for the hazard aspect of such areas. Finally, analogue modelling can be carried out in a lithosphere-scale, similar to that of Chapter 4. Lithospheric-scale analogue modelling includes the construction of an accurately scaled model of the Earth's lithosphere, consisting of ductile lithospheric mantle, brittle upper mantle, ductile lower crust, and brittle upper crust. Low viscosity asthenosphere is represented by Newtonian fluids, while lithospheric mantle is usually represented by power-law viscoelastic materials (Broerse et al., 2019). Such a study would assist in further investigating whether

transform fault evolution is a “bottom-up” process. Furthermore, lithospheric analogue modelling could provide a more accurate representation of how a transtensional or transpressional margin is structured, since isostasy and buoyancy can be incorporated in such models. This would result in a more accurate topographical representation of the amount of negative (in the case of transtension) or positive (in the case of transpression) change in the surface of the crust.

7.2.5 Increased data availability

Further to more modelling, another significant improvement in our understanding of the effects of plate motion changes in transform margins could come from a greater availability of data in such areas. In this study, I utilised freely available academic datasets and re-interpreted or used the findings of other workers in the areas of natural examples. While these datasets were adequate for the purposes of this work, access to higher resolution 3D seismic datasets would offer a much clearer image of the structural configuration of the natural examples. It is worth mentioning here that when the research on this thesis began, various geophysical companies were contacted for potential available data. However, by about 9 months into the project, with still no industry data obtained (as the industry was reluctant to share data with academics since continental transform margins were the new major exploration target), a decision was made to proceed with what was available in the public domain. Having access to 3D seismic (or a denser 2D line spacing) over a pull-apart basin would allow for direct one-to-one correlation between the model and nature, and significantly more observations can then be made. The same applies in general to any transform margin around the world. However, in the study of transform margins and transform faults, other forms of data can also be used to further advance our understanding of their evolution. For example, researchers can collect GPS data along a large continental transform fault such as the San Andreas or North Anatolian Fault. Such data can shed light on the strain field around these faults and can also be fed directly back to models for calibration and comparison.

7.3 Conclusions

In this thesis, a state-of-the-art cross-scale modelling approach is used to investigate the effects of changes in plate motions on transform margins and rift transform intersections.

In the first set of experiments, lithosphere-scale numerical models were developed to investigate the effect of oblique inheritance versus changes in plate motion vectors during the evolution of a rift-transform intersection. Analogue models to investigate the effect of changes in plate motion at the crustal-scale of rift-transform intersections were created in a second set of experiments. Finally, a specific analogue modelling experiment was designed to investigate the effect of a transtensional change in the plate motion vector in a releasing bend along a transform fault.

The numerical and analogue models produce structural patterns and topographic effects that show good agreement with natural examples. Hence, they provide an understanding of fault geometries, kinematics and temporal and spatial relationships of structural features developing in transform margins and rift transform intersections when changes in plate motion occur.

When a change in plate motion occurs that results in the transform margin undergoing transtension, there is a distinct pattern of fault evolution present in the Principal Displacement Zone. This is characterized by normal and oblique-normal faults accommodating the extensional and rotational component of transtension along the Principal Displacement Zone. With the gradual change of the plate vector, the Principal Displacement Zone also rotates to accommodate plate motion. In fully developed margins with active spreading, this change results in rifted margin asymmetry. These observations are in good agreement with real world data from:

a) The Gulf of California, where the gradual transtensional opening of the greater Gulf of California region created en-echelon pull-apart basins developing from south to north before they evolved into ridge-transform segments. Focusing on the Northern Gulf of California, the transtensional component of the area is accommodated by oblique-slip normal faults acting as the pull-apart basin boundary faults and onshore normal faults

that accommodate or have accommodated a component of rotation. Furthermore, examining the evolution of the N. Gulf of California pull-apart basin structure, there is great similarity between the physical analogue model (Chapter 6) and the N. GoC where the pull-apart basin is shaped as an asymmetrical triangle, bounded by strike-slip faults on either side.

b) The Gulf of Aden, where a combination of oblique inheritance and relative plate rotation leads to rifted margin asymmetry, where the margins associated with the outside corners of the rift-transform intersection are significantly wider than those associated with the inside ones.

c) The Bohai Basin in Northern China, where focused depocentres are observed along the transtensional Principal Displacement Zone, controlled by series of oblique-normal faults in both model and nature, and the existence of faults oblique to the main basin trend, indicating the presence of a transtensional component in the pull-apart basin's evolution.

When a change in plate motion occurs that results in the transform margin undergoing transpression, reverse faulting occurs to accommodate the plate overlap. Moreover, in a well-developed rift-transform-rift system, transpression occurs along the inside margin corners in the early stages of rifting, and transtension occurs along the transform margin profile after spreading has developed. These observations are in good agreement with natural examples from:

a) The Tanzania Coastal Basin, where thrust fronts develop to accommodate the rotational component of transpression. These thrust fronts are also often oblique-reverse (i.e. display both a reverse and strike-slip character) and are accompanied by strike-slip faults, or reactivated as such. As motion in the new direction continues, newer strike-slip faults develop and cut through the pre-existing fabric. This is observed both in lab experiments and in the natural example of the Davie Fracture Zone, where intra-oceanic crust positive flower structures occur next to or within the Davie Fracture Zone.

b) The Davis Strait, where a lithospheric-scale numerical model simulates a transpressional 25^{o} rotation with respect to the orthogonal extension direction, resulting in a diffuse zone of transtension where the Ungava Transform Zone is located and transpression on the inside corners of the rift-transform intersection.

Finally, it is noted through the numerical models that introducing a relative plate rotation in an orthogonal rift-transform system results in a longer transform margin activity lifespan and delayed spreading along the entire margin. This is due to the delay caused by the reorganisation of the diffuse strain patterns associated with transtension and transpression when a rotational change in plate motion occurs.

Fundamentally, the effects of changes in plate motion resulting in transtension and transpression on transform margins and rift-transform intersections appear to be a first-order (and potentially the most crucial) controlling factor in shaping the evolution of the world's transform margins.

References

Acocella, V., Faccenna, C., Funiciello, R., & Rossetti, F. (1999). Sand-box modelling of basement-controlled transfer zones in extensional domains. *Terra Nova, 11*(4), 149-156. http://dx.doi.org/10.1046/j.1365-3121.1999.00238.x

Allemand, P., & Brun, J. (1991). Width of continental rifts and rheological layering of the lithosphere. *Tectonophysics, 188*(1-2), 63-69. http://dx.doi.org/10.1016/0040-1951(91)90314-I

Allen, M. B., Macdonald, D. I. M., Xun, Z., Vincent, S. J., & Brouet-Menzies, C. (1997). Early Cenozoic two-phase extension and late Cenozoic thermal subsidence and inversion of the Bohai Basin, Northern China. *Marine and Petroleum Geology, 14*(7), 951-972. https://doi.org/10.1016/S0264-8172(97)00027-5

Allen, M. B., Macdonald, D. I. M., Xun, Z., Vincent, S. J., & Brouet-Menzies, C. (1998). Transtensional deformation in the evolution of the Bohai Basin, Northern China. *Geological Society, London, Special Publications, 135*(1), 215-229. https://doi.org/10.1144/GSL.SP.1998.135.01.14

Allken, V., Huismans, R. S., & Thieulot, C. (2012). Factors controlling the mode of rift interaction in brittle-ductile coupled systems: A 3D numerical study. *Geochemistry, Geophysics, Geosystems, 13*(5) https://doi.org/10.1029/2012GC004077

Ammann, N., Liao, J., Gerya, T., & Ball, P. (2018). Oblique continental rifting and long transform fault formation based on 3D thermomechanical numerical modeling. *Tectonophysics, 746*, 106-120. https://doi.org/10.1016/j.tecto.2017.08.015

Armijo, R., Meyer, B., Navarro, S., King, G., & Barka, A. (2002). Asymmetric slip partitioning in the Sea of Marmara pull-apart: A clue to propagation processes of the North Anatolian Fault? *Terra Nova, 14*(2), 80-86. https://doi.org/10.1046/j.1365-3121.2002.00397.x

Atwater, T., & Stock, J. (1998). Pacific-North America plate tectonics of the Neogene Southwestern United States: An update. *International Geology Review, 40*(5), 375-402. http://dx.doi.org/10.1080/00206819809465216

Autin, J., Bellahsen, N., Leroy, S., Husson, L., Beslier, M., & d'Acremont, E. (2013). The role of structural inheritance in oblique rifting: Insights from analogue models and application to the Gulf of Aden. *Tectonophysics, 607*, 51-64. http://dx.doi.org/10.1016/j.tecto.2013.05.041

Axen, G. (1995). Extensional segmentation of the main gulf escarpment, Mexico and United States. *Geology, 23*(6), 515-518. http://dx.doi.org/10.1130/0091-7613(1995)023<0515:ESOTMG>2.3.CO;2

Basile, C. (2015). Transform continental margins — part 1: Concepts and models. *Tectonophysics, 661*, 1-10. http://dx.doi.org/10.1016/j.tecto.2015.08.034

Basile, C., & Brun, J. P. (1999). Transtensional faulting patterns ranging from pull-apart basins to transform continental margins: An experimental investigation. *Journal of Structural Geology, 21*(1), 23-37. http://dx.doi.org/10.1016/S0191-8141(98)00094-7

Basile, C., Mascle, J., Popoff, M., Bouillin, J., & Mascle, G. (1993). The Ivory Coast-Ghana transform margin: A marginal ridge structure deduced from seismic data. *Tectonophysics, 222*(1), 1-19. https://doi.org/10.1016/0040-1951(93)90186-N

Baumgardner, J. R. (1985). Three-dimensional treatment of convective flow in the earth's mantle. *Journal of Statistical Physics, 39*(5-6), 501-511. https://doi.org/10.1007/BF01008348

Behn, M. D., Lin, J., & Zuber, M. T. (2002). Evidence for weak oceanic transform faults. *Geophysical Research Letters, 29*(24), 60-61; 60-4. https://doi.org/10.1029/2002GL015612

Bellahsen, N., Leroy, S., Autin, J., Razin, P., d'Acremont, E., Sloan, H., . . . Khanbari, K. (2013). Pre-existing oblique transfer zones and transfer/transform relationships in continental margins: New insights from the southeastern Gulf of Aden, Socotra island, Yemen. *Tectonophysics, 607*, 32-50. https://doi.org/10.1016/j.tecto.2013.07.036

Bennett, R. A., Rodi, W., & Reilinger, R. E. (1996). Global positioning system constraints on fault slip rates in southern California and northern Baja, Mexico. *Journal of Geophysical Research: Solid Earth, 101*, 21943-21960. https://doi.org/10.1029/96JB02488

Bennett, S. E. K., & Oskin, M. E. (2014). Oblique rifting ruptures continents: Example from the Gulf of California shear zone. *Geology, 42*(3), 215-218. https://doi.org/10.1130/G34904.1

Bennett, S. E. K., Oskin, M. E., & Iriondo, A. (2013). Transtensional rifting in the proto-Gulf of California near Bahía Kino, Sonora, México. *GSA Bulletin, 125*(11-12), 1752-1782. https://doi.org/10.1130/B30676.1

Bennett, S. E. K., Oskin, M. E., Iriondo, A., & Kunk, M. J. (2016). Slip history of the La Cruz fault: Development of a late Miocene transform in response to increased rift obliquity in the northern Gulf of California. *Tectonophysics, 693*, 409-435. https://doi.org/10.1016/j.tecto.2016.06.013

Berner, H., Ramberg, H., & Stephansson, O. (1972). Diapirism theory and experiment. *Tectonophysics, 15*(3), 197-218. https://doi.org/10.1016/0040-1951(72)90085-6

Bird, D. (2001). Shear margins. *The Leading Edge, 20*(2), 26/4/2016-150-159. https://doi.org/10.1190/1.1438894

Bird, P. (1978). Initiation of intracontinental subduction in the himalaya. *Journal of Geophysical Research: Solid Earth, 83*(B10), 4975-4987. https://doi.org/10.1029/JB083iB10p04975

Bos, B., & Spiers, C. J. (2002). Frictional-viscous flow of phyllosilicate-bearing fault rock: Microphysical model and implications for crustal strength profiles. *Journal of Geophysical Research: Solid Earth, 107*, ECV 1-1; ECV 1-13. https://doi.org/10.1029/2001JB000301

Bosworth, W. (1986). Comment and Reply on "Detachment faulting and the evolution of passive continental margins" COMMENT. *Geology, 14*(10), 890-891. https://doi.org/10.1130/0091-7613(1986)14<890:CARODF>2.0.CO;2

Brace, W., & Kohlstedt, D. (1980). Limits on lithospheric stress imposed by laboratory experiments. *Journal of Geophysical Research: Solid Earth, 85(B11)*, 6248-6252. https://doi.org/10.1029/JB085iB11p06248

Broerse, T., Norder, B., Govers, R., Sokoutis, D., Willingshofer, E., & Picken, S. J. (2019). New analogue materials for nonlinear lithosphere rheology, with an application to slab break-off. *Tectonophysics, 756*, 73-96. https://doi.org/10.1016/j.tecto.2018.12.007

Brun, J. P. (2002). Deformation of the continental lithosphere: Insights from brittle-ductile models. *Geological Society, London, Special Publications, 200*(1), 355-370. https://doi.org/10.1144/GSL.SP.2001.200.01.20

Brune, S., Popov, A. A., & Sobolev, S. V. (2012). Modeling suggests that oblique extension facilitates rifting and continental break-up. *Journal of Geophysical Research: Solid Earth, 117.* https://doi.org/10.1029/2011JB008860

Brune, S., & Autin, J. (2013). The rift to break-up evolution of the Gulf of Aden: Insights from 3D numerical lithospheric-scale modelling. *Tectonophysics, 607*, 65-79. https://doi.org/10.1016/j.tecto.2013.06.029

Brune, S., Williams, S. E., Butterworth, N. P., & Müller, R. D. (2016). Abrupt plate accelerations shape rifted continental margins. *Nature, 536*, 201. https://doi.org/10.1038/nature18319

Brune, S., Williams, S. E., & Müller, R. D. (2018). Oblique rifting: The rule, not the exception. *Solid Earth, 9*, 1187-1206. https://doi.org/10.5194/se-9-1187-2018

Burchfiel, B. C., & Stewart, J. H. (1966). "Pull-Apart" origin of the central segment of Death Valley, California. *GSA Bulletin, 77*(4), 439-442. https://doi.org/10.1130/0016-7606(1966)77[439:POOTCS]2.0.CO;2

Burg, J., Davy, P., & Martinod, J. (1994). Shortening of analogue models of the continental lithosphere: New hypothesis for the formation of the Tibetan Plateau. *Tectonics, 13*(2), 475-483. https://doi.org/10.1029/93TC02738

Burov, E. B. (2011). Rheology and strength of the lithosphere. *Marine and Petroleum Geology, 28*(8), 1402-1443. https://doi.org/10.1016/j.marpetgeo.2011.05.008

Carey, S. W. (1958). A tectonic approach to continental drift. Paper presented at the *Continental Drift: A Symposium,* Hobart: University of Tasmania. 177.

Chapman, D. S. (1986). Thermal gradients in the continental crust. *Geological Society, London, Special Publications, 24*(1), 63-70. https://doi.org/10.1144/GSL.SP.1986.024.01.07

Chatzaras, V., Tikoff, B., Newman, J., Withers, A. C., & Drury, M. R. (2015). Mantle strength of the San Andreas fault system and the role of mantle-crust feedbacks. *Geology, 43*(10), 891-894. https://doi.org/10.1130/G36752.1

Choi, E., Lavier, L., & Gurnis, M. (2008). Thermomechanics of mid-ocean ridge segmentation. *Physics of the Earth and Planetary Interiors, 171*(1), 374-386. https://doi.org/10.1016/j.pepi.2008.08.010

Coffin, M. F., & Rabinowitz, P. D. (1987). Reconstruction of Madagascar and Africa: Evidence from the Davie Fracture Zone and Western Somali Basin. *Journal of Geophysical Research: Solid Earth, 92*, 9385-9406. https://doi.org/10.1029/JB092iB09p09385

Corti, G., & Dooley, T. P. (2015). Lithospheric-scale centrifuge models of pull-apart basins. *Tectonophysics, 664*, 154-163. https://doi.org/10.1016/j.tecto.2015.09.004

Corti, G., Cioni, R., Franceschini, Z., Sani, F., Scaillet, S., Molin, P., . . . Keir, D. (2019). Aborted propagation of the Ethiopian rift caused by linkage with the Kenyan rift. *Nature Communications, 10*(1), 1-11. https://doi.org/10.1038/s41467-019-09335-2

Corti, G., Nencini, R., & Skyttä, P. (2020). Modelling the influence of pre-existing brittle fabrics on the development and architecture pull-apart basins. *Journal of Structural Geology, 131*, 103937. https://doi.org/10.1016/j.jsg.2019.103937

Crowell, J. (1974). Origin of late Cenozoic basins in Southern California: Society of economic paleontologists and mineralogists special publication *no. 22, 194*, p. 190-204.

Cruz, L., Teyssier, C., Perg, L., Take, A., & Fayon, A. (2008). Deformation, exhumation, and topography of experimental doubly-vergent orogenic wedges subjected to asymmetric erosion. *Journal of Structural Geology, 30*(1), 98-115. https://doi.org/10.1016/j.jsg.2007.10.003

Cserepes, L., Rabinowicz, M., & Rosembergâ€Borot, C. (1988). Three dimensional infinite prandtl number convection in one and two layers with implications for the earth's gravity field. *Journal of Geophysical Research: Solid Earth, 93*(B10), 12009-12025. https://doi.org/10.1029/JB093iB10p12009

D'Acremont, E., Leroy, S., Maia, M., Gente, P., & Autin, J. (2010). Volcanism, jump and propagation on the Sheba ridge, eastern Gulf of Aden: Segmentation evolution and implications for oceanic accretion processes. *Geophysical Journal International, 180*(2), 535-551. https://doi.org/10.1111/j.1365-246X.2009.04448.x

Daignieres, M., Fremond, M., & Friaa, A. (1978). Attempt to model lithospheric strains by using generalized Norton-Hoff material (an example-Himalayan collision). *Comptes Rendus Hebdomadaires Des Seances De l Academie Des Sciences Serie b, 286*(24), 371-374.

Darin, M. H., Bennett, S. E. K., Dorsey, R. J., Oskin, M. E., & Iriondo, A. (2016). Late Miocene extension in coastal Sonora, México: Implications for the evolution of dextral shear in the proto-gulf of California oblique rift. *Tectonophysics, 693*, 378-408. https://doi.org/10.1016/j.tecto.2016.04.038

Dauteuil, O., & Brun, J. (1993). Oblique rifting in a slow-spreading ridge. *Nature, 361*(6408), 145-148. https://doi.org/10.1038/361145a0

Dauteuil, O., Bourgeois, O., & Mauduit, T. (2002). Lithosphere strength controls oceanic transform zone structure: Insights from analogue models. *Geophysical Journal International, 150*(3), 706-714. https://doi.org/10.1046/j.1365-246X.2002.01736.x

Davaille, A., Gueslin, B., Massmeyer, A., & Giuseppe, E. D. (2013). Thermal instabilities in a yield stress fluid: Existence and morphology. *Journal of Non-Newtonian Fluid Mechanics, 193*, 144-153. https://doi.org/10.1016/j.jnnfm.2012.10.008

Davis, J. K., Lawver, L. A., Norton, I. O., & Gahagan, L. M. (2016). New Somali basin magnetic anomalies and a plate model for the early Indian Ocean. *Gondwana Research, 34,* 12-28. https://doi.org/10.1016/j.gr.2016.02.010

Davison, I., Faull, T., Greenhalgh, J., O Beirne, E., & Steel, I. (2016). Transpressional structures and hydrocarbon potential along the Romanche Fracture Zone: A review. *Geological Society, London, Special Publications, 431*(1), 235-248. https://doi.org/10.1144/SP431.2

De Paola, N., Holdsworth, R. E., McCaffrey, K. J. W., & Barchi, M. R. (2005). Partitioned transtension: An alternative to basin inversion models. *Journal of Structural Geology, 27*(4), 607-625. https://doi.org/10.1016/j.jsg.2005.01.006

Decker, K. (1996). Miocene tectonics at the Alpine-Carpathian junction and the evolution of the Vienna basin. *Mitteilungen der Gesellschaft der Geologie- und Bergbaustudenten in Österreich, 41*, 33–44.

Del Ventisette, C., Montanari, D., Sani, F., Bonini, M., & Corti, G. (2007). Reply to comment by J. Wickham on “Basin inversion and fault reactivation in laboratory experiments”. *Journal of Structural Geology, 29*(8), 1417-1418. https://doi.org/10.1016/j.jsg.2007.05.003

Dewey, J., Holdsworth, R., & Strachan, R. (1998). Transpression and transtension zones. *Geological Society, London, Special Publications, 135*(1), 1-14. https://doi.org/10.1144/GSL.SP.1998.135.01.01

Dietz, R. S. (1961). Continent and ocean basin evolution by spreading of the sea floor. *Nature, 190*(4779), 854-857. https://doi.org/10.1038/190854a0

Dombradi E., Sokoutis D., Bada G., Cloetingh S., & Horváth F., 2010. Modelling recent deformation of the Pannonian lithosphere: Lithospheric folding and tectonic topography. Tectonophysics, GeoMod 2008 special volume: "Quantitative modelling of geological processes", (Eds: Corti G., Ranalli G., & Sokoutis D.). *Tectonophysics 484* (2010) 103-118, https://doi.org/10.1016/j.tecto.2009.09.014

Doré, A. G., Lundin, E. R., Gibbons, A., Sømme, T. O., & Tørudbakken, B. O. (2016). Transform margins of the Arctic: A synthesis and re-evaluation. *Geological Society, London, Special Publications, 431*(1), 63-94. https://doi.org/10.1144/SP431.8

Dorsey, R. J., & Umhoefer, P. J. (2011). Influence of sediment input and plate-motion obliquity on basin development along an active oblique-divergent plate boundary: Gulf of California and Salton Trough. In C. Busby &A. Azor (Eds.), *Tectonics of sedimentary basins* (pp. 209-225) John Wiley & Sons, Ltd. https://doi.org/10.1144/SP431.2 10.1002/9781444347166.ch10

Duarte, J. C., Schellart, W. P., & Cruden, A. R. (2014). Rheology of petrolatum–paraffin oil mixtures: Applications to analogue modelling of geological processes. *Journal of Structural Geology, 63*, 1-11. https://doi.org/10.1016/j.jsg.2014.02.004

Dubinin, E. P., Grokholsky, A. L., & Makushkina, A. I. (2018). Physical modeling of the formation conditions of microcontinents and continental marginal plateaus. *Izvestiya, Physics of the Solid Earth, 54*(1), 66-78. https://doi.org/10.1134/S1069351318010056

Engebretson, D. C. (1985). Relative motions between oceanic and continental plates in the Pacific Basin. Geological Society of America, Special Papers, 206. https://doi.org/10.1130/SPE206-p1

Exon, N. F., & Willcox, J. B. (1978). Geology and petroleum potential of exmouth plateau area off western australia. *AAPG Bulletin, 62*(1), 40-72. https://doi.org/10.1306/C1EA47F2-16C9-11D7-8645000102C1865D

Exxon World Mapping Project. (1985). *Tectonic map of the world* (Exxon World Mapping Project ed.). Houston, USA: Exxon Production Research Company.

Farangitakis, G. -., Sokoutis, D., McCaffrey, K. J. W., Willingshofer, E., Kalnins, L. M., Phethean, J. J. J., . . . van Steen, V. (2019). Analogue modeling of plate rotation effects in transform margins

and rift-transform intersections. *Tectonics, 38*(3), 823-841. https://doi.org/10.1029/2018TC005261

Feng, D., & Ye, F. (2018). Structure kinematics of a transtensional basin: An example from the Llinnan subsag, Bohai Bay basin, Eastern China. *Geoscience Frontiers, 9*(3), 917-929. https://doi.org/10.1016/j.gsf.2017.05.012

Fossen, H. (2016). *Structural geology* Cambridge University Press.

Gadd, S. A., & Scrutton, R. A. (1997). An integrated thermomechanical model for transform continental margin evolution. *Geo-Marine Letters, 17*(1), 21-30. https://doi.org/10.1007/PL00007203

Geiger, M., Clark, D. N., & Mette, W. (2004). Reappraisal of the timing of the breakup of Gondwana based on sedimentological and seismic evidence from the Morondava basin, Madagascar. *Journal of African Earth Sciences,38* (4), 363-381. https://doi.org/10.1016/j.jafrearsci.2004.02.003

Gerya, T. (2010). Dynamical instability produces transform faults at mid-ocean ridges. *Science, 329*(5995), 1047-1050. https://doi.org/10.1126/science.1191349

Gerya, T. (2012). Origin and models of oceanic transform faults. *Tectonophysics, 522-523*, 34-54. https://doi.org/10.1016/j.tecto.2011.07.006

Gerya, T. V. (2013). Three-dimensional thermomechanical modeling of oceanic spreading initiation and evolution. *Physics of the Earth and Planetary Interiors, 214*, 35-52. doi:https://doi.org/10.1016/j.pepi.2012.10.007

Gerya, T. V. (2019). Short history of geodynamics and numerical geodynamic modelling. *Introduction to numerical geodynamic modelling* (2nd ed., pp. 4-8) Cambridge University Press.

Glerum, A., Thieulot, C., Fraters, M., Blom, C., & Spakman, W. (2018). Nonlinear viscoplasticity in ASPECT: Benchmarking and applications to subduction. *Solid Earth, 9*(2), 267-294. https://doi.org/10.5194/se-9-267-2018

Glerum, A., Brune, S., Stamps, D. S., & Strecker, M. R. (2020). Victoria continental microplate dynamics controlled by the lithospheric strength distribution of the east African rift. *Nature Communications, 11*(1), 1-15. https://doi.org/10.1038/s41467-020-16176-x

Goff, J. A., Bergman, E. A., & Solomon, S. C. (1987). Earthquake source mechanisms and transform fault tectonics in the Gulf of California. *Journal of Geophysical Research: Solid Earth, 92*, 10485-10510. https://doi.org/10.1029/JB092iB10p10485

Gomes, C. J. S. (2013). Investigating new materials in the context of analog-physical models. *Journal of Structural Geology, 46*, 158-166. https://doi.org/10.1016/j.jsg.2012.09.013

González-Fernández, A., Dañobeitia, J. J., Delgado-Argote, L., Michaud, F., Córdoba, D., & Bartolomé, R. (2005). Mode of extension and rifting history of upper Tiburón and Upper Delfín Basins, Northern Gulf of California. *Journal of Geophysical Research: Solid Earth, 110* https://doi.org/10.1029/2003JB002941

Gonzalez-Escobar, M., Suarez-Vidal, F., Hernandez-Perez, J. A., & Martin-Barajas, A. (2010). Seismic reflection-based evidence of a transfer zone between the Wagner and Consag basins: Implications for defining the structural geometry of the northern Gulf of California. *Geo-Marine Letters, 30*(6), 575-584. https://doi.org/10.1007/s00367-010-0204-0

González-Escobar, M., Suárez-Vidal, F., Sojo-Amezquita, A., Gallardo-Mata, C. G., & Martin-Barajas, A. (2014). Consag basin: Northern Gulf of California, evidence of generation of new crust, based on seismic reflection data. *International Geology Review, 56*(11), 1315-1331. https://doi.org/10.1080/00206814.2014.941023

González-Escobar, M., Mares Agüero, M. A., & Martin, A. (2020). Subsurface structure revealed by seismic reflection images to the southwest of the Cerro Prieto pull-apart basin, Baja California. *Geothermics, 85*, 101779. https://doi.org/10.1016/j.geothermics.2019.101779

Gregg, P. M., Behn, M. D., Lin, J., & Grove, T. L. (2009). Melt generation, crystallization, and extraction beneath segmented oceanic transform faults. *Journal of Geophysical Research: Solid Earth, 114* https://doi.org/10.1029/2008JB006100

Griggs, D. T. (1939). A theory of mountain building. *American Journal of Science, 237*, 611-650. https://doi.org/10.2475/ajs.237.9.611

Grokholskii, A. L., & Dubinin, E. P. (2006). Experimental modeling of structure-forming deformations in rift zones of mid-ocean ridges. *Geotectonics, 40*(1), 64-80. https://doi.org/10.1134/S0016852106010067

Gudmundsson, A. (1995). Stress fields associated with oceanic transform faults. *Earth and Planetary Science Letters, 136*(3), 603-614. https://doi.org/10.1016/0012-821X(95)00164-8

Guo, X., Wu, Z., Yang, X., Xu, H., Zhang, Z., Shi, X., & Sun, Z. (2009). The evolution of transtensional structure and numerical modeling of stress field, Linnan subsag, Bohai bay basin. *Marine Geology & Quaternary Geology, 29*(6), 75-82. https://doi.org/10.1007/s12517-017-2850-2

Hall, J. (1815). II. on the vertical position and convolutions of certain strata, and their relation with granite. *Transactions of the Royal Society of Edinburgh, 7*(1), 79-108. https://doi.org/10.1017/S0080456800019268

Harding, T. P. (1985). Seismic characteristics and identification of negative flower structures, positive flower structures, and positive structural inversion. *AAPG Bulletin, 69*(4), 582-600.

Harland, W. B. (1971). Tectonic transpression in Caledonian Spitzbergen. *Geological Magazine, 108*, 27-42. https://doi.org/10.1017/S0016756800050937

Heezen, B. C., Tharp, M., & Ewing, M. (1959). *The floors of the oceans: I. the North Atlantic.* Geological Society of America. https://doi.org/10.1002/iroh.19620470311

Heezen, B. C. (1960). The rift in the ocean floor. *Scientific American, 203*(4), 98-114.

Heezen, B. C., Bunce, E. T., Hersey, J. B., & Tharp, M. (1964). Chain and Romanche fracture zones. *Deep Sea Research and Oceanographic Abstracts, 11*(1), 11-33. https://doi.org/10.1016/0011-7471(64)91079-4

Heezen, B. C., Gerard, R. D., & Tharp, M. (1964). The Vema fracture zone in the equatorial atlantic. *Journal of Geophysical Research (1896-1977), 69*(4), 733-739. https://doi.org/10.1029/JZ069i004p00733

Heezen, B. C., Tharp, M., Blackett, P. M. S., Bullard, E., & Runcorn, S. K. (1965). Tectonic fabric of the Atlantic and Indian oceans and continental drift. *Philosophical Transactions of the Royal Society of London.Series A, Mathematical and Physical Sciences, 258*(1088), 90-106. https://doi.org/10.1098/rsta.1965.0024

Heine, C., Müller, R. D., & Norvick, M.,. (2002). Revised tectonic evolution of the Northwest shelf of Australia and adjacent abyssal plains. In M. Keep, & S. J. Moss (Eds.), *The sedimentary basins of Western Australia 3: Proceedings of the petroleum exploration society of Australia symposium, Perth, WA, 2002.*

Heister, T., Dannberg, J., Gassmöller, R., & Bangerth, W. (2017). High accuracy mantle convection simulation through modern numerical methods – II: Realistic models and problems. *Geophysical Journal International, 210*(2), 833-851. https://doi.org/10.1093/gji/ggx195

Heron, P. J., Peace, A. L., McCaffrey, K. J., Welford, J. K., Wilson, R., van Hunen, J., & Pysklywec, R. N. (2019). Segmentation of Rifts Through Structural Inheritance: Creation of the Davis Strait. *Tectonics*, 38, 1–20. https://doi.org/10.1029/2019TC005578

Heron, P.J., & Pysklywec R. N. (2016). Inherited structure and coupled crust-mantle lithosphere evolution: Numerical models of Central Australia, *Geophysical Research Letters, 43*(10), 4962-4970. https://doi.org/10.1002/2016GL068562

Heron, P. J., Pysklywec, R. N., & Stephenson, R. (2016). Lasting mantle scars lead to perennial plate tectonics. *Nature Communications, 7*(1), 11834. https://doi.org/10.1038/ncomms11834

Hess, H. H. (1962). History of ocean basins. *Petrologic Studies,* https://doi.org/10.1130/Petrologic.1962.599

Hirth, G., & Kohlstedt, D. (2004). In Eiler J. (Ed.), Rheology of the upper mantle and the mantle wedge: A view from the experimentalists Wiley. https://doi.org/10.1029/138GM06

Holdsworth, R. E., Tavarnelli, E., Clegg, P., Pinheiro, R. V. L., Jones, R. R., & McCaffrey, K. J. W. (2002). Domainal deformation patterns and strain partitioning during transpression: An example from the southern uplands terrane, scotland. *Journal of the Geological Society, 159*(4), 401-415. https://doi.org/10.1144/0016-764901-123

Holmes, A. (1931). XVIII. radioactivity and earth movements. *Transactions of the Geological Society of Glasgow, 18*(3), 559-606.

Houseman, G. (1988). The dependence of convection planform on mode of heating. *Nature, 332*(6162), 346-349. https://doi.org/10.1038/332346a0

Hu, S., O'Sullivan, P. B., Raza, A., & Kohn, B. P. (2001). Thermal history and tectonic subsidence of the Bohai Basin, Northern China: A Cenozoic rifted and local pull-apart basin. *Physics of the Earth and Planetary Interiors, 126*(3), 221-235. https://doi.org/10.1016/S0031-9201(01)00257-6

Hubbert, M. K. (1937). Theory of scale models as applied to the study of geologic structures. *GSA Bulletin, 48*(10), 1459-1520. https://doi.org/10.1130/GSAB-48-1459

Hubbert, M. K. (1951). Mechanical basis for certain familiar geologic structures. *GSA Bulletin, 62*(4), 355-372.

Huguen, C., Guiraud, M., Benkhelil, J., & Mascle, J. (2001). Synlithification deformation processes of the cretaceous sediments of the ivory coast-ghana transform margin: A way to detail the margin history. *Tectonics, 20*(6), 959-975. https://doi.org/10.1029/2001TC900015

Huismans, R., & Beaumont, C. (2011). Depth-dependent extension, two-stage breakup and cratonic underplating at rifted margins. *Nature, 473*, 74-78. https://doi.org/10.1038/nature09988

Humphreys, E. D., & Weldon II, R. J. (1991). Kinematic constraints on the rifting of Baja California. In J. P. Dauphin, & B. R. T. Simoneit (Eds.), *The gulf and peninsular provinces of the Californias* (pp. 217-228) AAPG Memoirs.

Iaffaldano, G., Bodin, T., & Sambridge, M. (2012). Reconstructing plate-motion changes in the presence of finite-rotations noise. *Nature Communications, 3*, 1048. https://doi.org/10.1038/ncomms2051

Illsley-Kemp, F., Bull, J. M., Keir, D., Gerya, T., Pagli, C., Gernon, T., . . . Kendall, J. M. (2018). Initiation of a proto-transform fault prior to seafloor spreading. *Geochemistry, Geophysics, Geosystems, 19*(12), 4744-4756. https://doi.org/10.1029/2018GC007947

Jacoby, W. (1973). Model experiment of plate movements. *Nature Physical Science, 242*, 130-134. doi:https://doi.org/10.1038/physci242130a0

Jeanniot, L., & Buiter, S. J. H. (2018). A quantitative analysis of transtensional margin width. *Earth and Planetary Science Letters, 491*, 95-108. https://doi.org/10.1016/j.epsl.2018.03.003

Jones, R. R., & Holdsworth, R. E. (1998). Oblique simple shear in transpression zones. *Geological Society, London, Special Publications, 135*(1), 35-40. https://doi.org/10.1144/GSL.SP.1998.135.01.03

Kachanov, L. M. (2004). *Fundamentals of the theory of plasticity* Dover Publications, Inc.

Karato, S. (2008). *Deformation of earth materials: An introduction to the rheology of solid earth*. Cambridge: Cambridge University Press. https://doi.org/10.1017/CBO9780511804892

Keondzhyan, V. P., & Monin, A. S. (1980). On the concentration convection in the earth's mantle. Paper presented at the *Doklady Akademii Nauk, , 253*(1) 78-81.

Keondzhyan, V., & Monin, A. (1977). Drift of continents and large-scale displacements of earths pole. *Izvestiya Akademii Nauk Sssr Fizika Zemli,* (11), 22-40.

Kincaid, C., & Olson, P. (1987). An experimental study of subduction and slab migration. *Journal of Geophysical Research: Solid Earth, 92*, 13832-13840. https://doi.org/10.1029/JB092iB13p13832

Klimetz, M. P. (1983). Speculations on the Mesozoic plate tectonic evolution of Eastern China. *Tectonics, 2*(2), 139-166. https://doi.org/10.1029/TC002i002p00139

Konstantinovskaia, E., & Malavieille, J. (2005). Erosion and exhumation in accretionary orogens: Experimental and geological approaches. *Geochemistry, Geophysics, Geosystems, 6*(2) https://doi.org/10.1029/2004GC000794

Koopmann, H., Schreckenberger, B., Franke, D., Becker, K., & Schnabel, M. (2016). The late rifting phase and continental break-up of the southern south Atlantic: The mode and timing of volcanic rifting and formation of earliest oceanic crust. *Geological Society, London, Special Publications, 420*(1), 315-340. https://doi.org/10.1144/SP420.2

Kronbichler, M., Heister, T., & Bangerth, W. (2012). High accuracy mantle convection simulation through modern numerical methods. *Geophysical Journal International, 191*(1), 12-29. https://doi.org/10.1111/j.1365-246X.2012.05609.x

Le Pichon, X. (1968). Sea-floor spreading and continental drift. *Journal of Geophysical Research, 73*(12), 3661-3697. https://doi.org/10.1029/JB073i012p03661

Le Pichon, X., & Hayes, D. E. (1971). Marginal offsets, fracture zones, and the early opening of the South Atlantic. *Journal of Geophysical Research, 76*(26), 6283-6293. https://doi.org/10.1029/JB076i026p06283

Le Pourhiet, L., May, D. A., Huille, L., Watremez, L., & Leroy, S. (2017). A genetic link between transform and hyper-extended margins. *Earth and Planetary Science Letters, 465*, 184-192. https://doi.org/10.1016/j.epsl.2017.02.043

Lee, E. Y., & Wagreich, M. (2017). Polyphase tectonic subsidence evolution of the Vienna basin inferred from quantitative subsidence analysis of the northern and central parts. *International Journal of Earth Sciences (Geologische Rundschau), 106*(2), 687–705. https://doi.org/10.1007/s00531-016-1329-9

Leroy, S., Razin, P., Autin, J., Bache, F., d,Acremont, E., Watremez, L., et al. (2012). From rifting to oceanic spreading in the gulf of aden: A synthesis. *Arabian Journal of Geosciences, 5*(5), 859-901. https://doi.org/10.1007/s12517-011-0475-4

Liang, J., Wang, H., Bai, Y., Ji, X., & Duo, X. (2016). Cenozoic tectonic evolution of the Bohai bay basin and its coupling relationship with Pacific plate subduction. *Journal of Asian Earth Sciences*, 127, 257-266. https://doi.org/10.1016/j.jseaes.2016.06.012

Liangjie, T., Guimei, W., & Xinhuai, Z. (2008). Cenozoic geotectonic evolution of the Bohai basin. *Geological Journal of China Universities*, 14(2), 191-198.

Lister, G., Etheridge, M., & Symonds, P. (1986). Detachment faulting and the evolution of passive continental margins. *Geology, 14*(3), 246-250. https://doi.org/10.1130/0091-7613(1986)14<246:DFATEO>2.0.CO;2

Lizarralde, D., Axen, G. J., Brown, H. E., Fletcher, J. M., Gonzalez-Fernandez, A., Harding, A. J., . . . Umhoefer, P. J. (2007). Variation in styles of rifting in the Gulf of California. *Nature, 448*(7152), 466-469. https://doi.org/10.1038/nature06035

Lonsdale, P. (1989). Geology and tectonic history of the Gulf of California. In E. L. Winterer, D. M. Hussong & R. W. Decker (Eds.), *The Eastern Pacific Ocean and Hawaii, geology of North America* (pp. 499-521) Geological Society of America.

Lorenzo, J. M. (1997). Sheared continent ocean margins: An overview. *Geo-Marine Letters, 17*(1), 1-3. https://doi.org/10.1007/PL00007201

Lorenzo, J. M., & Wessel, P. (1997). Flexure across a continent–ocean fracture zone: The northern Falkland/Malvinas plateau, south atlantic. *Geo-Marine Letters, 17*(1), 110-118. https://doi.org/10.1007/s003670050015

Luth, S., Willingshofer, E., Sokoutis, D., & Cloetingh, S. (2010). Analogue modelling of continental collision: Influence of plate coupling on mantle lithosphere subduction, crustal deformation and surface topography. *Tectonophysics, 484*(1), 87-102. https://doi.org/10.1016/j.tecto.2009.08.043

MacAulay, F. (2015). Sea lion field discovery and appraisal: A turning point for the north Falkland basin. *Petroleum Geoscience, 21*(2-3), 111-124. https://doi.org/10.1144/petgeo2014-044

Machetel, P., Rabinowicz, M., & Bernardet, P. (1986). Three-dimensional convection in spherical shells. *Geophysical & Astrophysical Fluid Dynamics, 37*(1-2), 57-84. https://doi.org/10.1080/03091928608210091

Magee, C., Stevenson, C. T. E., Ebmeier, S. K., Keir, D., Hammond, J. O. S., Gottsmann, J. H., . . . Jackson, M. D. (2018). Magma plumbing systems: A geophysical perspective. *Journal of Petrology, 59*(6), 1217-1251. https://doi.org/10.1093/petrology/egy064

Mann, P. (2007). Global catalogue, classification and tectonic origins of restraining- and releasing bends on active and ancient strike-slip fault systems. *Geological Society, London, Special Publications, 290*(1), 13-142. https://doi.org/10.1144/SP290.2

Mann, P., Hempton, M. R., Bradley, D. C., & Burke, K. (1983). Development of pull-apart basins. *The Journal of Geology, 91*(5), 529-554. https://doi.org/10.1086/628803

Mar-Hernández, E., González-Escobar, M., & Martin-Barajas, A. (2012). Tectonic framework of Tiburon basin, Gulf of California, from seismic reflection evidence. *International Geology Review, 54*(11), 1271-1283. https://doi.org/10.1080/00206814.2011.636988

Marishane, M., Dubois, A. J., Carillat, A., Charlies, E. A., Van Rensburg, T., Sanchez, W., . . . Skosana, G. (2014). Impact of the agulhas falkland transform fault on the petroleum system of three of its neighboring basins. *Source Rocks and Petroleum Systems, 76th EAGE Conference and Exhibition 2014, EAGE,*

Martín-Barajas, A., González-Escobar, M., Fletcher, J. M., Pacheco, M., Oskin, M., & Dorsey, R. (2013). Thick deltaic sedimentation and detachment faulting delay the onset of continental

rupture in the Northern Gulf of California: Analysis of seismic reflection profiles. *Tectonics, 32*(5), 1294-1311. https://doi.org/10.1002/tect.20063

Mascle, J. (1976). Atlantic-type continental margins – distinction of two basic structural types. *Anais Da Academia Brasileira De Ciencias,* (48), 191-197.

Matthews, K. J., Müller, R. D., Wessel, P., & Whittaker, J. M. (2011). The tectonic fabric of the ocean basins. *Journal of Geophysical Research: Solid Earth, 116* https://doi.org/10.1029/2011JB008413

Mauduit, T., & Dauteuil, O. (1996), Small-scale models of oceanic transform zones, *J. Geophys. Res.*, *101*(B9), 20195–20209, https://doi.org/10.1029/96JB01509

McClay, K. R. (1990). Extensional fault systems in sedimentary basins: A review of analogue model studies. *Marine and Petroleum Geology, 7*(3), 206-233. https://doi.org/10.1016/0264-8172(90)90001-W

McClay, K., & Dooley, T. (1995). Analogue models of pull-apart basins. *Geology, 23*(8), 711-714. https://doi.org/10.1130/0091-7613(1995)023<0711:AMOPAB>2.3.CO;2

McKenzie, D. (1967). The viscosity of the mantle. *Geophysical Journal International, 14*(1-4), 297-305. https://doi.org/10.1111/j.1365-246X.1967.tb06246.x

McKenzie, D. P., & Parker, R. L. (1967). The North Pacific: An example of tectonics on a sphere. *Nature, 216*(5122), 1276-1280. https://doi.org/10.1038/2161276a0

Mead, W. J. (1920). Notes on the mechanics of geologic structures. *The Journal of Geology, 28*(6), 505-523. https://doi.org/10.1086/622731

Mello, M. R., Filho, N. C. A., Bender, A., Barbanti, S. M., Takaki, T., Fontes, C. A., & Mohriak, M. (2013). New deepwater frontiers an ocean apart
. *Geo Expro, 10*(2), 6/5/2016.

Mercier de Lépinay, M., Loncke, L., Basile, C., Roest, W. R., Patriat, M., Maillard, A., & De Clarens, P. (2016). Transform continental margins – part 2: A worldwide review. *Tectonophysics, 693, Part A*, 96-115. http://dx.doi.org/10.1016/j.tecto.2016.05.038

Minear, J. W., & Toksoz, M. N. (1970). Thermal regime of a downgoing slab and new global tectonics. *Journal of Geophysical Research (1896-1977), 75*(8), 1397-1419. https://doi.org/10.1029/JB075i008p01397

Mohriak, W. U., & Leroy, S. (2013). Architecture of rifted continental margins and break-up evolution: Insights from the south Atlantic, north Atlantic and Red Sea–Gulf of Aden conjugate margins. *Geological Society, London, Special Publications, 369*(1), 497-535. https://doi.org/10.1144/SP369.17

Morgan, J. P., & Forsyth, D. W. (1988). Three-dimensional flow and temperature perturbations due to a transform offset: Effects on oceanic crustal and upper mantle structure. *Journal of Geophysical Research: Solid Earth, 93*, 2955-2966. https://doi.org/10.1029/JB093iB04p02955

Morgan, J. P., & Parmentier, E. M. (1984). Lithospheric stress near a ridge-transform intersection. *Geophysical Research Letters, 11*(2), 113-116. https://doi.org/10.1029/GL011i002p00113

Morgan, W. J. (1968). Rises, trenches, great faults, and crustal blocks. *Journal of Geophysical Research, 73*(6), 1959-1982. https://doi.org/10.1029/JB073i006p01959

Morley, C., & Alvey, A. (2015). Is spreading prolonged, episodic or incipient in the Andaman Sea? Evidence from deepwater sedimentation. *Journal of Asian Earth Sciences, 98*, 446-456. https://doi.org/10.1016/j.jseaes.2014.11.033

Morley, C. (2017). Cenozoic rifting, passive margin development and strike-slip faulting in the Andaman sea: A discussion of established v. new tectonic models. *Geological Society, London, Memoirs, 47*(1), 27-50. https://doi.org/10.1144/M47.4

Morley, C. K., & Searle, M. (2017). Regional tectonics, structure and evolution of the Andaman–Nicobar Islands from ophiolite formation and obduction to collision and back-arc spreading. *Geological Society, London, Memoirs, 47*(1), 51-74. https://doi.org/10.1144/M47.5

Morrow, T. A., Mittelstaedt, E., & Kim, S. (2019). Are segmented fracture zones weak? analytical and numerical models constrain anomalous bathymetry at the Clarion and Murray Fracture Zones. *Earth and Planetary Science Letters, 512*, 214-226. https://doi.org/10.1016/j.epsl.2019.02.010

Müller, R. D., Sdrolias, M., Gaina, C., & Roest, W. R. (2008). Age, spreading rates, and spreading asymmetry of the world's ocean crust. *Geochemistry, Geophysics, Geosystems, 9*(4), n/a-n/a. https://doi.org/10.1029/2007GC001743

Naliboff, J. B., Glerum, A., Brune, S., Péron-Pinvidic, G., & Wrona, T. (2020). Development of 3-D rift heterogeneity through fault network evolution. *Geophysical Research Letters, 47*(13), e2019GL086611. https://doi.org/10.1029/2019GL086611

Naliboff, J., & Buiter, S. J. H. (2015). Rift reactivation and migration during multiphase extension. *Earth and Planetary Science Letters, 421*, 58-67. https://doi.org/10.1016/j.epsl.2015.03.050

Nemcok, M., Rybár, S., Sinha, S. T., Hermeston, S. A., & Ledvényiová, L. (2016). Transform margins: Development, controls and petroleum systems – an introduction. *Geological Society, London, Special Publications, 431* https://doi.org/10.1144/SP431.15

Nonn, C., Leroy, S., Khanbari, K., & Ahmed, A. (2017). Tectono-sedimentary evolution of the eastern Gulf of Aden conjugate passive margins: Narrowness and asymmetry in oblique rifting context. *Tectonophysics, 721*, 322-348. https://doi.org/10.1016/j.tecto.2017.09.024

Oakey, G. N., & Chalmers, J. A. (2012). A new model for the Paleogene motion of Greenland relative to North America: Plate reconstructions of the Davis Strait and Nares Strait regions between Canada and Greenland. *Journal of Geophysical Research: Solid Earth, 117* https://doi.org/10.1029/2011JB008942

Oldenburg, D. W., & Brune, J. N. (1972). Ridge transform fault spreading pattern in freezing wax. *Science, 178*(4058), 301-304. https://doi.org/10.1126/science.178.4058.301

Peace, A., McCaffrey, K., Imber, J., Phethean, J., Nowell, G., Gerdes, K., & Dempsey, E. (2016). An evaluation of Mesozoic rift-related magmatism on the margins of the Labrador Sea: Implications for rifting and passive margin asymmetry. *Geosphere, 12*(6), 1701-1724. https://doi.org/10.1130/GES01341.1

Peace, A., McCaffrey, K. J. W., Imber, J., van Hunen, J., Hobbs, R. W., & Wilson, R. (2017). The role of pre-existing structures during rifting, continental breakup and transform system development, offshore west Greenland. *Basin Research, 30*(3) doi:https://doi.org/10.1111/bre.12257

Persaud, P., Stock, J. M., Steckler, M. S., Martín-Barajas, A., Diebold, J. B., González-Fernández, A., & Mountain, G. S. (2003). Active deformation and shallow structure of the Wagner, Consag, and Delfín basins, Northern Gulf of California, Mexico. *Journal of Geophysical Research: Solid Earth, 108*(B7),2355. https://doi.org/10.1029/2002JB001937

Persaud, P., Pérez-Campos, X., & Clayton, R. W. (2007). Crustal thickness variations in the margins of the Gulf of California from receiver functions. *Geophysical Journal International, 170*(2), 687-699. https://doi.org/10.1111/j.1365-246X.2007.03412.x

Persaud, P., Di Luccio, F., & Clayton, R. W. (2015). Rayleigh wave dispersion measurements reveal low-velocity zones beneath the new crust in the Gulf of California. *Geophysical Research Letters, 42*(6), 1766-1774. https://doi.org/10.1002/2015GL063420

Persaud, P., Tan, E., Contreras, J., & Lavier, L. (2017). A bottom-driven mechanism for distributed faulting in the Gulf of California rift. *Tectonophysics, 719-720*, 51-65. https://doi.org/10.1016/j.tecto.2016.11.024

Phethean, J. J. J., Kalnins, L. M., van Hunen, J., Biffi, P. G., Davies, R. J., & McCaffrey, K. J. W. (2016). Madagascar's escape from Africa: A high-resolution plate reconstruction for the Western Somali Basin and implications for supercontinent dispersal. *Geochemistry, Geophysics, Geosystems, 17*(12), 5036-5055. https://doi.org/10.1002/2016GC006624

Philippon, M., Willingshofer, E., Sokoutis, D., Corti, G., Sani, F., Bonini, M., & Cloetingh, S. (2015). Slip re-orientation in oblique rifts. *Geology, 43*(2), 147-150. https://doi.org/10.1130/G36208.1

Prol-Ledesma, R. M., & Morán-Zenteno, D. J. (2019). Heat flow and geothermal provinces in mexico. *Geothermics, 78*, 183-200. https://doi.org/10.1016/j.geothermics.2018.12.009

Qi, J., & Yang, Q. (2010). Cenozoic structural deformation and dynamic processes of the Bohai Bay Basin province, China. *Marine and Petroleum Geology, 27*(4), 757-771. https://doi.org/10.1016/j.marpetgeo.2009.08.012

Rahe, B., Ferrill, D. A., & Morris, A. P. (1998). Physical analog modeling of pull-apart basin evolution. *Tectonophysics, 285*(1), 21-40. https://doi.org/10.1016/S0040-1951(97)00193-5

Ramberg, H. (1967). Model experimentation of the effect of gravity on tectonic processes. *Geophysical Journal of the Royal Astronomical Society, 14*(1-4), 307-329. https://doi.org/10.1111/j.1365-246X.1967.tb06247.x

Ramberg, H. (1981). *Gravity, deformation, and the earth's crust: In theory, experiments, and geological application* Academic press.

Reber, J. E., Cooke, M. L., & Dooley, T. P. (2020). What model material to use? A review on rock analogs for structural geology and tectonics. *Earth-Science Reviews, 202*, 103107. https://doi.org/10.1016/j.earscirev.2020.103107

Reeves, C. V., Teasdale, J. P., & Mahanjane, E. S. (2016). Insight into the Eastern Margin of Africa from a new tectonic model of the Indian Ocean. *Geological Society, London, Special Publications, 431*(1), 299. https://doi.org/10.1144/SP431.12

Reid, D. I., & Jackson, H. R. (1997). A review of three transform margins off eastern Canada. *Geo-Marine Letters, 17*(1), 87-93. https://doi.org/10.1007/s003670050012

Reid, H. F., Davis, W. M., Lawson, A. C., & Ransome, F. L. (1913). Report of the committee on the nomenclature of faults. *GSA Bulletin, 24*(1), 163-186. https://doi.org/10.1130/GSAB-24-163

Rodriguez, M., Huchon, P., Chamot-Rooke, N., Fournier, M., Delescluse, M., & François, T. (2016). Tracking the paleogene india-arabia plate boundary. *Marine and Petroleum Geology, 72*, 336-358. https://doi.org/10.1016/j.marpetgeo.2016.02.019

Rose, I., Buffett, B., & Heister, T. (2017). Stability and accuracy of free surface time integration in viscous flows. *Physics of the Earth and Planetary Interiors, 262*, 90-100. https://doi.org/10.1016/j.pepi.2016.11.007

Rüpke, L. H., Schmid, D. W., Hartz, E. H., & Martinsen, B. (2010). Basin modelling of a transform margin setting: Structural, thermal and hydrocarbon evolution of the tano basin, ghana. *Petroleum Geoscience, 16*(3), 283-298. https://doi.org/10.1144/1354-079309-905

Rutter, E. H., & Brodie, K. H. (2004). Experimental intracrystalline plastic flow in hot-pressed synthetic quartzite prepared from brazilian quartz crystals. *Journal of Structural Geology, 26*(2), 259-270. https://doi.org/10.1016/S0191-8141(03)00096-8

Ryan, W. B. F., Carbotte, S. M., Coplan, J. O., O'Hara, S., Melkonian, A., Arko, R., . . . Zemsky, R. (2009). Global multi-resolution topography synthesis. *Geochemistry, Geophysics, Geosystems, 10*(3) https://doi.org/10.1029/2008GC002332

Rybacki, E., Gottschalk, M., Wirth, R., & Dresen, G. (2006). Influence of water fugacity and activation volume on the flow properties of fine-grained anorthite aggregates. *Journal of Geophysical Research: Solid Earth, 111* https://doi.org/10.1029/2005JB003663

Sanderson, D. J., & Marchini, W. (1984). Transpression. *Journal of Structural Geology, 6*(5), 449-458. https://doi.org/10.1016/0191-8141(84)90058-0

Sauter, D., Ringenbach, J. C., Cannat, M., Maurin, T., Manatschal, G., & McDermott, K. G. (2018). Intraplate deformation of oceanic crust in the West Somali Basin: Insights from long-offset reflection seismic data. *Tectonics, 37*(2), 588-603. https://doi.org/10.1002/2017TC004700

Schellart, W. P. (2000). Shear test results for cohesion and friction coefficients for different granular materials: Scaling implications for their usage in analogue modelling. *Tectonophysics, 324*(1), 1-16. https://doi.org/10.1016/S0040-1951(00)00111-6

Schellart, W. P., & Strak, V. (2016). A review of analogue modelling of geodynamic processes: Approaches, scaling, materials and quantification, with an application to subduction experiments. *Journal of Geodynamics, 100*, 7-32. https://doi.org/10.1016/j.jog.2016.03.009

Schettino, A. (2015). Plate motions. In A. Schettino (Ed.), *Quantitative plate tectonics: Physics of the earth - plate kinematics & geodynamics* (pp. 29-80). Cham: Springer International Publishing. https://doi.org10.1007/978-3-319-09135-8_2 Retrieved from https://doi.org/10.1007/978-3-319-09135-8_2

Schiffer, C., Peace, A., Phethean, J., Gernigon, L., McCaffrey, K., Petersen, K. D., & Foulger, G. (2018). The jan mayen microplate complex and the wilson cycle. *Geological Society, London, Special Publications, 470* https://doi.org/10.1144/SP470.2

Schubert, G., Turcotte, D. L., & Olson, P. (2001). *Mantle convection in the earth and planets*. Cambridge: Cambridge University Press. https://doi.org/10.1017/CBO9780511612879

Scrutton, R. A. (1979). On sheared passive continental margins. *Tectonophysics, 59*(1), 293-305. https://doi.org/10.1016/0040-1951(79)90051-9

Scrutton, R. A. (1982). Crustal structure of sheared passive continental margins. In R. A. Scrutton (Ed.), *Dynamics of passive margins volume 6* (pp. 133-140). Washington DC: American Geophysical Union.

Seiler, C., Gleadow, A. J. W., Fletcher, J. M., & Kohn, B. P. (2009). Thermal evolution of a sheared continental margin: Insights from the Ballenas transform in Baja California, Mexico. *Earth and Planetary Science Letters, 285*(1–2), 61-74. http://dx.doi.org/10.1016/j.epsl.2009.05.043

Shemenda, A. I. (1993). Subduction of the lithosphere and back arc dynamics: Insights from physical modeling. *Journal of Geophysical Research: Solid Earth, 98*, 16167-16185. https://doi.org/10.1029/93JB01094

Shemenda, A. I., & Grocholsky, A. L. (1994). Physical modeling of slow seafloor spreading. *Journal of Geophysical Research, 99*(B5), 9137-9153. https://doi.org/10.1029/93JB02995

Shen, Y., & Forsyth, D. W. (1992). The effects of temperature- and pressure-dependent viscosity on three-dimensional passive flow of the mantle beneath a ridge-transform system. *Journal of Geophysical Research: Solid Earth, 97*, 19717-19728. https://doi.org/10.1029/92JB01467

Sibrant, A. L. R., Mittelstaedt, E., Davaille, A., Pauchard, L., Aubertin, A., Auffray, L., & Pidoux, R. (2018). Accretion mode of oceanic ridges governed by axial mechanical strength. *Nature Geoscience, 11*(4), 274-279. https://doi.org/10.1038/s41561-018-0084-x

Sims, D., Ferrill, D. A., & Stamatakos, J. A. (1999). Role of a ductile décollement in the development of pull-apart basins: Experimental results and natural examples. *Journal of Structural Geology, 21*(5), 533-554. https://doi.org/10.1016/S0191-8141(99)00010-3

Smit, J., Brun, J. -., Fort, X., Cloetingh, S., & Ben-Avraham, Z. (2008). Salt tectonics in pull-apart basins with application to the Dead Sea Basin. *Tectonophysics, 449*(1), 1-16. https://doi.org/10.1016/j.tecto.2007.12.004

Sokoutis D., Bonini M., Medvedev S., Boccaletti M., Talbot C.J. & Koyi H., 2000. Indentation of a continent with a built-in thickness change: experiment and nature. *Tectonophysics; Special volume "numerical modelling" (Eds. S. Cloetingh & Podladchikov), v. 320*, pp 243-270. https://doi.org/10.1016/S0040-1951(00)00043-3

Sokoutis, D., Burg, J., Bonini, M., Corti, G., & Cloetingh, S. (2005). Lithospheric-scale structures from the perspective of analogue continental collision. *Tectonophysics, 406*(1), 1-15. https://doi.org/10.1016/j.tecto.2005.05.025

Srisuriyon, K., & Morley, C. (2014). Pull-apart development at overlapping fault tips: Oblique rifting of a Cenozoic continental margin, northern Mergui basin, Andaman sea. *Geosphere, 10*(1), 80-106. https://doi.org/10.1130/GES00926.1

Stagg, H. M. J., Alcock, M. B., Bernardel, G., Moore, A. M. G., Symonds, P. A., & Exon, N. F. (2004). *Geological framework of the outer Exmouth Plateau and adjacent ocean basins.* (Geoscience Australia Record 2004/13).

Stewart, J. R., Betts, P. G., Collins, A. S., & Schaefer, B. F. (2009). Multi-scale analysis of proterozoic shear zones: An integrated structural and geophysical study. *Journal of Structural Geology, 31*(10), 1238-1254. https://doi.org/10.1016/j.jsg.2009.07.002

Stock, J. M., Mountain, G. S., Diebold, J. B., Steckler, M. S., & Martin-Barajas, A. (2005). HiRes multi-channel seismic shot data from the northern gulf of california acquired during the R/V francisco de ulloa expedition UL9905 (1999). *Integrated Earth Data Applications (IEDA).,* https://doi.org/10.1594/IEDA/303735

Stock, J., & Hodges, K. (1989). Pre-Pliocene extension around the Gulf of California and the transfer of Baja California to the Pacific Plate. *Tectonics, 8*(1), 99-115. https://doi.org/10.1029/TC008i001p00099

Stoddard, P. R., & Stein, S. (1988). A kinematic model of ridge-transform geometry evolution. *Marine Geophysical Researches, 10*(3-4), 181-190. https://doi.org/10.1007/BF00310063

Sugan, M., Wu, J., & McClay, K. (2014). 3D analogue modelling of transtensional pull-apart basins: Comparison with the Cinarcik Basin, Sea of Marmara, Turkey. *Bollettino Di Geofisica Teorica Ed Applicata, 55*(4)

Sylvester, A. G. (1988). Strike-slip faults. *Geological Society of America Bulletin, 100*(11), 1666-1703.

Talwani, M., & Eldholm, O. (1973). Boundary between continental and oceanic crust at the margin of rifted continents. *Nature, 241*, 325. https://doi.org/10.1038/241325a0

Taylor, B., Goodliffe, A., & Martinez, F. (2009). Initiation of transform faults at rifted continental margins. *Comptes Rendus Geoscience, 341*(5), 428-438. https://doi.org/10.1016/j.crte.2008.08.010

Tchalenko, J. S. (1970). Similarities between shear zones of different magnitudes. *GSA Bulletin, 81*(6), 1625-1940. https://doi.org/10.1130/0016-7606(1970)81[1625:SBSZOD]2.0.CO;2

ten Brink, U. S., Katzman, R., & Lin, J. (1996). Three-dimensional models of deformation near strike-slip faults. *Journal of Geophysical Research: Solid Earth, 101*, 16205-16220. https://doi.org/10.1029/96JB00877

ten Grotenhuis, S. M., Piazolo, S., Pakula, T., Passchier, C. W., & Bons, P. D. (2002). Are polymers suitable rock analogs? *Tectonophysics, 350*(1), 35-47. https://doi.org/10.1016/S0040-1951(02)00080-X

Tentler, T., & Acocella, V. (2010). How does the initial configuration of oceanic ridge segments affect their interaction? insights from analogue models. *Journal of Geophysical Research: Solid Earth, 115* https://doi.org/10.1029/2008JB006269

Teyssier, C., & Tikoff, B. (1998). Strike-slip partitioned transpression of the san andreas fault system: A lithospheric-scale approach. *Geological Society, London, Special Publications, 135*(1), 143-158. https://doi.org/10.1144/GSL.SP.1998.135.01.10

Torrance, K. E., & Turcotte, D. L. (1971). Thermal convection with large viscosity variations. *Journal of Fluid Mechanics, 47*(1), 113-125. https://doi.org/10.1017/S002211207100096X

Tron, V., & Brun, J. (1991). Experiments on oblique rifting in brittle-ductile systems. *Tectonophysics, 188*(1-2), 71-84. https://doi.org/10.1016/0040-1951(91)90315-J

Tuck-Martin, A., Adam, J., & Eagles, G. (2018). New plate kinematic model and tectono-stratigraphic history of the east african and west madagascan margins. *Basin Research, 30*(6), 1118-1140. https://doi.org/10.1111/bre.12294

Tugend, J., Gillard, M., Manatschal, G., Nirrengarten, M., Harkin, C., Epin, M., . . . McDermott, K. (2018). Reappraisal of the magma-rich versus magma-poor rifted margin archetypes. *Geological Society, London, Special Publications, 476*, SP476.9. https://doi.org/10.1144/SP476.9

Turcotte, D. L. (1974). Are transform faults thermal contraction cracks? *Journal of Geophysical Research, 79*(17), 2573-2577. https://doi.org/10.1029/JB079i017p02573

Turcotte, D. L., & Schubert, G. (2002). *Geodynamics* Cambridge university press.

Umhoefer, P. J., Darin, M. H., Bennett, S. E. K., Skinner, L. A., Dorsey, R. J., & Oskin, M. E. (2018). Breaching of strike-slip faults and successive flooding of pull-apart basins to form the Gulf of

California seaway from ca. 8–6 ma. *Geology, 46*(8), 695-698. https://doi.org/10.1130/G40242.1

van Wijk, J., Axen, G., & Abera, R. (2017). Initiation, evolution and extinction of pull-apart basins: Implications for opening of the Gulf of California. *Tectonophysics, 719-720*, 37-50. https://doi.org/10.1016/j.tecto.2017.04.019

Vendeville, B., Cobbold, P. R., Davy, P., Choukroune, P., & Brun, J. P. (1987). Physical models of extensional tectonics at various scales. *Geological Society, London, Special Publications, 28*(1), 95. https://doi.org/10.1144/GSL.SP.1987.028.01.08

Wegener, A. (1912). Die entstehung der kontinente. *Geologische Rundschau, 3*(4), 276-292.

Weijermars, R. (1986a). Flow behaviour and physical chemistry of bouncing putties and related polymers in view of tectonic laboratory applications. *Tectonophysics, 124*(3-4), 325-358 https://doi.org/10.1016/0040-1951(86)90208-8

Weijermars, R. (1986b). Polydimethylsiloxane flow defined for experiments in fluid dynamics. *Applied Physics Letters, 48*(2), 109-111. https://doi.org/10.1063/1.97008

Weijermars, R. (1986c). Finite strain of laminar flows can be visualized in SGM 36-polymer. *Naturwissenschaften* 73, 33.

Weijermars, R., & Schmeling, H. (1986d). Scaling of newtonian and non-newtonian fluid dynamics without inertia for quantitative modelling of rock flow due to gravity (including the concept of rheological similarity). *Physics of the Earth and Planetary Interiors, 43*(4), 316-330. https://doi.org/10.1016/0031-9201(86)90021-X

Weijermars, R., Jackson, M. P. A., & Vendeville, B. (1993). Rheological and tectonic modeling of salt provinces. *Tectonophysics, 217*(1), 143-174. https://doi.org/10.1016/0040-1951(93)90208-2

Whaley, J. (2010). From gold coast to black gold. *Geo Expro, 7*(3), 6/5/2016.

Whittaker, J. M., Williams, S. E., Halpin, J. A., Wild, T. J., Stilwell, J. D., Jourdan, F., & Daczko, N. R. (2016). Eastern Indian Ocean microcontinent formation driven by plate motion changes. *Earth and Planetary Science Letters, 454*, 203-212. https://doi.org/10.1016/j.epsl.2016.09.019

Wickham, J. (2007). Comment on “Basin inversion and fault reactivation in laboratory experiments”. *Journal of Structural Geology, 29*(8), 1414-1416. https://doi.org/10.1016/j.jsg.2007.05.002

Wilcox, R. E., & Harding, T.DR seely, 1973. *Basic Wrench Tectonics: AAPG Bulletin, 57*(1), 74-96.

Willett, S. D. (1992). Dynamic and kinematic growth and change of a coulomb wedge. In K. R. McClay (Ed.), *Thrust tectonics* (pp. 19-31). Dordrecht: Springer Netherlands. doi:10.1007/978-94-011-3066-0_2 Retrieved from https://doi.org/10.1007/978-94-011-3066-0_2

Willingshofer E., Sokoutis D. & Burg J.P., 2005. Lithospheric scale analogue modelling of collision zones invoking a pre-existing weak zone. In “Deformation Mechanisms, Rheology and Tectonics: from Minerals to the Lithosphere” (Eds. Gapais D., Brun J.P. & Cobbold P.R.). *Geological Society, London, Special Publications, 243*, pp 277-294.

Willingshofer E., Sokoutis D., Beekman F., Schönebeck J-M., Warsitzka M., Rosenau M. 2018. Ring shear test data of feldspar sand and quartz sand used in Tectonic Laboratory (TecLab) at Utrecht University for experimental Earth Science applications. *GFZ Data Services., V.1. GFZ Data Services*. http://doi.org/10.5880/fidgeo.2018.072

Wilson, J. T. (1965). A new class of faults and their bearing on continental drift. *Nature, 207*(4995), 343-347. https://doi.org/10.1038/207343a0

Wilson, R. W., Klint, K. E. S., van Gool, J. A. M., McCaffrey, K. J. W., Holdsworth, R. E., & Chalmers, J. A. (2006). Faults and fractures in central west Greenland: Onshore expression of continental break-up and sea-floor spreading in the Labrador - Baffin bay sea. *Geological Survey of Denmark and Greenland Bulletin*, (11), 185-204. https://doi.org/10.34194/geusb.v11.4931

Withjack, M. O., & Jamison, W. R. (1986). Deformation produced by oblique rifting. *Tectonophysics, 126*(2), 99-124. https://doi.org/10.1016/0040-1951(86)90222-2

Woidt, W. -. (1978). Finite element calculations applied to salt dome analysis. *Tectonophysics, 50*(2), 369-386. https://doi.org/10.1016/0040-1951(78)90143-9

Woodcock, N. H. (1986). The role of strike-slip fault systems at plate boundaries. *Philosophical Transactions of the Royal Society of London.Series A, Mathematical and Physical Sciences, 317*(1539), 13-29. https://doi.org/10.1098/rsta.1986.0021

Wright, J. B. (1976). Fracture systems in nigeria and initiation of fracture zones in the south atlantic. *Tectonophysics, 34*(3), 43-47. https://doi.org/10.1016/0040-1951(76)90093-7

Wu, J. E., McClay, K., Whitehouse, P., & Dooley, T. (2009). 4D analogue modelling of transtensional pull-apart basins. *Marine and Petroleum Geology, 26*(8), 1608-1623. https://doi.org/10.1016/j.marpetgeo.2008.06.007

Zadeh, A. I., & Tackley, P. J. (2010). Finite element method. *Computational methods for geodynamics* (pp. 63-92) Cambridge University Press.

Zulauf, J., & Zulauf, G. (2004). Rheology of plasticine used as rock analogue: The impact of temperature, composition and strain. *Journal of Structural Geology, 26*(4), 725-737. https://doi.org/10.1016/j.jsg.2003.07.005

Zwaan, F., & Schreurs, G. (2017). How oblique extension and structural inheritance influence rift segment interaction: Insights from 4D analog models. *Interpretation, 5*(1), 119-138. https://doi.org/10.1190/INT-2016-0063.1

Appendices

Appendix A – Suppl. Material for Chapter 4

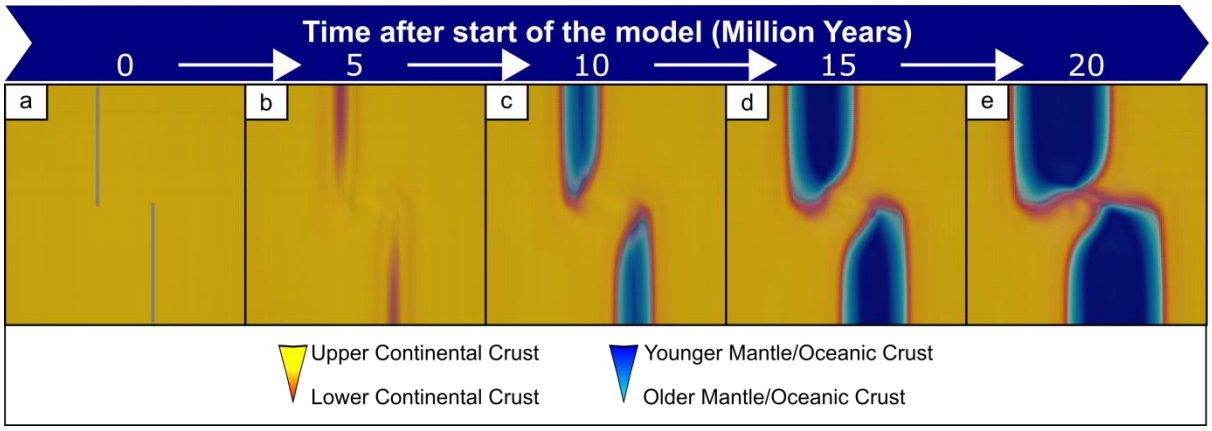

Figure A1 – Orthogonal rifting connectivity test (same offset as control model in Figure 4.3 in thesis without a connecting seed).

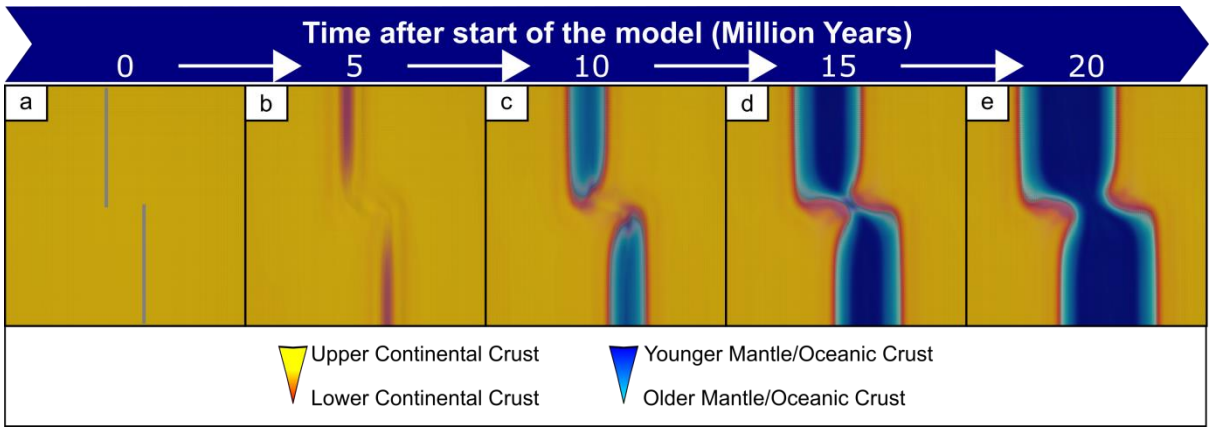

Figure A2 – Orthogonal rifting connectivity test (120 km offset between the two non-connected rift seeds).

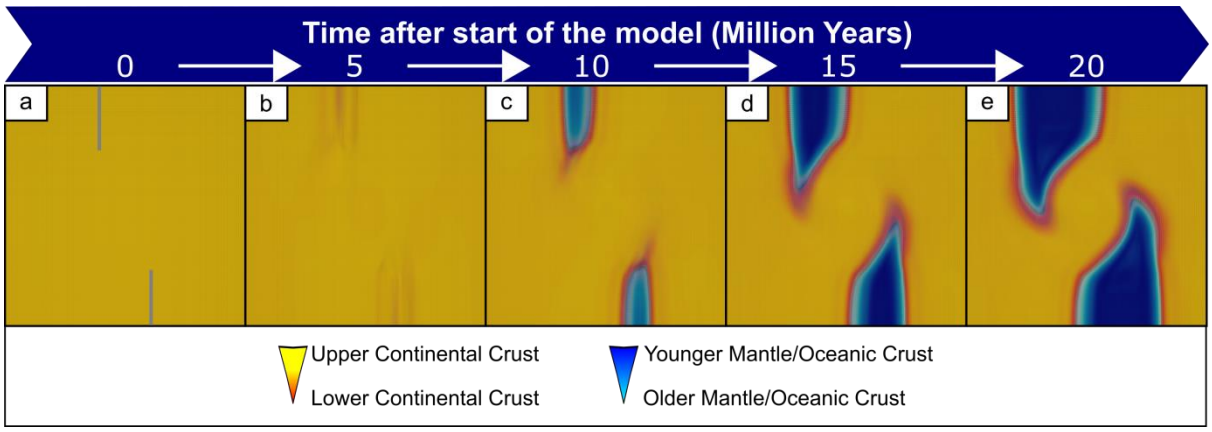

Figure A3 – Orthogonal rifting connectivity test, (same offset as control model in Figure A1 but with shorter rift seeds).

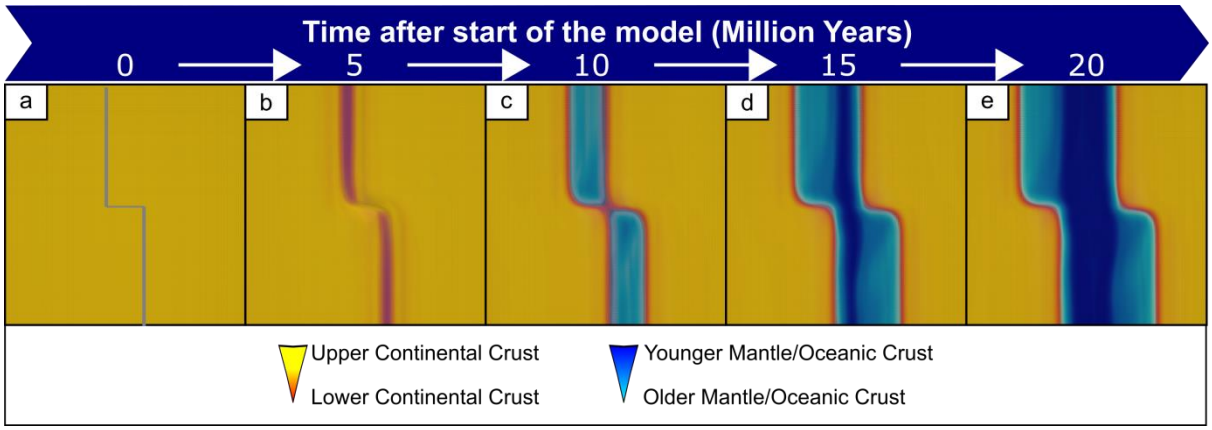

Figure A4 – Transform length test, same configuration as control experiment (Figure 4.3 in thesis) but with the rifts spaced 120 km apart.

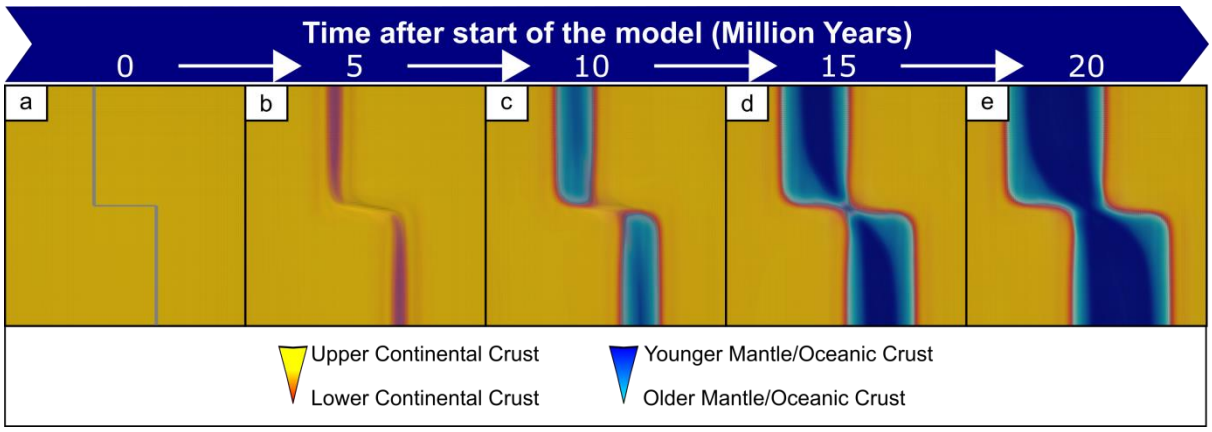

Figure A5 – Transform length test, same configuration as control experiment (Figure 4.3 in thesis) but with the rifts spaced 200 km apart.

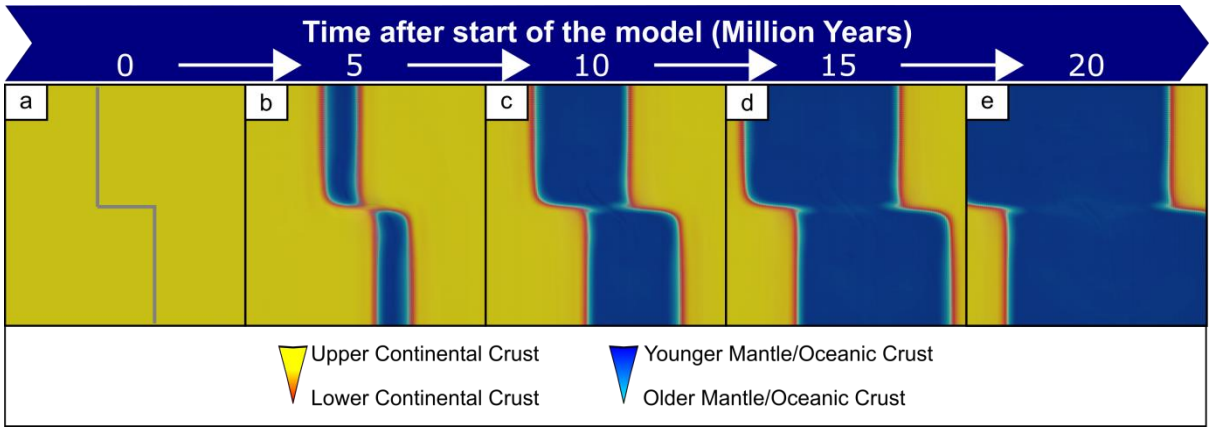

Figure A6 – Sensitivity test, same configuration as control experiment (Figure 4.3 in thesis) but with double the extension rate.

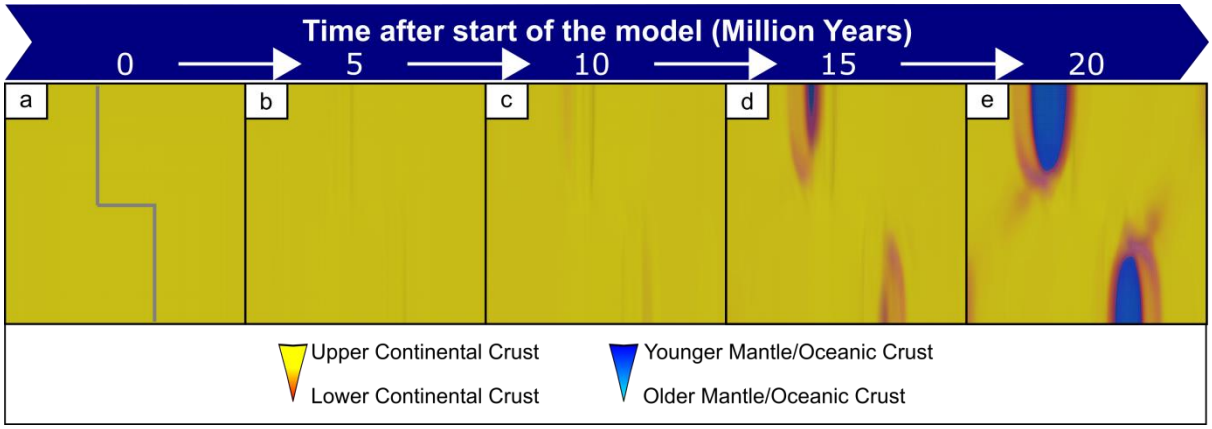

Figure A7 – Sensitivity test, same configuration as control experiment (Figure 4.3 in thesis) but with a 10 degree internal friction angle in the seed.

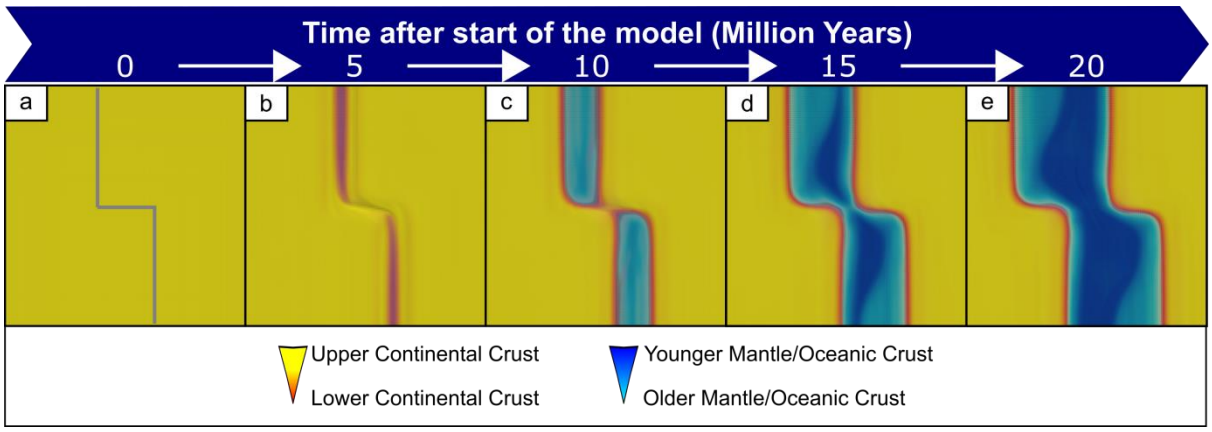

Figure A8 – Sensitivity test, same configuration as control experiment (Figure 4.3 in thesis) but with a 30 degree internal friction angle in the crust.

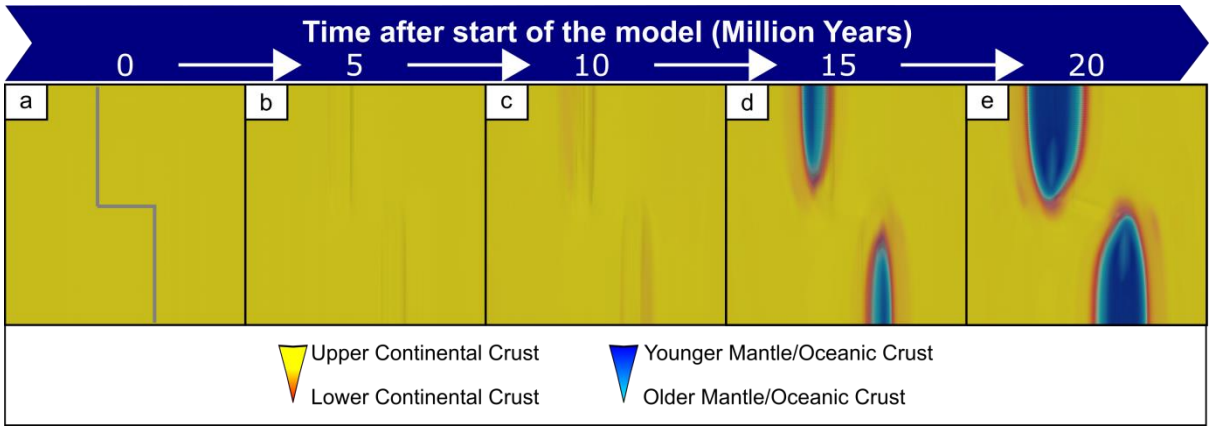

Figure A9 – Sensitivity test, same configuration as control experiment (Figure 4.3 in thesis) but with a 10 degree internal friction angle in the seed and a 30 degree internal friction angle in the crust.

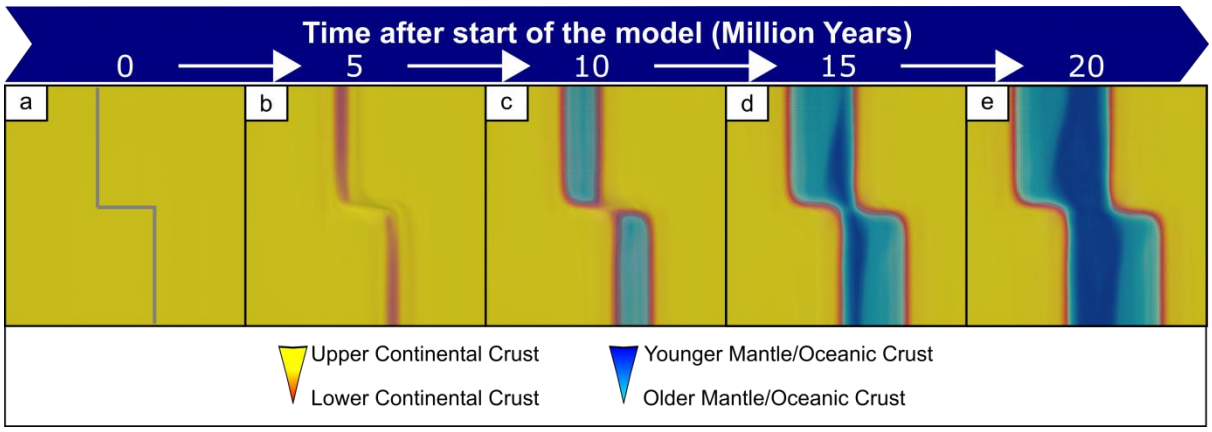

Figure A10 – Sensitivity test, same configuration as control experiment (Figure 4.3 in thesis) but with narrower plasticity intervals (0.03-0.3).

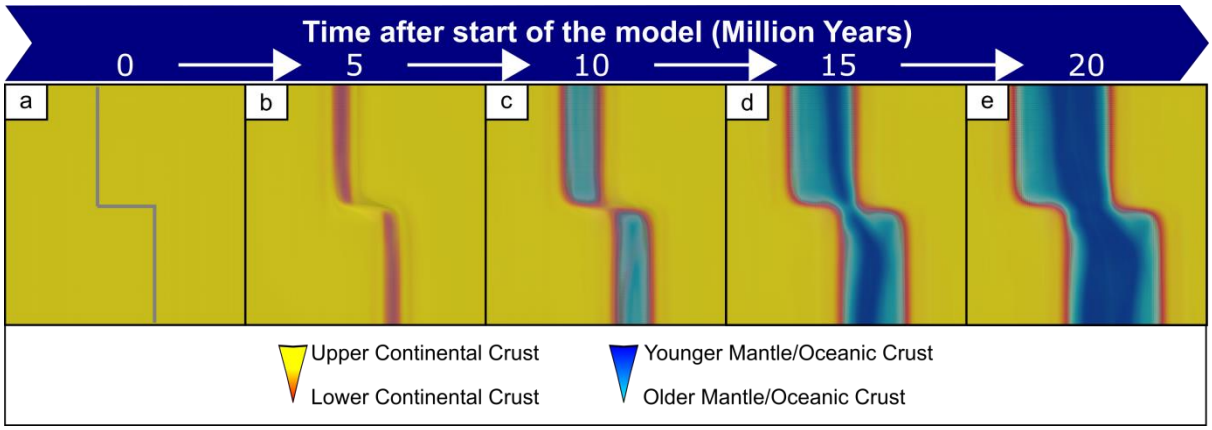

Figure A11 – Sensitivity test, same configuration as control experiment (Figure 4.3 in thesis) but with a reduced cohesion for all the layers.

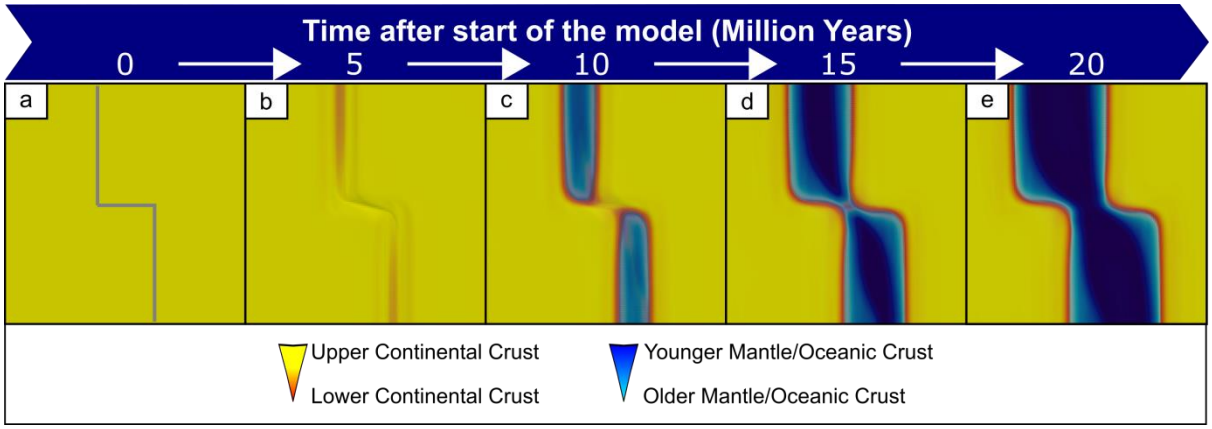

Figure A12 – Sensitivity test, same configuration as control experiment (Figure 4.3 in thesis) but with an increased top mantle temperature at 850 degrees.

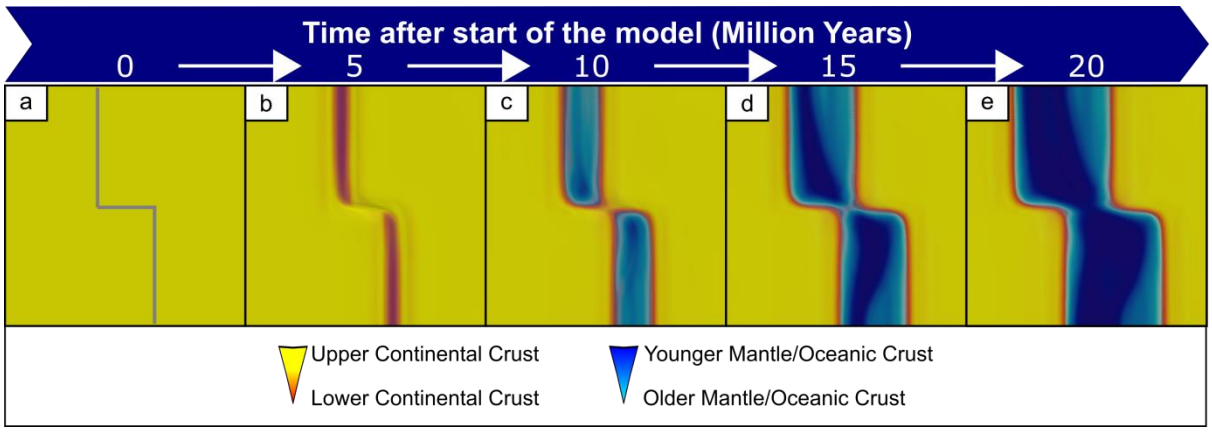

Figure A13 – Sensitivity test, same configuration as control experiment (Figure 4.3 in thesis) but with a reduced top mantle temperature at 800 degrees.

Experiment Supplementary Material

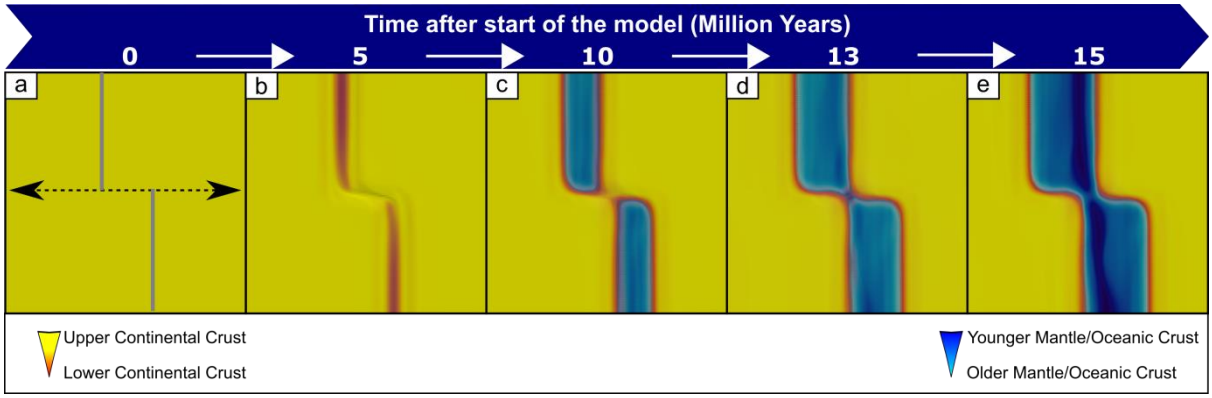

Figure A14 – Uninterpreted version of Figure 4.3 in the thesis.

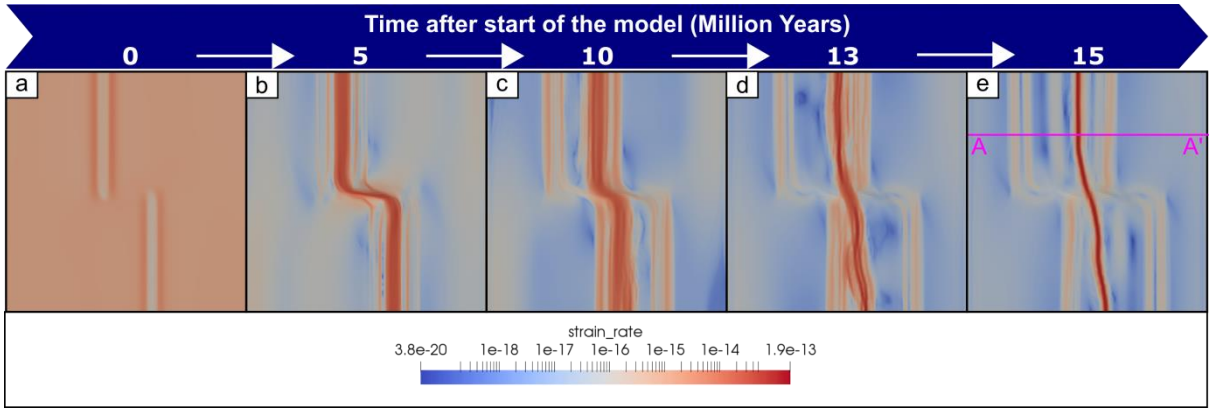

Figure A15 – Strain rate of the models shown in Figure 4.3 in the thesis. Panel e display cross-section shown in Figure A16.

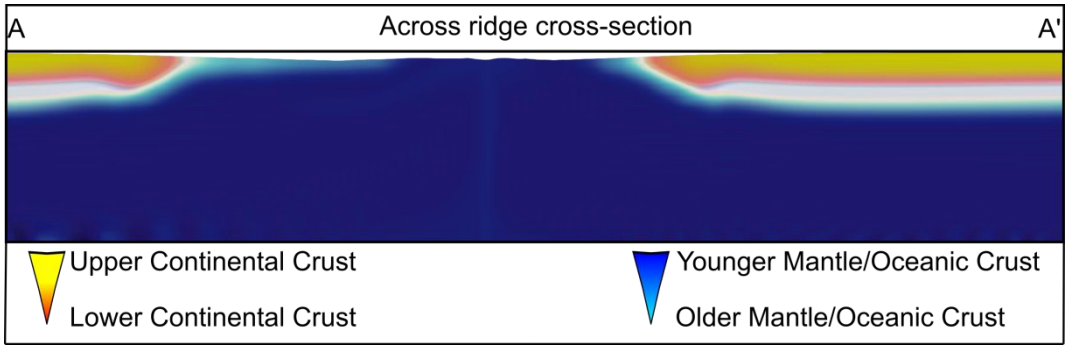

Figure A16 – Control experiment (Figure 4.3) cross sections. For cross-section locations refer to Figure A15.

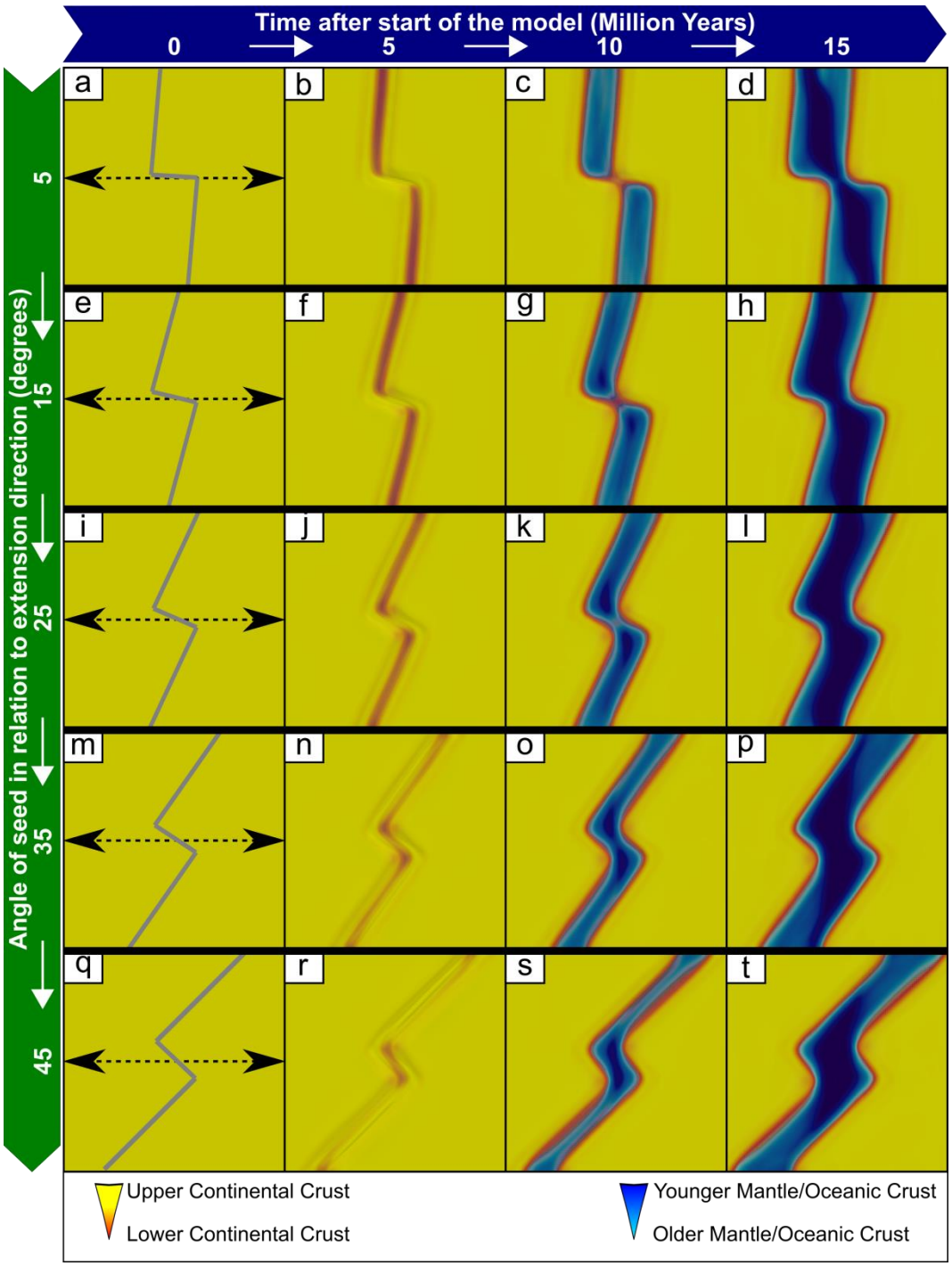

Figure A17 – Uninterpreted version of Figure 4.4 in the thesis.

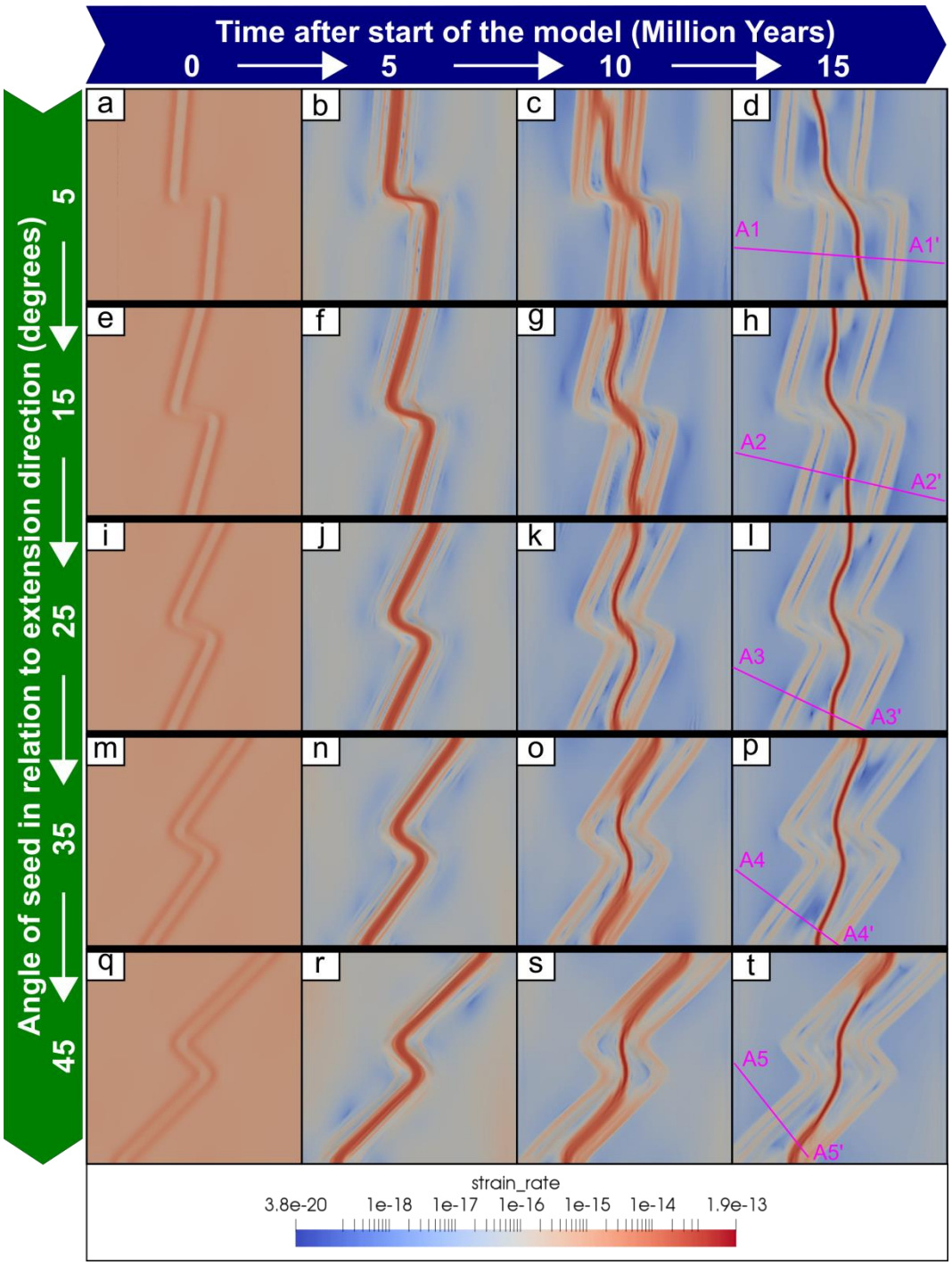

Figure A18 – Strain rate of the models shown in Figure 4.4 in the thesis. Panels d,h,l,p,t display cross-sections shown in Figure A20.

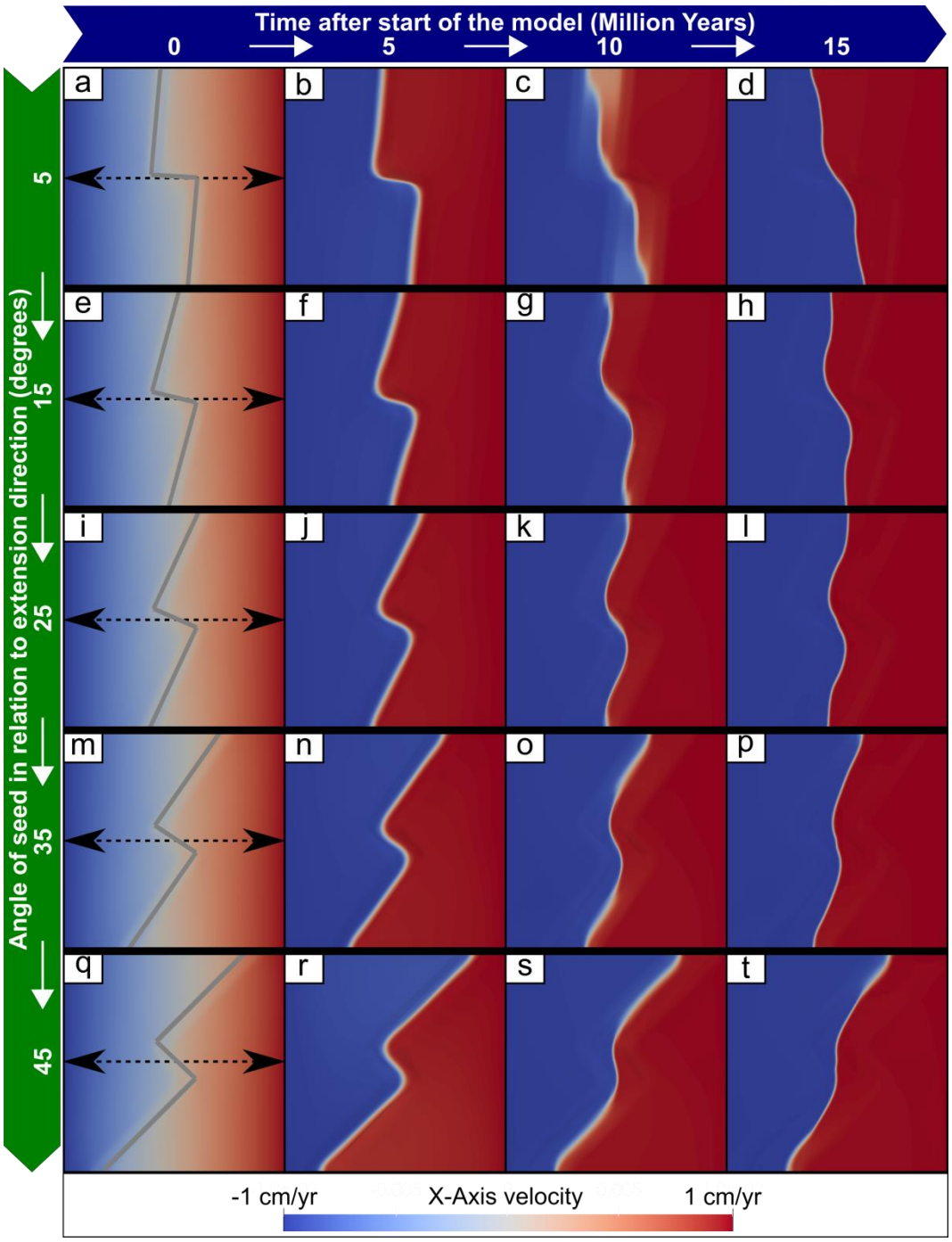

Figure A19 – X-Axis velocity plots of the models shown in Figure 4.4 in the thesis.

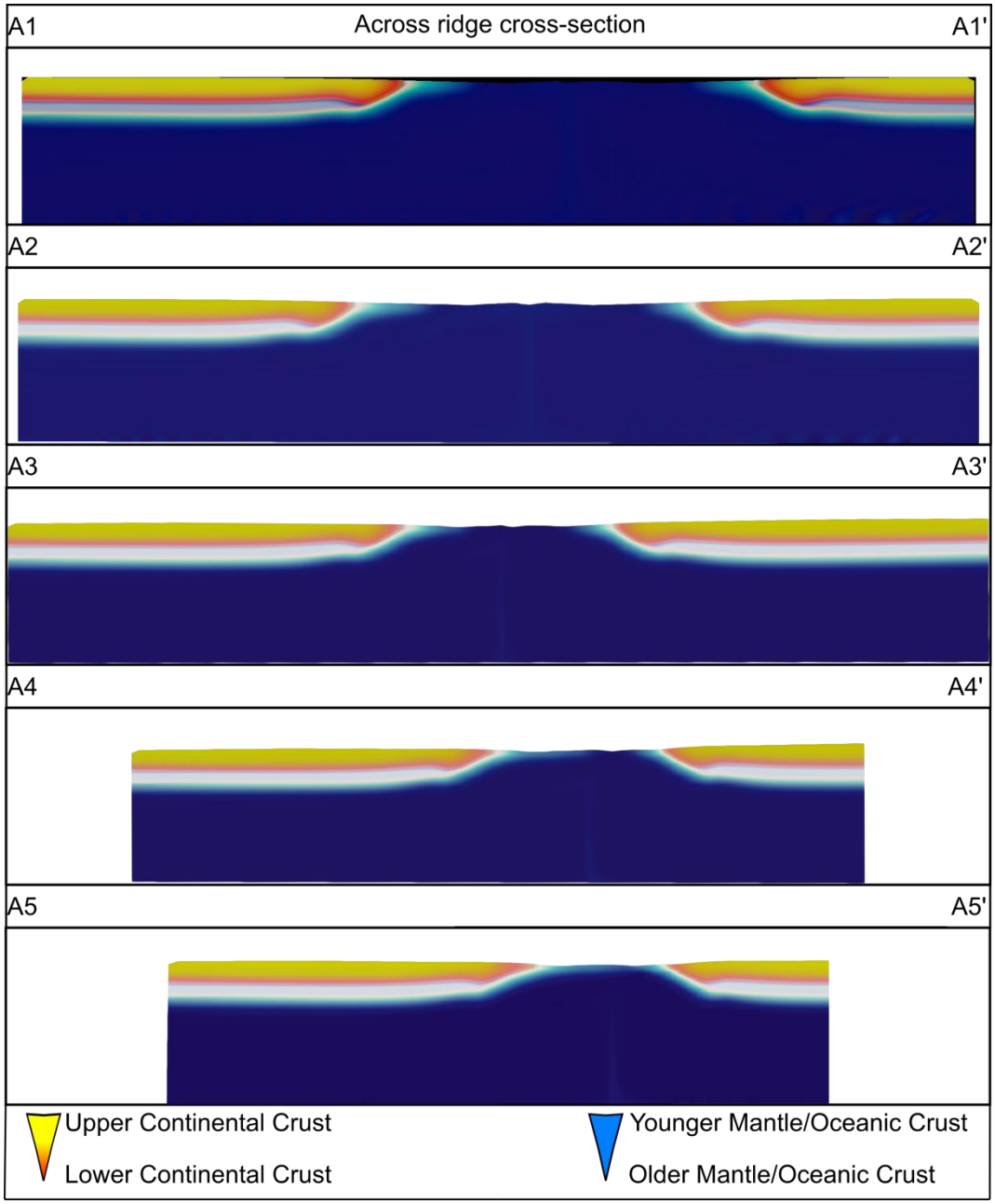

Figure A20 – Cross-sections across the spreading centres of Figure 4.4. Location of each cross section shown in Figure A18

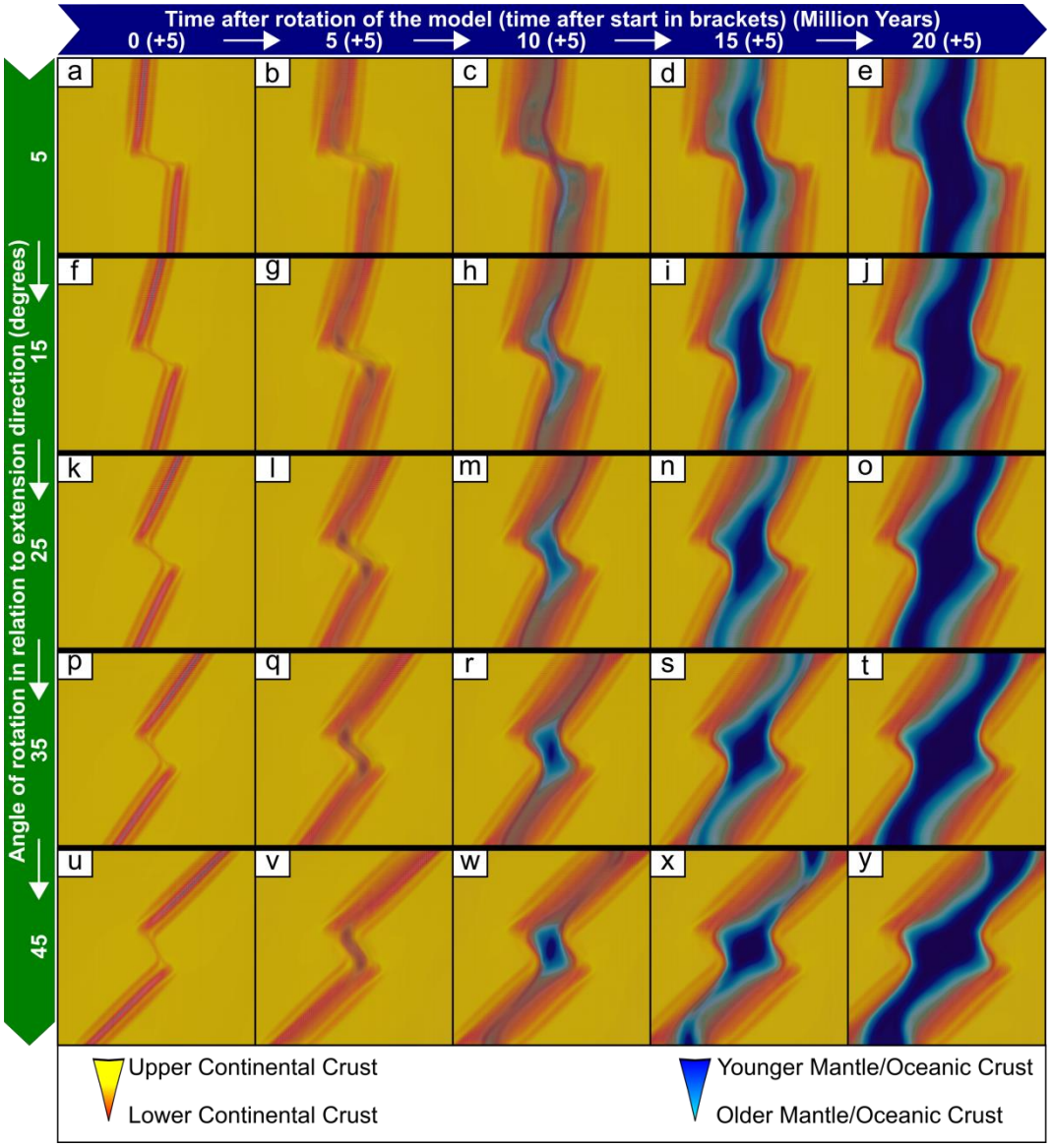

Figure A21 – Uninterpreted version of Figure 4.5 in the thesis.

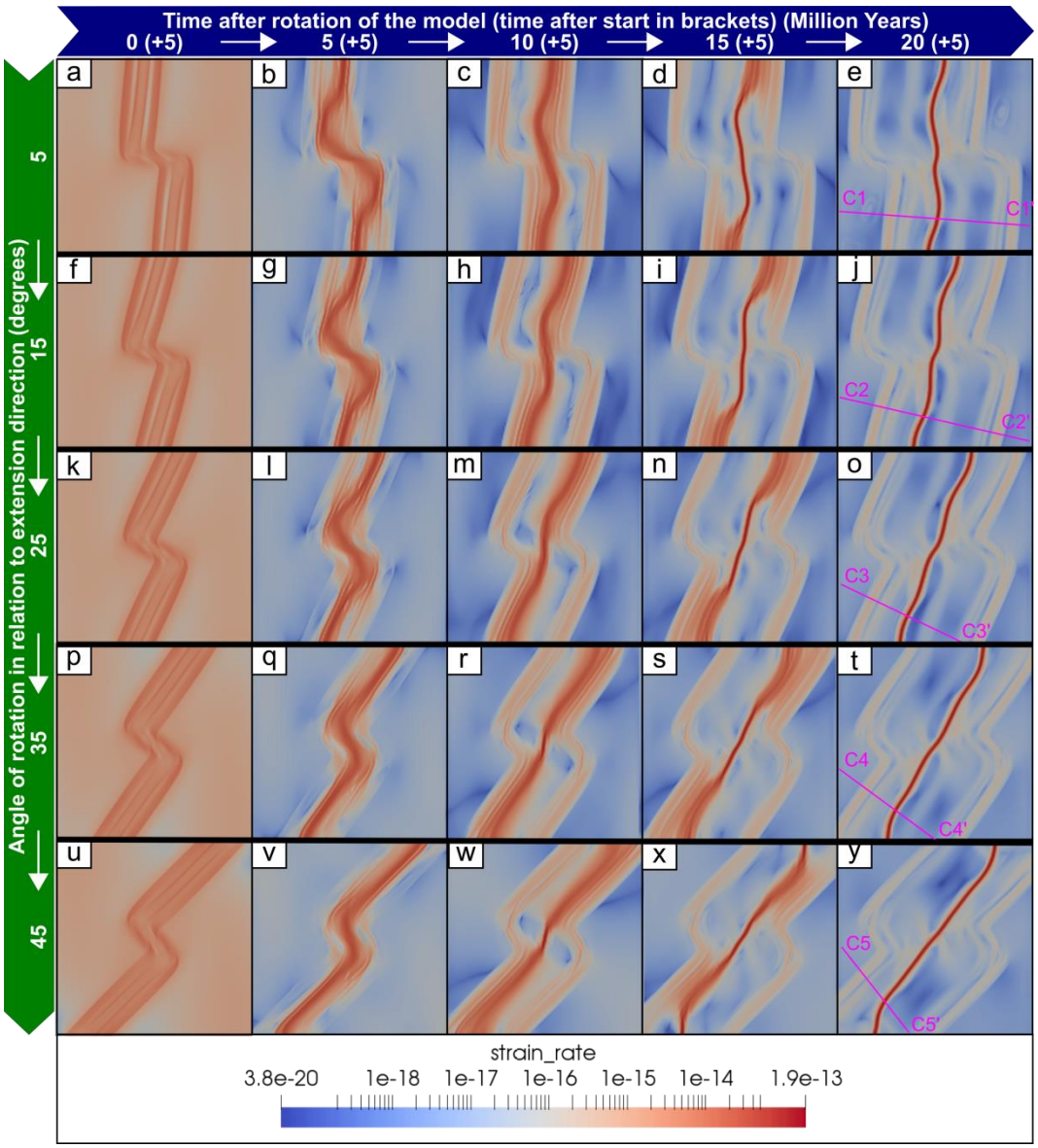

Figure A22 – Strain rate of the models shown in Figure 4.5 in the thesis. Panels e,j,o,t,y display cross-sections shown in Figure A24.

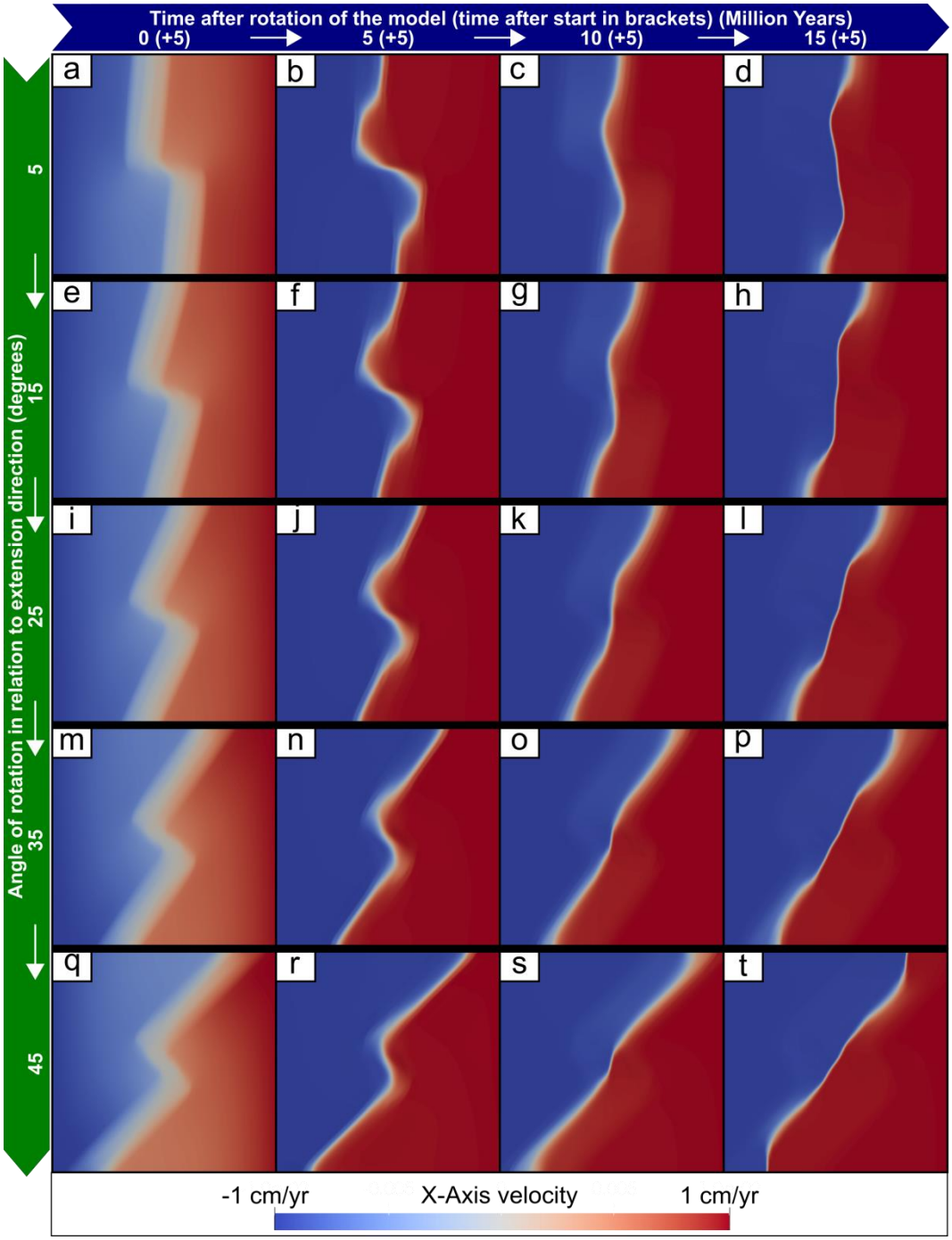

Figure A23 – X-Axis velocity plots of the models shown in Figure 4.5 in the thesis.

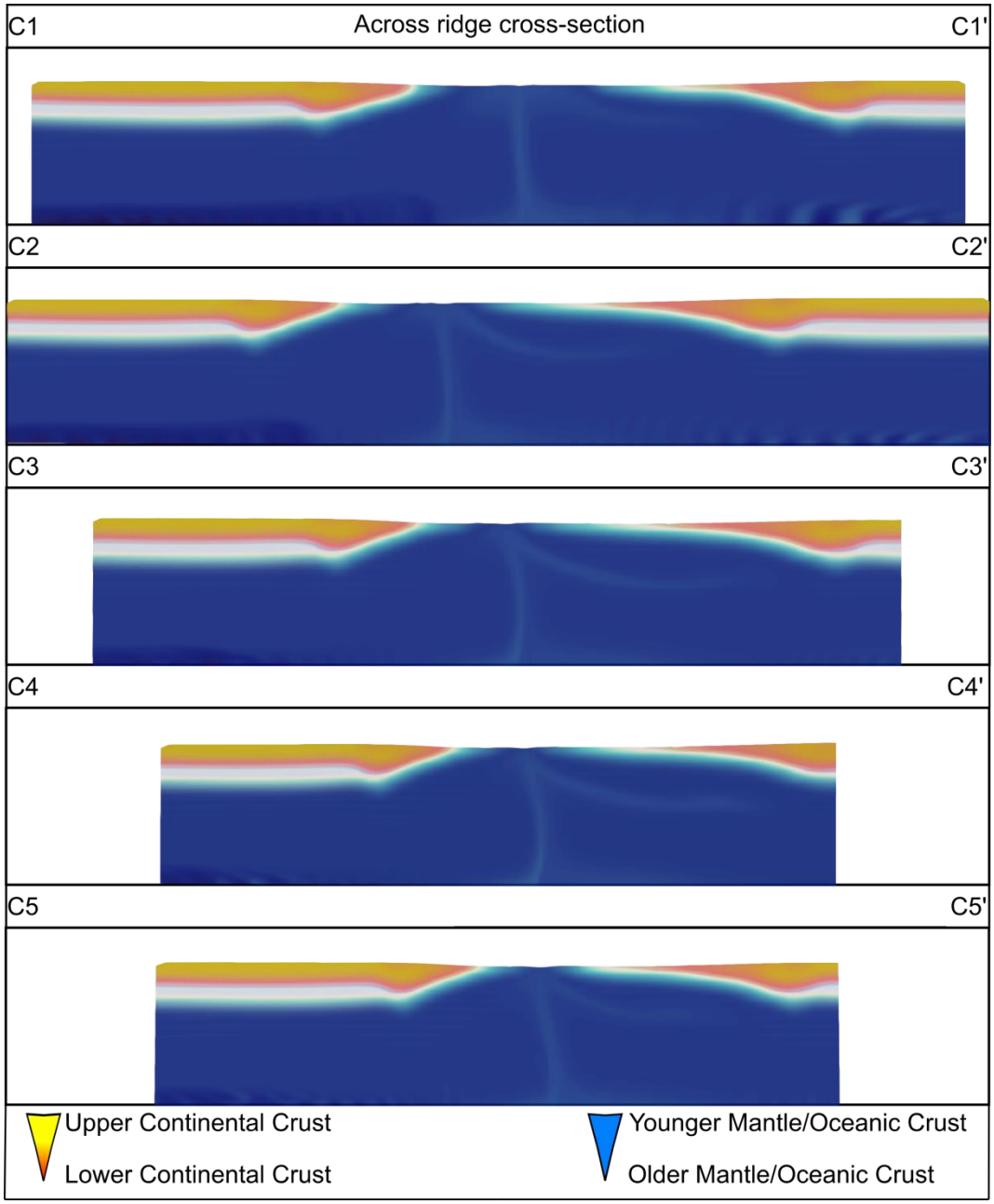

Figure A24 – Cross-sections across the spreading centres of Figure 4.5. Location of each cross section shown in Figure A22

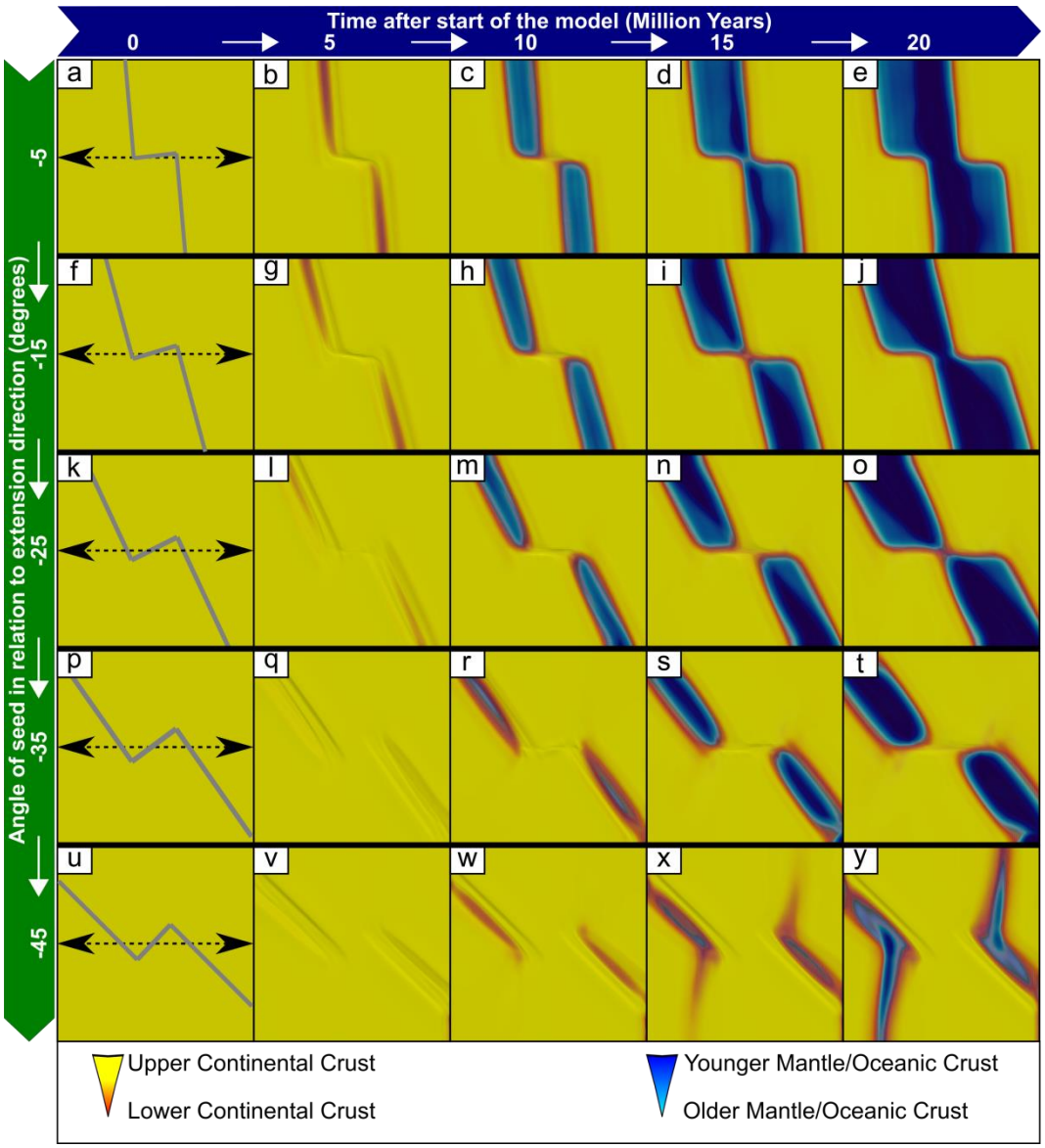

Figure A25 – Uninterpreted version of Figure 4.6 in the thesis

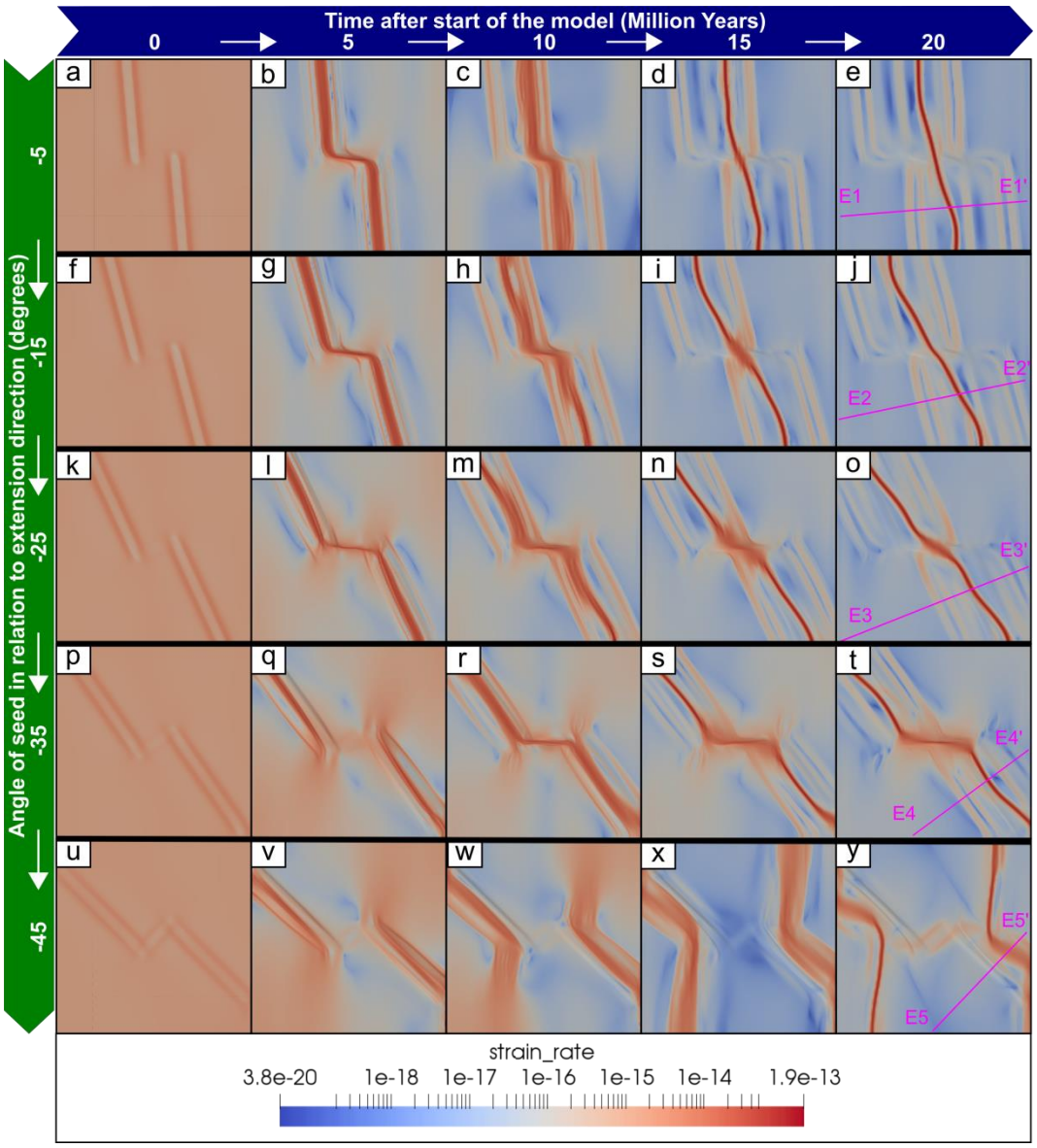

Figure A26 – Strain rate of the models shown in Figure 4.6 in the thesis. Panels e,j,o,t,y t display cross-sections shown in Figure A28.

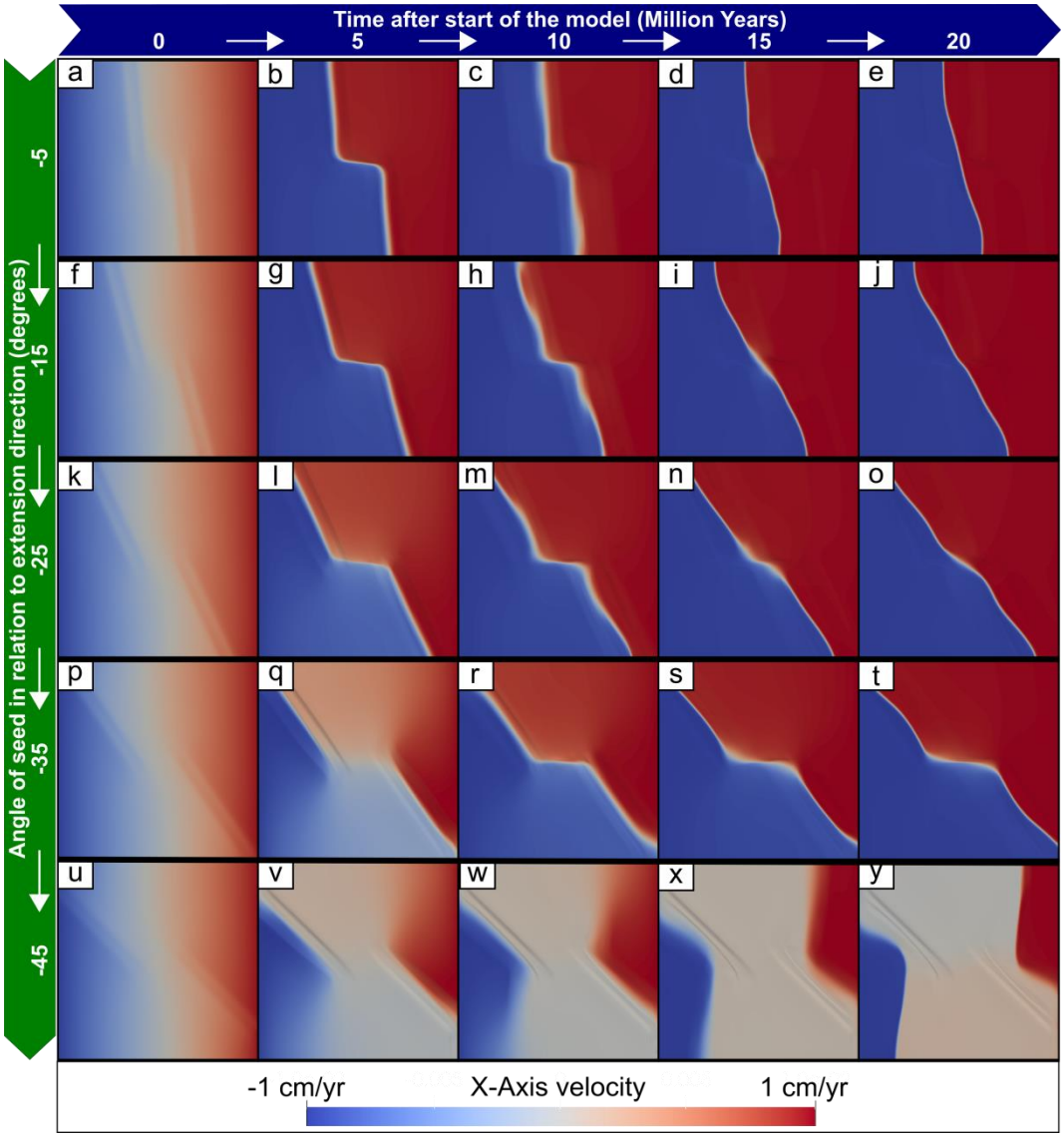

Figure A27 – X-Axis velocity plots of the models shown in Figure 4.6 in the thesis.

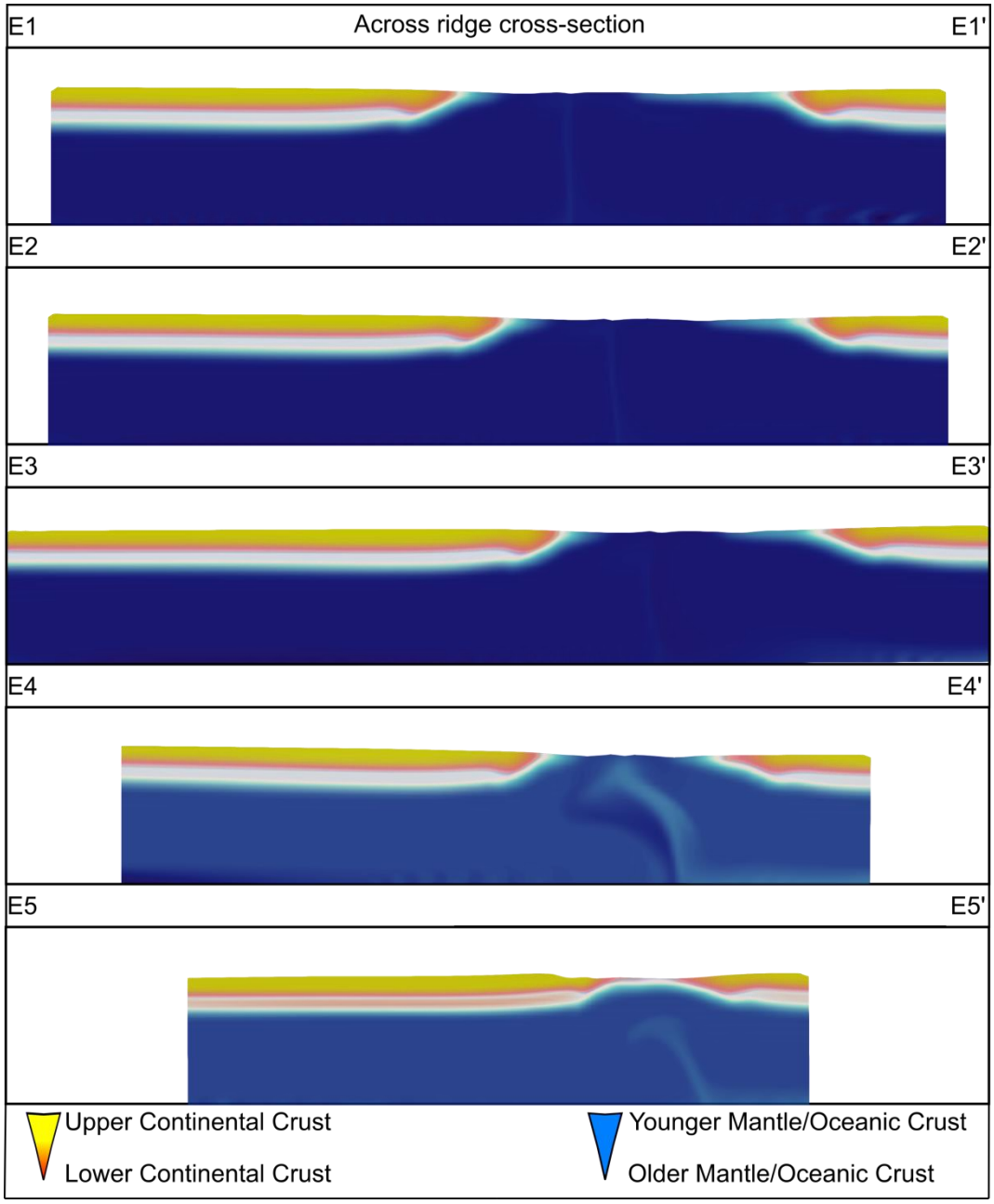

Figure A28 – Cross-sections across the spreading centres of Figure 4.6. Location of each cross section shown in Figure A26

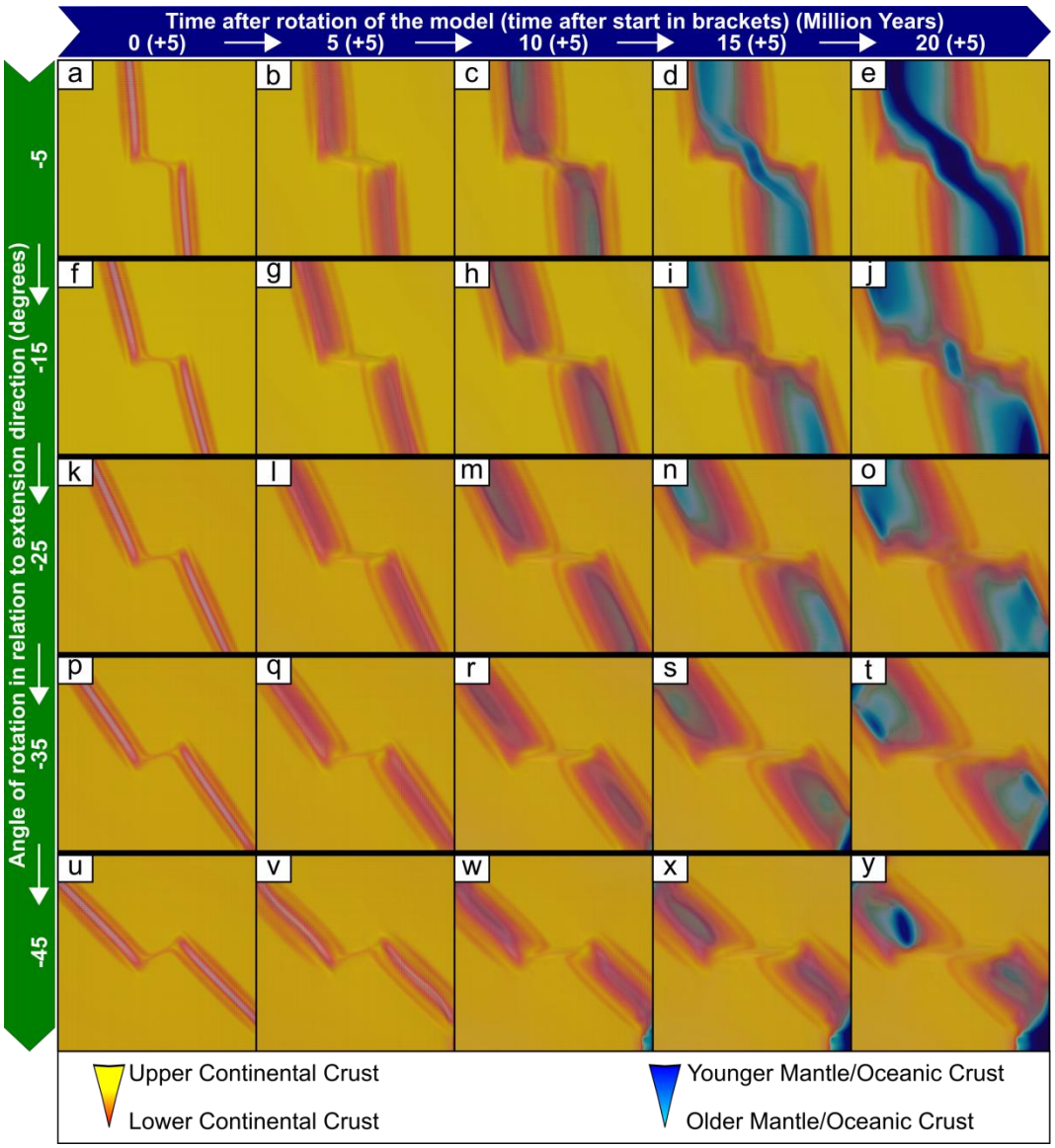

Figure A29 – Uninterpreted version of Figure 4.7 in the thesis.

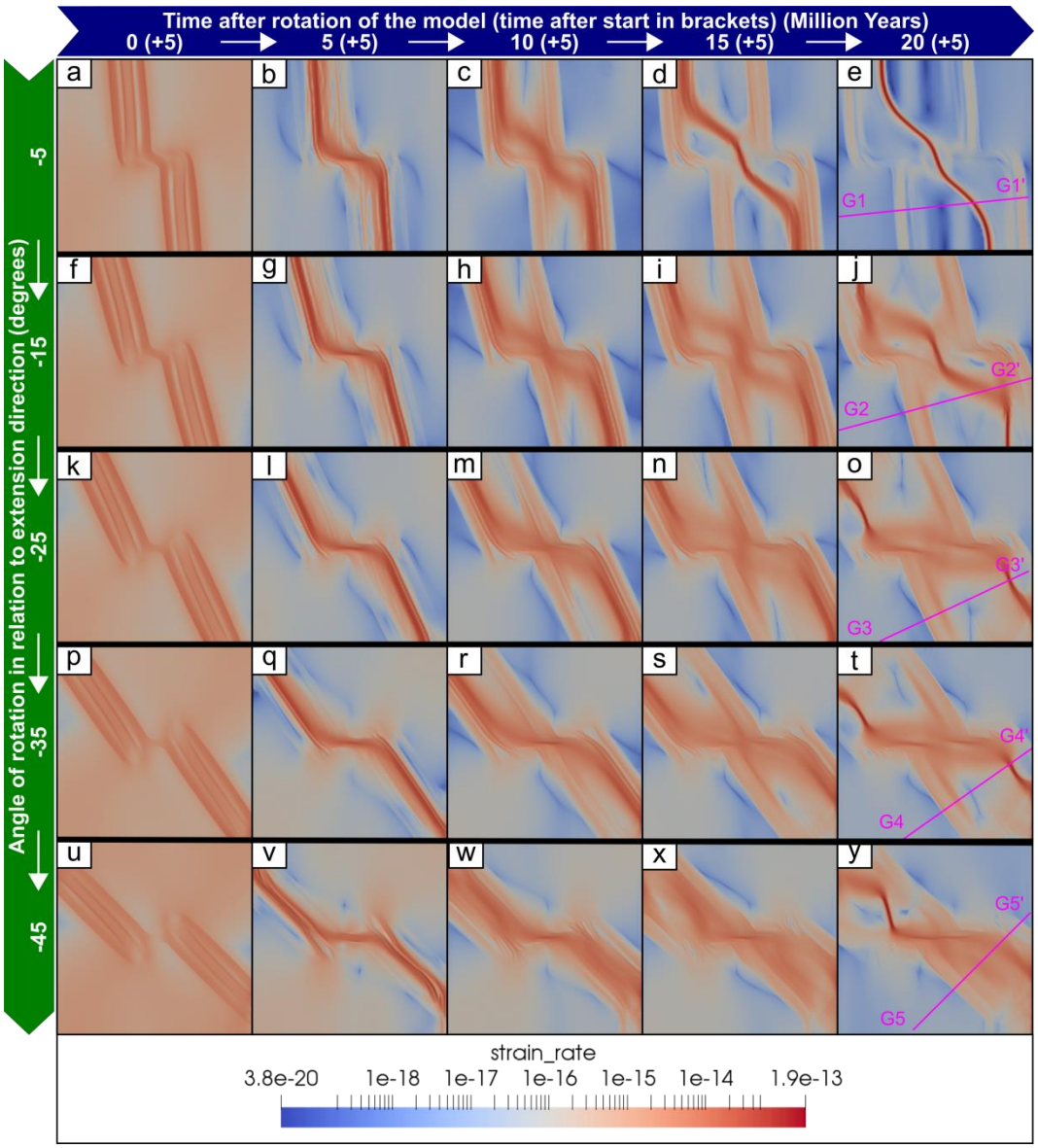

Figure A30 – Strain rate of the models shown in Figure 4.7. Panels e,j,o,t,y display cross-sections shown in Figure A32.

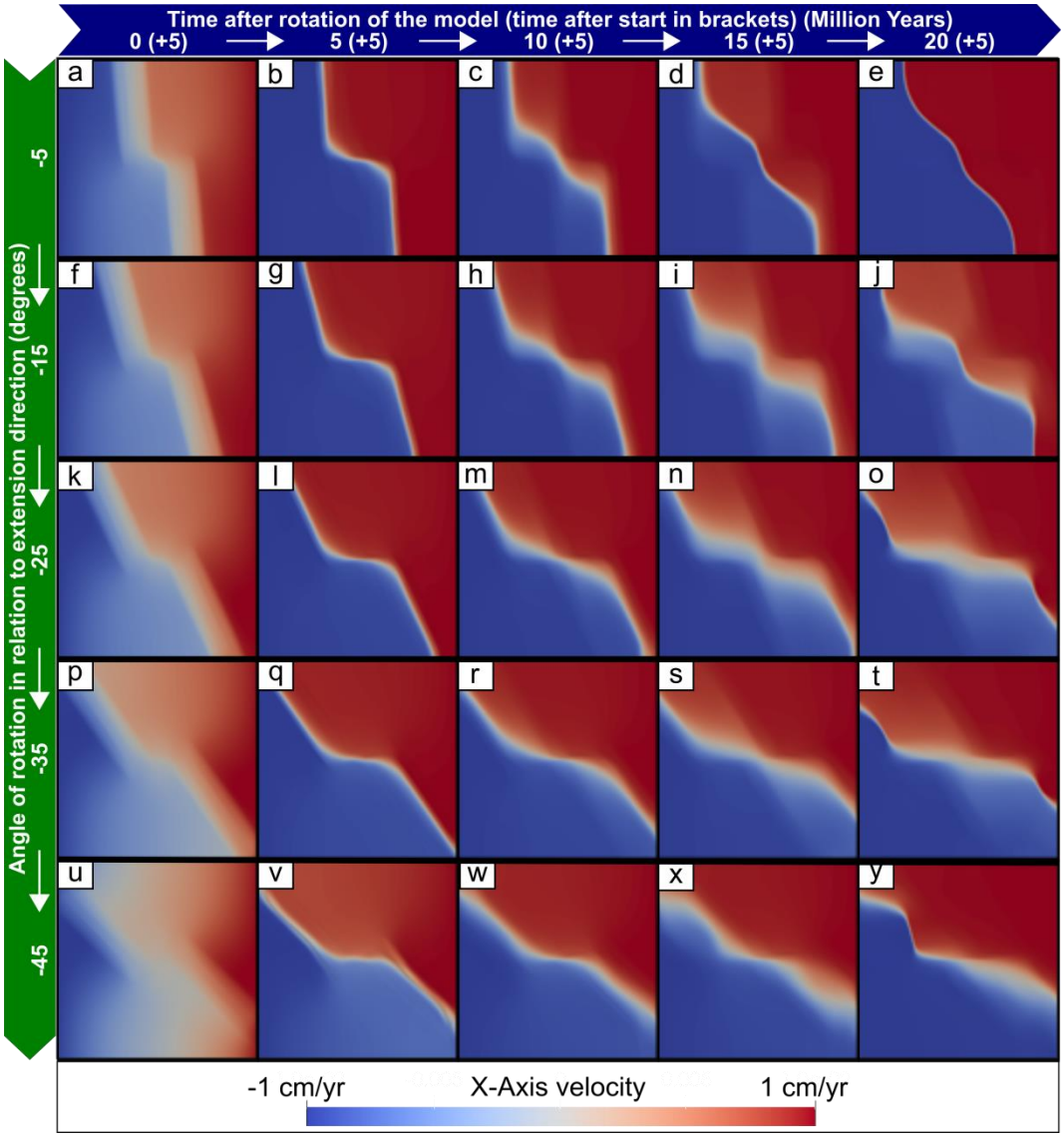

Figure A31 – X-Axis velocity plots of the models shown in Figure 4.7 in the thesis.

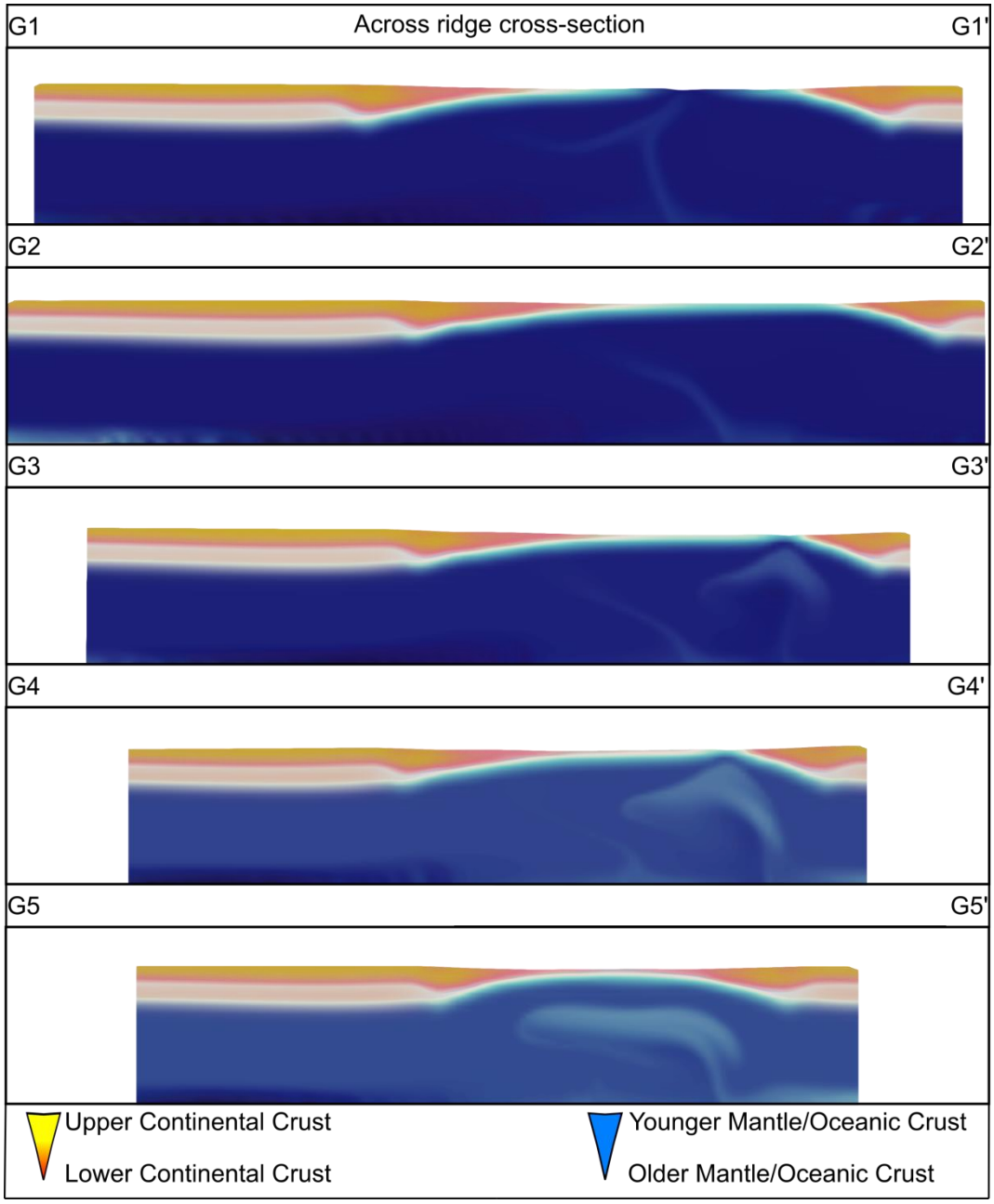

Figure A32 – Cross-sections across the spreading centres of Figure 4.6. Location of each cross section shown in Figure A30

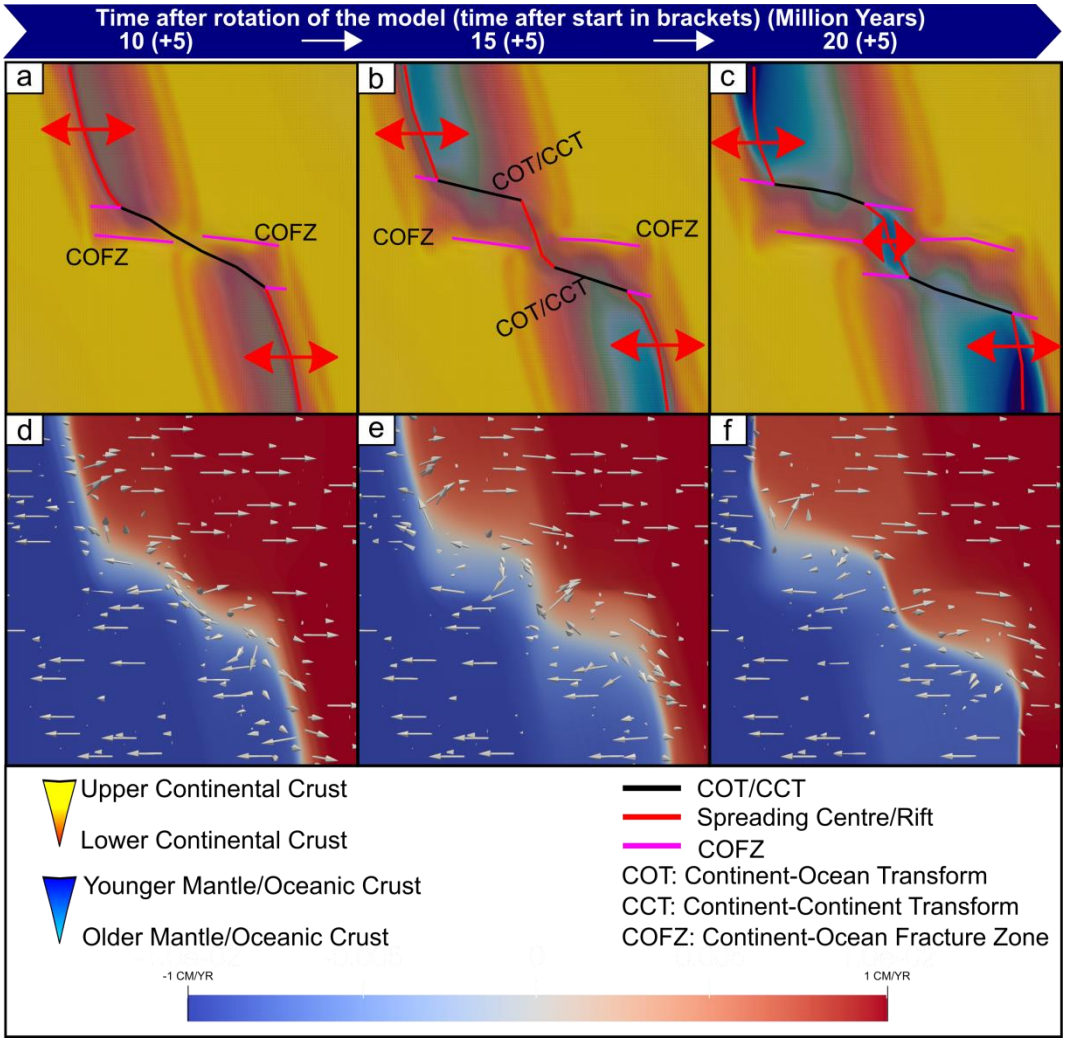

Figure A33 – a-c: Zoomed in version of the -15 transpressional rotation experiment (corresponds to Figure 4.7h), d-f: x velocity plots of the same snapshots. Arrows indicate the velocity direction every 4000 model nodes.

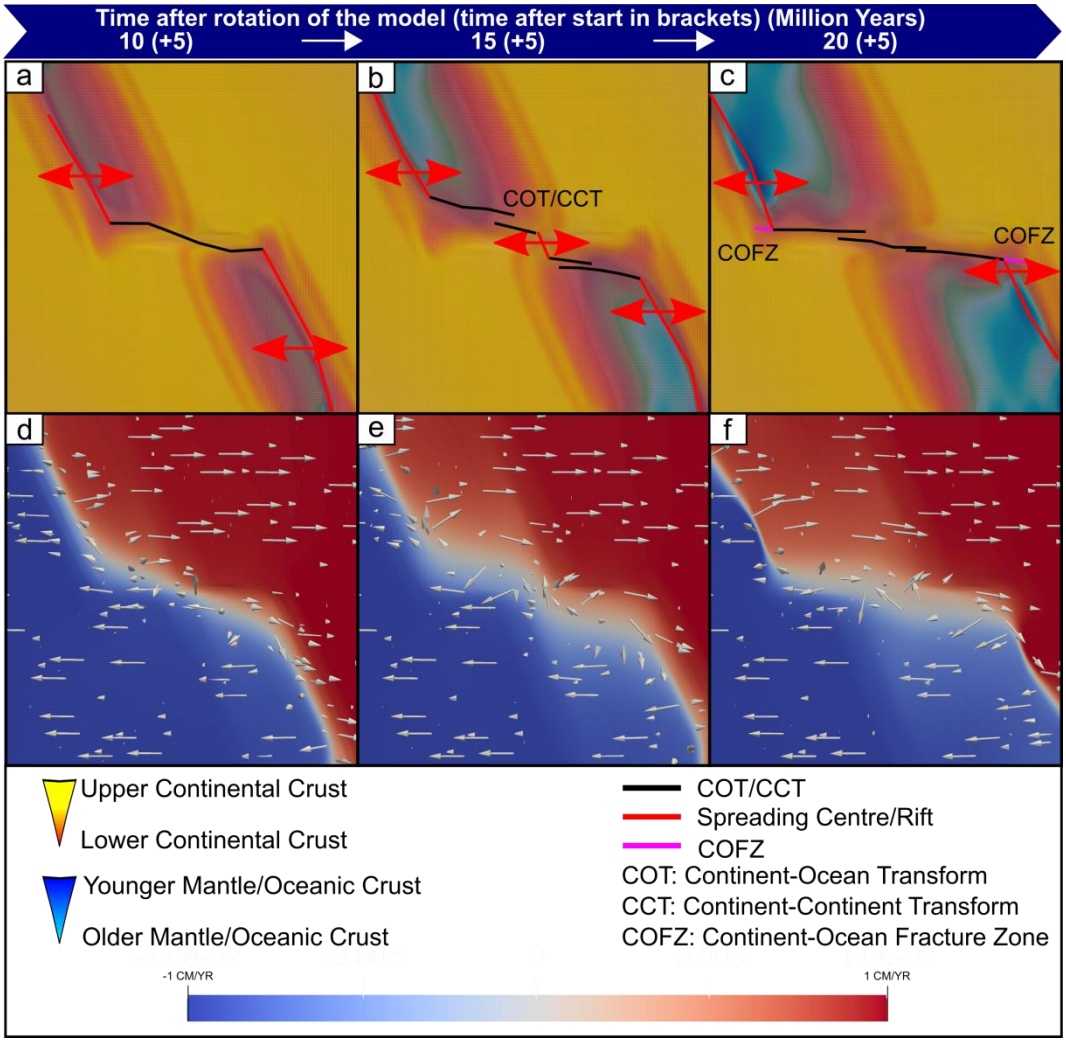

Figure A34 – a-c: Zoomed in version of the -25 transpressional rotation experiment (corresponds to Figure 4.7h), d-f: x velocity plots of the same snapshots. Arrows indicate the velocity direction every 4000 model nodes.

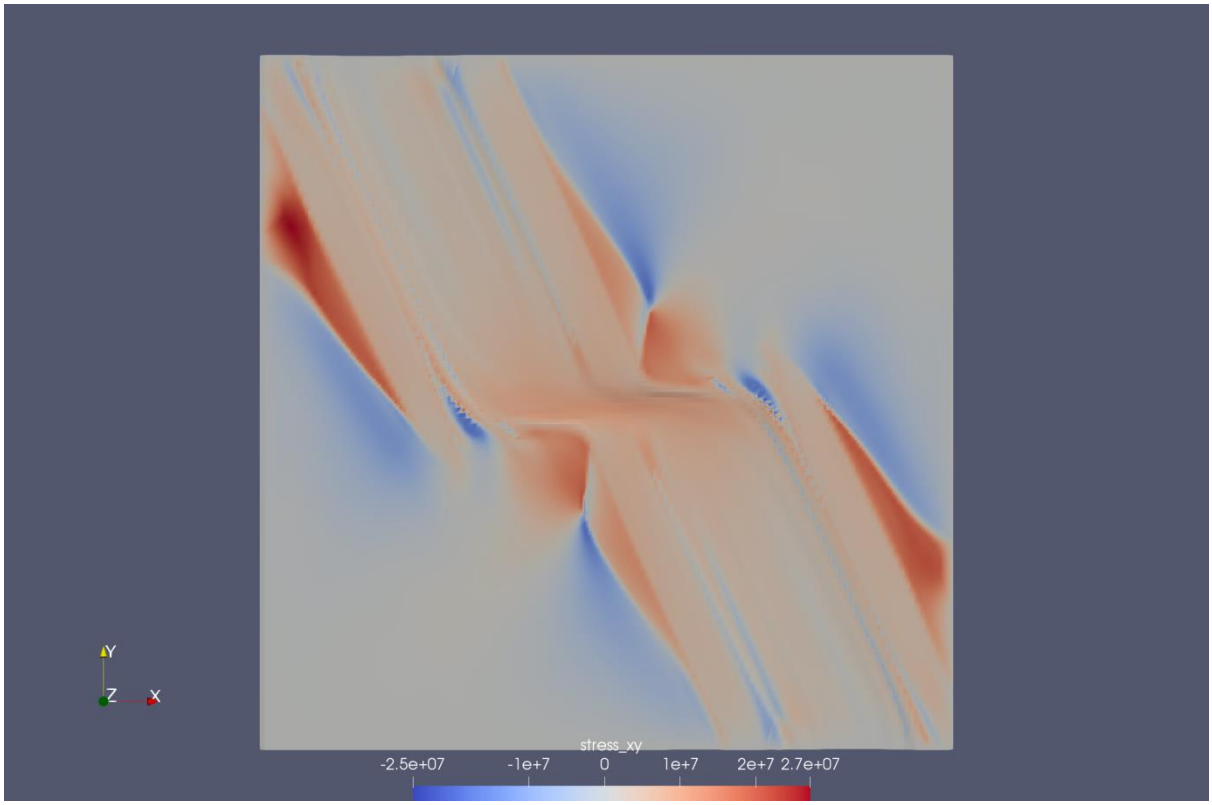

Figure A35 – Stress along the xy axis at 7.5 (+5) Ma after start of model 93 (corresponds to Figure 4.7k)

Parameter files: https://github.com/pfarangitakis/ASPECT-PRM

Appendix B – Suppl. Material for Chapter 5

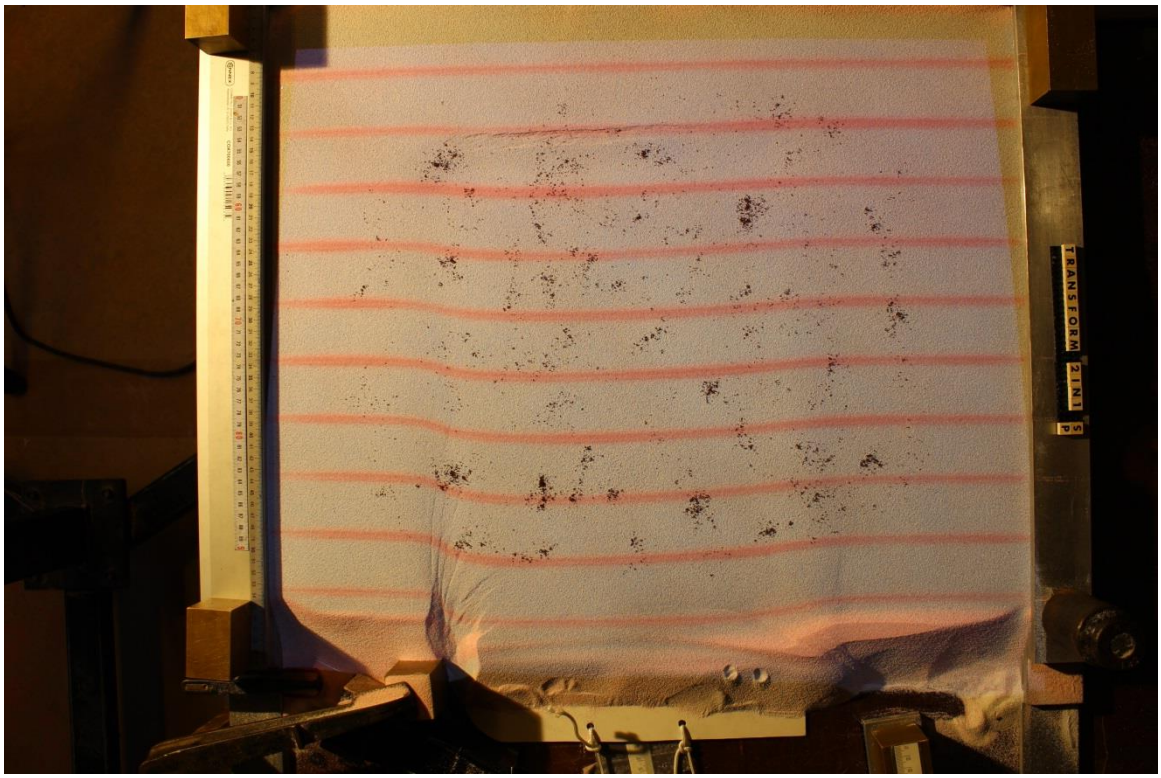

Figure B1 – Top view of Experiment 1 at the end of orthogonal rifting, without interpretation.

Corresponds to Figure 5.4a, e, f.

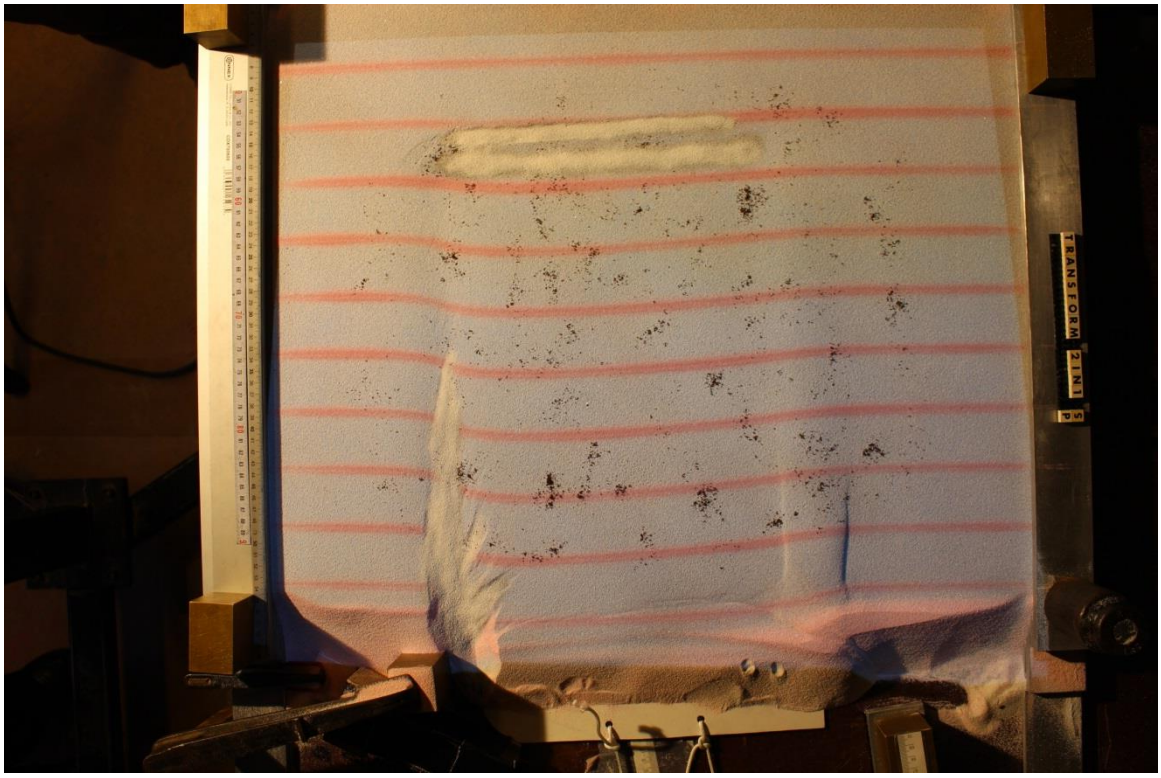

Figure B2 – Top view of Experiment 1 at the start of rotation, without interpretation. Corresponds to Figure 5.4b, g, h.

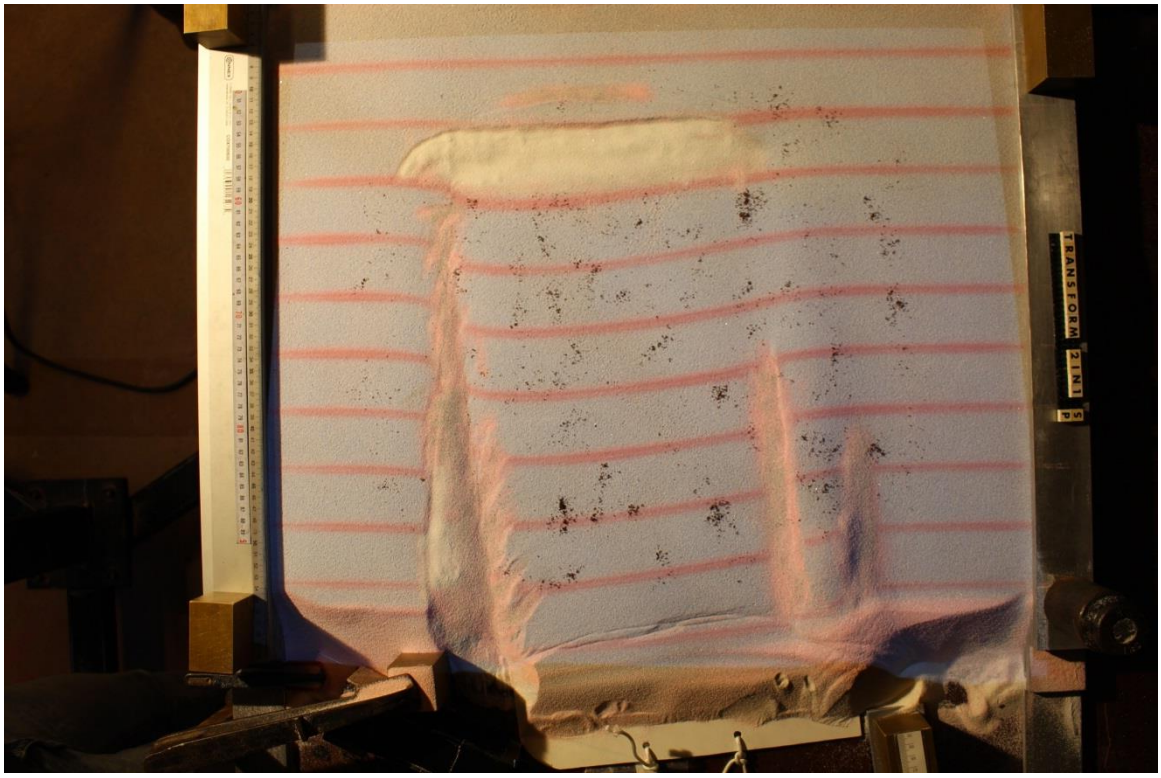

Figure B3 – Top view of Experiment 1 at the end of rotation, without interpretation. Corresponds to Figure 5.4c, i, j.

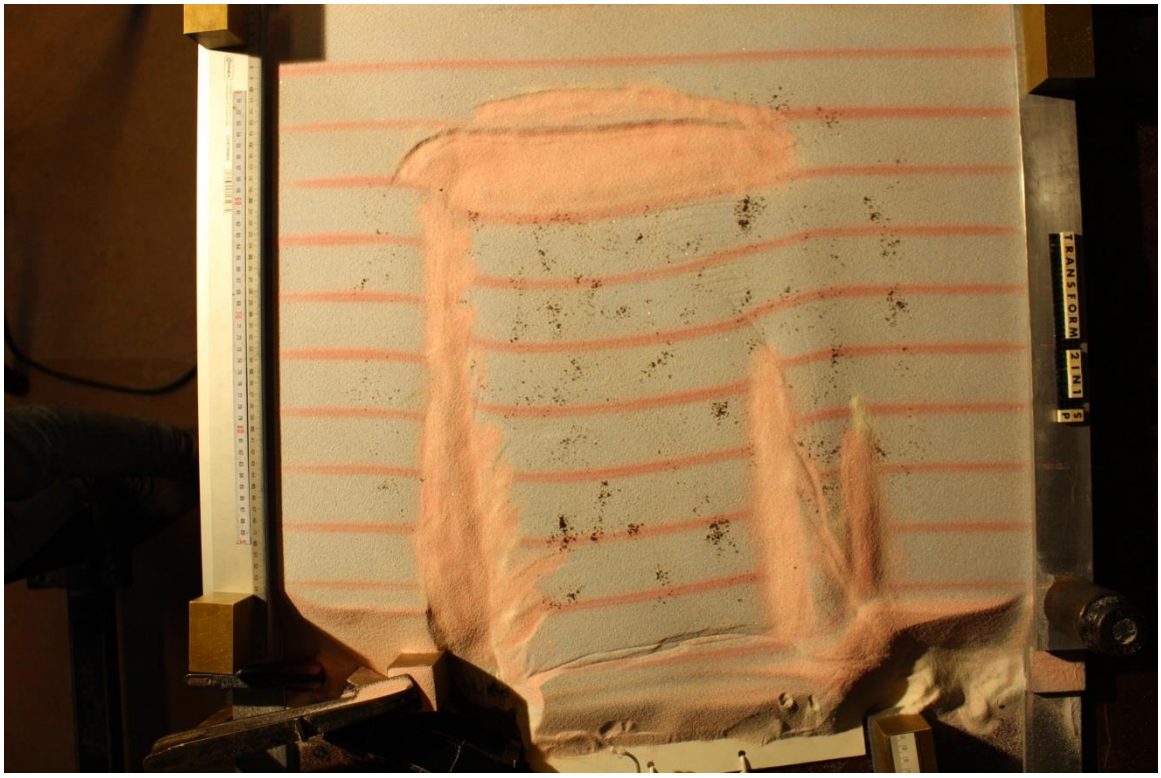

Figure B4 – Top view of Experiment 1 at the end of oblique rifting, without interpretation. Corresponds to Figure 5.4d, k, l.

Figure B5 – Top view of Experiment 2 at the end of orthogonal rifting, without interpretation. Corresponds to Figure 5.5a, e, f.

Figure B6 – Top view of Experiment 2 at the start of rotation, without interpretation. Corresponds to Figure 5.5b, g, h.

Figure B7 – Top view of Experiment 2 at the end of rotation, without interpretation. Corresponds to Figure 5.5c, i, j.

Figure B8 – Top view of Experiment 2 at the end of oblique rifting, without interpretation. Corresponds to Figure 5.5d, k, l.

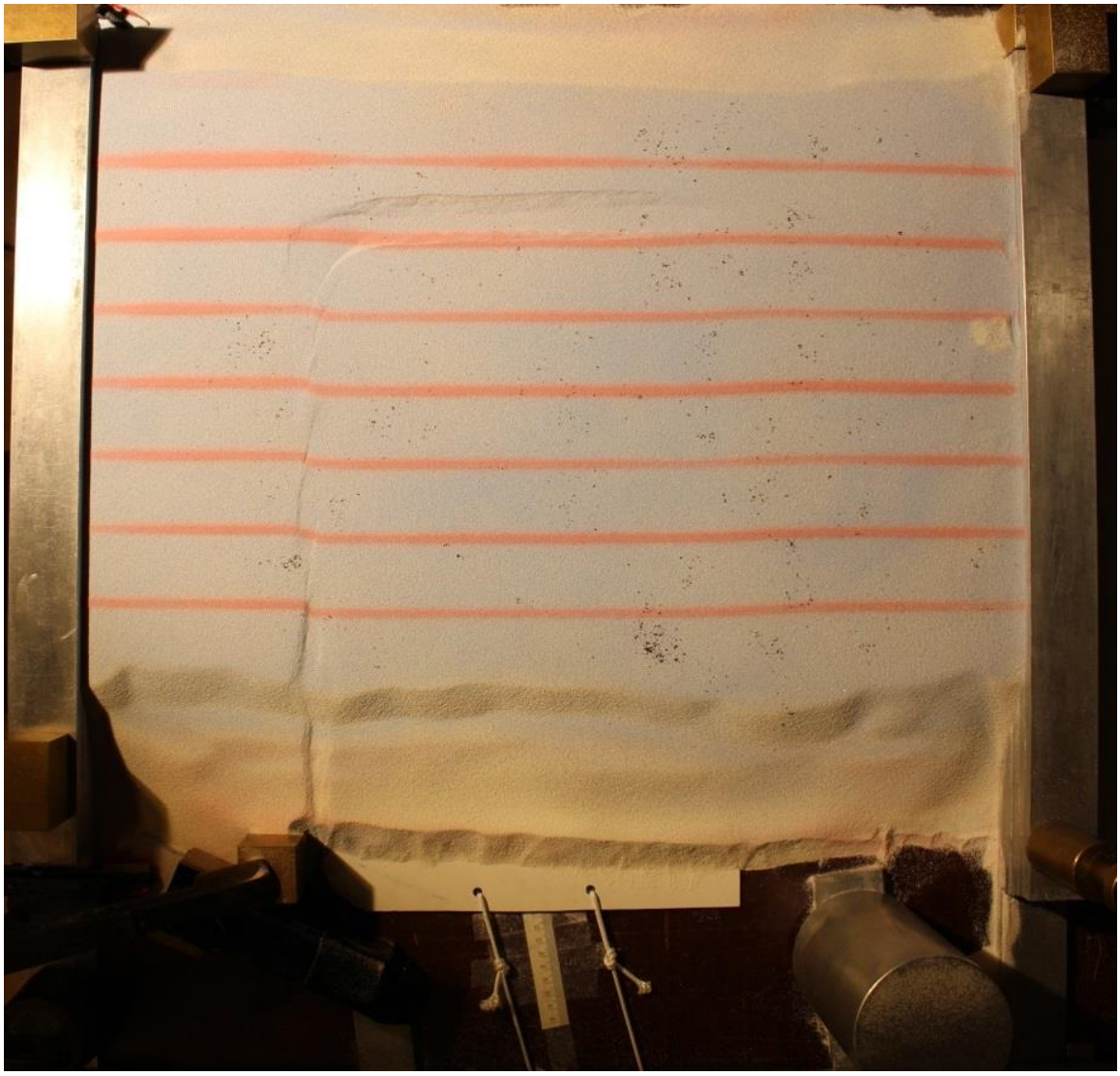

Figure B9 – Top view of Experiment 4 at the end of orthogonal rifting, without interpretation.

Corresponds to Figure 5.6a, e, f.

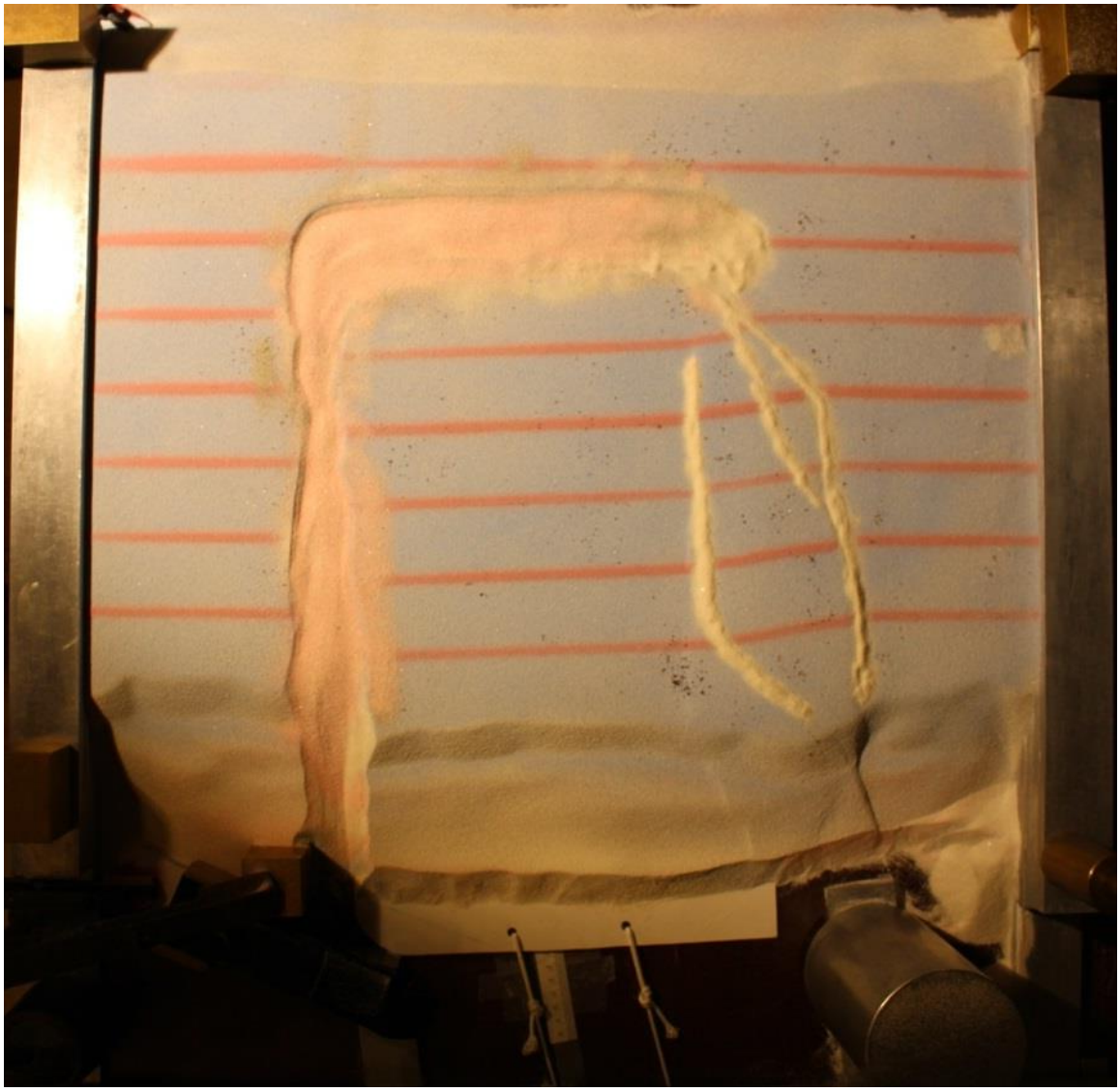

Figure B10 – Top view of Experiment 3 at the start of rotation, without interpretation. Corresponds to Figure 5.6b, g, h.

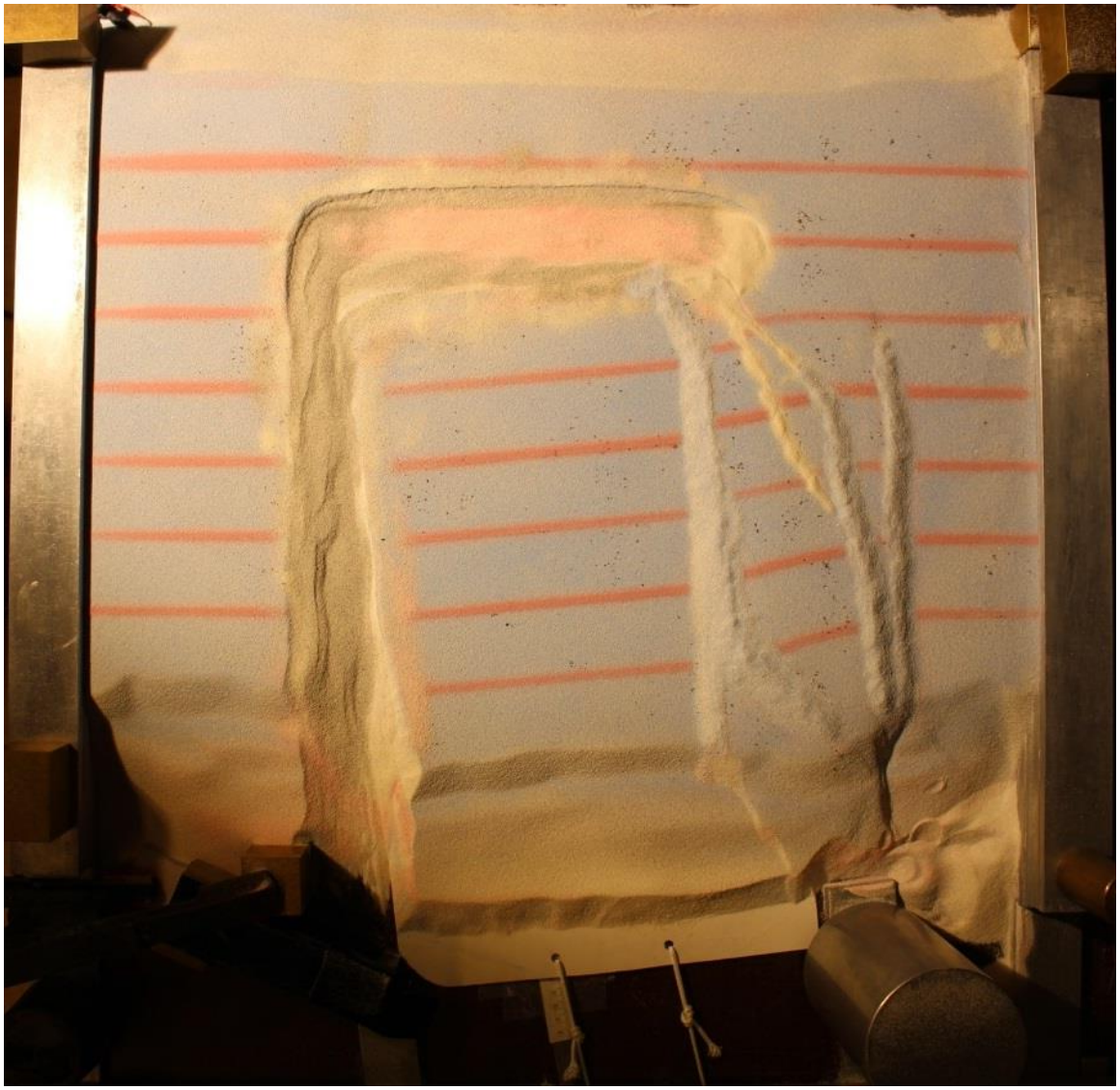

Figure B11 – Top view of Experiment 3 at the end of rotation, without interpretation. Corresponds to Figure 5.6d, i, j.

Figure B12 – Top view of Experiment 3 at the end of oblique rifting, without interpretation. Corresponds to Figure 5.6d, k, l.

Figure B13 – Uninterpreted cross-section across the transtensional zone zone of Experiment 2. Corresponds to Figure 5.7g,h.

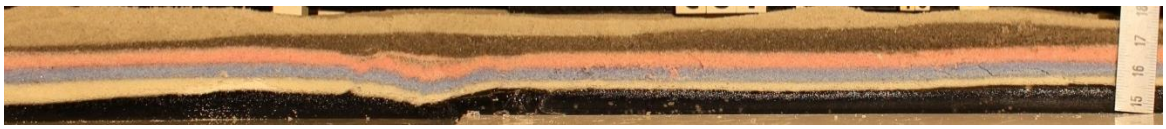

Figure B14 – Uninterpreted cross-section across the transtensional zone of Experiment 2. Corresponds to Figure 5.7i, j.

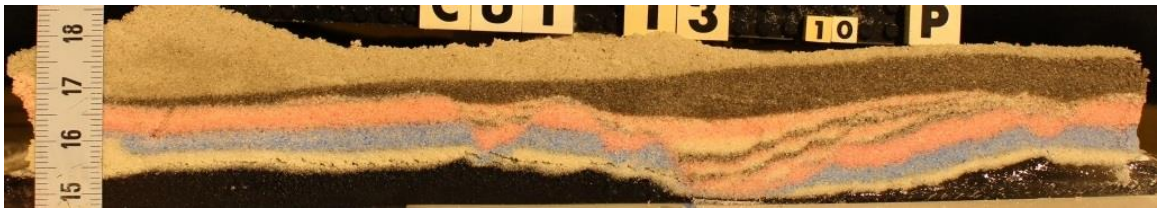

Figure B15 – Uninterpreted cross-section across the rift zone of Experiment 2. Corresponds to Figure 5.7d,e.

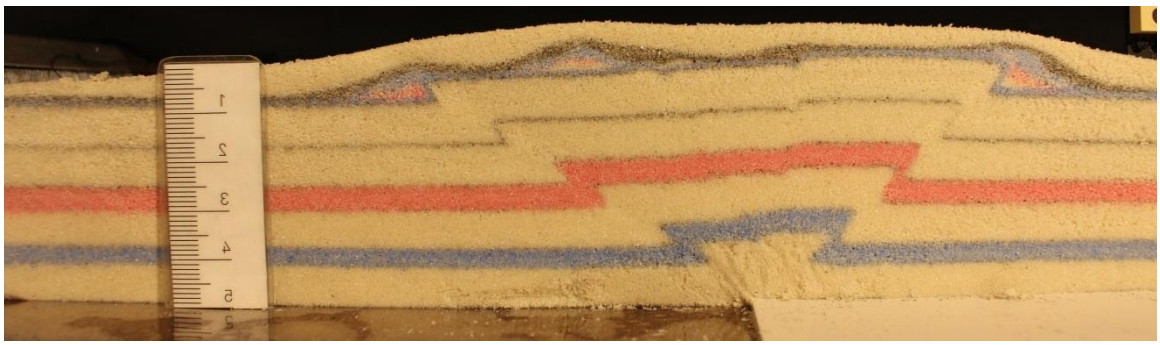

Figure B16 – Uninterpreted cross-section across the transpressional zone of Experiment 3. Corresponds to Figure 5.8f, g.

Figure B17 – Uninterpreted cross-section across the transpressional zone of Experiment 3. Corresponds to Figure 5.8d, e.

Appendix C – Suppl. Material for Chapter 6

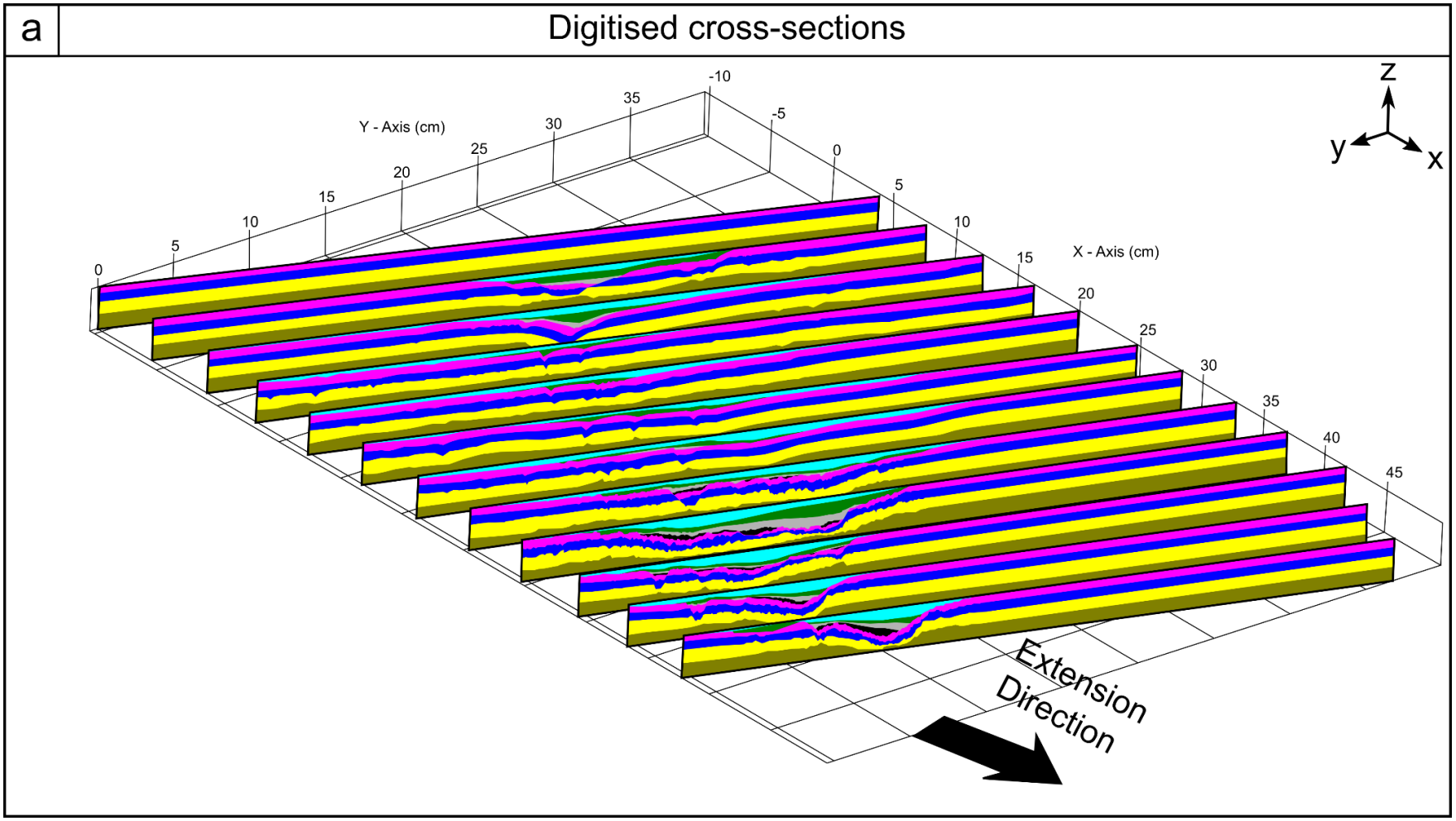

Figure C1 – Enlarged version of Figure 6.6a.

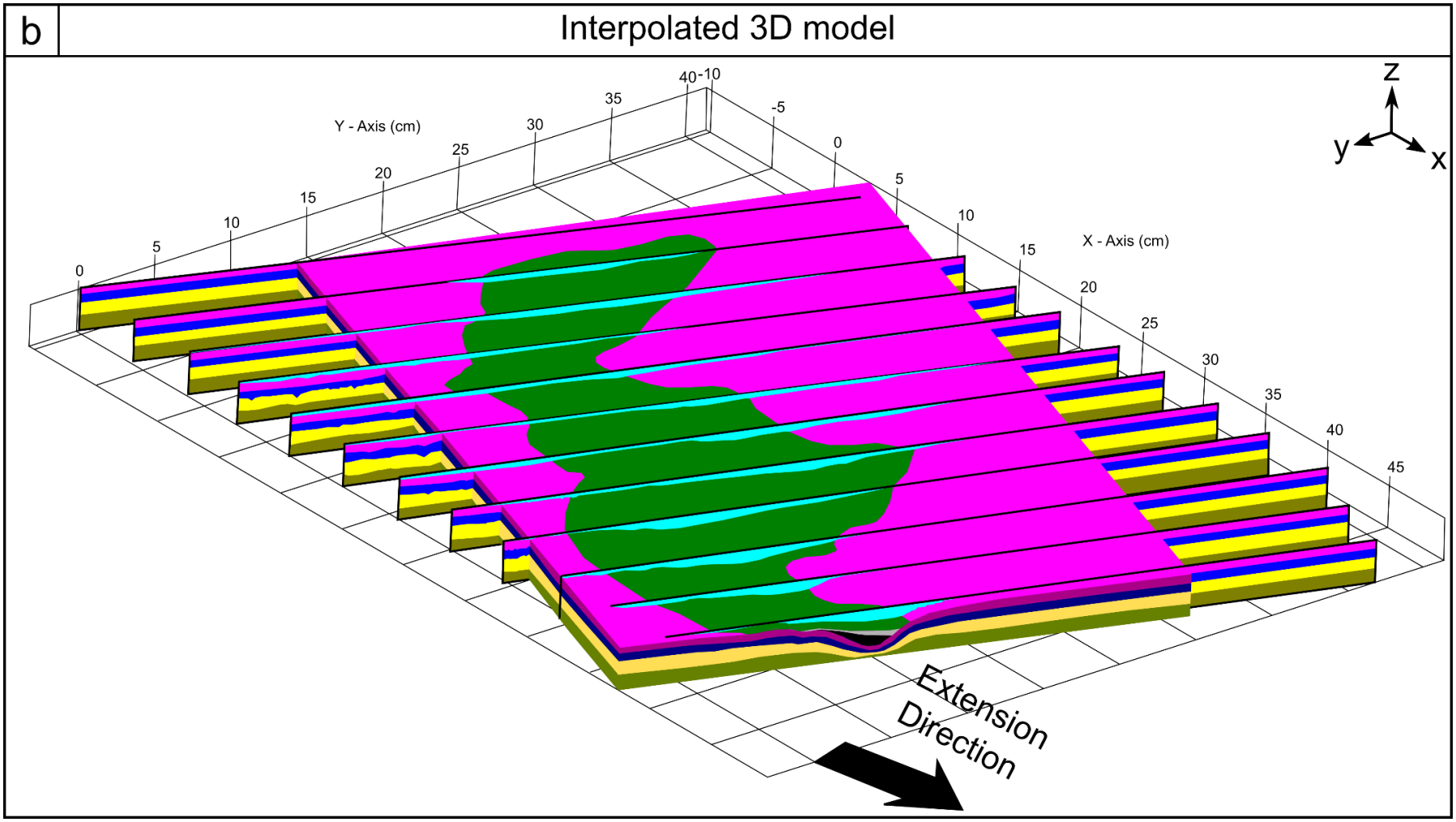

Figure C2 – Enlarged version of Figure 6.6b

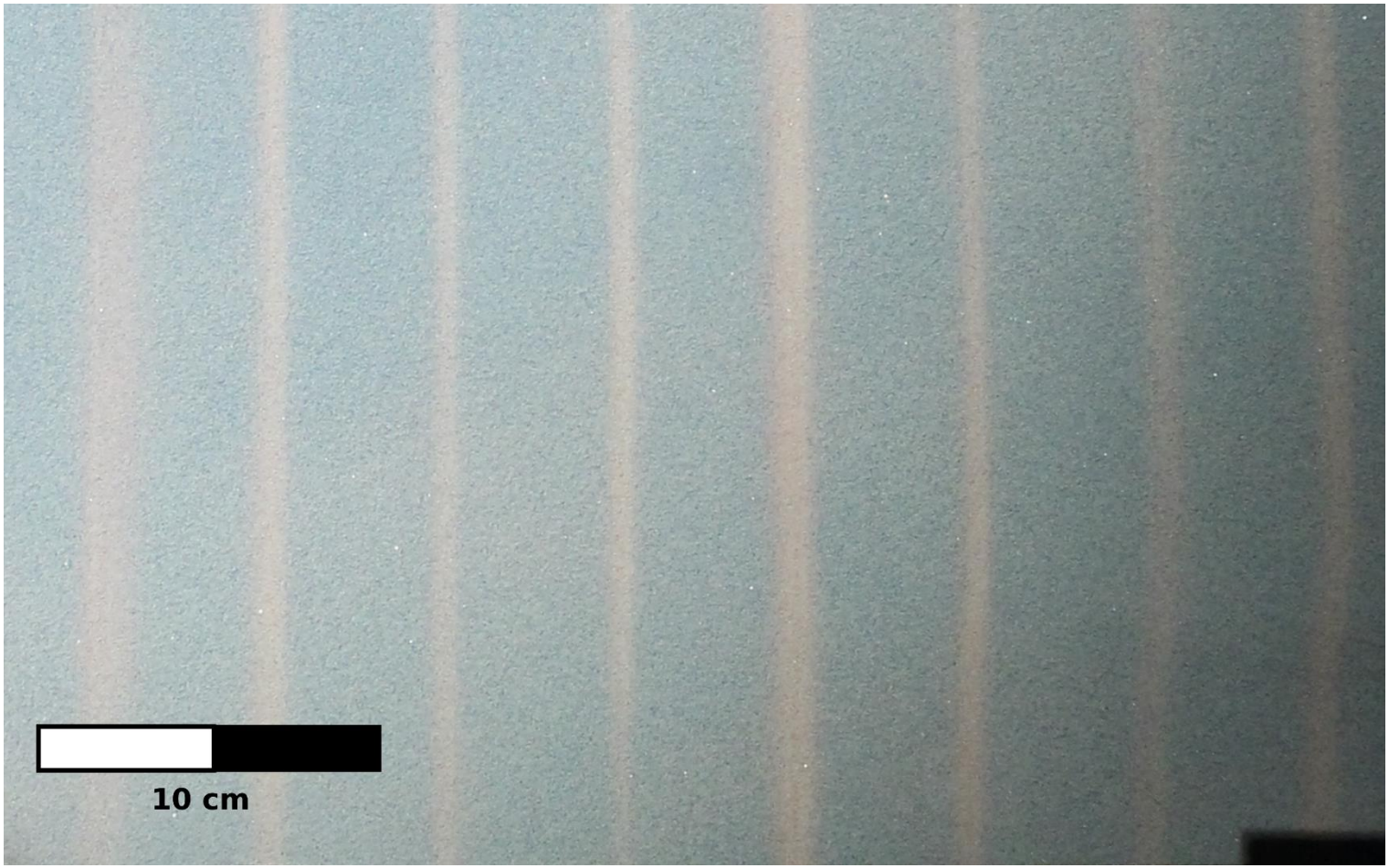

Figure C3 – Enlarged version of Figure 6.8a

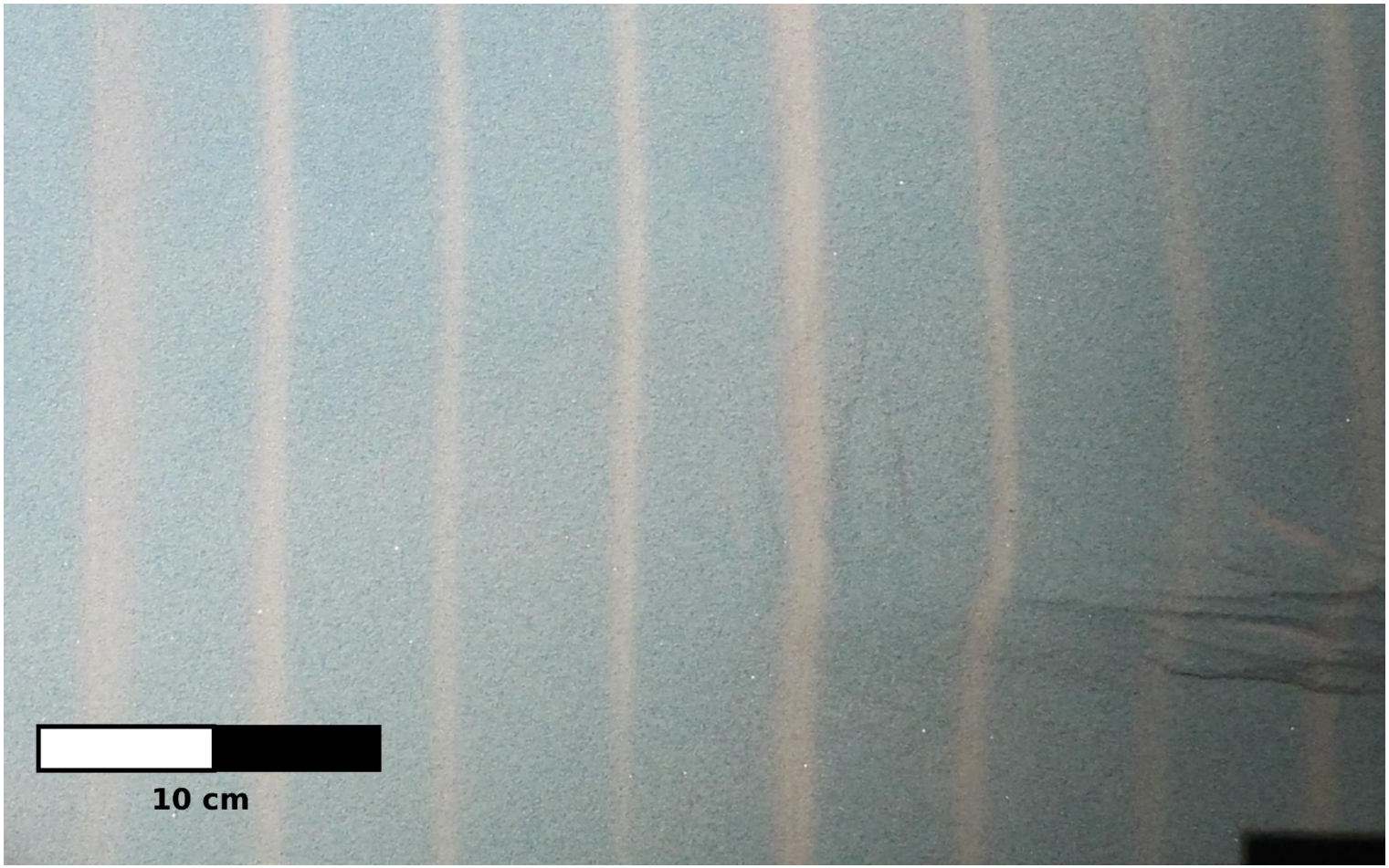

Figure C4 – Enlarged version of Figure 6.8b

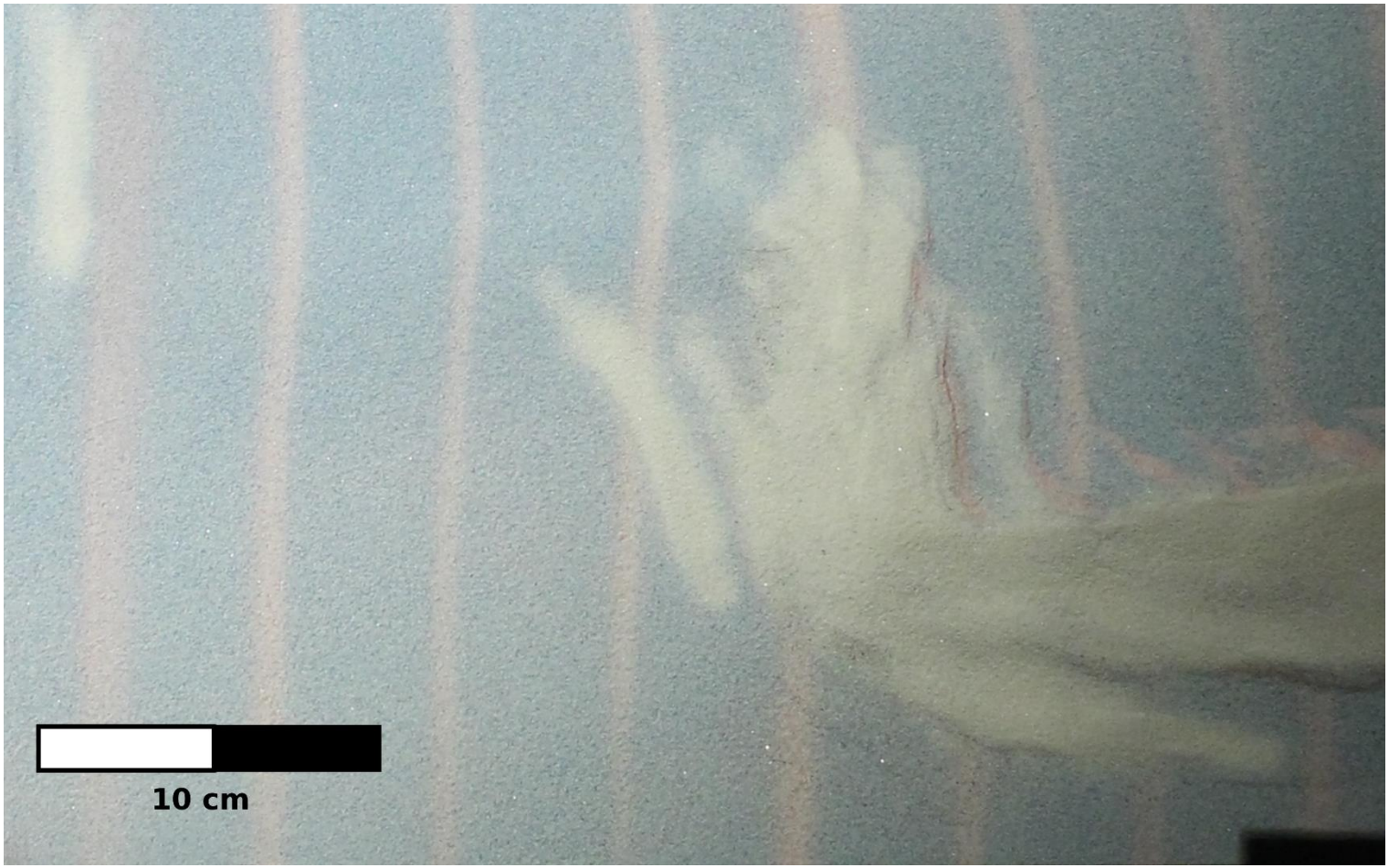

Figure C5 – Enlarged version of Figure 6.8c

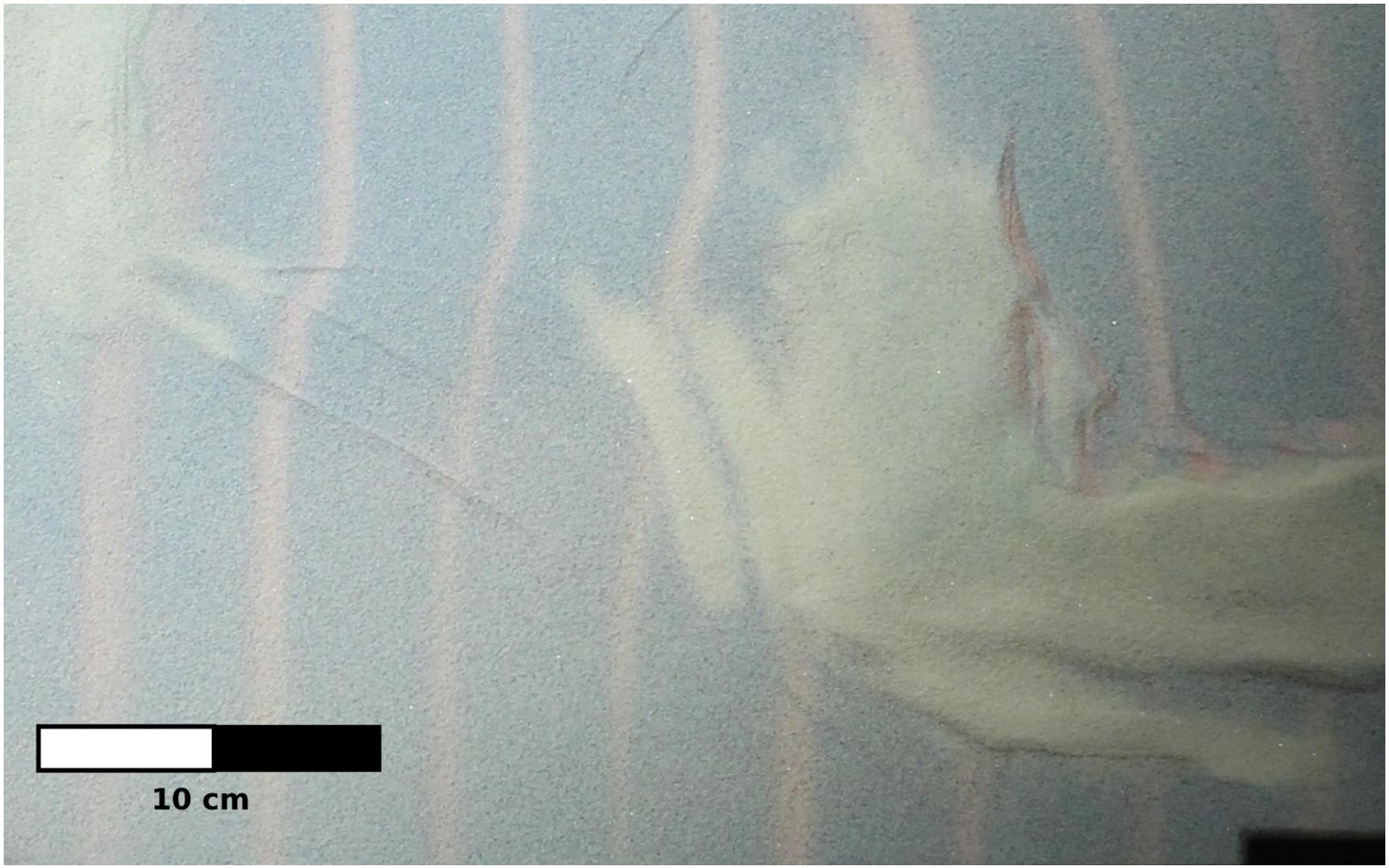

Figure C6 – Enlarged version of Figure 8d

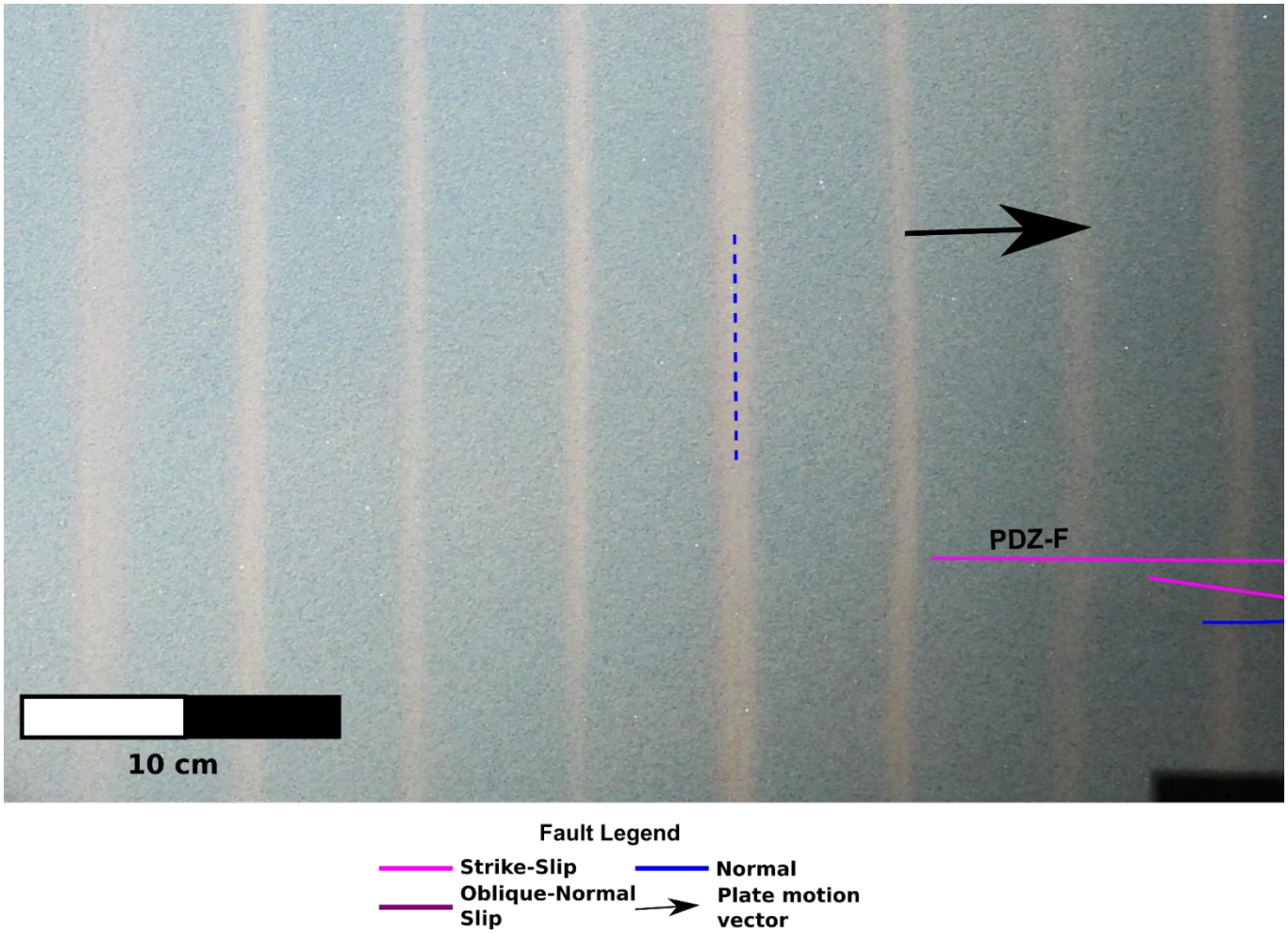

Figure C7 – Enlarged version of Figure 6.8e

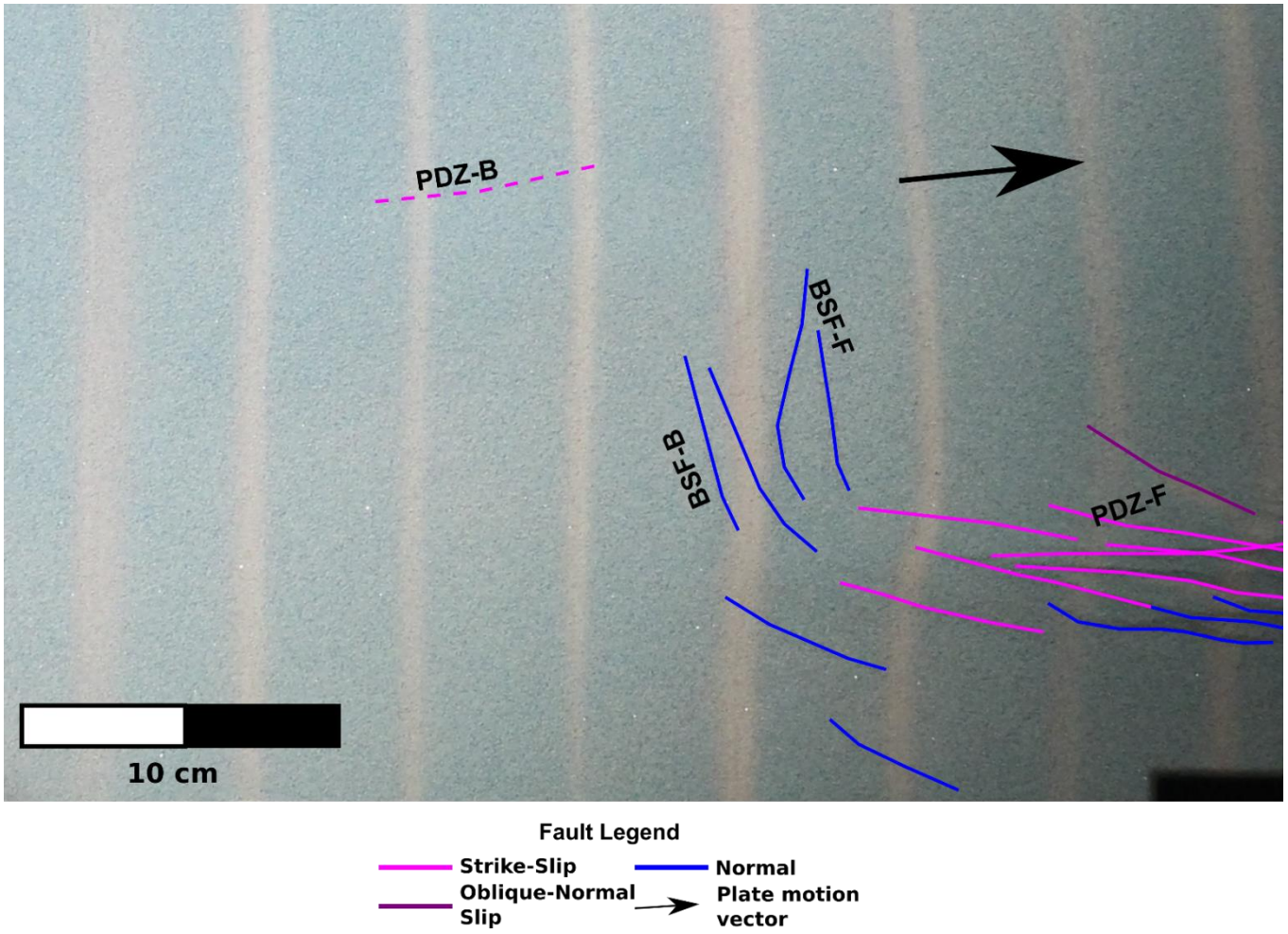

Figure C8 – Enlarged version of Figure 6.8f

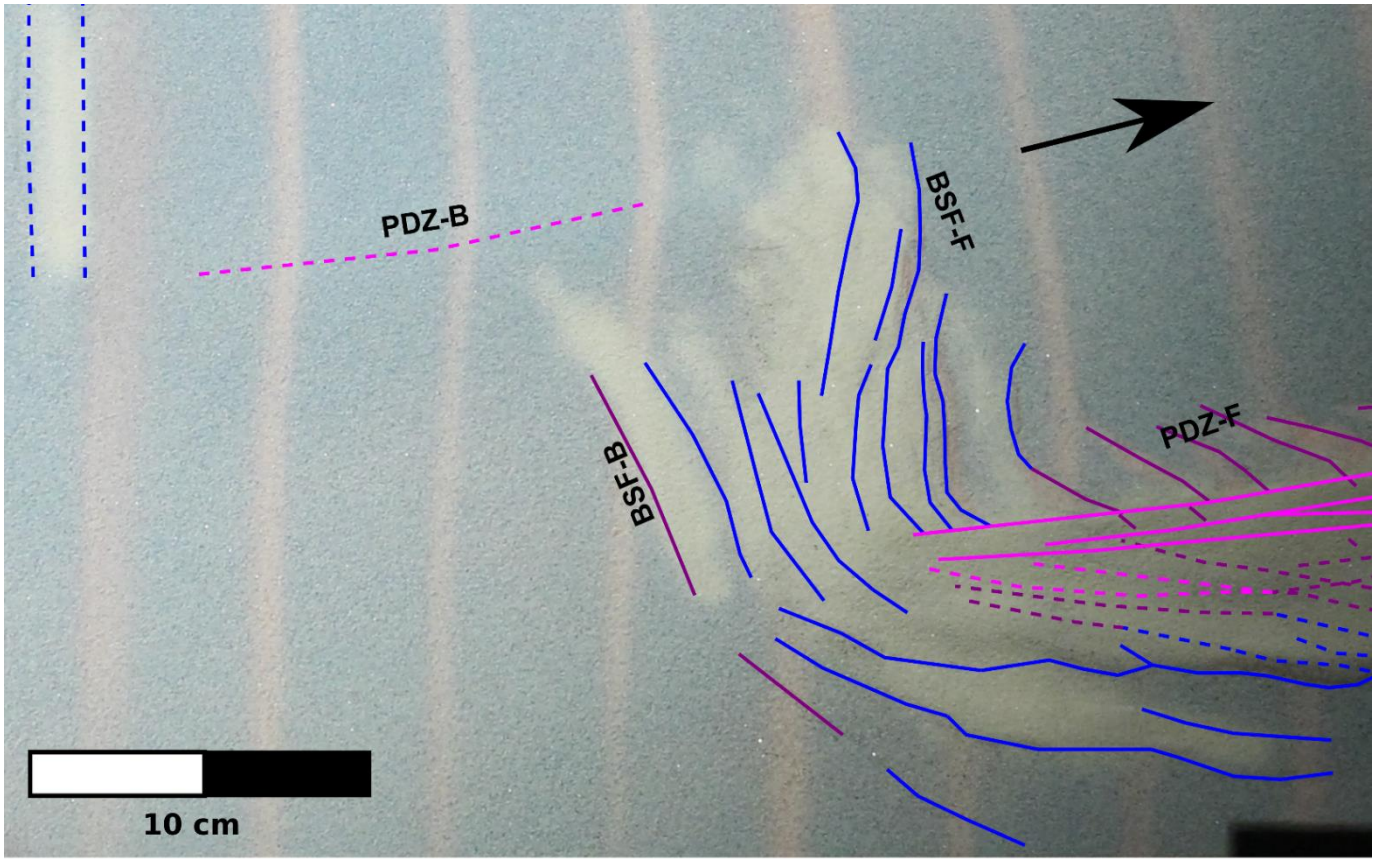

Figure C9 – Enlarged version of Figure 6.8g

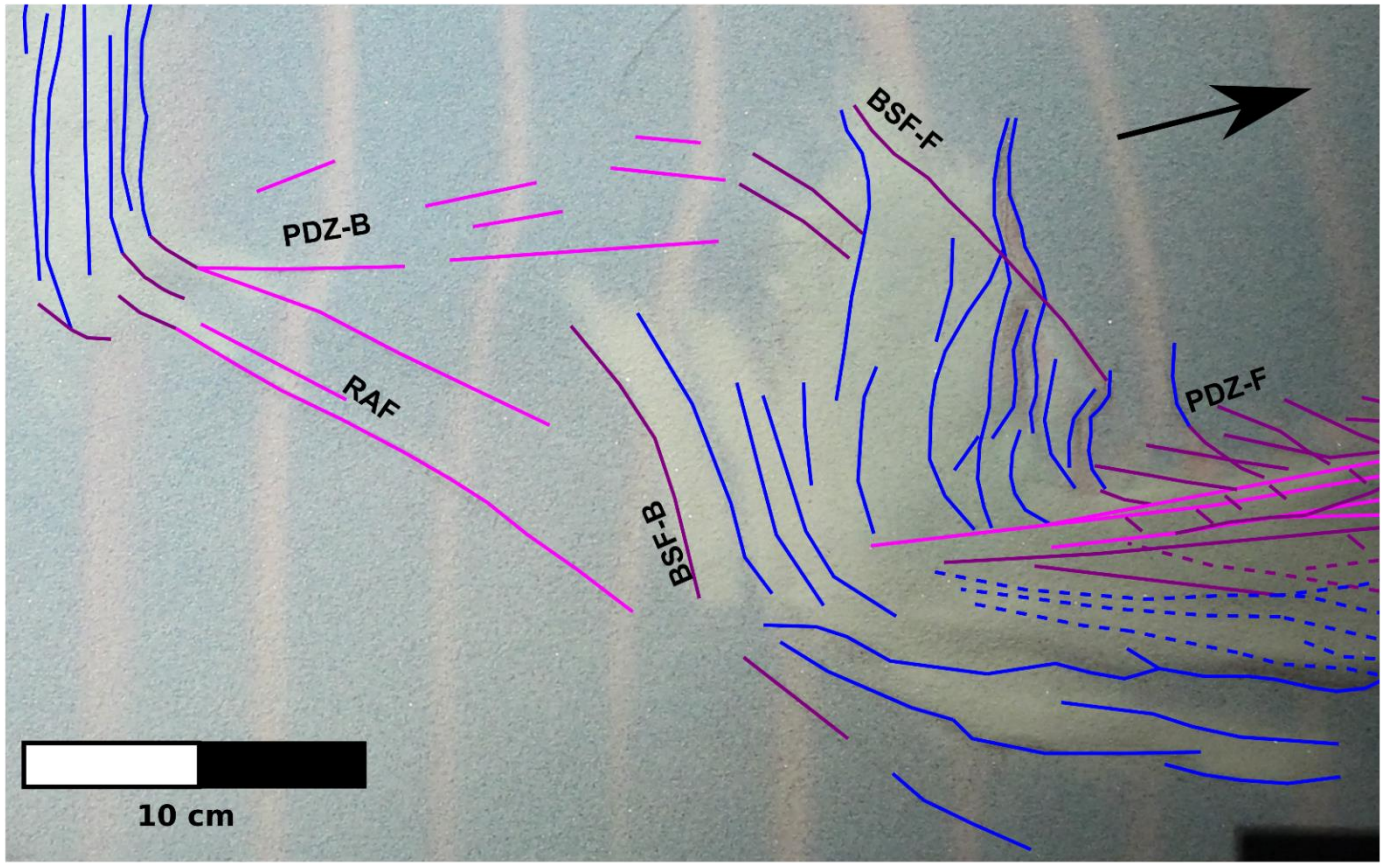

Figure C10 – Enlarged version of Figure 6.8h

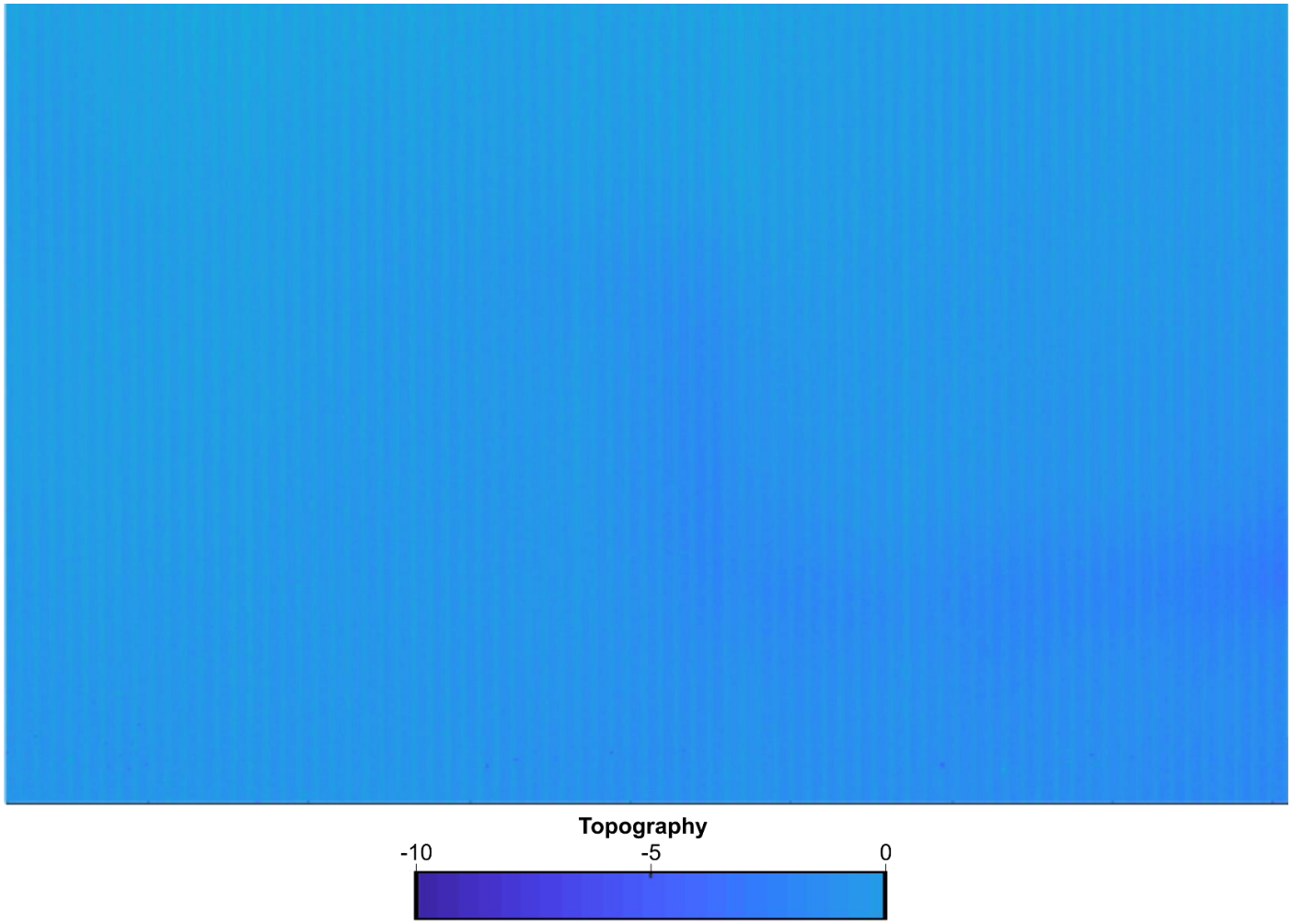

Figure C11 – Enlarged version of Figure 6.8i

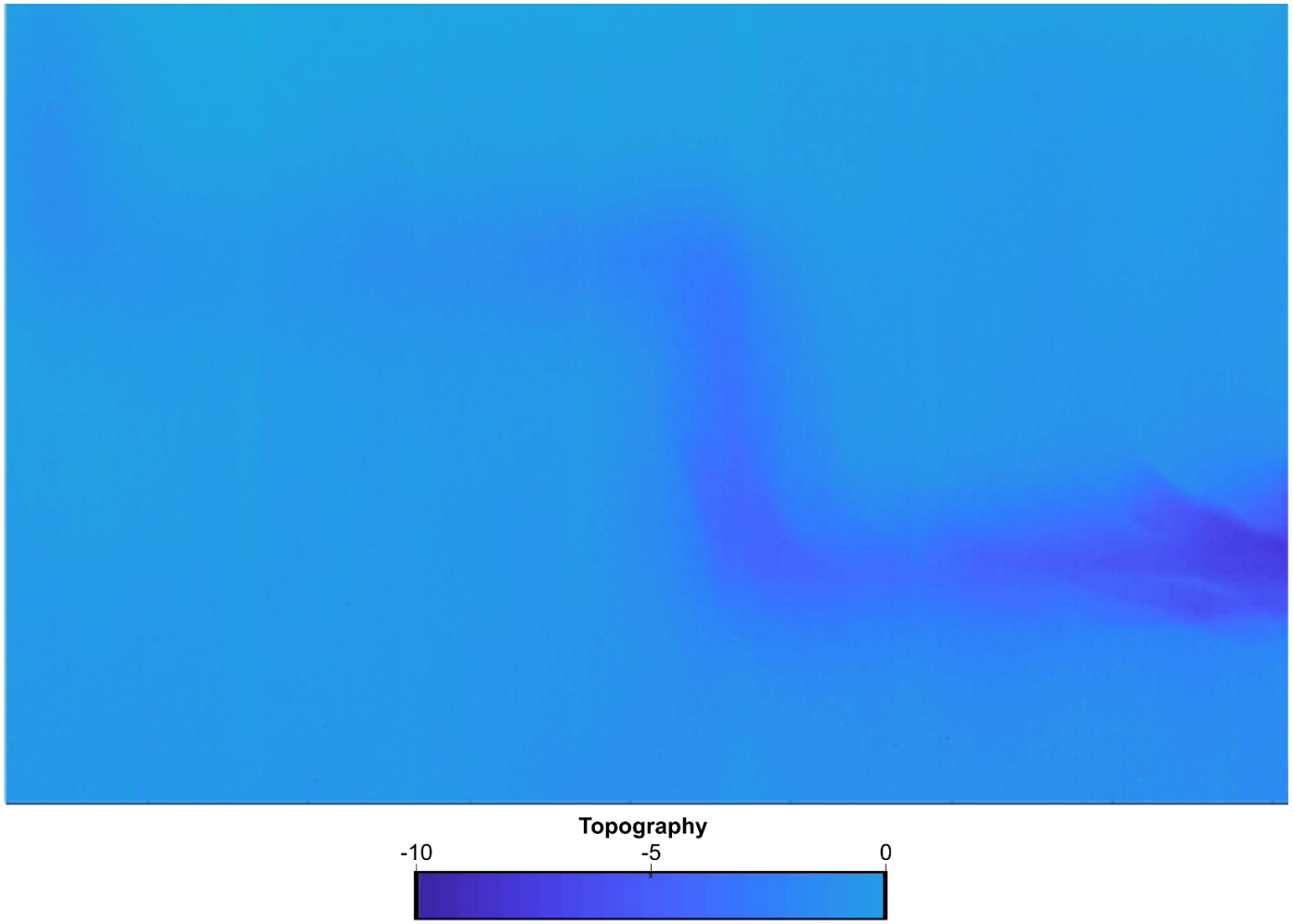

Figure C12 – Enlarged version of Figure 6.8j

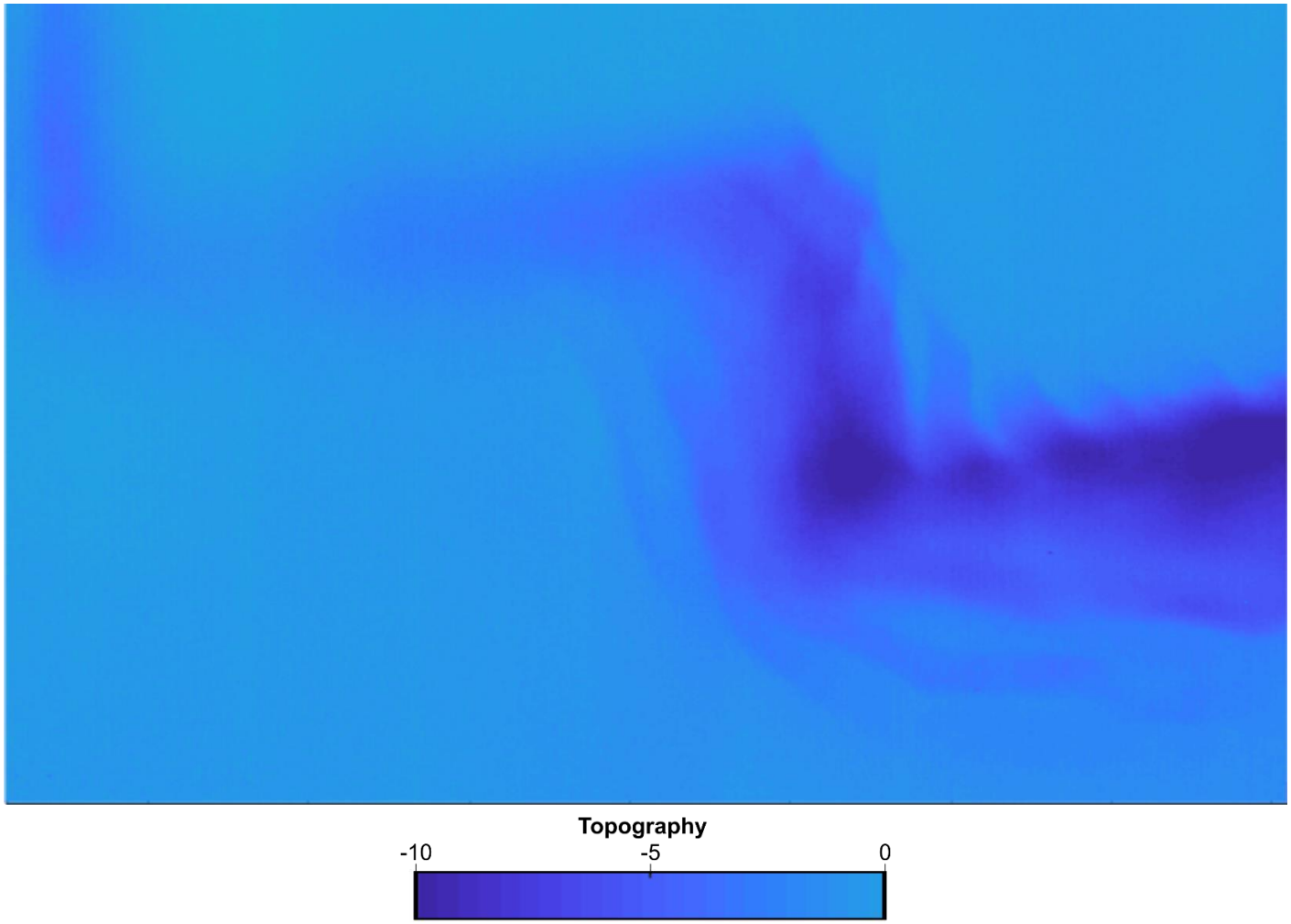

Figure C13 – Enlarged version of Figure 6.8k

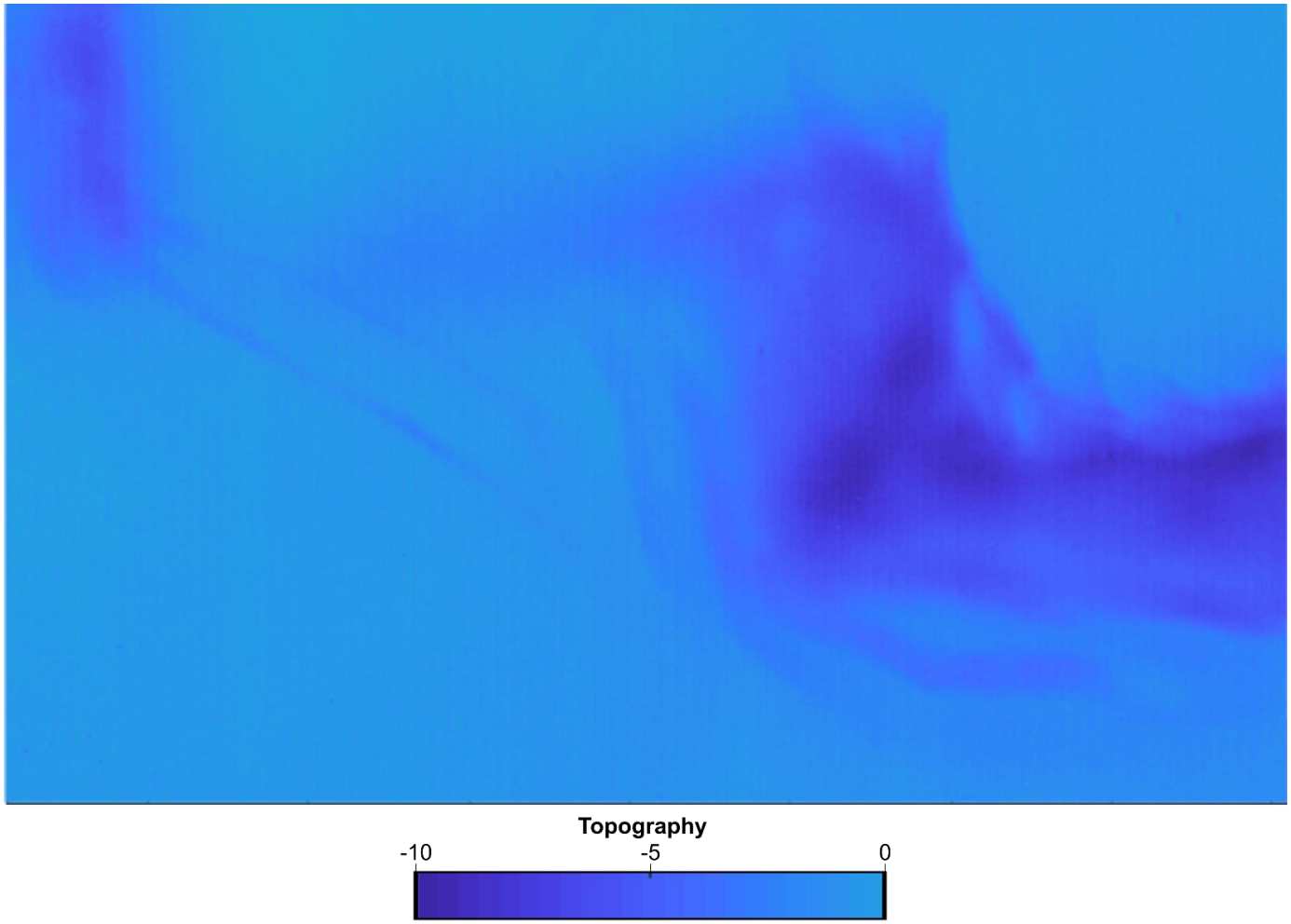

Figure C14 – Enlarged version of Figure 6.8l

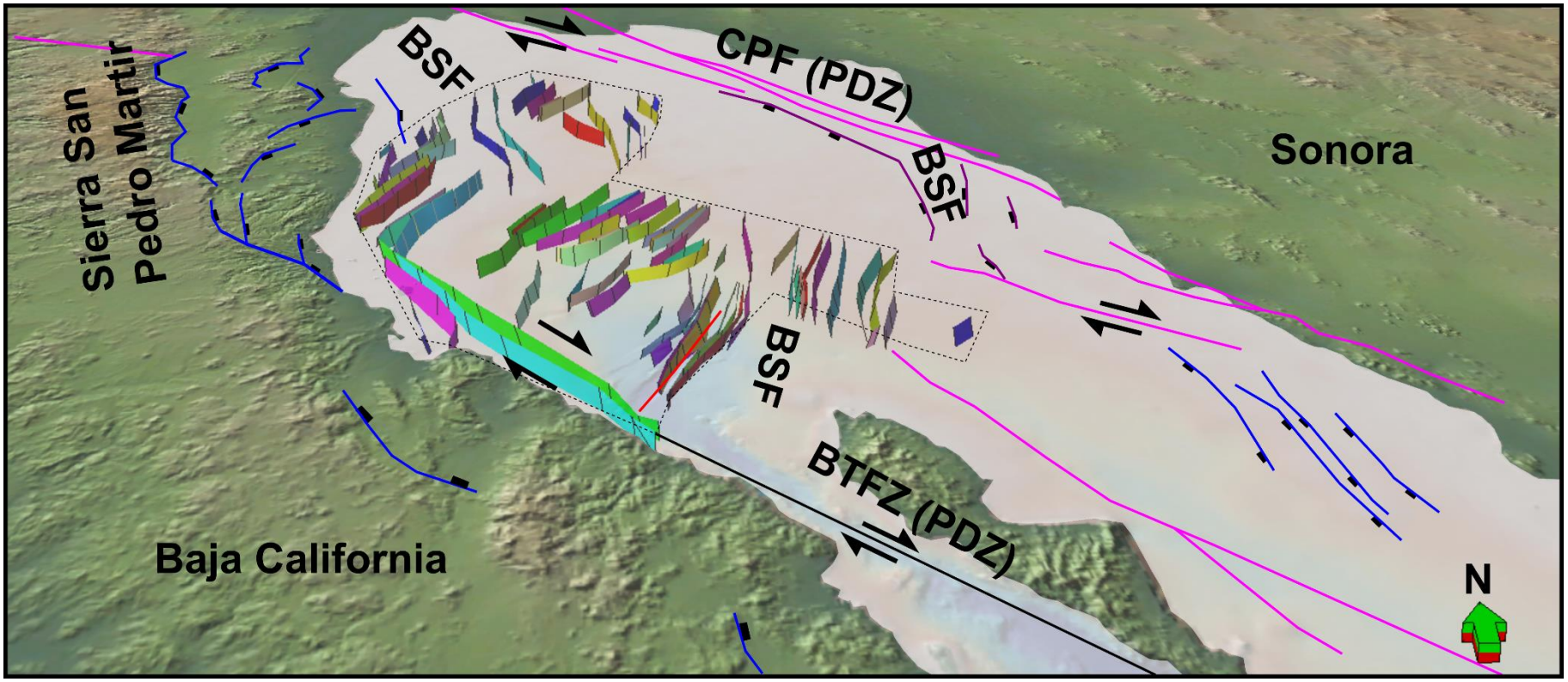

Figure C15 – Enlarged version of Figure 6.9b

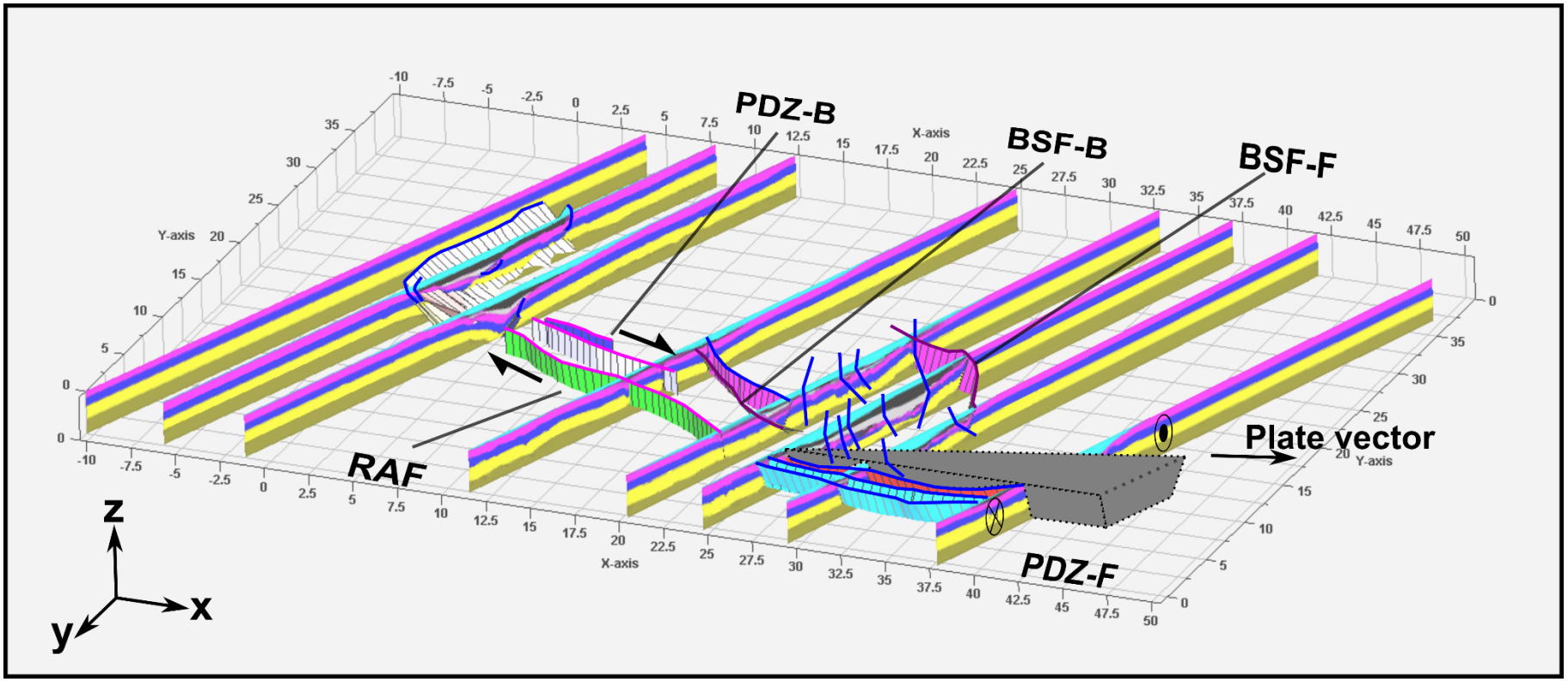

Figure C16 – Enlarged version of Figure 6.9d